Wireless Channel Characterization in the 5 GHz Microwave Landing System Extension Band for Airport Surface Areas

Final Project Report for NASA ACAST
Grant Number NNC04GB45G

Ohio University

School of Electrical Engineering and Computer Science
Avionics Engineering Center

Principal Investigator
David W. Matolak, Ph.D.

May 2006

Brief Table of Contents

Acknowledgements

Executive Summary

In this project final report, entitled "Wireless Channel Characterization in the 5 GHz Microwave Landing System Extension Band for Airport Surface Areas," we provide a detailed description and model representation for the wireless channel in the airport surface environment in this band. In this executive summary, we review report contents, describe the achieved objectives and major findings, and highlight significant conclusions and recommendations.

The report begins with a chapter on the project's goals and objectives, which include analytical and measured results gathered for developing the channel models. The introductory chapter also provides some discussion on the importance of this work, the overall project activities and their scope, and summarizes the contents of the remainder of the report. The second chapter contains a detailed literature review, including discussion of general channel modeling references, aeronautical channel references, and 5 GHz band channel references. It also cites a listing of publications generated from this work. Chapter three is an overview of channel modeling, which defines the primary channel parameters of interest, and introduces the mathematical notations used throughout the report. We describe which parameters were measured, which were computed from measurements, and which were estimated analytically. The third chapter also includes a brief discussion on specific uses of the channel parameters in wireless system design, and concludes with a description of measurement and modeling issues particular to airport surface areas, which yields division of the airport channel into three distinct propagation regions. In chapter four, we describe the measurements taken during this project. The test equipment and its capabilities are summarized, along with the test procedures. The three types of airports measured—large, medium, and general aviation—are also described. This fourth chapter also describes additional measurements made for point-to-point links on the airport surface, and when transmitting from an airport field site instead of the air traffic control tower. The chapter concludes with a summary of the measurement data and some example plots. Chapter five describes the extraction of channel parameters from the measured data. This includes data pre-processing, introduction of additional parameter definitions, and processing considerations in model development. These processing considerations lead to our development of two sets of channel models: a "high fidelity" model, and a "sufficient fidelity" model. Chapter six presents the actual channel models, beginning with a propagation path loss model, then detailing the channel impulse response models for the three airport sizes, three propagation regions within the airport, and for the high-fidelity and sufficient-fidelity cases. These models are also particularized to several values of channel bandwidth commonly employed. The chapter concludes with a brief verification of the model outputs, in comparison with measured data. The seventh chapter provides a summary, conclusions, and recommendations based upon the project results. A complete list of references and abbreviations is also provided, as are several appendices that support the main body of the report.

As described in Chapter 1, the project objectives we successfully attained are as follows:

1. Identification and Collection of Key References: Chapter two contains a discussion of the references. The reference list is of value for confirming that our work in the band and environment of interest was not previously done; for providing a resource list for others

5

wishing to study or continue this work; and for gathering information on experimental and analytical techniques employed in measurement and modeling.

2. Development of a Basic Airport Classification Scheme: We have developed a scheme, based upon both airport physical size and measured channel delay spread data, for classifying airports. Airports within a category exhibit largely similar channel characteristics, so once classified, an airport channel model can be selected.

3. Collection of Representative Channel Measurement Data: A measurement campaign was planned and conducted to gather data used for modeling propagation path loss and channel impulse response characteristics. We measured channel characteristics at two large airports, one medium airport, and three small (GA) airports. Measurements were also made for point-to-point links, and for transmission from an airport field site.

4. Development of Channel Models: Detailed Characteristics and Software: The measured data was used to construct mathematical models for the channel. These models are in the form of time-varying tapped delay lines—the most convenient form for both analysis and computer simulations. For propagation path loss, a simple analytical formula was developed. The models for the channel tap amplitudes (and phases) are statistical, and methods for generation of the random processes in simulation were developed.

The major findings of our work pertain to particular aspects of the channel characteristics. These findings are listed next.

1. Propagation path loss: We model path loss, in dB, as a logarithmic function of distance, relative to that at a reference distance d_0. Despite some limitations in collecting path loss data, we were able to estimate models for both line-of-sight open (LOS-O) areas, and for non-LOS areas with a substantially strong first-arriving signal, termed non-LOS-specular (NLOS-S) areas. For the line-of-sight open areas, path loss is well modeled by that of free space; for NLOS-S areas the reference distance is d_0=462 meters, at which path loss is 103 dB. Path loss increases at distances beyond d_0 at a rate of $10n\log_{10}(d/d_0)$, with n=2.23. We were unable to measure and model path loss for completely obstructed, NLOS areas. The measured standard deviation of the fit to the NLOS-S path loss model is 5.3 dB.

2. Fading channel amplitude statistics: Due to the significant differences between airport surface areas and many other common terrestrial communication environments (e.g., cellular), the amplitude statistics we measured were often distinctly different from those used in these terrestrial environments. Most significantly, for the airport surface environment we frequently found fading amplitude statistics worse than the widely used Rayleigh fading model. This applies to the channel from a mobile to either the air traffic control tower or to an airport field site. For point-to-point links with directional antennas, the fading amplitudes are well modeled as having very mildly fading Ricean statistics. For the severe "worse than Rayleigh" fading conditions, we also found that fading of

multipath components at different delays was often correlated, also in contrast to common terrestrial models.

3. Multipath persistence and non-stationarity: Because of the dynamic nature of the airport surface environment, the channel fading environment is time varying. Thus, over long enough time periods—on the order of a few milliseconds when platform velocity is large to a few hundred milliseconds for low velocities—the channel is statistically non-stationary. As a vehicle moves about on the airport surface, particularly near buildings and concourses, or in the vicinity of other vehicles, the multipath components of the channel at any given relative delay "come and go" in a manner that is best modeled as random. We have developed a random model for this "persistence process" that accounts for this effect. Although this effect has been known to exist for decades, it is only infrequently addressed in the literature, possibly due to the increased modeling complexity it requires. Our persistence model is straightforward, easily implemented, and realistically captures this important channel effect.

4. Fading rate and non-isotropic scattering: Although we did not directly measure Doppler spreads, for vehicle velocities on the airport surface, Doppler spreading can easily be bounded, and will be well below that of most common communication signaling rates. Fading will be very slow for any signaling rates above 100 kHz at velocities of 100 miles per hour and below; fading is even slower for lower velocities. For essentially all locations we measured (and visually observed) on all airports, scattering will be non-isotropic in azimuth about the receiver. This is unlike common terrestrial models for which the receiver is often surrounded by reflecting/scattering surfaces, but is not surprising given the nature of airport layouts.

Next we briefly cite the most significant conclusions and recommendations from this project. A more detailed discussion of both these topics appears in the final chapter of this report.

Conclusions

1. For bandwidths above about 1 MHz, the airport surface channel is very dispersive, and to be accurately modeled over even typical communication system packet durations (e.g., 10 milliseconds), requires a statistically non-stationary tapped delay line model, with detailed tap amplitude fading statistics, and pairwise tap correlation coefficients for all taps.

2. Fading in some cases is severe, characterized concisely as having amplitude statistics that are "worse than Rayleigh."

3. Amplitude fading is also very dynamic, with multipath components exhibiting random "birth-death" like behavior in time.

4. The airport surface area can be divided into three distinct propagation regions, from the least dispersive LOS-O, to the intermediate NLOS-S, to the most dispersive NLOS

region. Airports of all three sizes (large, medium, and GA) contain each of these regions, although the GA airports have very little NLOS conditions. The worst case is the NLOS region for large airports.

5. The use of airport field sites for transmission can not only enhance signal strength in areas that do not have a LOS to the air traffic control tower, but can also reduce the channel dispersion. The use of such field sites will be essential to reliable communication over the entire airport surface area.

6. Due to the often large buildings on or near the airport surface, significant, stable, multipath reflections will often be present in point-to-point links as well as in mobile links.

Recommendations

1. For reliable communication on the airport surface area in this band, candidate wireless technologies should employ these channel models in evaluation (and not those developed for other settings, e.g., cellular). The "sufficient fidelity" models should be used for this, with the appropriate bandwidth.

2. Given our limitations on path loss modeling, in particular for the NLOS region, it might be prudent to conduct a short measurement campaign to better measure and model propagation path loss in this region at large airports. In the absence of this, some care should be used in selecting a path loss model based upon other measurements for other terrestrial settings.

3. To maximize the utility of the airport surface communication network, it would be advisable to consider extending the range of the network to include some part of "terminal airspace." Additional investigation is required to assess the feasibility of this.

4. To effectively meet airport surface network requirements in terms of data throughput and reliability, a careful partition, or "channelization" of the 5 GHz MLS extension band should be designed. This should take into account our frequency domain channel characterizations.

Chapter 1: Introduction

1.1 Prologue

This report is the final report for the project entitled "Wireless Channel Characterization in the 5 GHz Microwave Landing System Extension Band for Airport Surface Areas." The work was supported by the NASA Glenn Research Center, under the Advanced Communications, Navigation, and Surveillance, Architectures and System Technologies (ACAST) program. This report covers work done during the project period from August 2004 through December 2005.

In this introductory chapter, we describe the goals and objectives of this project, primarily in the context of the analyses and measurements undertaken to attain these goals and objectives. Some definitions are also provided.

The importance of the results obtained in this project is also discussed, both in the context of general communication system design and deployment, and in terms of the significance of the results for the aviation community and its future use of the microwave landing system (MLS) frequency band. This "future use" represents a driving motivation for this work. Some specific examples of the utility of the channel characterization results are also briefly described here [1]; more detail on this appears in Chapter 3, the Channel Modeling Overview.

This chapter also summarizes the actual activities undertaken for completion of this project—measurements and analysis. The project scope is also clearly defined in this chapter. This introductory chapter concludes with a description of the contents of the remainder of this final report.

1.2 Project Goals and Objectives

1.2.1 Context of Goals and Objectives

For this report, we generally refer to those aims that are extensive or comprehensive as "goals," whereas those aims that are less extensive, yet still more than satisfy the minimum required outcomes, are deemed "objectives."[1] As is common in scientific and engineering work, these required outcomes themselves were formulated over a period of time near the beginning of the project. Generally here, we make the distinction between goals and objectives explicit, unless it is obvious from context, or not of significant consequence.

Worth discussing at the beginning of this section is the definition of "channel characterization," which appears in the project title. The precise working definition of "channel" we defer to Chapter 3; at this point it suffices to define the channel as the "object under study," specified by the complete set of parameters for the complete set of paths an electromagnetic wave in the frequency band of interest takes from transmitter to receiver, over the spatial region of interest. The set of parameters is also described in detail in Chapter 3. When we use the term characterization, we refer to a "good description" of the channel. This can begin with, and

---

[1] This convention for goals and objectives is often used, for example, by the National Science Foundation.

includes, a text description, but for engineering purposes, this good description must be quantitative, and as thorough as possible. Conversely, the thorough quantitative description must not be so complex as to limit its usefulness—thus a balance is sought. We provide some quantification of this in Chapter 5.

The "good description" must also be placed unambiguously in the context of other, related descriptions. Some of this is done by a literature review (Chapter 2). As implied by the prior statement regarding characterization complexity, the final characterization must have in mind some *use* of the description. The anticipated uses of the description obviously affect the final characterization in terms of its form, level of detail, etc. The primary anticipated use of this MLS band channel characterization is expected to be in the evaluation and comparison of different transmission schemes that may be deployed on the airport surface, in the MLS frequency band. In order to best assist this evaluation, the characterization should contain a set of channel "models." These models are defined by their structure, and by sets of parameters that are defined mathematically. In particular, these models can be used as elements, or blocks, in a cascade of models for the other components in a wireless communication system.

Figure 1.1 illustrates this idea. The rectangular block components of Figure 1.1 lie primarily within the physical layer (PHY) of the communications protocol stack, but settings/parameters of the data link layer (DLL) and medium access control (MAC) layer can also be incorporated. The figure can pertain to one or more simultaneously-operating wireless links, which may be independent or correlated. In this figure, performance requirements of the communication system specify many values for parameters of the transmission scheme (e.g., required bit rate), and also for the reception scheme (e.g., required packet error probability). For a given transmission/reception scheme, the performance evaluation outputs depend—often strongly—upon the channel model(s) used. If the performance evaluation outputs indicate the system will meet its requirements, then system design can proceed on to the higher layers of the protocol stack, or by refining or augmenting the lower layer designs. If the performance evaluation outputs aver that the transmission/reception scheme will not meet requirements, then, with knowledge of the channel, appropriate remedies can be added at one or both ends of the cascade, and the evaluation repeated. This general discussion will be continued in the sequel, and additional specificity will be given to explanation of this topic in Section 1.3.
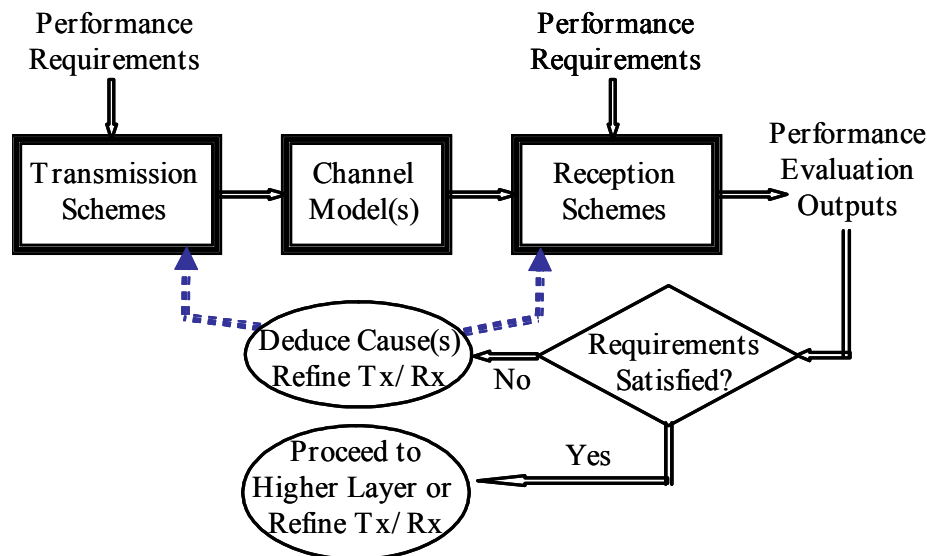
Figure 1.1. Conceptual illustration of use of channel model(s).

1.2.2 Project Goals

The project goals were articulated in an initial form in [1], then made more precise in [2]. These goals are as follows:

G1. Completion of a Comprehensive Literature Review and Initial Parameter Bounding

This goal consists of a complete literature review and estimates for limits to some of the channel parameters. The literature review is described in detail in the next chapter, and this part of the goal has been essentially achieved. Most of the review was conducted near the early part of the project, in which first general, and then specific references were gathered, organized, and reviewed. The literature review continued throughout the project duration.

Initial parameter bounding was intended to derive estimates for limits (upper and/or lower) on several channel parameters, including delay spread and coherence bandwidth, Doppler spread, and attenuation. Some of this was completed in the first quarter of the project, and these estimates are provided in Chapter 3. The purpose of this task was to obtain parameter value limits against which measurements could be validated. An additional use of the bounds is to enable prompt comparison with other channel environments (e.g., terrestrial cellular, or air-to-ground). The aim was to derive these estimates based upon information on the physical dimensions and composition of objects on and near the airport surface area, along with basic principles of physics. As noted in the description of the following goal, this was simply not possible with any degree of thoroughness due to the difficulty of obtaining airport environment information. Nonetheless, as stated, some initial parameter estimates were developed.

G2. Development of a Channel Classification Scheme

This goal was to develop a systematic method for classifying airport channels based upon detailed data on airport size, numbers of buildings and their characteristics, and local area information. This local area information includes descriptions of buildings outside but near the airport, highways and roadways outside but near the airport, nearby bodies of water, and any other large physical features near the airport such as hills, groves of trees, etc. With this information from a number of airports, along with the software models of the next goal, and the measured data from the subsequent goal, the most prominent airport features in terms of their affect upon the channel could be determined, and ranked in order of significance. The distribution (relative frequency) of these features could also be ascertained.

The ultimate use of this channel classification would the ability to quickly "assign" any airport to a "class" based upon its physical description. With each class is associated a channel model or set of models. The assignment of an airport to a class would be "streamlined" with experience, using the most prominent features noted above; only in the beginning of the effort would the detailed airport information be used.

Unfortunately, the type of information on airport characteristics listed above is not available in any centralized location. Each airport management organization does possess plan drawings, photographs, etc., for their own individual airport (or perhaps for several airports within a geographic region), but obtaining even this limited information, which is not always

completely current, was generally not easy or not quick. In addition, the information is not standardized in any way, so that comparison and classification would be slowed. We note that the absence of this type and quantity of organized information is not the fault of the airport management organizations or any other entity—a need for this type of database has apparently never arisen in the past.

Because of the lack of detailed information, this goal was essentially abandoned, and an approximate, empirical classification was adopted. This is described in the next section on objectives.

G3. Development of Validated Software Models for Attenuations and Delay Spreads

One part of this goal was to employ the channel modeling software package "Wireless InSite," from Remcom, Inc., to first construct, then validate by measurements, developed software models for the prediction of channel attenuation and delay spread in a given airport environment. As with the previous channel classification goal though, in order for the software to yield accurate predictions, a significant amount of information regarding the airport surface physical (and electrical) characteristics is required. Since much of this information is not readily available, we have deferred this goal to future work.

The software models for actual simulation of the channel dynamics have though been developed in careful detail, and these actually reside under goal G5, and are discussed in depth in Chapters 5 and 6. These are the models based upon measurements.

G4. Collection of a Comprehensive Set of Measurement Data

Within this goal are an interference assessment and the wideband channel sounding measurements. Although the definition of what constitutes a "comprehensive" set of measurements may be debatable, there are both practical constraints as to how many airports can be visited for measurements, and sufficiency considerations that eventually render additional measurement efforts beyond some point of limited value. Nevertheless, in the beginning of this project, the number of airports at which measurements were planned ranged from as few as three to more than ten. The types of airports considered were varied, from busy, urban airports to busy airports in wide open areas. (Note that the airports being discussed here are generally "large" airports, and do not include general aviation (GA) or "untowered/uncontrolled" facilities. Although we did measure and model for these smaller airports, the primary intent of the project was to characterize the channel for larger facilities.)

The wideband channel sounding measurements were to collect channel impulse response (CIR) characteristics for mobile platforms moving on the airport surface, through all areas in which aircraft and ground vehicles move. This goal was essentially met, via measurements at three large airports (and three GA airports).

Interference characterization consisted of both an analytical "survey" of existing emitters of electromagnetic radiation in the given band (permitted by regulatory authorities), and actual measurements of this interference. Both methods yielded the same conclusion: the MLS extension band is at present un-used in the airports we visited. Hence, this part of the goal was fully achieved.

G5. Development of Detailed Channel Simulation Models

This goal was to develop (and validate) comprehensive channel models, implemented in software (MATLAB ®). These models would include the effects of channel dispersion, fading, and the variation of these characteristics over time and space (airport "regions"). Propagation path loss was also to be modeled. The models were to be empirical, statistical models, supported also by theory, and which capture the primary behavior of interest for communications applications. Chapters 5 and 6 provide extensive detail for the models developed for this goal, which has been successfully achieved.

1.2.3 Project Objectives

These objectives were developed from the preceding goals. Some of the goals were ultimately deemed to be beyond what was actually needed. That is, for satisfying the primary aims of the project, not all the above goals required completion—at least not at the present time. For example, goal G2, the channel classification system, is likely not required in a comprehensive form at the present time, and could likely benefit from insights gained from some initial system deployment and experience. Attaining this goal could be more critical in the future when multiple wireless systems are to be deployed and will operate simultaneously at a given airport. Similarly, the airport "database-based" software models of goal G3, while very useful, are likely not mandatory for all airports, particularly at this time, prior to any substantial "congestion" in the MLS extension frequency band. As with goal G2, these models could be most beneficial after some initial system deployments.

The following list of objectives contains the most important features from the list of goals. Other than what we identify in Chapter 7 as items for future work, all these objectives have been successfully achieved.

O1. Identification and Collection of Key References

As noted in the first goal G1, we provide a detailed literature review in Chapter 2. This is of value for (1) clearly confirming that our work, in the band of interest and in the environment of interest, has not been previously done by anyone; (2) providing a resource for others who wish to study and/or continue this work; and, (3) gathering information on both desirable experimental techniques and analytical techniques to be employed in the measurement and modeling.

O2. Development of a Basic Airport Classification Scheme

This objective is our empirically-based alternative to the comprehensive classification of goal G2. In this scheme, based upon both airport physical size and measured delay spread data, we planned to devise a simple airport classification scheme, for which airports within a category exhibit largely similar channel characteristics. We proposed the following simple set of three airport categories: small, consisting of GA airports; medium; and large. The classification scheme is described in some detail in Chapter 3.

O3. Collection of Representative Channel Measurement Data

A measurement campaign was planned and then conducted to gather data for modeling propagation path loss and channel impulse response characteristics. The objective was to gather this data for a range of airport types, representative of "typical" airports in the US, as well as at least sampling some near worst-case settings. Channel characteristics at two large airports, one medium airport, and three small (GA) airports were measured. For each airport, a substantial amount of data was gathered; this is summarized in Chapter 4.

O4. Development of Channel Models: Detailed Characteristics and Software

This objective was to use the measured data to construct mathematical models for the channel. The models were to be developed in the form of tapped delay lines—the most convenient form for both analysis and computer simulations. For propagation path loss, a simple analytical formula was to be developed. Since the models for the channel tap amplitudes (and phases) are statistical, determination of the random process parameters associated with them was also to be done. The developed models contain *more* detail than originally planned.

1.3 Importance of Channel Models

The importance of accurate channel models is reviewed in this section, in terms of their effect on efficient communication system design. Also described is how this translates into the broader goal of supporting the aviation community's use of the MLS extension band in helping modernize airport operations.

1.3.1 Use of Channel Models in Communication System Design

The use of channel models for communication system design and evaluation is widespread, and universally accepted as an important element of system optimization. The discussion in this subsection is drawn in part from that in [1].

Mathematical characterization results provide fundamental knowledge for all physical layer waveform design and analysis. Well before building or deploying any system components, the use of thorough channel characterization information allows prediction and tradeoff studies that address various aspects of communication system design, such as communication link range, optimal channel (or subchannel) bandwidths, and system performance (bit error ratio, latency, etc.) for *any* potential waveform used across the channel [3]. The use of a model with as wide a bandwidth as possible is versatile in the sense that it allows generation of models for virtually any smaller value of bandwidth as well.

In addition, the physical layer performance characterization is indispensable for the design and performance prediction for higher layers in the communications protocol stack, which depend upon the physical layer for message transfer [4]. The physical layer performance directly affects the data link and medium access control layers, and through these layers, affects the performance of all higher layers.

Example physical and data link layer design items upon which the channel characterization has a significant effect include the following [5]:

- modulation(s) and corresponding detection schemes [5]
- forward error correction coding and companion interleaving schemes [6]
- antenna characteristics, including diversity antenna parameters [7]
- receiver processing algorithms, including those for synchronization, interference suppression, combining, etc., all of which are adaptive [8]
- signal bandwidths [3]
- adaptation algorithms for resource allocation in time, frequency, and spatial domains [9]
- physical facility siting rules [10]
- authentication and user ingress/egress latencies
- duplexing and multiplexing methods [8]
- security measures and performance (against eavesdropping, jamming, spoofing, etc.) [11]

Table 1.1 lists a number of important channel parameters and the signal design parameters they directly affect. The signal design parameters refer mostly to the physical and data link layers, but as noted, have impact directly upon higher layers. The parameters are defined in Chapter 3.

Table 1.1. Example channel parameters and the corresponding signal/system parameters they affect.

Channel Parameters	Affected Signal/System Design Parameters
Multipath delay spread T_M, and coherence bandwidth B_c	Signal bandwidth B, symbol rate R_s, chip rate R_c, subcarrier bandwidths
Channel attenuation α	Transmit power P_t, link ranges, modulation/detection type
Doppler spread f_D, and coherence time t_c	Data block or packet size, FEC type and strength, transceiver adaptation rates, duplexing method
Spatial correlation ρ_s, and temporal correlation ρ_t	Diversity method, FEC type, multiplexing method
Interference	Modulation, FEC type

The last row of Table 1.1 lists interference as a channel parameter. Although interference is not a result of the propagation channel itself, its presence cannot be ignored in signal design, and for any wireless system, can become a significant impediment to good performance.

The channel models contain mathematical descriptions that can be used for analysis, but often the analytical approach becomes intractable, at which point evaluation and tradeoff can be conducted and extended via companion computer simulations [12]-[14]. Thus the channel model consists not only of mathematical descriptions, but also the "implementation" of these mathematical descriptions in software.

A comment regarding adaptive systems is in order at this point. Specifically, several current and emerging wireless communication systems are being designed to be able to adjust many of their parameters in response to changing conditions (number of subscribers, interference, channel conditions, etc.). Yet even these systems have "configurable" parameters,

the optimal setting of which relies upon, or at least benefits from, knowledge of the channel. In addition, channel knowledge is useful for planning any future system upgrades. As the number of users and applications for the wireless systems increases, meeting the system capacity, data rate, security, and integrity requirements will become more and more challenging. Thus, the need for communication systems that can perform near optimum becomes greater. This further motivates the acquisition of accurate channel knowledge, since if a wireless communication system is deployed without a thorough channel characterization, the system will most certainly be sub-optimal. Well-known performance limits that can arise from not accounting for channel characteristics include an irreducible channel error rate that can preclude reliable message transfer, and severely limited data carrying capacity. Finally, for comparison of multiple, contending communication systems *before* any deployment, accurate channel knowledge is vital for a fair and common evaluation. The channel models developed here can be used by any researchers or engineers who evaluate the performance of waveforms or systems on this channel. Since the models are based upon both theory and measurements, they are in this dual sense more "realistic" than models based upon analysis alone.

Knowledge of channel statistics can be used in system design in many very specific ways. Here we provide just a few examples of how the channel model can explicitly be used; some additional detail on this appears in Chapter 3.

1. For multicarrier OFDM systems (such as the IEEE 802.11/16 [15]), a guard time or "cyclic prefix" is employed specifically to avoid intersymbol interference caused by multipath dispersion. The length of this guard time should be as long as (or longer than) the channel impulse response, and this impulse response length is directly quantified by the channel delay spread we measure and incorporate into our models.

2. When the channel taps are highly correlated (which we have found in many cases), the amount of attainable time diversity, or multipath diversity, is greatly reduced over that which is available with uncorrelated taps. Thus, simpler combining or equalization schemes should be used, as more complex ones offer little benefit other than an often very small gain in received signal energy. This offers design guidance for both narrowband (equalizer) and direct-sequence spread spectrum (RAKE) single carrier schemes.

3. For multicarrier OFDM, multicarrier direct sequence (MC-DS) spread spectrum (SS) systems, or frequency-hopped (FH) SS, the channel coherence bandwidth should be used in design. For FH schemes, the average hop frequency difference should be larger than the coherence bandwidth to attain frequency diversity. In the MC-DS case, depending upon complexity and performance requirements, the coherence bandwidth is used to select both the number of subcarriers and their bandwidths (~chip rates). The coherence bandwidth is also of use in OFDM systems, as it can provide guidance for how the input data bits are distributed across subcarriers, and the data rate of each subcarrier.

4. For specifying link parameters such as transmit power levels, antenna gains, receiver amplifier quality (e.g., noise figure), and link margins, the path loss models provide invaluable information.

1.3.2 International Significance of the MLS Extension Band

Through industry support functions such as the Integrated Communications, Navigation, and Surveillance (ICNS) conferences and ACAST workshops over the past several years, NASA has identified protection of the 5000-5150 MHz band for aviation use as a top priority, for the following reasons:
- GPS navigation and WAAS/LAAS enhancements are circumventing the need for MLS deployments, leaving much of the MLS band either quiet or underutilized;
- Spectrum at 5 GHz presents enormous potential for revenue to short range, wideband wireless networking OEMs (e.g., 802.11/16 vendors);
- Spectrum auctions in or near this band present potential revenue streams for the federal government.

The combination of these factors has heightened the need to justify the continued use of this spectrum for aviation purposes.

The International Civil Aviation Organization (ICAO) is working to ensure that this spectral band remains allocated for aeronautical services. To this end, ICAO is preparing documents for submission at the International Telecommunication Union's (ITU) World Radio Conference (WRC), whose next major meeting is in 2007. United in the effort to support ICAO in this endeavor are the United States Federal Aviation Administration (FAA), and the European Union's aviation administration, EuroControl.

Specifically regarding WRC-2007, there are several agenda items that address the use of aviation spectrum. The following excerpt is an example of one of the most significant agenda items, item 1.6:

"To consider allocations for the aeronautical mobile (R) service in parts of the bands between 108 MHz to 6 GHz, and to study current frequency allocations that will support the modernization of civil aviation telecommunication systems."

This agenda item affords the opportunity to have areas of spectrum between 108 MHz and 6 GHz characterized for aeronautical mobile route services (AM(R)S).

Another reason why ICAO is interested in maintaining exclusive aeronautical allocation of the MLS extension band is simply to allow for *future* services. With the continued expansion of airport operations, growth in airline travel, and modernization of airports and air travel systems worldwide, the need for new communications applications and services will inevitably grow. Existing aeronautical frequency bands (e.g., VHF) are either fully used at present, or are near "saturation."

Hence, the results of this channel characterization have been, and are being, presented to domestic and international governing bodies so that there is a sound engineering argument for use of this band for wideband signaling on the airport surface, and so that this band may be included in regards to Agenda Item 1.6. Additional supporting information regarding the international significance of this band appears in Appendix A.

1.4 Project Activities and Scope

This section briefly describes the project activities and scope. The primary activities were the collection of measured data, and the subsequent processing of this measured data for

developing the set of channel models. These two activities are described in the next two subsections.

In addition to, and in support of, these two main activities, we also worked on the following tasks:

1. Collection and review of pertinent literature;
2. Specification and purchase of test equipment;
3. Collection and analysis of airport information for measurement planning and airport classification;
4. Development of measurement test plans;
5. Coordination with FAA, NASA, and airport personnel for measurement execution;
6. Composition of update documents for support of NASA in ICAO meetings;
7. Composition and presentation of papers for dissemination of interim results at conferences;
8. Development of basic models, and understanding, of use of Remcom Wireless InSite channel modeling software;
9. Participation in meetings with FAA and NASA personnel regarding project progress, and future work.

The scope of the project work was to characterize the wireless channel in airport surface environments, in the 5 GHz Microwave Landing System Extension band. As noted at the beginning of this chapter, channel characterization consists of development of descriptions, channel classes, and mathematical models and their corresponding software implementations. This explicitly excludes characterization in any other frequency band, although some aspects of the characterization are capable of being translated, at least approximately, to other frequency bands. The work also excludes characterization of air-to-ground (A/G) (and by reciprocity, this also means ground-to-air, G/A) channels. Yet, as with frequency band translations, some features of the airport surface characterization may also be of use in development of air-ground channel models.

1.4.1 Measurement Campaigns

The measurement campaigns can be viewed as the project activity most critical to success. Measurements were taken at several (large) airports. At each of these airports, measurements were made over a period of from one to three days. Detail on the measurements appears in Chapter 4. The basic measurement activities consisted of the following:

1. Review of test plan and procedures with airport personnel, adjustment if needed;
2. Set up of transmitter at air traffic control tower (ATCT), followed by calibration;
3. Mobile testing: transmission from ATCT, reception at mobile ground vehicle;
4. Non-mobile testing: transmission from ATCT, reception at field site;
5. Mobile testing, field site transmission: transmission from field side, reception at mobile ground vehicle

During measurements, the collected data was stored for future processing. In addition, numerous photographs and some short video clips were taken. Appendix C contains the detailed test plan and procedures.

1.4.2 Analysis and Modeling

The analysis and modeling activities were conducted in conjunction with measurements. Some analyses, such as initial parameter estimation, were done prior to any measurements. Others were applied directly to measured data, to derive channel parameters. The analysis employed well-known principles of physics, and corresponding mathematics (algebra, calculus, probability, statistics, etc.).

The modeling activities included review of existing techniques and models, application of mathematical techniques for pre-processing data, organizing and classifying data sets, and running statistical parameter fitting routines. Chapters 5 and 6 describe these procedures in detail.

1.4.3 "Added" Activities

In addition to the activities conducted to satisfy the objectives, throughout the course of this project we were able to complete additional activities that were not originally planned. First, in addition to taking measurements and developing models for channels at large airports, we were also able to measure and model for small (GA) airports. Second, in view of the possibility of deploying fixed (non-mobile) transceivers on the airport surface in a future network, we also made some measurements and developed initial models for the fixed point-to-point channel from the ATCT to these airport surface field sites. Third, given the propagation conditions measured, and generalizing the concept of the fixed transceivers, we made measurements and developed initial models for the mobile channel in which the transmitter was located at an airport surface field site, instead of at the ATCT. Finally, although essentially unrelated to this project, with the use of the measurement equipment, we were able to collect data and develop models for the wireless channel in a vehicle-to-vehicle (VTV) setting, in a number of environments. This has potential future application in proposed "intelligent transportation systems."

1.5 Contents of Report

The remainder of this report is organized as follows. In Chapter 2, we provide the detailed literature review. This review consists of citations for general channel modeling and measurement references, and specific aeronautical channel references. We discuss relationships to our project in terms of setting, frequency band, measurement approach, etc. The chapter also identifies several papers useful for processing the measured data. Chapter 2 also lists the several papers we have published from this work, including papers still in preparation.

In Chapter 3, we provide an overview of the topic of channel characterization and modeling. We discuss the common types of models, and how and where they are used. The most important channel parameters and their interrelationships are described. Also provided are some specific examples of how knowing these channel parameters can be directly used in communication system specification and design. Finally in Chapter 3, aspects of the channel characterization particular to the airport surface environment are discussed.

In Chapter 4 we have a detailed description of the measurements, including an overview of the test procedures. A brief summary of the primary measurement equipment system, the

channel sounder, is also given. The airports at which measurements were taken are described, and some of the airport characteristics are identified for the different categories of airports. We also describe the point-to-point, and field-site-transmission measurements. The chapter ends with a summary of the measurements, some example measurement results and interpretation.

Chapter 5 contains a description of the extraction of channel parameters from the measured data. This begins with a description of the pre-processing of the measured data, followed by discussions of some considerations affecting model complexity and fidelity. We also provide explanation of some of the parameters required to understand the measurement results and the modeling approach. Finally in this chapter, we introduce our approach and rationale for development of both "sufficient fidelity" and "high fidelity" channel models.

In Chapter 6, using the results of Chapter 5, we describe the detailed channel models for large, medium, and small airports, including the individual models for the three separate propagation regions within the airport environment. The modeling procedure is illustrated for several values of bandwidth, and for both "high-fidelity," and "sufficient-fidelity" cases. Example path loss models are also given. This chapter ends with a comparison of the model outputs with measured data, for the purpose of model validation.

In Chapter 7, the report is reviewed with a summary and conclusions. Highlighted here are the new and atypical findings, and suggestions for future work. A set of explicit recommendations is also provided.

Chapter 2: Literature Review

2.1 Introduction

In this chapter we provide a literature review. The review covers both books and papers used in this research. For the papers, we cite references in various areas of channel characterization for several environments, and also specifically for the aeronautical environment. We conclude this chapter with a list of papers generated from this research. We note also that additional references are cited throughout the remainder of this report, in places where they are most appropriate. This chapter covers the majority of the references.

2.1 Books

First, we cite [5] as a very thorough, general text reference on digital mobile communications. This text's 2nd chapter provides a fairly complete coverage of propagation modeling, channel impulse response characterization, and statistics. Focus is on the terrestrial environment. Reference [6] is another good, general reference on digital communications, with a clear and concise derivation of how Rayleigh fading statistics arise in a mobile channel.

The text [10] is one of the few books dedicated specifically to propagation, channel modeling, and measurements. Another is [16], which focuses more on electromagnetics. Parsons' book [10] is comprehensive, and provides much tutorial material on channel classification, path loss modeling, and statistical fading models. Treatments of diversity, and radio network planning are also included in this second edition.

Reference [14] is another useful text, like that of [10], but with a focus on modeling the various random processes typically employed in fading channel characterization with deterministic functions, specifically the sum of sinusoids method (usually attributed to Jakes [17]). The author provides a very thorough study of this method, which may have limitations in terms of the time duration for which the deterministic process accurately reflects the desired random process. Nonetheless, this treatment is useful for constructing many models. The book by Jakes [17] is now something of a "classic" in the area of mobile communications references. It derives various, now commonly used, models, including the Rayleigh amplitude distribution, and the "Clarke" Doppler spectrum for two-dimensional (2D) isotropic scattering. Finally, [18] is another classic reference on communications. Chapter 9 of [18] has an excellent discussion of fading channels and their correlation functions. This discussion includes an outstanding introduction, which covers the definition of fading from a practical perspective.

2.2 Tutorials and Definitions

Reference [19] is a comprehensive and seminal reference that defines with mathematical rigor and clear logic the various input and output relationships between signals transmitted over linear, time-varying channels. The most often used assumptions for the wireless channel seen in the literature to this day were developed in this paper. These are the wide-sense stationarity

(WSS) in frequency of a ("narrowband") bandpass channel, the uncorrelated scattering (US) between multipath components at different delays, and the combined WSSUS models. This paper is also useful for its definition of channel correlation functions, delay spread functions, and the scattering function, all of which are also commonly used today.

In [20], one of the authors of [18] provides a tutorial reference on fading. It begins with a discussion of the phenomenological effects behind fading, and short and long term types of fading, then moves into the statistical characterization of randomly varying channels in terms of correlation functions. The Rayleigh model is emphasized. Discussion of various physical causes of fading (troposcatter, ionospheric reflection), as well as a review of fading simulation and fading mitigation techniques is also included.

Reference [21], a publication by the ITU, provides basic definitions of multipath propagation terms (delay spread, etc.). This is useful for its conciseness. Also potentially useful are the definitions for the parameters "delay window," which is the duration in delay that contains a certain percentage of energy, and the "delay interval," which is the duration in delay between delay values that exceed a given value for the first time in the upward (+ going) direction, and for the last time in the downward (- going) direction.

Last in this category of references is [22]. This paper was one of the first to develop the so-called "composite" or "mixture" distributions for the fading amplitude in mobile channels. In essence, the fading amplitude is given by a combination of two distributions. The most commonly-cited "Suzuki" model is one in which the mean power of the Rayleigh-distributed received signal is distributed lognormally. This model for the probability density function (pdf) is an integral form, and hence is cumbersome analytically. Reference [5] describes cases where this integral pdf can be simplified to a more convenient product of pdfs form. This particular model is commonly used in simulations. The author (of [22]) provides some comparison with measured data for more common (non-mixture) distributions (well-known Ricean, lognormal, Nakagami, Rayleigh), and found best agreement with the Nakagami and lognormal distributions.

2.3 Path Loss and Shadowing

As with the phenomenon of fading, the investigation of propagation path loss also has a fairly long history. We cite some well-known references here. In [23], one of the first efforts to gather a set of comprehensive propagation measurement results is reviewed. The results are for propagation path loss, taken in and around Tokyo, Japan. Path loss for a range of frequencies, in several environment and terrain types, is plotted in numerous curves. Additional curves also contain correction factors for a range of antenna heights, different city sizes, terrain features (e.g., bodies of water), etc. This reference is widely cited, and often used in software path loss models. Reference [24] uses the results of Okumura, et. al. [23] to derive path loss estimates in the form of equations. All the essential results of [23] are provided in convenient equation form, including the correction factors.

In [25], the authors provide a good overview of path loss measurements, with modeling based upon the *10nlog(distance)* relationship, with *n* the path loss exponent. This paper is a concise introduction to the topic, with good examples of measured results. Reference [26] is another ITU document, which actually refers to path loss in an aeronautical setting. This document has a brief discussion on the origin of the presented path loss curves (namely the "IF-77" model from Johnson and Gierhart, 1977), which were generated (analytically) using

geometric optics with an LOS and ground-reflected ray, and combined with some measurements for correction. Path loss curves for a number of frequency bands, and transmitter/receiver height pairs are provided. The curves contain three sets, applicable to path loss for 5%, 50%, and 95% of the time, where for the *x*% curve, the path loss is *less* than the curve value for *x*% of the time. The lowest transmitter/receiver height values are 15 m/1 km. The curves provided also rely on a few other assumptions (atmospheric constants, etc.).

Another ITU document of interest is [27]. This document provides equations for path loss, based upon some measurements. Many of the settings are urban/suburban, and account for antenna heights and physical dimensions of objects such as streets and buildings. Some of this may be applicable to airport environments, with the limitation that most of the models specify application for ranges less than 1 km.

A reference that pertains to the suburban environment is [28]. This paper presents results of measurements at 1.9 GHz over a very large range of areas (95 existing macrocells). The typical *10nlog(distance)* relationship (with *n*=path loss exponent) was employed successfully, and the exponent *n* was modeled as Gaussian, with mean a non-linear function of base station antenna height. The mean function coefficients and variance were defined as a function of terrain type, and lognormal shadowing was also accounted for. The modeling approach, in which a large number of path loss measurements were collected, sorted, and fitted, and yielded Gaussian (and lognormal) parameters, is potentially useful for such large data sets.

In [29], equations for computing the signal attenuation due to rain as a function of carrier frequency and rain rate (in mm/hour), are provided. For the 5 GHz band, this is mostly insignificant except for the most extreme rainfall rates. For example, for rainfall rates of 100mm/hour, attenuation is approximately 0.3 dB/km. Thus, for all but exceptional cases and for the longest of distances on the airport surface, the effects of rain on path loss are negligible.

In [30], the authors report on very short range (< 100 m) path loss vs. distance and frequency, in three ISM bands (900 MHz, 2.4 GHz, and 5.8 GHz), for antennas that are very low to the ground (~5 cm). Data were collected and summarized for multiple area types, and the authors showed that the plane earth path loss model (single reflection) yields good agreement with some measured data, but that when additional energy is available from more than one reflection, the plane earth path loss model *over*estimates path loss.

The phenomenon of shadowing is often grouped with the effect of path loss. Most often, shadowing (roughly defined as blockage or obstruction of a transmission path over large distances relative to a wavelength) is modeled as having a lognormal distribution [5]. Reference [31] is one that discusses the use of the "duration of stay" of fades, roughly equivalent to the inverse of the average fade duration: the duration of stay is approximately equal to the average time the received envelope is above a given level. This reference provides some data on the second-order statistics of shadowing.

The most commonly cited model used to simulate shadowing is that in [32]. Reference [33] contains a generalization of the typical stochastic model for shadowing, essentially extending the model to two spatial dimensions. The sum of sinusoids approach is taken to approximate the presumed Gaussian shadowing in dB (which is the usual lognormal model for shadowing). The results show good agreement with theoretical results, in terms of the shadowing autocorrelation. The drawback to the approach is that the number of sinusoidal components required for the two-dimensional model is substantially larger than that for the usual one-dimensional model; the authors employed 50 sinusoids in their simulations. In addition, the

model assumes a circular symmetry of shadowing about the mobile, which will be applicable in some, but not all, environments.

2.4 Aeronautical and Satellite Channels

We include the topic of satellite channels in our review because for many settings, such as the air-to-ground case, the aeronautical and satellite communication environments are very similar. Although our focus is on the airport surface area, we include these satellite references for the insight they may provide, and for completeness. We also note that a portion of the MLS extension band is used for mobile satellite feeder links (from fixed ground sites to low-earth orbiting satellites).

In [34], the author analyzes the channel between an aircraft and a satellite. He uses his system and correlation functions [19] to characterize this channel, assuming primarily some scattering from the earth surface. Reference [35] is specifically aimed at communication between a satellite and a point on the earth. In this area, it is a now-classic reference for mobile satellite channel models, and is a good example of a "multi-state" model, in which the channel conditions can be cast as fitting more than one statistical "state." Based upon measured data, the authors develop the "Lutz model," which is a 2-state model for the amplitude probability density function (pdf). State one is a Ricean pdf, and state two is a Rayleigh pdf with a log-normally distributed mean power. With each state is associated a state probability—the probability of the channel being in that given state. The state-two pdf is available only as an integral expression, so is not very convenient. Good agreement with measured data was obtained using this model. Also, they show that the Doppler spectrum is typically not the same as the "Clarke" spectrum, since scattering about the receiver is not generally isotropic in the mobile satellite setting (unless the receiver is in a large city). This also arises because the Clarke spectrum assumes that scattering is two-dimensional.

Reference [36] describes models for fading for aeronautical-satellite links, and accounts for tropospheric effects (e.g., attenuation), ionospheric effects (e.g., scintillation), and multipath effects. Some of this material is from [34].

An early reference for aeronautical air-to-ground channels is [37]. The model employed in this paper consists of a dominant line-of-sight (LOS) component, and a "perturbation," the combination of which is cast in terms of a multiplication factor that multiplies the received signal. The perturbation is a function of the (earth) surface reflection coefficient, distance, and frequency. For narrowband signals, this technique represents a fairly nice way to model for its simplicity. In addition, for this narrowband case, the authors obtained reasonable agreement with measurements. As indicated by the title, [38] is something of a simplified model for the air-to-ground (A/G) channel. It is similar to [37], but less rigorously developed. This paper provides a very coarse analysis and characterization of an A/G channel, and assumes Gaussian statistics based upon a large number of reflected paths. Some other simplifying assumptions make the final results for amplitude distribution and correlation functions questionable.

A more recent reference pertaining to the aeronautical channel, including A/G and G/G cases, is [39]. (In fact, this paper is one of the few recent references that deals explicitly with aeronautical channels.) Worst-case and average delay and Doppler spreads were cited (some based upon geometry, not measurements), for four "phases of flight," including "parking," "taxi," "arrival," and "en-route." Two of the models here—for the "en-route" and takeoff/landing cases—were based upon some measurements taken at VHF. The "taxi" and

"parking" case models are based solely upon models for terrestrial cellular environments, which are substantially different from the airport surface environment. In addition, use of Rayleigh/Ricean statistics is not well justified. Well-known channel simulation techniques are covered, and a brief discussion of multicarrier system performance for the en-route case is given.

Finally, [40] is a recent work for the "aeronautical telemetry" channel. The aeronautical telemetry channel is one that uses a high-gain, tracking antenna at the ground site, so this model is rather application-specific. With this narrow-beam antenna, the channel was found to have an LOS signal, a dominant ground reflection, and a secondary reflection that can be well-modeled as having a Gaussian distributed amplitude.

2.5 Measurement, Simulation, and Data Processing Techniques

In [41], the author describes a measurement technique much like that which we employ. This (now "classic") reference was one of the first to employ channel impulse response measurements obtained with a spread spectrum sliding correlator to compute delay spreads and Doppler spreads for a land mobile radio channel. It presents a very good description of the channel sounder method of operation, and provides example measured data from the soundings. Absolute delay, rms delay spread, and delay window values were presented, as well as Doppler spectra at fixed delays.

Reference [42] is useful for its methods applied in organizing and analyzing channel measurement data. Despite its different application (measurements in a factory building), this paper provides a very thorough treatment of how to collect and sort statistics of channel measurements. Power delay profiles were measured, and organized according to four different parameters: LOS/NLOS (S) conditions, Tx-Rx distance (D), local spatial position (X, on grid of points separated by $\lambda/4$), and location (P, area of 1 m^2). The authors found lognormal fading to apply for large scale conditions (changing D), and also for some small scale conditions (changing X), which is unusual, but possibly specific for their factory environments. The characterization of distributions of the number of multipath components is also good (and is of course also site-specific). The authors also found that the propagation path loss exponent was a weak function of delay, and their computation of the temporal and spatial correlation functions was clear and concise.

The topic of the short paper [43] is estimation of an important fading parameter, the Ricean "K-factor." This paper describes a very simple method to estimate the K factor from measured data. Measurements pertain to a single frequency (or band much smaller than the channel coherence bandwidth), and to durations longer than the channel coherence time. By computing time average power and the second moment of this power, the K factor can be estimated. Corroborating measurement results are provided. Similarly, reference [44] pertains to estimation of the rate of change of the wireless channel, via measurement of the Doppler spectrum. These authors developed a method to determine the Doppler spread of a wireless channel from measurements of single-tone received power vs. time. Assuming wide-sense stationarity, the authors show how to compute Doppler power spectra for slowly varying channels. This method is fairly simple, and useful, and may prove to be a useful means of computing Doppler spectra for airport surface channels.

The paper [45], which formed part of the book [14], describes the approach of using sums of sinusoids to simulate Rician (and even Nakagami) random processes. Although the authors

consider only two types of Doppler power spectral densities (Clarke and Gaussian), the method seems generally applicable to any spectrum shape. They find the sinusoid amplitudes and frequencies that minimize L_2-norms of the pdf, and autocorrelation, respectively. They also describe simpler methods with slightly reduced accuracy. The biggest limitation appears to be that since the sinusoid amplitudes are equal, the deterministic simulation output yields an accurate autocorrelation and Doppler power spectrum for only a limited time, especially if the number of sinusoids is small. Nonetheless, it contains a rigorous analysis and some useful results that could be employed in simulation.

In [46], the authors investigate the channel delay spread based upon measurements taken in Toronto, CA, in the cellular frequency band (910 MHz). The authors contend that many previous papers have overestimated rms delay spread values. Their measurements support this contention. They also describe a very useful method for computing a threshold applied to power delay profile measurements, below which all measurements are considered to emanate from noise (either thermal or impulsive). This method has served as guidance for a similar thresholding technique we apply.

Related to delay spread is its approximate reciprocal, the correlation, or coherence bandwidth. In [47], the author performs a focused review of the estimation of frequency correlation functions, essentially refining the definitions of correlation or coherence bandwidths. He outlines a method to determine if the uncorrelated scattering (US) assumption is valid, specifies precise conditions to ascertain the actual presence of channel fading, and also describes a method to estimate wide sense stationarity (WSS) in time. A new estimate for the frequency correlation function, the frequency correlation estimate (FCE), is developed, which does not rely on the WSS assumption. Several good examples are provided. The techniques in this paper are used directly in our data processing.

2.6 References Pertaining to the 5 GHz Frequency Band

In light of the dearth of work conducted to investigate the MLS band in detail, and because of the similarity of channel characteristics for different but close frequency bands, several references that studied the 5 GHz channel were collected and reviewed.

In [48], the authors report on empirical work for an indoor channel at 5.3 GHz, and bandwidth 53.75 MHz. Measurements were taken in four office environments (one an airport corridor) with both LOS and non-line-of-sight (NLOS) conditions. Delays were characterized via the cumulative distribution functions of rms delay spread. The measured path loss was fit to a log-distance model, which yielded propagation path loss exponent n, and area path loss standard deviation. Computations of spatial and frequency correlation were made, but not very clearly explained. Finally, small scale (channel impulse response, CIR) models were also developed using tapped delay line structures. As is commonly done, Rayleigh and Ricean statistics were used to model the amplitude distributions of the taps.

Several of the same authors contributed to [49], applicable to outdoor environments. In this paper, the authors considered propagation characteristics in the 5.3 GHz ISM band in outdoor settings. They derived parameters for the typical "*10nlog10(distance)*" path loss models for both LOS and NLOS cases, in several different environments they term urban, suburban, and rural. They also compiled results for rms delay spreads and spatial correlations, and developed a closed-form mathematical model for the number of significant multipath components in the

channel impulse response (similar to [42]). Maximum values of rms delay spread found were on the order of 100 ns, for distances up to 300 m. One other interesting measurement was that of rms delay spread and received power vs. azimuthal angle of arrival, obtained using directive antennas. For the urban environment, they found that most of the power was received over an angular spread of much less than 360°, typically on the order of 90°, indicating non-isotropic scattering.

Reference [50] is a report that discusses an analysis for the MLS propagation environment based upon electromagnetic field theory, with suitable approximations. The author included some corroboration with measurements, but the measurements were coarse by today's standards. (This is not meant to be disparaging--just a fact of technological and academic progress.) For the cases that compare with measurements, the measurements are primarily of the ratio of received multipath power to LOS power, much akin to a Rice factor, and for the most part, the calculations are within about 6 dB of measured values, although for some cases, differences more than 10 dB are evident. The measurements were narrowband, but the computer program from which they compute their parameters could conceivably be augmented to "broaden" the bandwidth. Although this report contains much of interest for a full-wave electromagnetic estimation of the wireless channel, there are several comments worth making: first, there was no real modeling of non-LOS cases, but some modeling of shadowing. This is logical, since they were specifically interested in the actual operation of a microwave landing system, which presumes the presence of a LOS component. For modeling the airport surface channel, we are interested in both LOS and NLOS cases. Second, several software packages (e.g., Wireless InSite) are available today that can be used to more quickly and more accurately perform the computations they did, and can then be compared with our measurements. Third, no modeling of path loss was done, although the method could possibly be extended to compute this. Last, since the author did no broadband modeling, nor computation of channel delay spreads, coherence bandwidths, or Doppler effects, the work is not detailed enough for use in investigations of communication system performance.

Another interesting reference in this category is [51]. The authors in this paper propose a new model for wireless channels, which takes into account both direction of arrival (DOA) and direction of departure (DOD) information, obtained at the receiver and transmitter, respectively. The model is essentially a spatial (angular) generalization of the conventional channel models that characterize power versus delay, over time. Some short range measurement results were provided for the 5.2 GHz band, using a 120 MHz signal. Measuring such channels requires antenna arrays and some fairly complex processing. In addition, actually taking advantage of such information requires antenna arrays at both transmitter and receiver, yet the generalized model may be of interest for future multiple-input, multiple-output (MIMO) systems.

2.7 Additional References of Potential Interest

For point-to-point microwave channels, reference [52] is a valuable resource. This paper is also viewed as a classic. For this work, microwave links at 2, 4, 6, and 11 GHz were studied. These links employ very directive antennas (~45-50 dB gain) over well-engineered paths. Fading in this setting is caused by atmospheric stratification, yielding a two-ray (or "simplified three-ray") model. Statistics for the frequency of the spectral null and the two amplitude

coefficients were presented, and for some cases this fading can be similar to Ricean. The paper collection in [53] contains [52] and several other references for this type of channel.

For additional wideband results, in [54], the authors report on "single-input, multiple output" (SIMO) measurements made with an 80 MHz sounding signal over short range (< 1 km) in a campus-like environment in Belgium. Omnidirectional antennas were used, and the receiver employed two antennas and an RF switch that allowed alternate measurements on the two receive antennas. The authors computed equivalent Ricean K-factors (using the method of [43]) and delay spreads, as a function of link distance, but it was not clear how much data was used in these computations. A fair amount of discussion and measured results on the correlation between the signal received on the two antennas was also presented. Relationships among these parameters were also characterized (e.g., K-factor vs. delay spread), and some of this type of characterization may be of interest for new insights into wireless channel modeling.

An overview of the ultra-wideband (UWB) channel is given in [55]. This paper pertains to UWB channels for very short range applications. The authors cite multiple measurement campaigns, and collect results from an IEEE 802.15.3a working group on the current models. The models are similar to indoor models, such as that in [56], which characterize the CIR as consisting of clusters of impulses. This paper [55] provides statistics for such "personal area network" (PAN) model applications.

2.8 Publications Generated from this Research

Here we provide a list of publications generated from this research. This includes conference papers [57]-[61]. Reference [57] was the first publication on this work in the open literature, and was intended to provide a brief introduction to the project and some example initial findings. In [58] a more detailed description of results and initial models for the Cleveland airport was provided. Reference [59] provides an introduction to the point-to-point channel measurement results for airport surface areas. The VTV channel measurement and modeling results were summarized in brief in [60], and the small airport results reviewed in [61].

We also intend to prepare at least three journal papers for submission. These will address the measurements and modeling as described in this report [62], [63], and also include a VTV journal paper [64]. Additional research results may be reported as refinement of the modeling is completed.

Chapter 3: Channel Modeling Overview

3.1 Introduction

In this chapter, we provide an overview of the topic of channel modeling. Our intent here is to provide sufficient description to allow interpretation of the modeling results. Specifically, the overview is intended to allow the reader to connect the models with their use. We do not include a comprehensive discussion in all areas, since that is already obtainable in several good references, e.g., [10]. We do devote some of the discussion to coverage of channel features for which some new (or atypical) results were obtained.

We begin this chapter with a short description of common channel parameters. This includes a tabulated list, modified from [1], which summarizes key parameters. We then broadly define the two types of channel models in widespread use—deterministic and statistical—and briefly discuss where each type of model is most appropriate. For the statistical class, we describe in some detail the several most important channel parameters, and also provide some discussion on statistical distributions commonly encountered in channel modeling. We also provide a short discussion of our initial parameter bounds. To aid in understanding, we also provide some specific examples of how knowledge of channel characteristics and specific channel model parameters can be employed in communication system design. Last in this chapter we provide a discussion of aspects of modeling that are unique to the airport surface environment, in preparation for subsequent chapters.

3.1.1 Important Channel Parameters

Several widely used channel parameters include attenuation, multipath delay spread, and Doppler spread. These parameters have nearly self-evident definitions; they will be defined in the sequel. With knowledge of even just these three parameters, a communication system designer can estimate not only the detrimental effects the channel will have on any given signaling scheme, but he or she can also estimate the need for, and complexity of, "remedies" to counteract these detrimental effects. The designer can also estimate the achievable link range (distance) and component specifications required to attain this range.

Multipath delay spread is essentially the duration of the channel impulse response. It is reciprocally related to the coherence bandwidth, which is a measure of the channel's frequency selectivity. The coherence bandwidth expresses the width of contiguous frequency spectrum over which the channel affects a signal equally, i.e., at each frequency within the coherence bandwidth, the channel's effect upon any signal (at that specific frequency, i.e., a tone) transmitted through the channel is the same. The channel "effect" of primary interest is the amplitude. The Doppler spread is essentially the range of frequencies over which a transmitted tone is spread as a result of transiting the channel. This Doppler spread is reciprocally related to the coherence time, which is a measure of the rate of channel time variation. The coherence time has a definition directly analogous to that of the coherence bandwidth given previously, with replacement of "frequency" by "time."

Ultimately of course, the channel parameters are a direct result of the physics of propagation. Physical link attributes that directly affect the above-mentioned parameters are link range and the spatial locations of transmitter and receiver, antenna characteristics (e.g., height, directivity, and variation with frequency), mobile velocities, carrier frequency, and local reflector, scatterer, and absorber electrical parameters. Particularly in mobile settings, many of these factors are both temporally and spatially varying, so that precise analytical characterizations are difficult, if not impossible, even with accurate knowledge of local parameters. This is a primary motivation behind the use of statistical models.

Table 1 presents a brief summary of these channel parameters (attenuation, multipath delay spread, Doppler spread, and coherence bandwidth and coherence time). This table is an updated version of the table in [1]. It provides simple parameter definitions, comments on how the parameter is specified, and in the last column, an indication of whether, in this particular project, the parameter was measured, computed from measurements, or only estimated from analysis.

The table also contains descriptions for three additional "parameters." These are the number of channel "taps" in the channel model (L), the power delay profile (PDP), and the parameter probability density function ($p_z(x)$). As with the other parameters, more detail will be provided on these three subsequently; at this point only brief descriptions are given. The number of taps L (a positive integer) represents the length of the channel impulse response (CIR), relative to the signal symbol duration. Thus, for different symbol rates, L changes. We address this directly in Chapters 5 and 6, where we develop channel models for different bandwidths.

The power delay profile describes *how* power is distributed versus delay; the extent of the profile is a measure of the delay spread, which in a sense gives a measure of how long it takes for energy to arrive at the receiver from the transmitter. For this PDP "parameter," we are primarily interested in the functional dependence of received power versus delay. This functional dependence, along with the statistics of the channel taps, provides a measure of the severity of the channel's dispersion.

Finally, the probability density function $p_z(x)$ is listed to indicate that a specific parameter (z) is best modeled as random. Parameters that are typically modeled as random are amplitude and phase, but there are numerous others that lend themselves to this treatment.

Table 3.1. Channel parameters and definitions.

Channel Parameter	Definition (units)	Comments	Measured, Computed from Measurements, or Analysis?
T_M	*Multipath delay spread*: extent, in delay, of the CIR, usually weighted by energy (seconds)	• Most often specified statistically via r.m.s. value; maximum and minimum values also of interest • Typically account for all impulses within some threshold (e.g., 25 dB) of "main" impulse	Measured
B_c	*Coherence bandwidth*: bandwidth over which channel affects a signal equally (Hz)	• Reciprocally related to T_M, often estimated as a/T_M, a=small constant >0 • Precisely, values of frequency separation at which channel amplitude correlation falls to some value, e.g., 0.5, 0.1 • Measure via Fourier Transform of PDP, correlation of spectral components	Computed from Measurements
f_D	*Doppler spread*: maximum value of Doppler shift incurred by signal (Hz)	• Estimate analytically via classical physics, i.e., $f_D=vcos(\theta)/\lambda$, v=maximum relative Tx-Rx velocity, θ=angle between propagation vector and velocity vector, λ=wavelength • Measure via Fourier Transform of spaced-frequency, spaced-time correlation function, at fixed delay	Analysis
t_c	*Coherence time*: time over which channel remains ~ constant (seconds)	• Reciprocally related to f_D • As with B_c, desire values of time separation at which channel correlation falls to some specified value • Measure via spaced-time correlation function, or compute from f_D	Analysis
α	*Attenuation:* power loss, function of frequency and distance (unitless, dB)	• Analytically "estimatable" via traditional physics, e.g., free-space ($20log(4\pi d/\lambda)$ dB), "plane-earth" models • Multiple models available in software	Measured
L	*Impulse Response Length*: length, in signal elements, of CIR (unitless integer)	• Depends upon signal element (bit, symbol, chip) duration • Estimated as $\lceil T_M/T \rceil$; T=smallest signaling duration, $\lceil x \rceil$=smallest integer $\geq x$	Computed from Measurements
PDP	*Power delay profile*: distribution of received power versus delay (unitless, relative to CIR peak)	• Expresses distribution of power over delay (plot or equation) • Often modeled as exponentially decaying with delay, or uniform over $[0,T_M)$ • Measure directly using channel sounder	Measured
$p_z(x)$	*Probability density function of random variable z* (unitless)	• Random variable can be varying in time, frequency, space • Common amplitude distributions: Rayleigh, Ricean, Nakagami • For phase, common distributions are uniform, Gaussian	Computed from Measurements

3.2 Channel Model Types and Their Applications

In theory, there could be as many types of channel models as there are types of communication links. In practical terms, this is neither desirable, nor necessary. For guided wave transmission schemes (those that use wires, cables, waveguides, lightguide fibers, etc.), given the electrical and geometrical parameters of the guiding structure, electromagnetic field theory principles can be used to determine the guide's effect upon signals with great accuracy. In fact, for such wave guiding structures, manufacturers typically provide the channel parameters such as attenuation and group delay as part of the guide's specifications. Other than small deviations from the specified values, attributable to such things as manufacturing tolerances, these guiding structures can be viewed as completely deterministic channels. For wireless systems though, the channel is not typically under the direct or complete control of the system designer or operator. Yet in some circumstances, much of what might appear to be beyond the designer's control, can at least be constrained. In these cases, the channel can be modeled as deterministic, to first order. This is the first major class of channels that we address here.

We make note that strictly, use of the term deterministic must be done with some caution, since in wireless settings, even the most careful design cannot circumvent all contingencies, and if atypical events occur, they can at least be treated as random. For example, it is not unheard of for birds to nest or otherwise "block" parts of antenna structures. A famous example of this was when Penzias and Wilson of Bell Laboratories were first discovering the cosmic microwave background radiation [65]. Clearly, "unpredictable" events can and do occur despite the greatest pains taken by communications engineers. Fortunately, these types of events are rare, and often easily remedied. For our purposes, we assume that the probability of such events is small enough so that they can be neglected in our wireless case. (In addition, we have no adequate database from which to develop models for such rare and interesting events!)

Also, from the perspective of electromagnetic field theory, *any* given wireless channel could be viewed as being purely deterministic, and hence channel characteristics could be calculated to any arbitrary degree of precision, at any point in space at any time—*if* only one had knowledge of all appropriate electrical and geometrical parameters, and *if* one could solve the field theory equations (Maxwell's equations) rapidly and accurately enough. In many settings though, the required knowledge translates to a *very* large amount of data, and hence renders this approach impractical. For example, for transmission near the earth's surface, the transmitted wave might encounter refraction through the atmosphere, reflection from large obstacles, scattering from small obstacles, partial absorption through foliage, and diffraction around building edges or surfaces, in addition to traveling along a "direct" path to the receiver. If the number of obstacles, edges, surfaces, etc., is large, such as in a built up (or even forested) environment, accurate parameter knowledge alone would be difficult to obtain for the dozens to hundreds of objects involved. In mobile communication settings, where transmitter, and/or receiver, or even reflectors and scatterers are moving, many of these factors would be both temporally and spatially varying, so that precise analytical characterizations would be even more difficult, even if one had possession of accurate knowledge of local parameters. This motivates the use of statistical channel models, the other major class of channel model types.

For essentially all cases, wireless channels are modeled as linear filters, and hence are characterized completely by their channel impulse response (CIR), or equivalently, their transfer function. Our discussion thus focuses upon this response and its characterization. We restrict attention henceforth to wireless channels.

3.2.1 Deterministic Channel Models, Path Loss, and CIR Form

Perhaps the simplest possible channel is that of "free space," most closely approximated by actual interstellar space, but reasonably well-approximated by much of the earth's troposphere, at least for moderate distances and for altitudes where effects of the earth's surface can be neglected. Satellite communication systems often use the free space model as their first order channel model [66], both for satellite to/from earth links, and for satellite to satellite links. In the free space case, the well known Friis transmission formula [67] can be used to predict the propagation loss, or path loss. Other terms for this path loss are basic transmission loss, spreading loss, and simply, attenuation. The loss refers explicitly to the ratio of transmitted to received power, and this ratio is most commonly given in decibels (dB).

In this free-space case, the channel impulse response is given by a single impulse:

$$h(\tau;t) = \alpha(t)\delta(\tau - \tau_0(t)) \tag{3.1}$$

where in anticipation of subsequent modeling, we have generalized notation somewhat from the simplest possible form. Here, $h(\tau;t)$ represents the channel response at time t to an impulse input at time $t-\tau$, and the channel output would be obtained via the convolution of this response with the input signal, where the convolution is taken with respect to the delay variable τ. This tacitly assumes that the rate of channel time variation is slow with respect to the rate of variation of the input signal (since convolution is applicable strictly for linear time *in*variant systems).

For time-invariant cases, e.g., for non-mobile conditions, the response is the same for all time, thus we can drop the "t" dependence and write as

$$h(\tau) = \alpha\delta(\tau - \tau_0), \tag{3.2}$$

where τ represents the delay variable. [This arises by noting that, for time invariance, the response at time t to an impulse input at time $t-\tau$ must equal the response at time $t+T_0$ to an impulse input at time $t+T_0-\tau$, for *any* constant T_0, i.e., $h(\tau,t)=h(\tau,t+T_0)$. Set $T_0=-t$, and obtain $h(\tau,t)=h(\tau,t-t)=h(\tau,0)=h(\tau)$, which is the standard time-invariant CIR, since the output at time zero from an impulse input at time $-\tau$ is the same as the output at any time τ due to an impulse input at time zero.]

The impulse "weight" $\alpha(t)$ in (3.1) corresponds to the attenuation, and for non-time-varying cases, we denote simply by α as in (3.2). The time varying delay $\tau_0(t)$ represents the propagation delay, or "group delay" of the signal through the medium; in time invariant cases this degenerates to τ_0. The CIR of (3.2) is the simplest form possible, with only two parameters, the attenuation α and the delay τ_0. Note that the form of (3.2) implies that α is actually a "gain," so we represent path loss as $1/\alpha$, or rather, for path loss in terms of power, we use $1/\alpha^2$.

Specifically for free-space, we can use the Friis transmission formula to obtain α^2, the ratio of received power to transmitted power, as a function of distance and frequency. In dB, we have path loss equal to

$$PL_{FS}(d,f) = -20\log_{10}(\alpha) = 20\log_{10}(4\pi df/c)\ \text{dB}, \tag{3.3}$$

with d the distance, f the frequency, and c the speed of light. For the free space condition, path loss increases as the square of both distance and frequency. In a situation with mobility, if we know the form of the change of distance as a function of time, with appropriate geometric equations and kinematic[2] equations from physics, we can easily compute $\alpha(t)$ and $\tau_0(t)$. Thus, time-varying deterministic models can be developed.

In deterministic settings where the free-space model is inappropriate, determination of α and τ_0 may be substantially more complicated, but in principle, with knowledge of the geometrical and electrical parameters of the reflectors/diffractors/etc., other models can be used to determine the propagation path loss. Perhaps the other most well known path loss model is the "plane earth model," which applies for transmission between two antennas mounted at or near the earth's surface. Again in dB, for the plane earth case, path loss is given by the formula

$$PL_{PE}(d, h_1, h_2, f) = 20\log_{10}\left\{\frac{2\pi df/c}{\sin[2\pi h_1 h_2/(cd/f)]}\right\} \cong 20\log_{10}\left\{\frac{d^2}{h_1 h_2}\right\}, \qquad (3.4)$$

with d the link distance, and the h's the heights of the two antennas. The very good approximation ($20\log_{10}[d^2/(h_1 h_2)]$) is quite accurate when h_1 and h_2 are both much less than distance d. Path loss increases as the fourth power of distance in this case. Because of their relatively simple form, both the free space and plane earth models can be used for rapid estimates of path loss.

Once again—in principle—given all the electrical, geometric, and kinematic parameters, we could compute the resulting electromagnetic field at any point in space distant from the transmitting antenna. This underlies the model classification as deterministic. As emphasized though, in many practical situations this knowledge is unavailable or insufficiently accurate. In addition, even if it is available and accurate, we may require significant computational resources to solve the electromagnetic field equations, which could constrain how fast we could estimate electric field strengths and received powers, and thus limit the velocities for which our calculations apply. Finally worth noting here is that in complicated environments with mobility, we are most often not interested in the exact value of field strength (or its square, proportional to received power density) at a specific point, but in some average value over a small spatial extent. This spatial extent is usually a few wavelengths.

Numerous path loss (or "field strength") prediction models have been developed over the years. Many are based on electromagnetic field theory, and may include various diffraction theories and ray-tracing techniques [68]. Generally speaking, the larger the amount of, and the greater the accuracy of the environmental data used as inputs in these models, the better their ability to predict channel effects accurately. Even so, many of these models do not attempt to predict exact values, but instead provide a "range" of values for a given parameter such as path loss. This range directly addresses the lack of precision inherent in such models, and thus portends the use of statistical treatments.

One very widely used formulation for path loss modeling is the "$10n\log_{10}(distance)$" formulation, where the parameter n is denoted the path loss exponent. Most often this path loss equation is given in the following form [5]:

---

[2] We make the assumption that all platform and scatterer velocities are much smaller than that of light, hence treatment via classical—non-relativistic—physics suffices.

$$PL_{n,\sigma}(d) = A + 10n\log(d/d_0) + X \tag{3.5}$$

where the path loss between transmitter and receiver at distance d, $PL_{n,\sigma}(d)$, and quantities A and X are in decibels (dB), and distances d and d_0 are typically in meters. The parameter A is a "fitting parameter," that in effect adjusts the intercept point of this equation: the path loss is a linear function of the logarithm of the distance ratio d/d_0. The parameter A is found from the data directly; it can also be estimated using the known transmit power, antenna gains, and RF line losses, along with the measured received power at reference distance d_0. The parameter X is a Gaussian (normal) random variable, with zero mean, whose variance σ^2 is found from measured data, obtained using least-squares curve fits. Typical values for the standard deviation of X are from 6-12 dB, for cellular bands, in urban areas [5]. The reference distance d_0 is generally chosen to be a small distance, within the far field of the antennas, and based upon the intended link range. For example, in indoor areas where maximum link distances are on the order of tens of meters, d_0=1 m, and for large outdoor terrestrial cells where maximum link distances are on the order of a few tens of kilometers, d_0=1 km [25]. For the airport surface communication system, the link ranges are likely to be on the order of a few kilometers, hence a reference distance value of 10-50 m or so would be convenient. For the Tx antenna mounted on the ATCT, it was generally not possible to obtain measurements at 10 m, so a larger value—roughly the minimum attainable with the Tx antenna atop the tower and the receiver at the tower base—was employed. The effect of this reference distance upon the resulting models is not critical.

Much of this discussion has focused upon path loss, or the specification of the parameter α in (3.1). Although the delay τ_0 can often be estimated as well, its estimation is typically not a major concern for communication systems, since it is usually only relative timing, with respect to signal symbol boundaries, that matters. (Absolute delay may of course be of interest for other applications, such as geolocation, for example.)

The form of (3.1) also implies that the channel is not dispersive, i.e., it does not vary with frequency. The channel frequency variation in this case is given by the Fourier transform of $h(\tau;t)$, where transformation is respect to the variable τ. We denote this channel transfer function $H(f;t)$, and note again that in time-invariant cases, we may drop the t-dependence. In equation form we have

$$H(f;t) = F\{h(\tau;t)\} = \int_{-\infty}^{\infty} \alpha(t)\delta(\tau - \tau_0(t))e^{-j2\pi f\tau}d\tau = \alpha(t)e^{-j2\pi f\tau_0(t)} \tag{3.6}$$

which means that in the frequency domain, the channel imposes a time-varying amplitude $\alpha(t)$ and phase $(-2\pi f\tau_0(t))$ upon the signal. For static conditions, we have $H(f) = \alpha e^{-j2\pi f\tau_0}$. A tacit assumption made in the use of (3.5) is that the rate of time variation is slow; this corresponds to the same assumption applied to the CIR and its use to obtain the channel output via convolution.

In the most rigorous analysis, if $\alpha(t)$ varies rapidly compared with the signal of interest, the conclusion of frequency non-selectivity is no longer valid. When this occurs, digital signal pulse shapes are not preserved upon transmission through the channel. In most practical cases today, this rapid amplitude variation (fading) is not encountered. A notable example exception to this would be low-data-rate communication with *very* high speed platforms such as rockets.

Generalizing (3.1) to allow for channel dispersion, we can express the channel impulse response as follows:

$$h^{(e)}(\tau;t) = \sum_{k=0}^{L(t)-1} z_k(t)\alpha_k(t)\exp\{j[\omega_{D,k}(t)(t-\tau_k(t)) - \omega_c(t)\tau_k(t)]\}\delta[\tau - \tau_k(t)]$$

$$= \sum_{k=0}^{L(t)-1} z_k(t)\alpha_k(t)\exp\{-j\phi_k(t)\}\delta[\tau - \tau_k(t)]$$

(3.7)

where again, the function $h(\tau;t)$ represents the response of the channel at time t to an impulse input at time $t-\tau$. In this formulation we adopt the model of a multipath propagation environment, but channel dispersion can also occur due to other factors, the most common being explicit bandlimiting (filtering), and frequency variation of material/electrical parameters, the latter of which pertains mostly to very broadband signals. Current ultrawideband (UWB) signals may require such models. Also, (3.7) appears in the form of "discrete impulses," which can be interpreted as the channel imposing specific discrete attenuations, phase shifts, and delays upon any signal transmitted. In some cases, such as HF troposcatter channels, this discreteness may not be appropriate, and the baseband CIR is a continuous function of both τ and t [3]. For our channel of interest—the wireless airport surface channel in the MLS extension band—the discrete form of (3.7) is sufficiently accurate. This is because this form of the CIR is "narrowband" in the sense that the parameters themselves (α's, τ's) do not vary appreciably with frequency. Clearly as the bandwidth one considers increases beyond certain limits, this will not be true [69]. Yet for frequencies at UHF and above, for bandwidths of tens to hundreds of mega-Hertz (MHz) or even more, this frequency-invariance is a very good approximation [70].

With (3.7), we have generalized the CIR form beyond that typically seen in texts [5] to allow for the following:

- an "environment" classification (superscript "e" on h); this will be used in our case to denote CIRs for the various regions within airports;
- a time-varying number of transmission paths (line of sight and/or multipath echoes) $L(t)$;
- a "persistence process" $z(t)$ accounting for the finite "lifetime" of propagation paths, and;
- the explicit time variation of carrier frequency $\omega_c(t)$ to account for transmitter oscillator variations and/or carrier frequency hopping.

For our purposes in subsequent model development, we will make use of the first and third of these generalizations. The third generalization (persistence process) actually imposes the second generalization (time-varying number of paths).

Note also that the CIR of (3.7) is complex—it is the "complex envelope," or "lowpass equivalent" response, from which the actual bandpass channel response $h_B(\tau;t)$ is obtained via the formula $h_B(\tau;t)=2Re\{h(\tau;t)e^{j\omega_c t}\}$, with $Re(x)$ denoting the real part of x, and $\omega_c=2\pi f_c$, with f_c the carrier, or "center" frequency. (The factor of two is required to enable use of the usual convolution procedure for obtaining the channel lowpass output response from the lowpass input signal [3].) Most often for simulation and analysis, the complex envelope is used.

The terms within (3.7) are defined as follows:

- analogous to the amplitude α of (3.1), $\alpha_k(t)$ represents the kth received amplitude at time t;
- the argument of the exponential term $\phi_k(t)$ represents the kth received phase at time t;
- the kth echo path is associated with a time-varying delay $\tau_k(t)$;

- the δ function is a Dirac delta (or "impulse");
- the radian carrier frequency is $\omega_c(t)=2\pi f_c(t)$;
- the term $\omega_{D,k}(t)=2\pi f_{D,k}(t)$ represents the Doppler shift associated with the kth received multipath echo, where $f_{D,k}(t)=v(t)f_c\cos[\theta_k(t)]/c$, where $v(t)$ is relative velocity and $\theta_k(t)$ is the spatial angle between the kth arriving signal propagation vector and the velocity vector.

Figure 3.1 shows a block diagram of the channel model of (3.7).
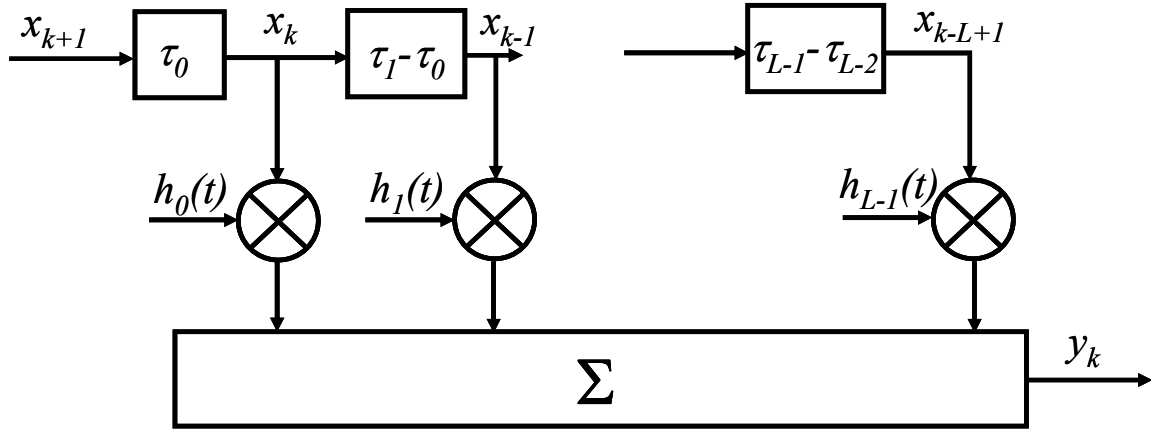
Figure 3.1. Block diagram of channel model of (3.7); $h_i(t) = z_i(t)\alpha_i(t)e^{j\phi_i(t)}$.

In this figure, which is often termed a "tapped delay line" (TDL) model, the input symbols are denoted by the x's, and the output symbols by the y's, with k a time index. The blocks that contain the τ's are delays, and the tap complex amplitudes are given by the h's, specifically, for the ith tap, we have from (3.7) $h_i(t) = z_i(t)\alpha_i(t)e^{j\phi_i(t)}$. For results from our measurements, each of these delay blocks represents a symbol (spread spectrum "chip") time of 20 nanoseconds, except the first delay τ_0, which represents the bulk propagation delay of the first arriving signal. With the 20 nanosecond interval between "taps," this model pertains to a 50 MHz bandwidth. We also generate models for smaller values of bandwidth, by vectorially combining tap processes; this is described in Chapter 5.

Note that (3.7) can reduce to (3.1) when all the echo delays are nearly the same. In that case $\alpha(t)$ is a complex process with amplitude and phase. This "collapsing" of the CIR can also simply arise when the resolution of the channel description or measurement does not permit (or require) the distinguishing of echoes closer in delay than some minimum value $\Delta\tau$, and when multiple echoes are present within this minimum delay value. In this case these echoes are said to be "unresolvable." The value of $\Delta\tau$ is approximately equal to the reciprocal of the signal bandwidth used. For example, with a channel sounder measurement bandwidth of B_M=50 MHz, $\Delta\tau \cong 20$ nanoseconds. This bandwidth corresponds to distance resolution of approximately 6 meters.

The relationships among the individual terms within the phase $\phi_k(t)$ (argument of the exponential) are also worth some discussion. From (3.7), this phase is

$$\phi_k(t) = -\omega_{D,k}(t)[t - \tau_k(t)] + \omega_c(t)\tau_k(t) = -2\pi f_{D,k}(t)[t - \tau_k(t)] + 2\pi f_c(t)\tau_k(t) \qquad (3.8)$$

The exponential of each of these terms (e.g., $e^{-j2\pi f_k t}$) can be viewed as a "phasor" rotating at a given frequency (e.g., $-f_k$).

1. $-2\pi f_{D,k}(t)t = -2\pi f_m(t)t cos[\theta_k(t)]$ corresponds to a phasor rotating at a frequency of $f_{D,k}(t) = f_m(t)cos[\theta_k(t)]$, where f_m denotes the maximum Doppler frequency shift associated with velocity v, that is, $f_m(t) = v(t)f_c/c$, thus the phasor rotates at $f_{D,k}(t) = f_c cos[\theta_k(t)]v(t)/c$. The complete phasor term is $-2\pi f_c cos[\theta_k(t)](v(t)/c)$. Since $v << c$ (and $cos(\cdot) \leq 1$), this phasor rotates at a very small fraction of the carrier frequency f_c;

2. $2\pi f_{D,k}(t)\tau_k(t) = 2\pi f_m(t)cos[\theta_k(t)]\tau_k(t)$ corresponds to a phasor with rotation frequency $f_m(t)cos[\theta_k(t)]\tau_k(t)/t = f_c cos[\theta_k(t)]\{\tau_k(t)/t\}\cdot\{v(t)/c\}$. This "phasor" also generally changes very slowly for most cases, even if $\tau_k(t)$ changes at a rate nearly equal to t, because again, in our setting $v(t) << c$.

3. $2\pi f_c \tau_k(t)$ corresponds to a phasor with rotation frequency $f_c \tau_k(t)/t$; here even though τ_k generally changes slowly, since f_c is typically large (e.g., 5×10^9 in the MLS band case), $f_c \tau_k$ can change very significantly for delay changes on the order of $1/f_c$ (~0.2 nanoseconds for the MLS band).

Thus, for our case, with platform velocities much less than c, the rate of change of the phase of each term in (3.7) is dominated by this third term. In addition, for the MLS band frequencies, this phase term can change over the entire range of 2π radians (360°) with a delay change of approximately 0.2 nanoseconds; this delay change corresponds to a travel distance change of around 6 cm, which is the wavelength at frequency 5 GHz.

3.2.2 Statistical Channel Models

We have already stated some of the reasons why statistical channel models are appealing. Another reason for their use is that in mobile settings, where platform location and orientation can take a nearly infinite number of values, it is not realistically possible to characterize the channel for each and every possible location. This would constitute characterization in a point-to-point fashion for all these locations.

In the case of statistical models, we make the assumption that certain channel parameters can be well modeled as random, but the form of the CIR—that of (3.7)—still applies. In terms of (3.7), the phase $\phi_k(t)$ of the kth component can often be modeled as random. As discussed, these phase terms can vary rapidly: even if the path delays themselves vary slowly, the products of the delays multiplied by the large carrier frequency vary rapidly. For the case when the channel delay spread is much less than a signal symbol duration, the paths are not resolvable, and appear, to the receiver, to have essentially all the same delay, denoted τ_0. When this is the case, *and* when the path amplitudes are all approximately equal, the model in (3.3) can be simplified slightly:

$$h^{(e)}(\tau;t) \cong \alpha(t)\delta[\tau - \tau_0(t)] \sum_{k=0}^{L(t)-1} z_k(t) \exp\{ j[\omega_{D,k}(t - \tau_k(t)) - \omega_c(t)\tau_k(t)]\} \qquad (3.9)$$

where here in (3.9), we have let all the $\tau_k(t) \cong \tau_0(t)$. In this case, the summation contains only the persistence process and the phasor for each path. This type of channel is called a flat fading channel, which refers to the absence of frequency selectivity in the frequency response—the summation is a complex constant at any time t. In terms of the *model*, these phasors in the sum are distinguishable since even though all the delays are *nearly* the same, the products of the carrier frequency times the delays will not be. When the persistence process is not included, and $L(t)\sim L$ is large, the summation can be approximated as the familiar complex Gaussian random process. This is the conventional Rayleigh fading model. In this case, the process $\alpha(t)$ could be used to represent other slowly varying propagation effects, such as the shadowing effects of obstacles; in terrestrial settings this shadowing is typically modeled as having a lognormal distribution, as noted in Chapter 2. This composite product form for the channel amplitude response (lognormal multiplied by Rayleigh) was originally suggested in [71]. It was shown in [5] to be equivalent to the Suzuki distribution, obtained by representing the mean of the signal amplitude as a lognormal process, and then averaging over the lognormal process. The presence of the persistence processes $z_k(t)$ could invalidate the Gaussian (Rayleigh) approximation, in particular when $L(t)$ is not large.

In this formulation, or that of (3.7), we keep the persistence process distinct from the path amplitudes, since the effects can be of different magnitude even though in some cases the effects come from similar physical phenomena: the path amplitudes are the result of the product of the atmospheric losses and all the relevant reflection coefficient magnitudes, and potentially some diffraction losses, foliage losses, etc., whereas the persistence process is intended to represent broader scale effects that model explicit blockage of a path and motion-induced introduction/removal of paths (e.g., by a mobile passing beyond a reflector). Clearly the set $\{z_k(t)\}$ and the process $L(t)$ are related; in any given situation either one or the other, but not both, might be used; as noted above, and as will be shown in the chapter on channel modeling, we will use the persistence processes.

If the path amplitudes ($\alpha_k(t)$'s) are not all approximately equal, the model of (3.9) can not be used. Specifically, if one path is dominant, the resulting model is the familiar Ricean one. It can be represented by returning the $\alpha_k(t)$'s to inside the summation, and then splitting the summation into two components, one with the single dominant path, and the other the sum form as in (3.7). The lognormal (or other model for) shadowing can be imposed as well. Note that for the Ricean and Rayleigh models of the form of (3.9) we still assume that all delays are clustered near a common value $\tau_0(t)$, and the *spread* of delays is much smaller than any signaling interval. These models can also be used for the individual taps of (3.7) and Figure 3.1. Since the persistence process has not seen much attention in the literature, there are no well established models for it. Our initial model will be a random "switching" process, or Markov chain.

The presence of the persistence process could be used to account for the transition between Rayleigh and Ricean behavior observed in particular in measurements of the mobile satellite channel [35]; as we discuss in Chapter 5, these transitions have also been observed in our measurements. When the path amplitudes are unequal, and there is no single dominant path, the resulting random process model is much more complicated. One formulation is described in [72] (note the date!). This model assumes that the path amplitudes are known but the phases are still considered random, and the cumulative distribution function of the resulting channel

amplitude is an infinite sum of the ratio of Bessel functions. This elegantly derived distribution is cumbersome to use at best. Yet, if $L(t)$ and these $\{\alpha_k(t)\}$ were approximately constant for a reasonable time period (many signal symbol intervals), this distribution could be computed for certain cases. The primary virtue of this would be validating the theory—it is unlikely to be more useful than other amplitude distributions in computer simulations.

Another fading amplitude model that is seeing much current use is the Nakagami-m model [73]. This is most general, and via selection of the model parameter m, can represent the entire range from Rayleigh to Ricean to non-fading Gaussian. As with the Ricean, this distribution also has a second parameter, the mean-square value. As it was selected to fit empirical data, it has no direct physical significance, in contrast to the Rayleigh and Ricean models. The flexibility of this model is though very attractive from both analytical and simulation perspectives. There is also a less-commonly used version of the Nakagami, the Nakagami-q model [73]. This version pertains to a restricted range of fading parameter, and can be approximated by the more common Nakagami-m model.

The last common amplitude model we address is the Weibull model [74] As with the Nakagami-m model, this model is based not on an underlying theory of propagation effects, but upon measurements. Also as with the Nakagami-m model, the Weibull model offers substantial flexibility, as it also has two parameters.

In Table 3.2 we summarize these probability densities. For all except the lognormal distribution, the mean-square value is Ω. For some of these densities, the corresponding cumulative distribution function (cdf) is known in closed form. These cdfs are sometimes known as "fading probabilities," since they describe the probability of the amplitude being below some level.

For the channel phase processes ($\phi_k(t)$ of (3.8)), the most commonly used distributions are the uniform (from 0 to 2π radians), or the Gaussian. The latter is applicable for the Ricean fading case when the Rice factor is large enough.

Finally on this topic, we note that the tapped delay line model of Figure 3.1 does not indicate relationships among the various tap random processes. From the perspective of generating these random processes in simulation, and also for analysis, modeling the processes as independent of one another is simplest. Yet this situation does not always model reality. As noted in the literature review, for simplicity, and for narrow bandwidths and rich scattering environments, the WSSUS model is widely employed. For wider bandwidths and moderate amounts of scattering, the WSSUS model is simply unrealistic, which results in the tap random processes being correlated. The pairwise correlations are typically specified by correlation coefficients (e.g., r_{ij} for α_i and α_j). For more than two taps, these correlations are described by a matrix of coefficients. This topic is discussed in detail in Chapter 5.

Table 3.2. Commonly used fading probability density functions.

Distribution Type	Probability Density Function	Comments
Rayleigh	$$p_R(r) = \frac{2r}{\Omega} exp\left[-\left(\frac{r^2}{\Omega}\right)\right]$$	• Widely used for ease of analysis • Derived from Central Limit Theorem arguments
Ricean	$$p_{Ri}(r,K) = \frac{2r(1+10^{K/10})}{\Omega} exp\left[\frac{-r^2(1+10^{K/10})}{\Omega} - 10^{K/10}\right] I_0\left(2r10^{K/20}\sqrt{\frac{1+10^{K/10}}{\Omega}}\right)$$	• Rice, or "K-factor" is equal to k=(LOS power)/(Scattered power), K=10log(k) (dB) • For $k\to 0$, pdf $\to$ Rayleigh • For $k\to$large, pdf $\to$non-fading • I_0 = modified Bessel function of first kind, zero order
Nakagami-m	$$p_N(r,m) = \frac{2m^m r^{2m-1}}{\Gamma(m)\Omega^m} exp\left[\frac{-mr^2}{\Omega}\right]$$	• $m \geq 0.5$ • Γ=Gamma function
Weibull	$$p_w(r) = \frac{b}{a^b} r^{b-1} exp\left[-\left(\frac{r}{a}\right)^b\right]$$	• b = shape factor, determines fading severity a = scale parameter $= \sqrt{\Omega/\Gamma[(2/b)+1]}$
Lognormal	$$p_L(r,\mu,\sigma) = \frac{10}{r\ln(10)\sqrt{2\pi\sigma^2}} exp\left\{-[10\log(r)-\mu]^2/(2\sigma^2)\right\}$$	• For r= received power (V^2), and w= power in dBW; pdf of w is Gaussian, with mean = μ, standard deviation = σ.

3.2.3 Example Model Applications

In this section we provide some additional examples of how the developed channel models can be applied. Several additional examples were provided in Section 1.3.1.

1. For single-carrier DS-SS (CDMA) systems, the length of the impulse response (L) determines how long the corresponding RAKE receiver should be, in terms of the number of taps. Typically the value of L is determined based upon some desired value of captured signal energy, and also upon the persistence of a given path. Similar comments pertain to single-carrier non-spread systems—there for equalizers—although for these systems, with data rate comparable to that of the DS-SS systems, channel bandwidth is much smaller, and so the required value of L is also substantially smaller. Examples of this are addressed in Chapter 6.

2. As pointed out in Section 1.3.1, the channel coherence bandwidth can be used for selecting channel bandwidths for frequency diversity. In addition, it can be used to select the bandwidths of channels when dividing up the available frequency spectrum for different types of links and applications. In this case, for any links that are non-mobile (fixed) and point to point, the coherence bandwidths are generally larger, and these links admit higher data rates with simpler transceivers.

3. The channel fading amplitude statistics can be used to analyze and simulate performance of *any* waveform used across the channel, as noted. The fading amplitude random processes can be used to test power control algorithms, link margins, and other control algorithms such as timing or carrier tracking.

4. For fixed links, identification of the spatial angular distribution of power can be used to configure spatial diversity antennas, and even the selection of antenna gain (e.g., directional vs. omnidirectional). From the perspective of a field site, if significant levels of received power are obtained in some angular direction, additional field sites should generally *not* be placed along those angular directions, if possible. If placement in those directions is unavoidable, care should be taken to minimize interference, e.g., through frequency, time, spatial, or code division.

5. Also for fixed links, knowledge of the delay spread versus spatial angle can be used. One way in which this may be used is in designing or configuring reception schemes that employ both angular and time diversity. In this approach, for placing a new site with respect to an existing site, angles at which large delay spreads are present may actually be desired.

Additional discussion on this topic is provided in the chapter on channel modeling.

3.3 Channel Aspects Unique to the Airport Surface Environment

In this section, we provide some discussion regarding unique features and characteristics of the airport surface environment. The actual measurements and the specific airports at which measurements were made are described in some detail in the next chapter.

Within a given airport of a particular class (Large, Medium, or GA) we have areas that are different from other areas in terms of their propagation characteristics. As in many terrestrial channel models, there are line-of-sight (LOS) and non-LOS (NLOS) regions. Many terrestrial channel models also specify an environment type [5]. For example, in cellular settings, there are

three common environment types: rural, urban, and suburban. Although these regions are subject to interpretation, and differ from country to country or even within a country or region of a country, the intent is to delineate broadly the channel characteristics applicable in different settings. For instance, the "rural" area may not be exactly rural, but even if an area just outside a city is wide open enough, and has a sparse enough distribution of buildings, it will share more in terms of channel characteristics with truly rural areas than it will with so-called suburban, or urban, channels. Even though the channel classification may not be perfect, the division into a small number of classes is useful for comparison and description.

For the airport classes[3], by *large* airports we mean first that the airport is a busy one, with many large airplanes moving around throughout the day. In addition to the large airport terminal building(s) and its concourses, large airports also often have other buildings on the airport property, such as airline hangars, maintenance buildings, parking garages, and GA buildings and their "terminals." Other large objects such as fuel and water tanks may also be present. Finally in this class, since large airports are invariably near large cities, airports in this class also usually have many large buildings just outside the airport property. These large buildings are often hotels or office buildings. Example airports in this class at which we have taken measurements are the Miami International Airport (MIA) and the John F. Kennedy International Airport (JFK). Figure 3.2 illustrates some of these features at JFK.

Figure 3.2. View of some large airport features at JFK, taken from ATCT.

Our second class of airports is the *medium* airport class. These airports have much in common with the large airports. They also have buildings on the airport surface, but their buildings are not as large, or as numerous. For example, a medium airport would have only one

---

[3] We note that our airport classes—large, medium, and GA—are only for the purposes of this study and for channel characterization, and do not represent any official (e.g., FAA, or ICAO) designation.

main terminal building. Also, being in cities of lesser size than the large airports, the medium airports will not have as many nor as large-sized buildings surrounding the airport property. The airports in this class are though significantly bigger and busier than GA airports, our final class. An example medium airport we have measured is Cleveland Hopkins International Airport (CLE). Figure 3.3 illustrates some of these features. Note the distinct absence of many large buildings outside the airport, beyond the runways at the top of the figure. Also worth pointing out for both the large and medium airports is that the ATCT height is well above that of any airport buildings, and also above that of surrounding buildings outside airport property. This is by design, of course, but this is a feature that distinguishes the airport surface from other terrestrial settings—the cellular setting is an example, since its base station antenna heights may often not be much above the local building heights.

Figure 3.3. View of some medium airport features at CLE, taken from ATCT.

The *GA* airport class is well known, and needs little further explanation. The GA airports typically do not serve large commercial airlines, and their runways and structures are significantly smaller than even "small" airports in the medium class. The example GA airports at which measurements were made are the Ohio University Airport, in Albany, OH, the Burke Lakefront Airport in Cleveland, and the Tamiami Airport in Kendall, FL. Figure 3.4 shows a photograph of the OU airport, typical of a GA class.

Figure 3.4. View of GA airport at OU, taken from "crow's nest" atop AEC hangar.

As noted in Chapter 1, our airport classification is based on the size and local characteristics of the airport, but we also take into account measured data, primarily delay spread. In fact, it was not until after we had observed the MIA delay spread data, and compared that to the CLE results, that we returned to photographs to confirm the significant differences in local environment features between these two airports, and thus created the medium airport class.

In terms of our CIR model (3.7), the superscript "*e*" for environment takes on values *L*, *M*, or *GA*, for our large, medium, and GA airport classes, respectively. As noted previously, there are both LOS and NLOS regions on an airport. Once again, after taking measurements and analyzing data, we were able to devise a second set of classes, which we call "regions," applicable to any single airport of any class. Specifically, given the class *L*, *M*, or *GA*, there exist multiple regions on the airport surface, with distinct propagation features. As with the airport size set, we have classified the airport regions into a set of three: LOS-Open (LOS-O), NLOS-Specular (NLOS-S), and NLOS. Hence the superscript "*e*" for environment in (3.7) requires two variables for its complete specification: the airport class or size (*L*, *M*, or *GA*), and the region (LOS-O, NLOS-S, or NLOS).

For these three regions, the LOS-O areas are those clearly visible from the ATCT, with no significant scattering objects nearby, e.g., runways and some taxiways. The NLOS-S regions represent again the regions in between the other two, and exhibit mostly NLOS conditions, but with a noticeable, often dominant, specular, or first-arriving component in the PDP, in addition to lower energy multipath components. This region is encountered for example near terminal buildings, where a significant signal component diffracted around a building roof may be received. The NLOS regions represent areas of the airport that have a completely obstructed LOS to the ATCT. These regions have the largest values of delay spreads, and are often near the airport gates.

Clearly, aircraft inhabit all three of these regions as they move about the airport surface, whether undergoing arrival or departure. When considered over a long enough time period (typically milliseconds), the airport wireless channel is thus a statistically *non*-stationary channel, in contrast to most terrestrial channel models. At the large airports, in some areas, the presence

of large buildings yields persistent, long-delay multipath echoes, also in contrast to most terrestrial models, where these types of echoes would not exist or persist. As will be described, we develop models for each region, for each class of airport.

Given that our models are developed based on measurements at a limited number of airports, one question that might arise is the following: does every individual airport need its own channel model, and even if not, can we select which channel model to use for an arbitrary airport? The answer to this two-fold question is no, of course not every airport needs its own channel model, and yes, we can select an appropriate model for an arbitrarily selected airport. As with environment classification in cellular channel modeling, our classification scheme is not perfect, but it should be fairly easy to categorize any given airport according to our criteria. In addition, as will be described in Chapter 5, within any airport size class and region, we will have multiple sets of models (at least average, and worst-case), so that if one is unsure which model to employ, one can err on the side of caution and use the conservative, worst-case models.

3.4 Initial Parameter Estimates

Initial estimates for some of the parameters were made at the very beginning of the project. This was done as one result of an internship by Ohio University graduate student J. T. Neville at NASA GRC, in Summer 2004. A good starting point for the estimation of channel delay spread and Doppler spread was given in [39]. That author breaks the modeling of aeronautical channels down into various scenarios. These include parking, taxi, arrival/departure, and en-route. A table of values similar to that given in [39] appears here as Table 3.3, taken from [75]. For the Doppler values, we assumed a carrier frequency of 5060 MHz. The maximum Doppler shift occurs when the aircraft is flying directly towards or directly away from the ground station, e.g., a 0° or 180° spatial angle. Without measurements, and without detailed environment descriptions for any airports (as noted in Chapter 1), our initial estimates were coarse, and it was deemed too speculative to estimate any channel parameter details.

Channel delay profiles for the parking, taxi, and arrival/departure scenarios are *assumed* to take on an exponential form in [39]. Measurements for this are provided in Chapters 5 and 6. The one sided exponential delay power spectrum is eq. (7) of [39], repeated here:

$$p_\tau(\tau) = \begin{cases} \dfrac{1}{\tau_{slope}\left(1 - e^{-\tau_{\max}/\tau_{slope}}\right)} e^{-\tau/\tau_{slope}}, & if\ 0 < \tau \le \tau_{\max} \\ 0, & else \end{cases} \qquad (7\ of\ [39])$$

In this equation, τ_{max} is the maximum delay, $1/\tau_{slope}$ is the slope, and τ is the delay variable. The notion of a maximum delay inherently assumes some lower limit on resolvable amplitude value, relative to the maximum. Reference [39] does not address attenuation. Path loss exponent estimates are also listed in Table 3.3.

Table 3.3. Some Initial Aeronautical Scenario Channel Parameter Estimates.

	Parking Scenario	Taxi Scenario	Arrival/Takeoff Scenario
Range of Aircraft Velocity (m/s) (**all from [39]**)	0 … 5.5	0 … 15	25 … 150
Maximum Doppler Shift (Hz)	92.767	253	2,530
Maximum Delay (s)	9×10^{-6}	2×10^{-6}	10×10^{-6}
Delay Slope Time (s) (**all from [39]**)	1.0×10^{-6}	0.108×10^{-6}	1.0×10^{-6}
Path loss Exponent	3-4	2-3	2

Chapter 4: Channel Measurements

4.1 Introduction

This chapter contains a description of the channel measurements. We begin with a short description of the channel sounder test equipment and the test procedures we followed during the measurements. The actual airports at which measurements were taken are then described, with example photographs. Following this is a section on the measurements made for the other communication "settings." By this we mean those settings for which transmission/reception is not specifically between transceivers at the ATCT and a mobile unit on the airport surface. These two settings are (1) transmission between a "field site" transmitter and a mobile unit; and (2) transmission between the ATCT and a non-mobile unit at an airport field site.

The final section provides a summary of the measurement results, and some interpretation. This summary contains information on the measurement campaign itself, several example figures, and summary statistics from the measurements.

4.2 Channel Sounder Overview

The channel sounder is the set of test equipment used to measure the channel's characteristics. For this, a transmitter unit is required to launch a signal into the (unknown) channel, and a receiver unit is required to collect the signal output from the channel. These two units together are denoted "the sounder." In this section we provide a concise, high-level description of the sounder equipment itself, followed by a summary of the principle of its operation.

4.2.1 Channel Sounder Equipment

The two units of the channel sounder are the transmitter and the receiver. Additional required electronics/electrical equipment includes the AC power supplies for these units, and the battery pack for the mobile receiver unit. We also used an uninterruptible power supply (UPS) to enable moving the transmit unit from its calibration location to the actual transmit location. The UPS was also used for other measurements made with the transmitter used in a mobile mode (in addition to the receiver being mobile).

To use the sounder, a laptop computer is also required, connected to the receiver unit via an RS-232 cable. This laptop is used for receiver configuration and setup, as well as data recording. Low-loss RF cables to the antennas for both units are also required. For the mobile and field site transmitter tests, the antennas were omnidirectional monopoles; for the point-to-point tests, directional horn antennas were used. The list of key specifications for the sounder is provided as a section in Appendix C, the Detailed Test Plan and Procedures document.

Additional equipment used in the course of the measurements included a transmitter platform on which the transmitter was mounted, RF adaptors and attenuators, a digital camera, and other miscellaneous items. A more complete list of these items also appears in Appendix C.

Figure 4.1 provides several photographs of the sounder equipment, illustrating its compact size. Additional photographs appear in Appendix C.
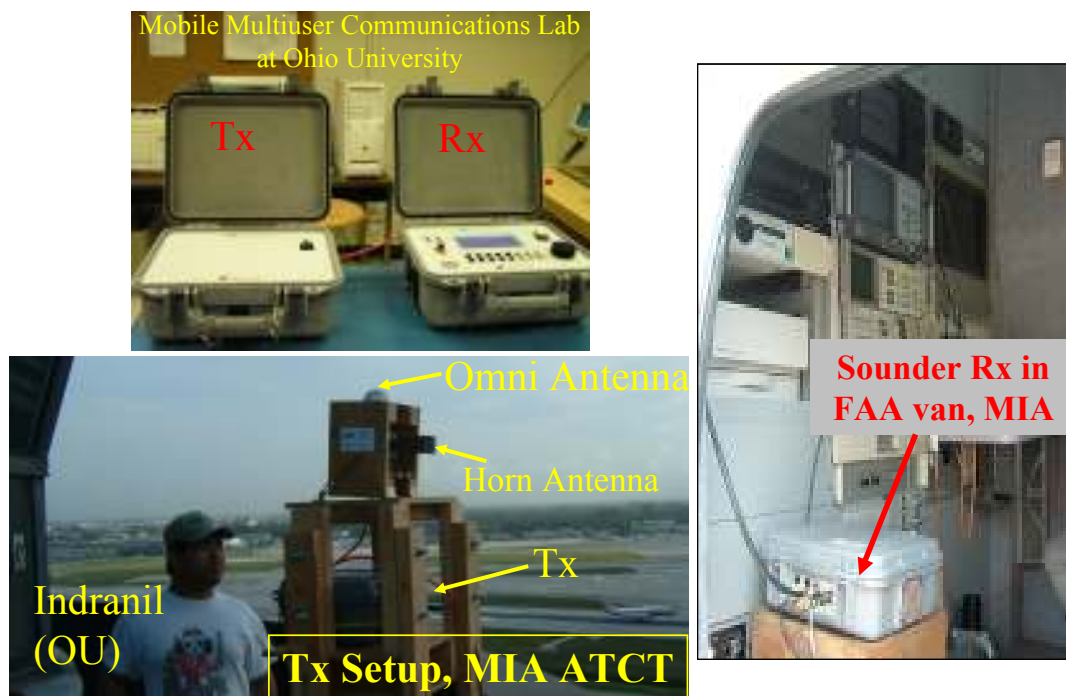
Figure 4.1. Photographs of the channel sounder units in the laboratory and in the field.

4.2.1 Channel Sounder Operation Principles

As noted in Chapter 3, we model the channel as a linear filter. This filter is slowly time-varying, with the rate of time variation dependent upon the velocities of transmitter, receiver, and local reflectors and scatterers. For all our measurements, mobile receiver velocities were relatively low; most of the time below about 20 miles/hour (mph), with a maximum velocity of approximately 35 mph.

With the linear filter model, the channel is completely described by its impulse response $h(\tau;t)$, which again is defined as the output of the channel at time t, due to an impulse input at time $t-\tau$. Procedurally then, all we must do is send the probing signal from the transmitter, and receive and record it at the receiver. This is illustrated in Figure 4.2, where for simplicity we've assumed a time-invariant channel. In the context of this figure, the sounder transmitter is the impulse generator, and the sounder receiver is the recording receiver.
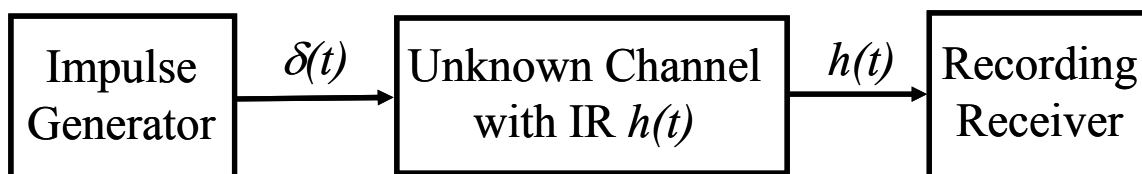
Figure 4.2. Theoretical procedure for measuring channel impulse response.

This particular approach is sometimes used, but there are several potential difficulties in practice. The first of these is the generation of the impulse function $\delta(t)$, which is strictly a zero-duration pulse with unit energy. Clearly this is unrealizable, but as semiconductor technology has advanced, very short duration pulses on the order of tens of nanoseconds are easily generated. Unfortunately these pulses are of very modest energy, and so must be amplified to enable transmission over distances of interest. This leads to another difficulty with the method of Figure 4.2: the linear amplification requirements of the transmitter. The spectrum of the pure impulse is white—equal power over all frequencies. For non-zero pulse durations the spectrum has finite support, and will also have some non-flat shape. In order for the impulse input to the channel to faithfully probe the channel's response at all frequencies (of interest), the amplifier must be very linear across the entire frequency band of interest, since non-linear distortion can dramatically alter the signal spectrum. Thus to attain link distances as large as possible, the amplifier must operate linearly at high power—a difficult and costly requirement.

The receiver of Figure 4.2 also has some challenging requirements. It too must operate linearly, and its bandwidth must also be wide enough to capture the transmitted signal energy plus any spectral spreading due to Doppler effects. In addition, for our application, where we wish to measure the channel over only some small portion of the spectrum (roughly 60 MHz in the 5 GHz MLS extension band), we need bandpass filtering, and frequency translations of the baseband signals. In most measurements we are also interested in averaging some of the channel responses, and by collecting multiple impulses, the receiver is able to gather more signal energy so that the CIR estimate can employ an adequate signal-to-noise ratio (SNR). Finally, the use of a high-energy impulse transmission can be susceptible to impulsive noise and narrowband interference.

A more popular method for channel sounding that avoids some of the difficulties of the "direct" approach of Figure 4.2 employs spread spectrum signaling. This is the approach our sounder, manufactured by Berkeley Varitronics Systems, Inc. [78], uses. The spread spectrum signal is a direct-sequence (DS) type of signal, which uses a high rate "chip" sequence to modulate a sinusoidal carrier in the band of interest. Each "chip" in the signal $c(t)$ emulates the impulse $\delta(t)$ in Figure 4.2, but these chips are transmitted continuously at rate R_c, which relaxes the peak power requirements of the transmitter. Figure 4.3 illustrates this approach.
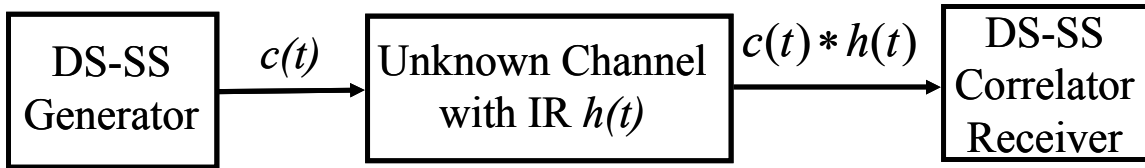
Figure 4.3. Direct-sequence spread spectrum procedure for measuring channel impulse response.

Note that the output of the channel is not the CIR exactly, but is a convolution of the chip signal with the actual CIR. Thus the time, or delay resolution of this method is limited to the chip duration $T_c = 1/R_c$. Multiple channel impulses that are within T_c seconds of each other appear "smeared" together as a single pulse. The receiver correlates the channel output signal with a local replica of the spreading signal $c(t)$, to obtain the CIR estimate. This CIR estimate is a good approximation of the CIR if the autocorrelation of the function $c(t)$ approximates an impulse.

The well-known maximal-length pseudo-noise (PN) sequences ("*m*-sequences") satisfy this property [76], and our sounder uses such a sequence. This spread spectrum technique has been known for decades, and was in some sense pioneered by Cox [41], [77]. The mathematics behind the technique is explained in [77] in abbreviated fashion; more detail is provided in [10].

For tracking slow time variation, the spreading waveform is sent repeatedly, and the receiver correlates continuously. The sounder described in [41] and [77] is a "sliding correlator," which operates by having the clock frequencies (chip rates) be slightly different at the transmitter and receiver, so that the sequence of one "slides" by the sequence of the other in time as it correlates. Our sounder uses a "stepped correlator," which operates similarly, but the two clocks are not of different frequencies—instead, the receiver correlates at one value of delay (τ) for some period, outputs that result, shifts its delay by T_c, correlates again and outputs the result, etc. In this way, the sounder probes over the entire unambiguous delay range of the sounder. This unambiguous delay range is given by the length of the PN sequence L=255 chips multiplied by the chip time T_c=20 nanoseconds, equal to 5.1 μseconds in our case. This limits the spread of delays our sounder can unambiguously resolve, i.e., if an actual multipath echo of delay larger than 5.1 μseconds longer than our first-arriving impulse is received, it will be "wrapped" around, and appear as a delay within the 5.1 μsecond range. The 5.1 μsecond delay corresponds to a distance *difference* between multipath components of approximately 1.5 km. This distance difference is not likely to occur in the short range settings of the airport surface.

The stepped correlator collects energy over multiple "symbols," where a symbol is the set of L chips, here of duration 5.1 μseconds. For our sounder output rate of 2 power delay profiles (PDPs) per second, this corresponds to a correlation, in each delay bin, of 383 symbols or approximately 1.953 milliseconds per delay bin. The PDP value in each bin represents the power collected over this duration, and this power is proportional to the square of the CIR amplitude value.

For measurement in the MLS extension band, the PN sequence $c(t)$ modulates a sinusoidal carrier in that frequency band. The modulation is binary phase-shift keying (BPSK). The receiver employs two quadrature channels (*I* for "in-phase," and *Q* for "quadrature"), hence in addition to power, we also collect amplitude and phase information. The receiver also collects the total received signal power ("RSSI," for received signal strength information).

Because of the limited sounder transmit power (2 Watts, or 33 dBm), the link range of the sounder is limited; the receiver sensitivity—the lowest value of total input power at which the receiver can collect accurate PDP data—is specified as -85 dBm, although individual multipath component power levels may be far below this. Simple link budget equations using a free-space path loss model (applicable, coarsely, to LOS-O settings) yield an approximate maximum range of nearly 4 km. This value of link distance has been attained in some measurements, and is adequate for many large airports (e.g., Miami, JFK).

4.3 Test Procedures

In this section we provide a short description of the actual test procedures. As previously indicated, a detailed description of actual procedures is provided in Appendix C. Prior to any measurement campaign, substantial coordination between our team and local airport authorities had to take place. The first milestone was to obtain from the FAA a Special Temporary Authorization to transmit at the test frequency band, at the selected airport. Before this could be

obtained, a radio frequency interference (RFI) study had to be conducted by the FAA, to ensure that our sounding transmissions would not interfere with any existing services, and also to ensure that no radio emissions would be present that could interfere with the sounding measurements. All this required that we provide information on our sounder's transmission characteristics, which was done. At all airports measured, these milestones were met easily and promptly.

A secondary consideration was the request and granting of permission for international graduate students to be allowed access to airport facilities. This too was achieved readily, after completion of some forms.

Before any testing, we also created a draft set of test routes on the airport surface. This was done by selecting points on an aerial photograph of the airport, and if available, also on drawings of the airport property. The test routes aimed to cover taxiways, gates, cargo areas, access roads, etc., both on and near the airport property.

Local airport authorities were contacted to schedule a testing period. Typically we required at least three days to conduct a thorough set of tests at any given airport. For most measurements, we arrived at the airport on a Monday, and first met with the airport personnel. This included the airport manager and some staff, particularly those technicians who would assist us in setting up and conducting tests, and driving around the airport surface. At these introductory meetings, we described our efforts in the overall context of ACAST, and airport modernization effects, and also discussed testing specifics. These specifics included the times required for conducting tests, including equipment calibration; actual data recording locations; airport ingress and egress requirements (badging, escorting, security, etc.); driving rules; and any other airport-specific regulations and adjustments (e.g., re-routing due to construction activity). A "walk through" to inspect ATCT areas where the Tx could be set up was also conducted. A final "review" meeting was also conducted with the local airport authorities after measurements were complete, and prior to our departure from the airport.

After discussing and negotiating all these things, and getting the transmit equipment in place at the ATCT, the first task prior to actual sounding measurements was the calibration of the sounder. We also termed this calibration "training." This required several hours at minimum, and was done to lock the precision Rubidium oscillators in the Tx and Rx, so that during measurements, drift of either unit's frequency would not cause the test measurements to be distorted. Once we had the equipment on site, for measurements subsequent to those on the initial day, we trained the equipment overnight. Generally speaking, the longer the training time, the more closely the sounder oscillators are locked, and the longer the available test time. Most testing runs on the airport surface took between 30 and 60 minutes, but some were longer.

During this training, the transmitter platform was set up at the ATCT. For all airports, this was done either on a "catwalk," or for JFK, on a section of a roof-like platform. The transmitter platform is a wooden structure we fabricated to contain the Tx unit, its power supply, the UPS, and the Tx antenna (see Figure 4.1). The platform was anchored to prevent movement, and covered with a tarpaulin if left outside unattended. The antenna was downtilted by approximately 45°, based upon measured antenna patterns (see Appendix E). During the training period, the Rx antenna and RF cable were also attached to the vehicle to be used for driving around the airport.

Once the training period was complete, we disconnected the sounder Rx and its battery (and the attached laptop pc), and as quickly as feasible moved this all down from the training location near the top of the ATCT to the vehicle that was to be used for driving around the airport surface. Once in the vehicle, the sounder Rx was connected to the antenna (outside the

vehicle, attached in advance) via the low-loss RF cable. Radio contact was maintained between the Tx team and the Rx team in the vehicle via walkie-talkies. Periodic communication was maintained to begin testing, and to assess progress. The Tx team also communicated to the mobile Rx team any visible complications possible during driving, for example, the approach of an aircraft that the mobile van would need to avoid.

Throughout the testing procedure, channel PDP data was recorded on the laptop pc. The testing route consisted of travel between numbered points, and the data file for each segment of travel was tagged with airport name, date, and segment end point numbers. One member of the Rx team was also responsible for taking notes on the surrounding environment, to correlate environmental effects with channel measurements. At each measurement location, the mobile vehicle was stopped to take a GPS location reading, and to close one data file and open the next. Upon completion of the test route, the Rx team returned to the ATCT, and the Tx and Rx were re-connected for training for the next set of measurements.

Typically, the travel route was traversed as planned for the first measurement run. Depending upon some of the results of the first test run, some of the testing route segments were not covered during subsequent routes. One reason for this was low signal level in some areas due to both long distances and to complete obstruction of the LOS path. This is illustrated in Figure 4.4, which shows an aerial view of the Miami International Airport. In this figure, with the Tx at the ATCT, the received signal level at points 16 and 17 was below the Rx threshold for much of the time, due to the effects mentioned. Thus in subsequent runs we avoided this area (but did re-visit it during the field site measurements, described in what follows). Other areas that were not granted "repeat visits" included some of the LOS-O areas, which incurred very little multipath propagation, and so were of lesser interest than the more dispersive areas.

Figure 4.4. Aerial view of Miami International Airport, showing numbered test locations.

4.4 Descriptions of Airports Measured

In this section we provide a description of the airports at which measurements were taken. This includes large/medium airports, and the small (GA) airports. An extensive set of photographs, and some drawings, are provided in Appendix E. As per the airport classification discussion in Chapter 3, we discuss large, medium, and small (GA) airports.

The selection of actual airports at which measurements were made was done on the basis of convenience, and airport characteristics. For example, the first airport at which we measured was the Ohio University airport, in Albany, OH. This GA airport is readily accessible, and enabled us to conduct our first set of field tests before embarking on larger measurement campaigns. The next airport at which we measured was Cleveland Hopkins International Airport (CLE), due to its proximity to Ohio University and to NASA GRC; the nearby GA airport Burke Lakefront, in Cleveland was also measured during our trip to Cleveland. The remaining airports were selected to be larger, busier airports: Miami International Airport (MIA) in Miami, FL, and John F. Kennedy International Airport (JFK) in New York, NY. The GA airport Tamiami, in Kendall, FL, was also measured during the Miami trip.

4.4.1 Large Airports

These airports are MIA and JFK, measured in June 2005 and August 2005, respectively. The MIA aerial view was shown in Figure 4.4. A comparable view for JFK is shown in Figure 4.5. As with MIA, most testing was done near terminal buildings, concourses, and other buildings on the airport surface, with some testing along perimeter and access roads. No LOS-O regions were tested in either of these airports, as noted.

A good photograph of part of the area in JFK is shown in Figure 3.2. This figure is from the ATCT, taken looking toward the lower right of Figure 4.5 (roughly toward point #22). Another photograph, looking approximately toward point #10 in Figure 4.5, is shown in Figure 4.6. The Manhattan skyline can be dimly seen in the distance. Figure 4.7 shows another view of the airport surface, from the ATCT, showing the scale of ground vehicles, planes, and buildings. This was taken during a "slow" time of day, but there are more than 10 jets parked, several jets taxiing, and more than 20 ground vehicles parked and moving about this portion of the airport surface, illustrating the potential activity level. The size of the concourse and terminal buildings, which are significant obstructions and diffractors, is also apparent in this figure. Finally for JFK, Figure 4.8 shows a picture of the ATCT, taken from the airport surface, from very near the point marked "ATCT" on Figure 4.5. The location of the sounder transmitter is indicated.

For MIA, similar features can be observed. Figure 4.9 shows a view from the MIA ATCT, toward the downtown section of Miami. During the course of testing, in our ground vehicles (at all the airports) we drove in and around both parked and moving jets, near concourses and loading areas, beside, behind, and in front of groups of other ground vehicles, essentially visiting all areas of the airport surface a ground vehicle or plane would go. In signal processing terms, we believe that we have adequately spatially sampled the environment.

Figure 4.10 shows a view of the two ATCTs in MIA, from one of the taxiways, in a LOS-O area. The sounder Tx was mounted on the older (shorter) ATCT, but this did not cause any unusual problems except for occasional obstructions. Figure 4.11 shows a closer view of the two towers. Rather against the odds for Miami, we did not encounter any rain during testing!
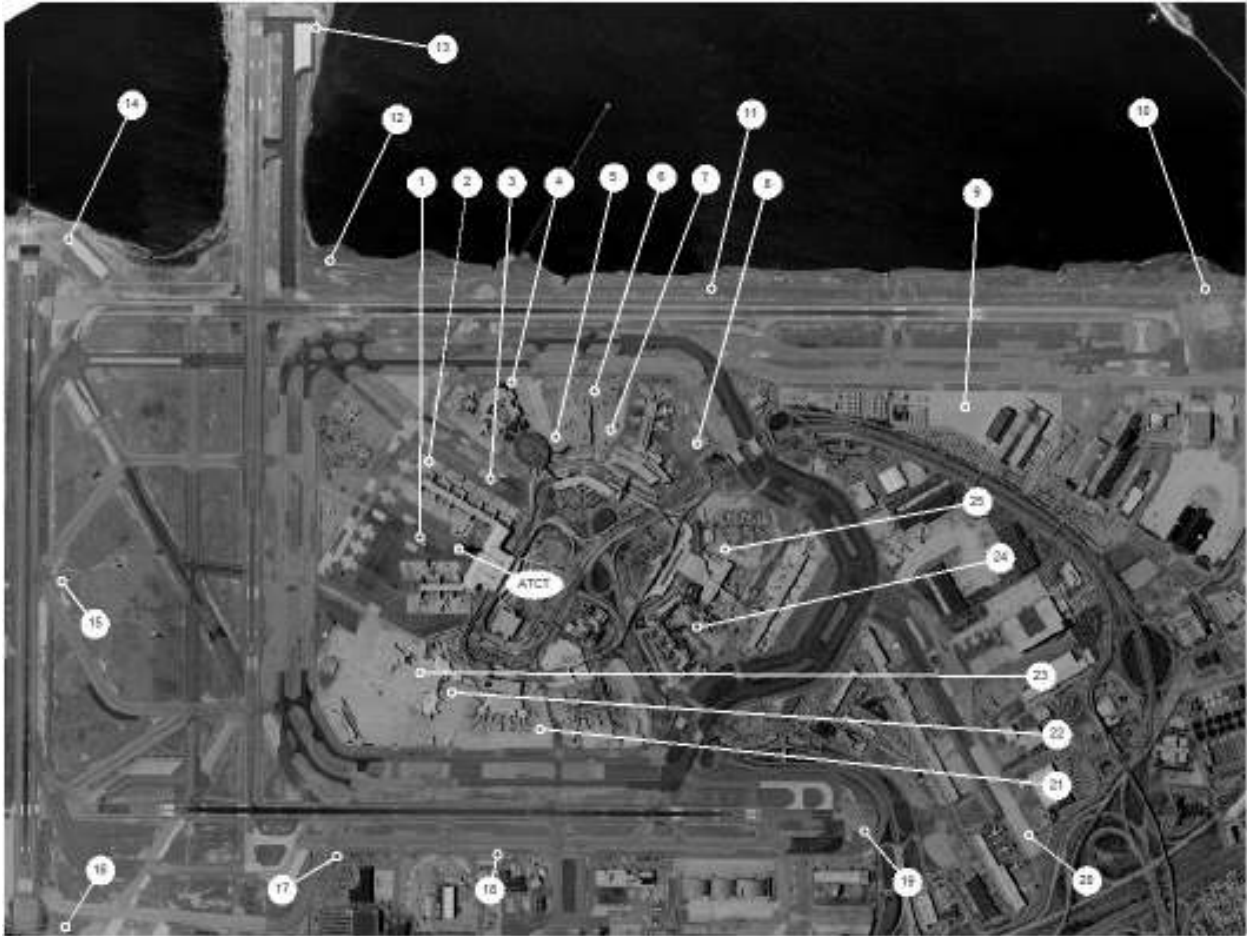
Figure 4.5. Aerial photograph of JFK International Airport, showing numbered measurement locations.

Figure 4.6. Photograph of JFK International Airport, from ATCT, toward Manhattan.

Figure 4.7. Photograph of JFK International Airport, from ATCT, showing portion of airport surface.

Tx Location

Figure 4.8. Photograph of JFK International Airport ATCT, showing Tx location.

Figure 4.9. Photograph of MIA International Airport from ATCT, toward downtown Miami.

Figure 4.10. View of two ATCTs in MIA, from taxiway, in LOS-O area.

Figure 4.11. Close view of two ATCTs in MIA, from near a gate, in LOS-O area.

4.4.2 Medium Airports

The single medium sized airport at which measurements were taken was Cleveland Hopkins International (CLE), measured in March 2005. An aerial photo of CLE, with the numbered measurement test points, appears in Figure 4.12.

As with the large airports, CLE had buildings on and beside the airport surface, but generally fewer and smaller buildings than on the large airports. Figure 4.13 shows a view looking down one of the concourses during a fairly busy time. Note the presence of some snow cover on the grass areas. We noted some probable enhancement of the ground-reflected signal in some of the LOS-O measurements, attributable to this snow. In Figure 4.14, we show another photo from the ATCT, in which the OU mobile van (containing the sounder Rx) and the FAA escort van, are behind a taxiing jet.
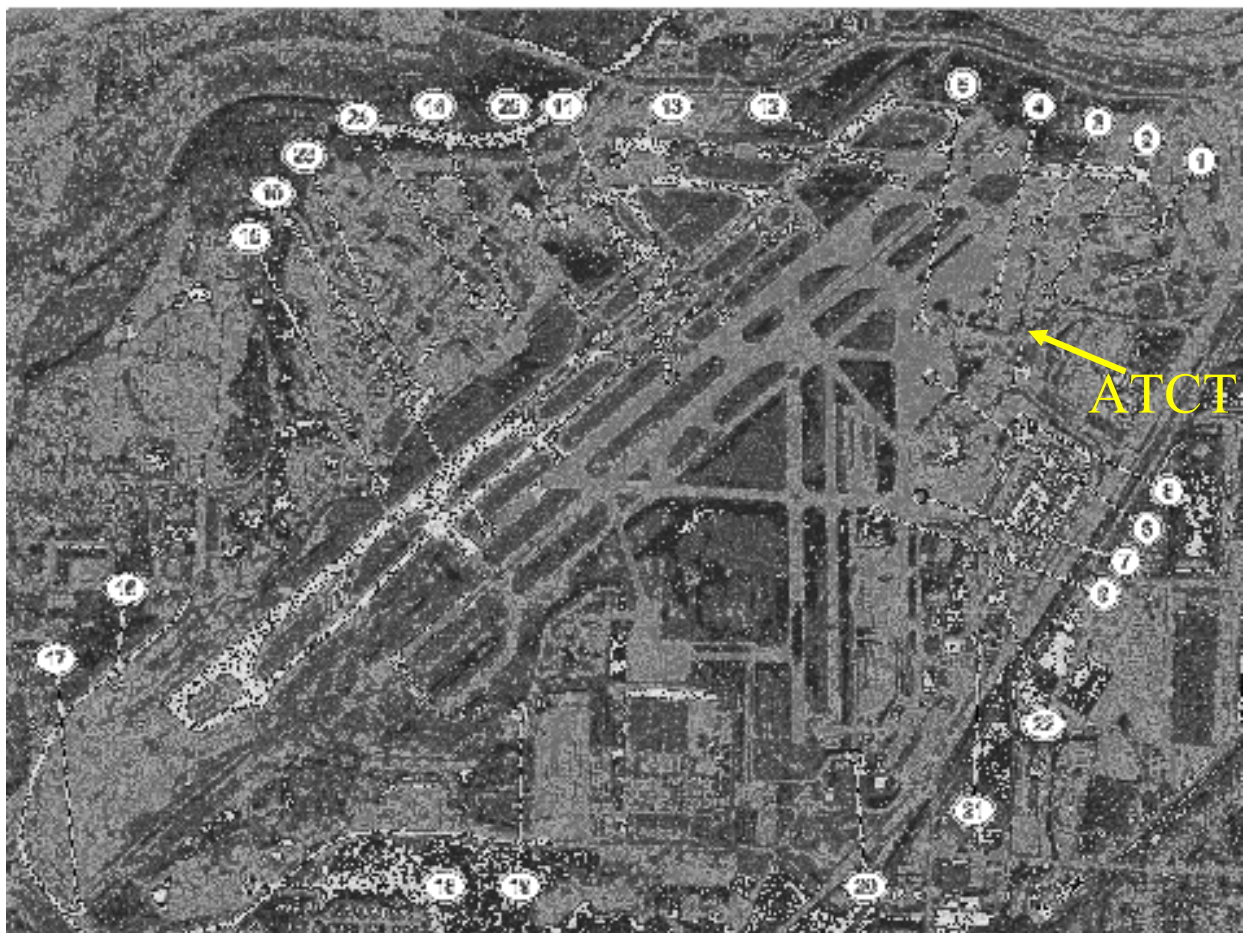
Figure 4.12. Aerial photograph of Cleveland Hopkins International Airport, showing numbered measurement locations.

Figure 4.13. Photograph of CLE International Airport from ATCT.

Figure 4.14. Photograph of FAA and OU mobile vans at CLE International Airport, from ATCT.

4.4.3. Small (GA) Airports

For the small airports, we were generally unable to obtain good aerial photographs. Given the much smaller size of these facilities, this was not a problem. In Appendix E, we have scanned some drawings for these facilities. In this section we provide some additional discussion with photographs.

Figure 4.15 shows another view of the OU Airport. In this figure, the view is from the "crow's nest," which is on the roof of the AEC hangar building, looking away from the runway and taxiway areas. Other hangars can be seen on the left, equipment sheds on the right, and the McFarland AEC office building near the center. Reflection and scattering occurred from all these objects, and also from the parked cars. Measurements at the OU airport were made in February and March 2005.

Figure 4.15. View of "back" of OU Airport, from "crow's nest" atop AEC hangar building.

Another view shows the AEC mobile van on one of the OU airport taxiways in Figure 4.16. Note that this is, as in most runway areas of all airports, a wide open (LOS-O) area.

Figure 4.17 shows a view of the sounder Tx mounted on its platform, atop a shed near the end of the runway at Tamiami airport in Kendall, FL. Several members are the measurement team provide an idea of scale. At Tamiami, in June 2005, we were unable to arrange transmission from their ATCT, thus had to use this location, with an antenna height of approximately 5 m. The results for this channel thus have much in common with "field site" transmitter measurements, described in the next section. Figure 4.18 shows another view of Tamiami.

Figure 4.16. View of AEC mobile van on taxiway at OU airport.

Figure 4.17. View of sounder Tx and some of the measurement team atop shed at Tamiami Airport.

Figure 4.18. View of Tamiami airport from transmit site.

The third GA airport was Burke Lakefront, in Cleveland, measured in March 2005. Figure 4.19 shows a view looking back toward downtown Cleveland, showing some of the large buildings that were likely reflectors for some of the measurement locations. As can be surmised from the name, Burke Lakefront is on the lake—Lake Erie—and hence no significant reflectors are generally present on the water side. Figure 4.20 shows another view of Burke Lakefront, showing the mobile van moving between parked GA aircraft on one side of the ATCT. In Figure 4.21 we show another photo of Burke Lakefront, with Lake Erie and a large ship docked nearby.

Figure 4.19. Photo from Burke Lakefront ATCT looking away from runway, toward downtown Cleveland.

Figure 4.20. View of AEC van traveling between parked GA aircraft at Burke Lakefront Airport.

Figure 4.21. AEC van, escort van, and parked planes at Burke Lakefront.

4.5 Point-to-Point and "Field Site Transmission" Measurements

To deploy a wireless network on the airport, it is useful to have multiple "nodes," or points to which mobile units can link. This is true for several reasons. One is that, in some locations, due to long distances or large obstructions or both, adequate signal strength may not be attainable from the ATCT. Another is capacity—a larger number of mobile units can be supported with multiple "base nodes." Also, for network robustness in the presence of any single node failure, alternate connection points are valuable. There are also needs for direct, point-to-point links from field sites to the ATCT. An example application is transport of airport surface radar data.

In view of this, we also took measurements of two other types, as noted at the beginning of this chapter. The point-to-point links were from the ATCT to an airport field site, using directional antennas. These antennas were either "10 dB" or "20 dB" standard gain horns. For these, the gains and beamwidths are as given in Table 4.1. These parameter values were measured in our antenna test chamber. Polar gain plots of the two antennas appear in Appendix E. For measurements at Cleveland, two 10 dB horns were used. For the Miami measurements, one 10 dB (Tx) and one 20 dB horn (Rx) was used. No point to point measurements were made at JFK.

Table 4.1 Parameters of horn antennas used in point-to-point measurements.

Parameter	10 dB Horn	20 dB Horn
Gain (dB)	8.5	17
3 dB Beamwidth (degrees)	60 azimuth; 60 elevation	30 azimuth; 15 elevation
10 dB Beamwidth (degrees)	100 azimuth; 120 elevation	50 azimuth; 30 elevation

Because of the antenna directionality, multipath was significantly attenuated, so these channels are far less dispersive, and far less time varying, than the mobile channels. In these measurements, in addition to measuring the channel when both antennas were aimed at each other (boresight), we also took measurements when the receiver antenna, located at the field site, was rotated through the full 360° in azimuth. This provides some information on potential multipath sources, and the variation of received power versus azimuth angle. A photograph showing point to point measurements in Miami, taken from the field site looking back toward the ATCT, is shown in Figure 4.22. Channel models were also developed for these measurements, and are described in detail in Chapter 6. The orientation of the antennas at one of the point-to-point sites is shown in Figure 4.23.

The final measurement setting we denote the "airport field site" (AFS) transmitter measurements. For these, transmission was *from* a field site (similar to that in Figure 4.22), with reception at the mobile van. This enabled us to gather channel characteristics for such settings, and in particular, allowed us to explore regions of the airport that were distant and shadowed from the ATCT. Figure 4.24 shows a view from one of the AFSs in Miami, looking toward approximately the 90° angle in Figure 4.23. The high-gain horn is shown in the foreground in the lower right.
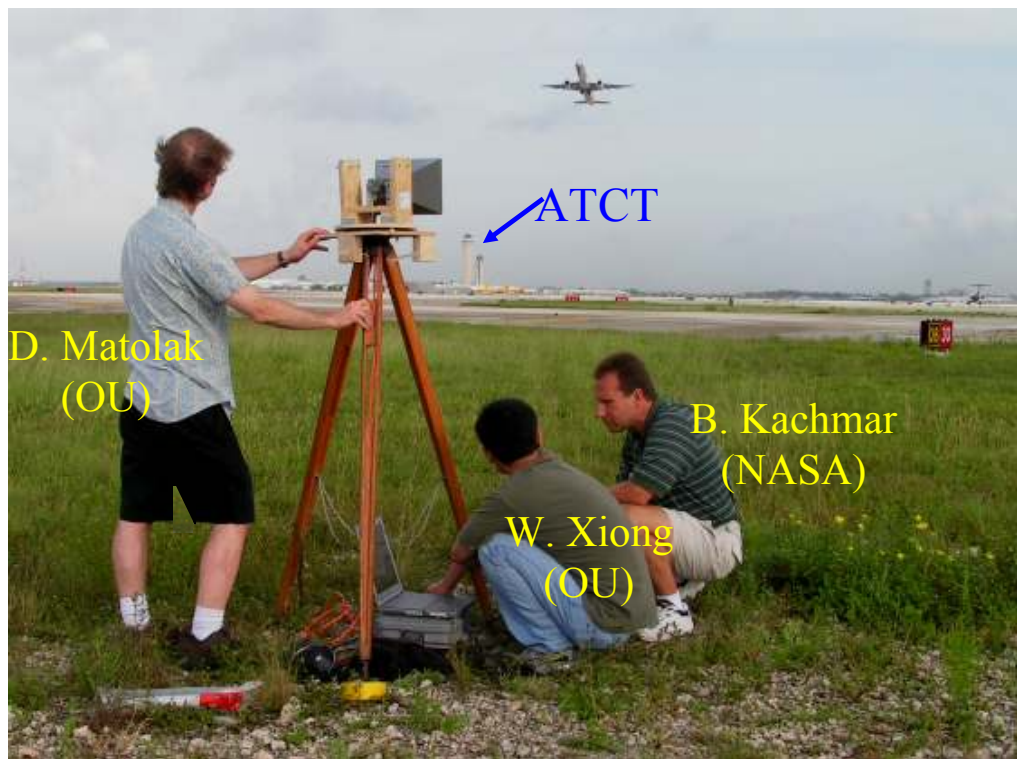
Figure 4.22. Field site measurement at Miami International Airport.
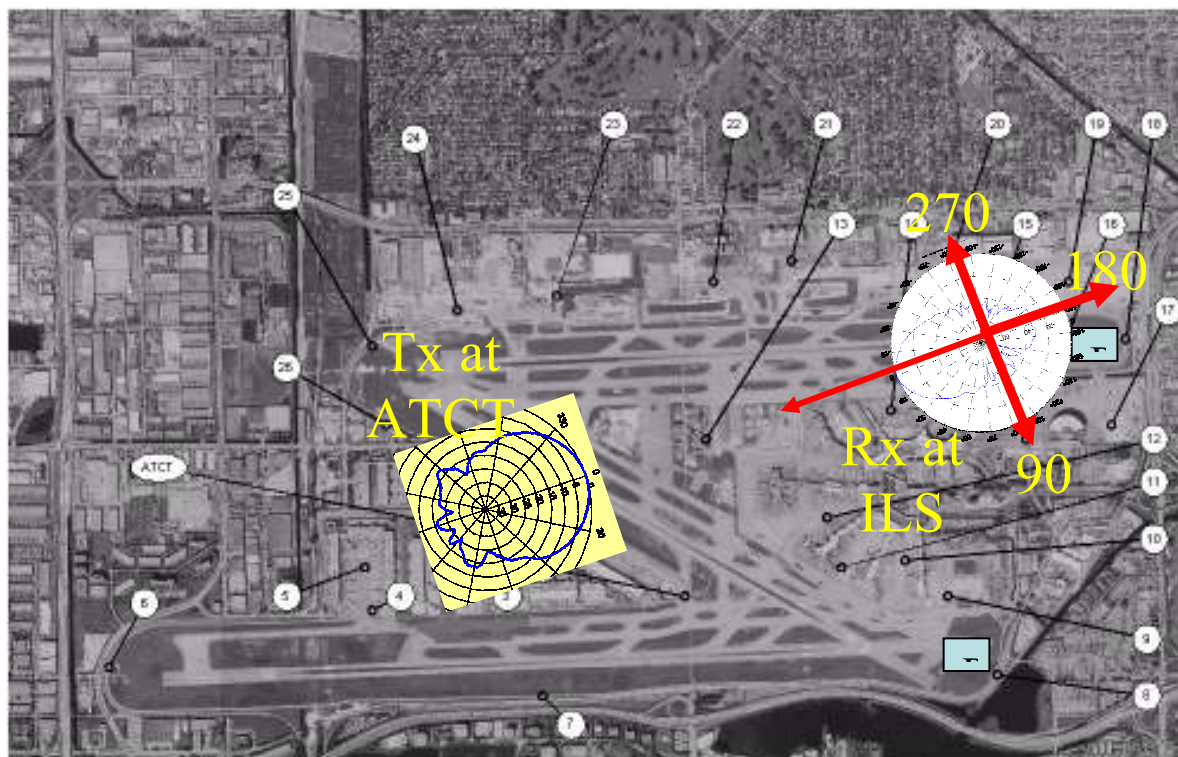
Figure 4.23. Aerial view of Miami International Airport, showing antenna orientations for one of the point to point measurements.

Figure 4.24. View from field site transmitter, Miami.

4.6 Measurement Result Summary

In this section we provide a high-level summary of the measurement results. This is intended to give the reader a sense of the scope of the project and the amount of data collected, and also to summarize some of the channel statistics. Example plots for some parameters are also provided, with detailed models in Chapter 6.

Table 4.2 summarizes the amount of data, taken in terms of the number of PDPs at each airport, for each of the three settings. Not all settings were measured in each airport. The abbreviations BL=Burke Lakefront, and TA=Tamiami. After data pre-processing (described in Chapter 5), each PDP consists of 255 samples, one for each chip of the spreading sequence. Each sample is represented by a two-byte word, for both I and Q channels, RSSI, phase, etc.

Table 4.2 Summary of measured PDPs for three settings.

Airport	Total Number of PDPs		
	Mobile	**Point to Point**	**Field Site Transmit**
JFK	13,796	—	9,512
MIA	12,249	2,598	2,317
CLE	2,627	2,326	—
OU	1,108	—	—
BL	908	—	—
TA	5,203	—	—

Table 4.3 breaks this data down further into measurements in each of the three airport propagation regions, LOS-O, NLOS-S, and NLOS. For the point to point measurements, there were only LOS-O conditions, so all data for this setting appears in Table 4.2. In addition to the number of PDPs for each region, we also list the values of root-mean-square (RMS) delay spread (DS) that were used as dividing points for classification: values of RMS-DS less than or equal to $\sigma_{\tau 1}$ indicate the PDP is in the LOS-O region, values of RMS-DS between $\sigma_{\tau 1}$ and $\sigma_{\tau 2}$ denote the PDP is in the NLOS-S region, and values of RMS-DS above $\sigma_{\tau 2}$ indicate PDPs in the NLOS region. The use of RMS-DS is not the only means for making this division into regions, but as will be illustrated in Chapter 5, it is a useful and common one. Note that for JFK, MIA, and TA, we had no LOS-O data, hence only $\sigma_{\tau 2}$ is specified.

Table 4.3 Summary of measured PDPs for each propagation region. RMS-DS values (σ_τ's) in ns.

Airport	Total Number of PDPs				
	Mobile			Field Site Transmit	
	NLOS ($\sigma_{\tau 2}$, ns)	NLOS-S ($\sigma_{\tau 1}$, ns)	LOS-O	NLOS ($\sigma_{\tau 2}$, ns)	NLOS-S ($\sigma_{\tau 1}$, ns)
JFK	6,693 (800)	7,103	—	7,272 (800)	2,240
MIA	6,299 (1000)	5,950	—	909 (1000)	1,408
CLE	1,332 (500)	852 (125)	443	—	—
OU	—	1,108	—	—	—
BL	—	652 (125)	256	—	—
TA	2,248 (500)	2,955	—	—	—

In Table 4.4, we tabulate our summary values of measured RMS-DS. We have quantified the mean, maximum, and minimum values for the airports.

Table 4.4 Summary of measured RMS-DS values for three settings.

Airport	RMS-DS (nanoseconds) [min; mean; max]					
	Mobile			Point to Point	Field Site Transmit	
	NLOS	NLOS-S	LOS-O	LOS-O	NLOS	NLOS-S
JFK	[800; 1,469; 2,456]	[21.4; 311; 798.7]	—	—	[802; 1,475; 2,433]	[5.8; 317.3; 799.5]
MIA	[1,000; 1,513; 2,415]	[23.1; 459; 999.9]	—	[5.6; 163; 249]	[1,000; 1,625; 2,451]	[8; 443; 997]
CLE	[500; 1,206; 2,472]	[125; 295; 499]	[14; 65; 124]	[1; 18.12; 202]	—	—
OU	—	[14; 293; 2,416]	—	—	—	—
BL	—	[126; 429; 2,427]	[5; 44; 124]	—	—	—
TA	[502; 1,390; 2,404]	[15; 256; 499]	—	—	—	—

To this point we have primarily discussed temporal spreading of the signal by the channel, quantified by RMS-DS. This temporal spreading has implication for frequency selectivity; as noted in Chapter 3, we employ a frequency correlation estimate (FCE) [47], akin to a correlation, or coherence, bandwidth. This will be defined in more depth in the subsequent chapters, but in essence involves using Fourier transforms of PDPs and cross-correlating spectral components. For this summary, in Table 4.5 we list bandwidths for which frequency correlation takes values of 0.9, 0.5, and 0.2, with the frequency separation associated with the 0.9 value meaning essentially fully correlated channel effects, and the frequency separation associated with the correlation value of 0.2 meaning essentially uncorrelated channel effects.

Regarding interpretation of these FCE values, the bandwidth values we cite are associated with the smallest frequency separation for which the FCE attains the correlation value. For the NLOS case, due to our frequency resolution limit (255 points in 50 MHz for approximately 196 kHz per frequency bin), it is difficult to determine the frequency separation for which the FCE reaches 0.9. Note also that for the point-to-point data, we have averaged the FCEs over the locations at each airport—more detail on this is given in Chapter 6. For the MIA FCE point-to-point case, the FCE never falls below 0.6, so the frequency separation for correlation values of 0.5 and 0.2 is 50 MHz. Finally here, the FCEs for the field site transmitter settings are only for a portion of the airport. More discussion on this also appears in Chapter 6.

Table 4.5 Summary of computed FCE values for three settings.

Airport	FCE (MHz) for Correlation of [0.9; 0.5; 0.2]					
	Mobile			Point to Point	Field Site Transmit	
	NLOS	NLOS-S	LOS-O	LOS-O	NLOS	NLOS-S
JFK	[NA; 1.56; 18.8]	[4.7; 15.2; 21.5]	—	—	[NA; 1.56; 18.8]	[4.3; 14.8; 16.8]
MIA	[NA; 0.78; 14.8]	[1.56; 15.2; 22.3]	—	[15.2; 50; 50]	[NA; 1.16; 13.6]	[4.3; 11.7; 16.8]
CLE	[NA; 10.1; 21.4]	[5.9; 17.1; 22]	[6.6; 17.6; 22.6]	[4.7; 12; 22.2]	—	—
OU	—	[3.9; 12.5; 21.4]	—	—	—	—
BL	—	[3.5; 13.2; 19.6]	[6.6; 16 ;2 1.4]	—	—	—
TA	[NA; 9; 16]	[3.9; 14.1; 20.8]	—	—	—	—

Finally for this chapter's tabulated summaries, in Table 4.6 we provide some information on channel tap amplitude statistics. As will be explained in detail in the following chapters, there are several statistical models commonly used for amplitude statistics. The tap associated with the first arriving signal generally has the least amount of fading; often this tap is an LOS component, or nearly so (e.g., diffracted). Because of this, it is often well modeled by the Ricean distribution, characterized by its Ricean "K-factor," the ratio of power in the specular component to that in the scattered components that make up this first tap. A larger K-factor indicates less severe fading, and K is usually given in dB. For Rayleigh fading, the K factor is -∞ dB.

As will be seen, for different channel bandwidths, the channel model has a different number of taps, so here, we don't provide statistics for all taps. Instead, we provide values for the range of the Weibull distribution "shape factor" β, across *all* remaining taps (other than the first). This shape factor is analogous to the Ricean K-factor: $\beta =2$ constitutes Rayleigh fading, and smaller values of β mean more severe fading, larger values mean less severe fading. Additional things to note are that for the NLOS setting, the first tap is generally not strong, so the Ricean characterization does not apply. For the NLOS setting, we hence have no 1st-tap K-factor, and the Weibull β parameter applies to all taps. In the point-to-point case, the range of K factors for the first tap applies here only to the "boresight" antenna alignment (again, more on this in Chapter 6).

Table 4.6 Summary of computed Ricean *K*-factor values and range of Weibull *β*-factors for three settings.

| Airport | K-factors (dB); and Range of β-factors (min; max) | | | | | |
| | Mobile | | | Point to Point | Field Site Transmit | |
	NLOS	NLOS-S	LOS-O	LOS-O	NLOS	NLOS-S
JFK	(1.42; 2.09)	10.1 (1.67; 2.18)	—	—	(1.52; 2.1)	10.8 (1.58; 2.05)
MIA	(1.51; 2.13)	9.3 (1.66; 2.04)	—	(23–25)	(1.74; 2.8)	8.4 (1.5; 1.73)
CLE	(1.59; 2.25)	9.5 (1.77; 1.89)	13.1 (1.69; 2.2)	(14.1–15)	—	—
OU	—	8.9 (1.75; 2.36)	—	—	—	—
BL	—	12.5 (1.7; 2.73)	14.5 (1.88; 2.4)	—	—	—
TA	(1.4; 1.87)	11 (1.54; 2.02)	—	—	—	—

A few example plots are now provided for illustration. Figures 4.25-4.27 show PDPs for an LOS-O region, an NLOS-S region, and an NLOS region, respectively. The latter two are from the JFK airport, whereas the LOS-O PDP is from CLE. The RMS-DS values are listed on the plots, along with the mean energy delay (μ), and the 90% energy delay window (W_{90}). These latter parameters are defined in the next chapter. As expected, the energy is spread in time most for the NLOS case, second-most for the NLOS-S case, and least for the LOS-O plot. The RMS-DS and delay window values illustrate this concisely. We also note that there may be some impulses beyond our maximum unambiguous delay range in Figure 4.27. These would be "wrapped around" to within the 5.2 microsec window. This effect is fortunately rare, and this particular PDP is one of our worst-case ones. Given the rich scattering present in these PDPs, the statistics (RMS-DS in particular) would not be significantly changed by several low-energy multipath components beyond the maximum unambiguous delay range.

$\mu_\tau = 89$ nsec
$\sigma_\tau = 52$ nsec
$W_{90} = 20$ nsec
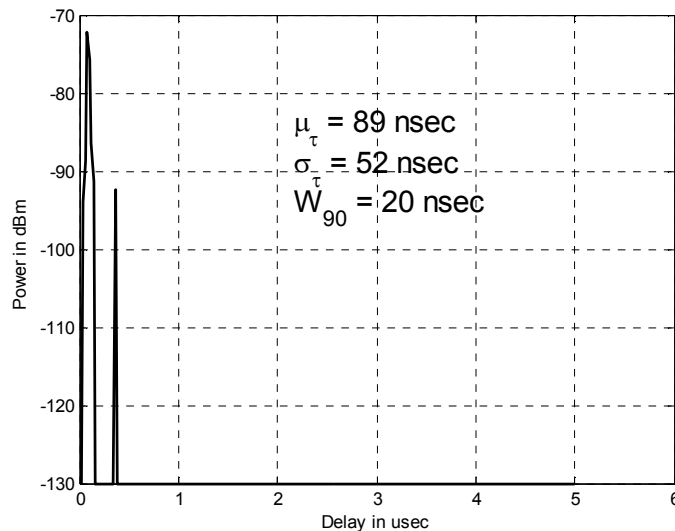
Figure 4.25. Example PDP for CLE, LOS-O region.
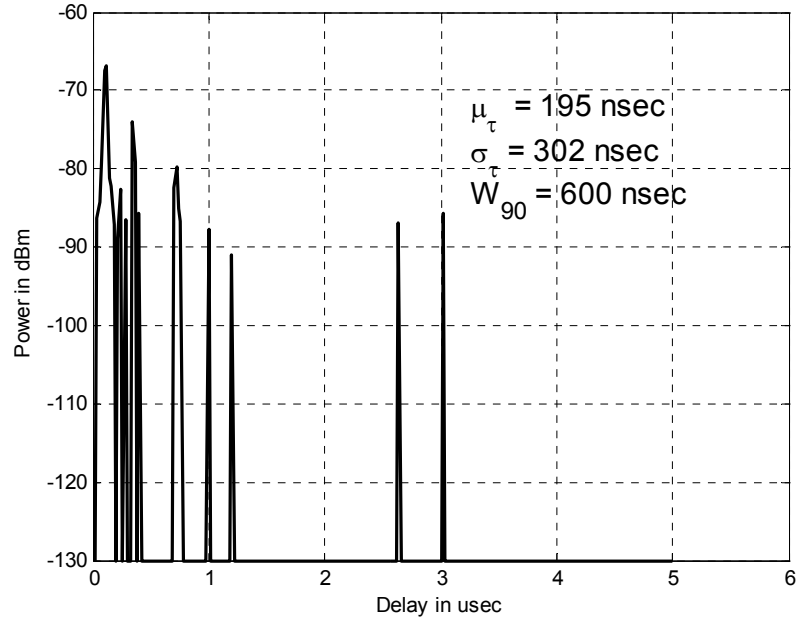
Figure 4.26. Example PDP for JFK, NLOS-S region.
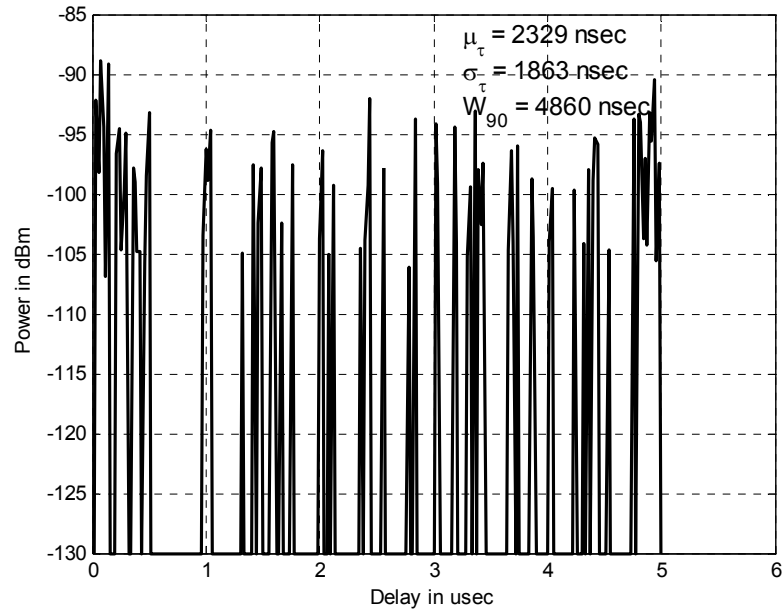
Figure 4.27. Example PDP for JFK, NLOS region.

In Figure 4.28 we show the time evolution of an NLOS PDP, showing how the received components fade in time. Fades of more than 10 dB are evident for the main (first) tap. Figure 4.29 shows a plot of the time-varying transfer function $H(f,t)$, for an NLOS case in MIA. This figure is obtained by Fourier transforming the consecutive PDPs, as in Figure 4.28.
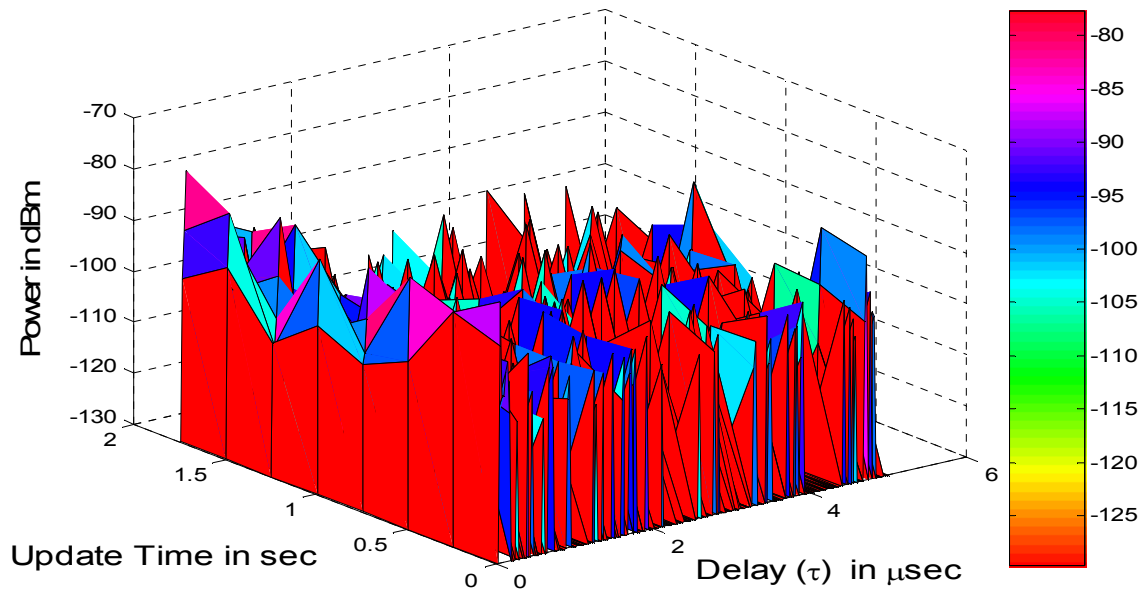
Figure 4.28. Example PDP vs. time for JFK, NLOS region.
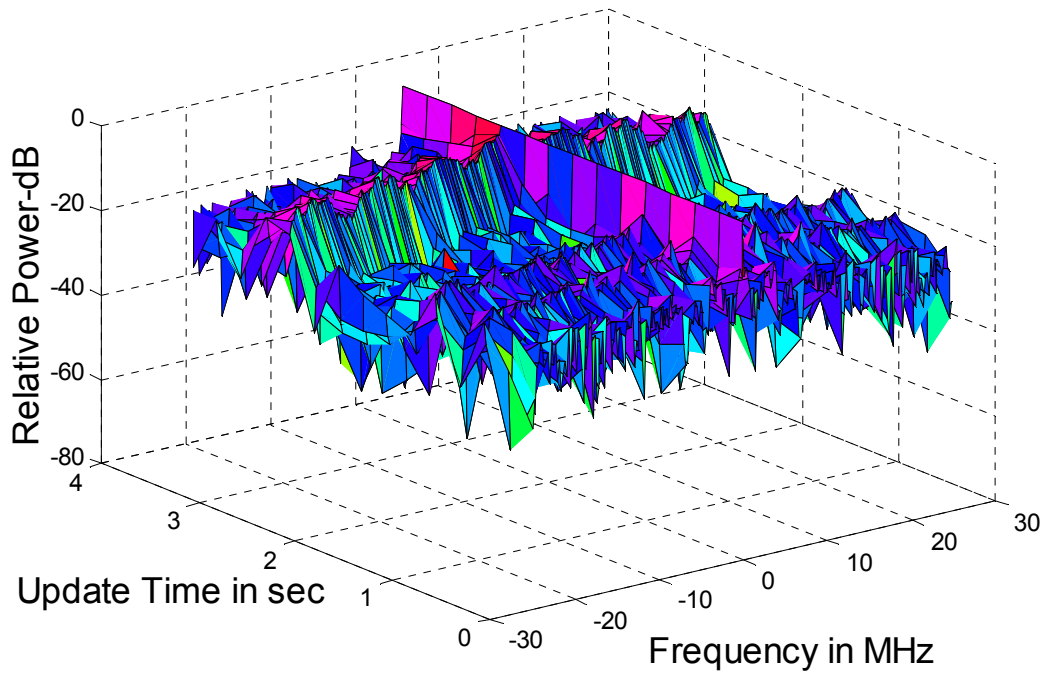
Figure 4.29. Example transfer function vs. time for JFK, NLOS region.

Next, Figure 4.30 shows an example FCE for the NLOS-S setting in JFK. For this figure, obtained by averaging 7,103 PDPs, the frequency separations for which the channel correlations are 0.9, 0.5, and 0.2 are 4.7 MHz, 15.2 MHz, and 21.5 MHz, respectively.
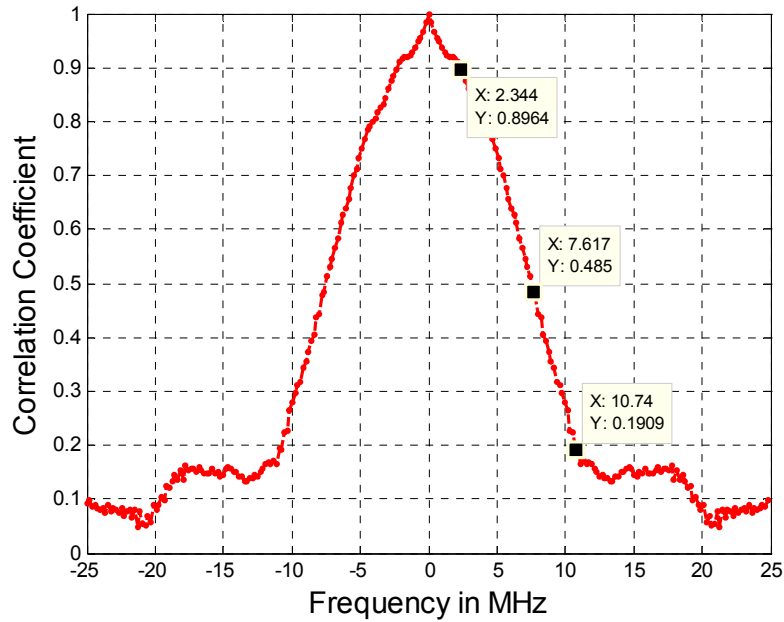
Figure 4.30. FCE for NLOS-S setting, JFK.

Finally, in Figure 4.31, we show a histogram for the distribution of RMS-DS data obtained for JFK. This clearly shows the presence of two distinct "modes," corresponding to the two different channel regions, NLOS-S and NLOS. Additional plots and statistics are given in the subsequent chapters.
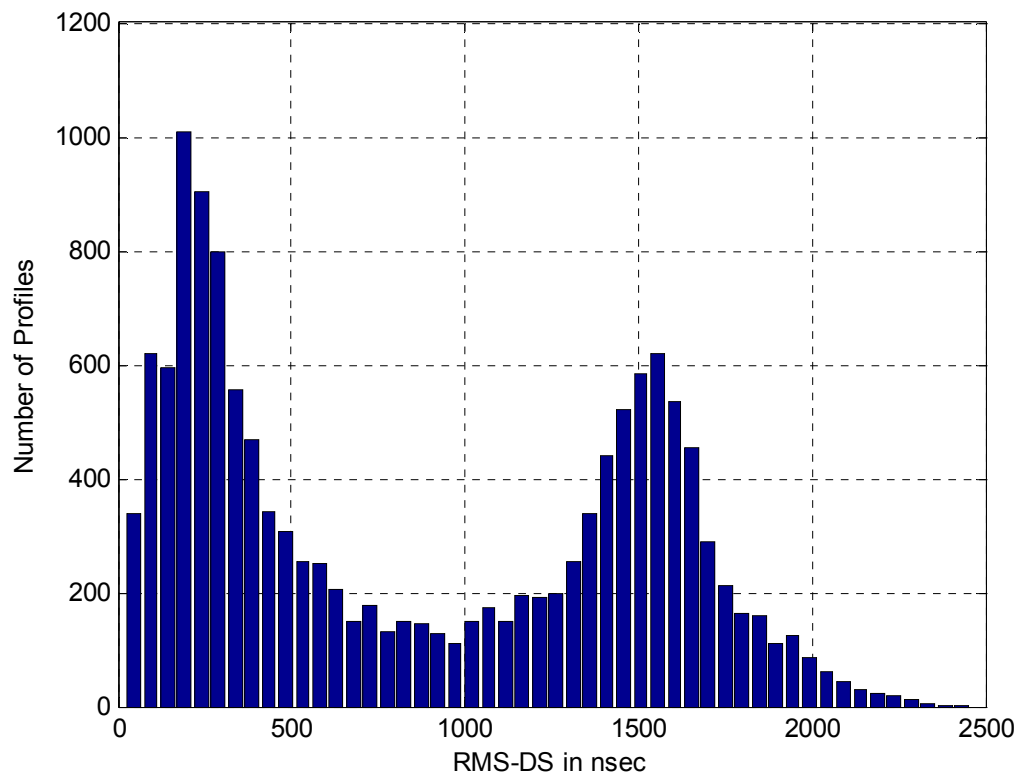
Figure 4.31. Histogram of RMS-DS values for all PDP data, JFK.

Chapter 5: Extraction of Parameters for Channel Model Development

5.1 Introduction

In this chapter we describe the steps necessary for data pre-processing, and also define the key parameters that we use to describe our channel models. This pre-processing is needed to extract the pertinent features of the CIR, and discard effects such as those due to "noise." Discussions regarding the trade-offs between model implementation complexity and the accuracy of the channel description are provided.

5.2 Data Pre-Processing

In this section we describe the pre-processing steps necessary to convert the "raw" data files collected during the measurement campaigns (described in Chapter 4) into data files that are used for the development of the channel models. The pre-processing consists of format translation (to translate sounder data into data readable by our primary software package, MATLAB®), noise thresholding to eliminate the effects of thermal noise "spikes," and multipath thresholding, to effect a suitable compromise between model fidelity and implementation complexity.

5.2.1 Channel Sounder Calibration and Limitations

The sounder records Impulse Response Estimates (IREs), which are our estimates of the CIR, as discussed in Chapter 4, at each measurement point. To isolate the effect of the sounder's autocorrelation from the actual channel CIRs, it is necessary to determine an autocorrelation curve for the sounder itself. This process is sometimes referred to as a "calibration" in the literature. The preferred method of doing this calibration is to perform a "back-to-back" test on the sounder, in which the Tx is connected to the Rx through a short length of high-quality RF cable. An attenuator is also used to set the Rx input power level appropriately. We have done this for our sounder, and have confirmed that the measured autocorrelation for our sounder is very close to being an impulse. Figure 5.1 shows the autocorrelation curve obtained from a back-to-back measurement with the sounder; we also provide an exponential curve fit for the autocorrelation values, in dB units. The sounder was calibrated for a BW of 50 MHz. The autocorrelation curve falls to -14 dB for the first chip (chip time is 20 nanoseconds) and -31 dB for the fourth chip! For use with IREs taken from channel measurements, any measured impulse that is equal to or below the autocorrelation value is ascribed to autocorrelation, and is not counted in collecting the IRE statistics.

We also point out that for all measurements, the Tx and Rx must be calibrated for some time to align the oscillators (see Appendix C). Calibration (or, "training") yields us a so called "reliable measurement time," denoted T_{meas}. We have found through numerous tests that the

Rubidium oscillators in both Tx and Rx are stable enough that very accurate channel sounding data can be obtained with actual measurement times beyond T_{meas}, up to three times T_{meas}. Some of our testing times did exceed T_{meas}, up to approximately $2T_{meas}$ in CLE, for example. Based upon our controlled tests, we are confident that all our data is valid.
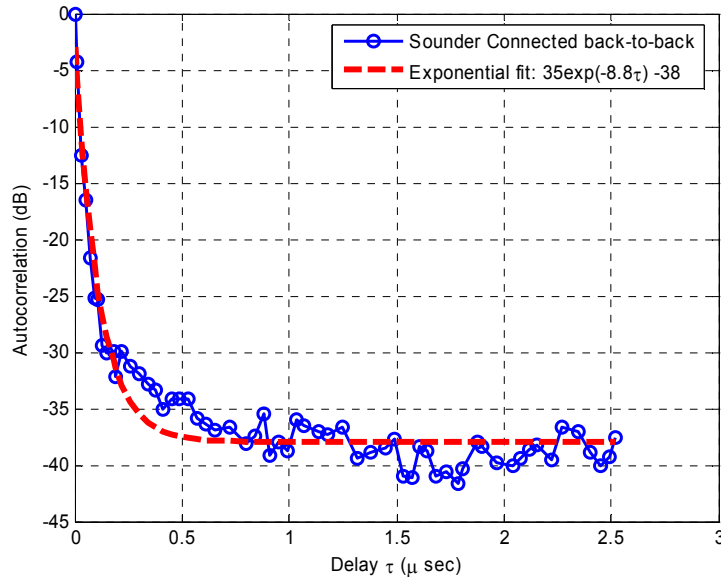
Figure 5.1 Autocorrelation curve for the channel sounder in back-to-back mode, using a BW of 50 MHz.

5.2.2 Data Format Translation

As described in Chapter 4, the "raw" data collected during the measurement campaigns is stored in a laptop computer. The channel sounder records the raw data as a matrix with a unique time stamp on each row. This raw data is in a proprietary format—a *.rap* format (a patented format used by BVS [78]). In order to use these files in MATLAB, we need to convert these files into ASCII format. The manufacturer BVS has provided us software (called "Chameleon"), which converts the data files from their *.rap* format to a *.out* format. The *.out* files are in ASCII format. Chameleon allows us to input the fields we want to see in the *.out* files. Figure 5.2 provides a screen shot of the front-end of the Chameleon software. The software allows us to convert one file at a time. Each file is a collection of many records—a series of PDPs taken over a segment of travel at an airport. The output of Chameleon can be imported into MATLAB routines using the MATLAB "csvread" command.
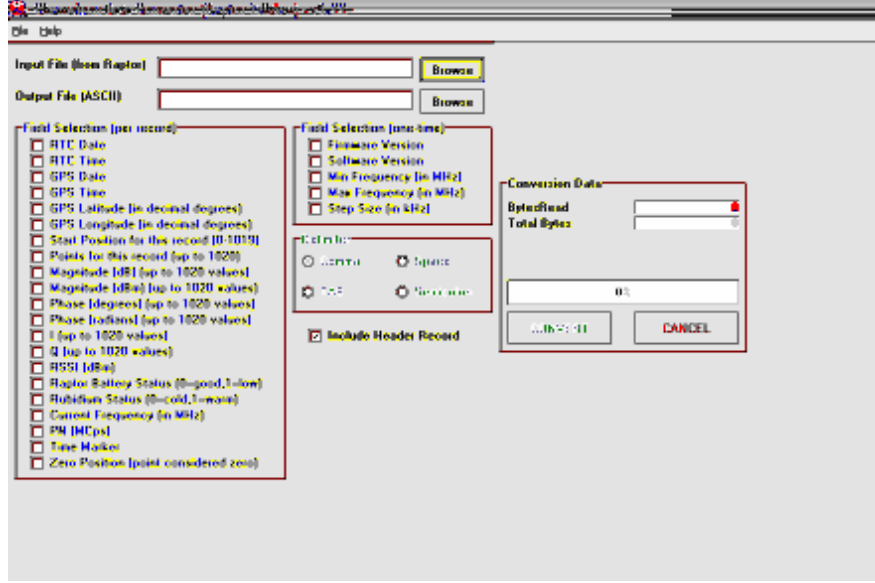
Figure 5.2. Screen capture for Chameleon (format conversion software).

Referring to Figure 5.1, the fields that we have used in Chameleon are as follows:

1. Magnitude (dBm): PDP sample power values in dBm. The sample power is expressed using 2 bytes, which gives us a dynamic range of ~48 dB;
2. Phase (radians): phase associated with each sample value in radians;
3. *I* channel value (dB): PDP sample value on the in-phase channel;
4. *Q* channel value (dB): PDP sample value on the quadrature channel;
5. RSSI (dBm): Received Signal Strength Indicator for each row;
6. GPS Latitude: Latitude of the location where the data was collected;
7. GPS Longitude: Longitude of the location where the data was collected.

The term "sample" denotes the correlated output value for a given delay in units of half-chips; the output sampling rate is twice the chip rate R_c, for our 50 MHz chip rate.

Table 5.1 shows an example data recording after using Chameleon. The PDP data is recorded every 0.5 seconds. Each column provides the field value from the above description. The sample values from each column are used to determine the Power Delay Profile (PDP) at that time instant.

Table 5.1 Chameleon output format for the nth record.

Time Stamp for n^{th} record	Magnitude (dBm) for 1st sample of nth record	Phase (radians) for 1st sample of nth record	Magnitude (dBm) for 2nd sample of nth record	Phase (radians) for 2nd sample of nth record	...	Magnitude (dBm) for 1020th sample of nth record	Phase (radians) for 1020th sample of nth record	GPS Latitude for n^{th} record	GPS Longitude for n^{th} record	RSSI for n^{th} record

The nth record provided in Table 5.1 is further divided into 3 sub-records:

1. PowerRecord lists all the power values, in dBm, for 1020 samples. The minimum value recorded is -130 dBm. The PowerRecords are the "un-pre-processed" versions of the PDPs.
2. PhaseRecord lists all the phase values in radians for 1020 samples.
3. GPS_RSSI lists the GPS latitude, longitude, and RSSI for the record.

Example of these sub-records are provided in Table 5.2.

Table 5.2. Sub-records generated for nth record.

Magnitude (dBm) for 1st sample	Magnitude (dBm) for 2nd sample	…	Magnitude (dBm) for 1020th sample

Phase (radians) for 1st sample	Phase (radians) for 2nd sample	…	Phase (radians) for 1020th sample

GPS Latitude for nth record	GPS Longitude for nth record	RSSI for nth record

5.2.3 Note for 50 MHz PDPs

As discussed in Chapter 4, the PN code used in the channel sounder has a length of 255 chips with a bandwidth (BW) of either 25 MHz or 50 MHz. The sounder records the data with a sampling rate of 100 MHz. So for the 50 Mcps mode, we are oversampling by 2 and for the 25 Mcps mode, we oversample by 4 samples/chip. For the 25 MHz mode, Chameleon outputs a PowerRecord with 1020 samples, since we have 255 chips (1020 samples/4), in which case it provides us a maximum possible unambiguous delay range of 10.2 µsec. Similarly for the 50 MHz chip rate, we have a maximum possible unambiguous delay range of 5.1 µsec, as noted in Chapter 4. For the 50 MHz rate, instead of recording 510 samples, the sounder still records 1020 samples. This is due to hardware and buffering constraints in the sounder. In this case, samples 511-1020 are a copy of the first 510 samples, and can be discarded. Figure 5.3 shows an example PowerRecord for an actual collected data record taken in the laboratory. Note that the values for samples 134 and 644 are the same.
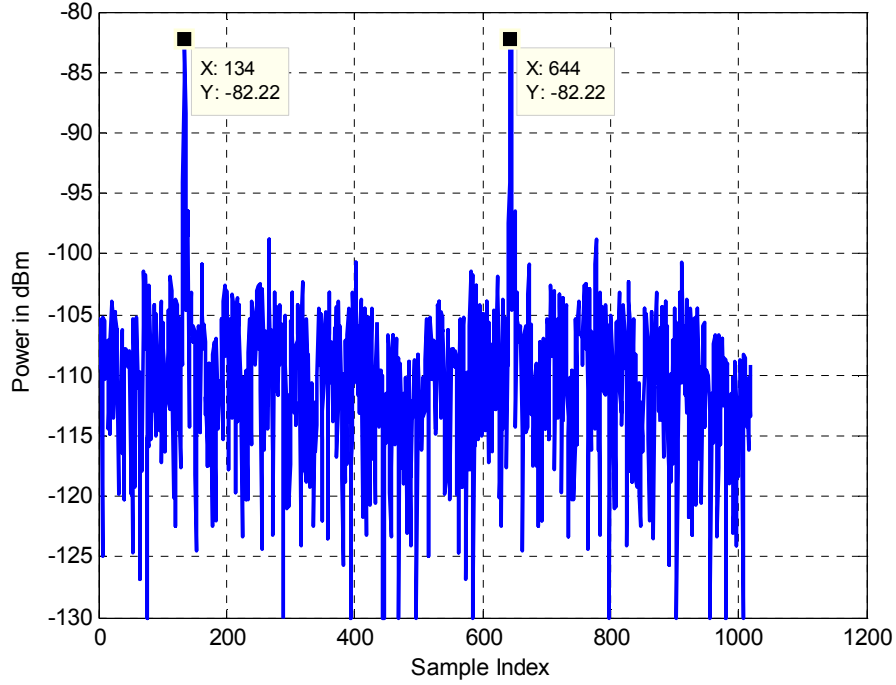
Figure 5.3. Example PowerRecord for 50 Mcps after using Chameleon.

Since we used only the 50 Mcps mode during all measurements, for the remaining data processing, we discard values of samples (511-1020) for both PowerRecord and PhaseRecord.

5.2.4 Noise Thresholding

The PowerRecords provide information regarding the dispersion of the propagation environment: they provide an estimate of the power associated with each multipath component. As with all communication systems, the PowerRecords are also affected by thermal noise. In order to minimize the effects of this thermal noise, it is necessary to separate valid multipath components from noise. We have used the method outlined in [46], which determines a noise threshold (NT_j) for the jth PowerRecord by enforcing a constant false alarm rate (CFAR) for each PowerRecord. The CFAR algorithm is widely used in radar related applications for determination of noise thresholds [46]. The value of NT_j is determined using the noise variance $(\sigma_n^j)^2$ of the jth PowerRecord. True thermal noise can be assumed to be Rayleigh distributed in amplitude (two Gaussians, one each on *"I"* and *"Q"*) [46]. Given this model, the probability that the noise amplitude will exceed some level z_0 is given by

$$P(z_0) = exp\left(\frac{-z_0^2}{2(\sigma_n^j)^2}\right) \tag{5.1}$$

The estimated median level σ_m^j (for the jth PowerRecord) can be found by setting $z_0 = \sigma_m^j$, and by equating (5.1) to ½, we get,

$$\sigma_n^j \cong 0.8493\sigma_m^j \tag{5.2}$$

After using noise thresholding, we guarantee that a maximum of one noise sample may be mistaken as a valid multipath in each PowerRecord. This gives us a CFA probability (CFAP) (P_f) as listed in Table 5.3. In this table, η is a constant that is obtained from the following equation:

$$P_f(\eta) = \exp\left(\frac{-\eta^2}{2}\right). \tag{5.3}$$

Table 5.3. Parameters for CFAR algorithm.

Mode	Number of Samples in Each PowerRecord	CFAP for the Mode	η for the Mode
25 MHz	1020	9.8×10^{-4}	3.72
50 MHz	510	2×10^{-3}	3.52

Continuing with the CFAR algorithm, from (5.3) and Table 5.3, we get,

$$NT_j = \eta\sigma_n^j. \tag{5.4}$$

We estimate σ_m^j for each PowerRecord and then use (5.2) to find its respective noise standard deviation σ_n^j. In order to estimate σ_m^j, we need to first determine the likely noise samples from each PowerRecord. For each PowerRecord, we must select a threshold, below which the samples can be considered to be from noise (only). We define this threshold as our user-selected dynamic range (USDR). For context, in reference [48], for each PDP the authors discard all sample values that are below 20 dB of the maximum value of that PDP. The reasons for applying this USDR are first, low energy multipath is difficult to track for even advanced receiver processing, and second, these low-energy components do not significantly contribute to the aggregate energy collected at the receiver. For all of our processing requirements, we have employed a USDR of 25 dB, since we don't anticipate receiver techniques will be able to effectively gather and track any multipath that is below 25 dB of the maximum (unless SNR is extraordinarily large). Even if receivers can track these components, inclusion of them often greatly increases the channel model complexity. Using this USDR, we estimate σ_m^j and then obtain NT_j for each PowerRecord using (5.2), Table 5.3, and (5.4).

Next, we list the steps that are used to complete the noise thresholding on the PowerRecords:

1. Using Table 5.3, determine the values of CFAR (CFAP) and η depending on the mode of the channel sounder;

2. Separate out the samples in the jth PowerRecord that are below the USDR;
3. Determine the median value σ_m^j for the samples separated in step 2;
4. Use (5.2) and (5.4) to determine the noise threshold NT_j;
5. In the jth PowerRecord, set all samples below NT_j to their minimum value, -130 dBm;
6. Repeat steps 2-5 for each PowerRecord.

Figure 5.4 provides an example set of PowerRecords before and after applying our noise thresholding algorithm. As can be seen, the noise thresholding does nothing to those multipath components that are within approximately 25 dB of the main (largest) component.
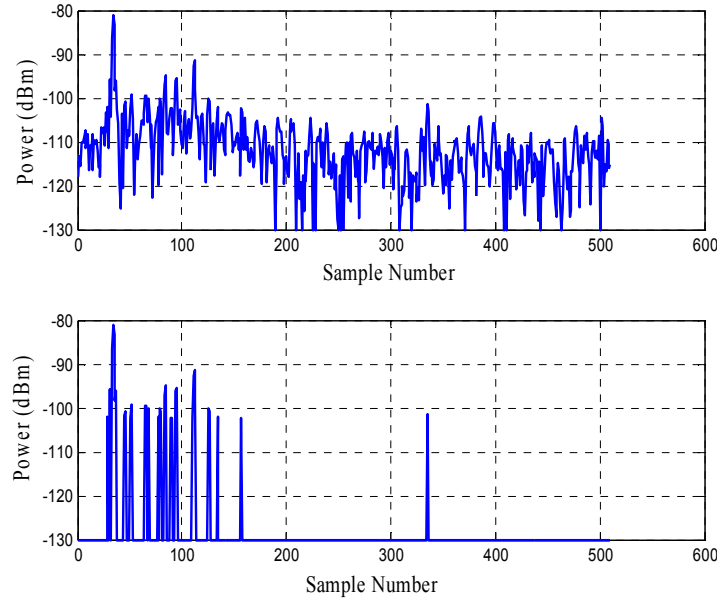
Figure 5.4. Example PowerRecord for 50 MHz channel bandwidth.

5.2.4 Converting PowerRecords to PDPs for Different Bandwidths

After implementing the noise thresholding on the collected PowerRecords, we need to convert these PowerRecords into PDPs depending on the bandwidth of the desired channel model. As discussed in section 5.2.1, for our 50 Mcps rate, we have 510 samples for each PowerRecord and each PhaseRecord. Each sample of this PowerRecord can be assumed to be an aggregate for all the multipath "rays" that arrive at the channel sounder's receiver within the delay bin of 10 nanosec (since the sampling rate is 100 MHz). Depending on the bandwidth of the channel, we need to combine samples, vectorially, to obtain the corresponding PDP. It is possible to do this since each sample has both a phase value and a power value associated with it, and using complex addition, one can add the samples to get the corresponding chip samples. Table 5.4 lists the number of samples to be combined to determine the PDP for a given bandwidth.

Table 5.4. Number of samples/chip for different bandwidths.

Channel Bandwidth	50 MHz	10 MHz	5 MHz	1 MHz
Number of Samples to be Combined	2	10	20	100
Number of Chips in Each PDP	255	51	25	5

Now recall eq. (3.7), the equation for our CIR:

$$h^{(e)}(\tau;t) = \sum_{k=0}^{L(t)-1} z_k(t)\alpha_k(t)\exp\{-j\phi_k(t)\}\delta[\tau - \tau_k(t)].$$

After the vector addition of the samples according to the desired channel bandwidth, we obtain a set of (amplitudes, delays, phases)=(α's, τ's, ϕ's) for each Impulse Response Estimate (IRE), where the IRE consists of $h(\tau;t)$ constructed from the set (α, τ, ϕ). The α's and τ's are used to determine the corresponding PDP for each IRE, as follows:

$$P^{(e)}(\tau;t) = \sum_{k=0}^{L(t)-1} z_k(t)\alpha_k^2(t)\delta[\tau - \tau_k(t)] \tag{5.5}$$

Since the α^2's are proportional to power, the PDP itself contains no phase information. In Figure 5.5, we show the same PDP for different BWs. As can be seen, the delay resolution decreases as the bandwidth decreases, as expected.
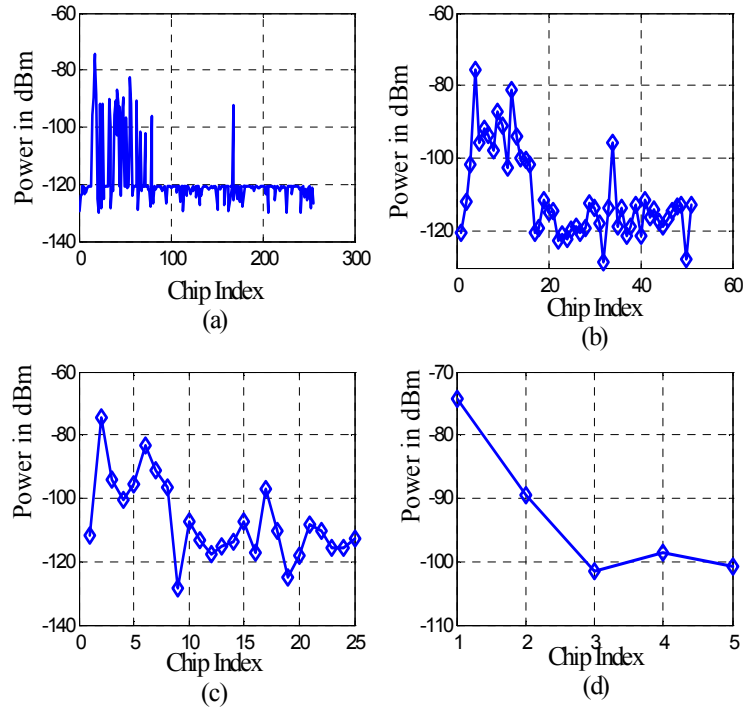
Figure 5.5. PDPs for different BWs: (a) 50 MHz, (b) 10 MHz, (c) 5 MHz, and (d) 1 MHz.

5.2.6 Multipath Threshold

Each PDP can be thought of as a collection of different multipath components (rays) arriving at different delays. The ray model assumes plane wave propagation, a good approximation for our frequency band and distances. The energy in each of the multipath components varies depending on the individual path taken by the signal to reach the receiver. Depending on the characteristics of the dispersive medium, we will receive some strong, some medium, and some weak multipath components. As already discussed, channels are generally implemented as tapped-delay line models. To keep the implementation complexity at a reasonable level and also to have as precise a description of the channel as possible, the system designer must neglect some weak multipath components below a certain threshold. We refer to this threshold as our "Multipath Threshold" *(MT)*. It is something of an engineering "judgement call" on the part of the designer as to what the value of *MT* should be. In the open literature, researchers have adopted different values of this parameter, depending on the application for which the model is being developed. Reference [48] assumes a *MT* of 20 dB, i.e., in any given PDP, any multipath that is below 20 dB of the maximum value of that PDP is discarded. Yet, we do find contemporary channel models [79] that have provision for channel taps that are within 25 dB of the main peak. What is important to determine is how selection of a certain *MT* affects the depiction of the actual physical channel. We have compared the RMS-DS statistics (see Chapter 3, and subsequent sections of this chapter) of the PDPs after applying different values of *MT*. Values of 20, 25, and 30 dB were used for the *MT*. As an example illustration, the results for all data from CLE are presented in Figure 5.6. This plot shows the relative frequency of RMS-DS versus the value of RMS-DS. It is interesting to note that the statistics of RMS-DS using a *MT* of 25 dB or 30 dB are *very* close to each other. They differ most at the low values of RMS-DS. We have found this to hold for all other data sets as well. Hence for all our data processing we have used an *MT* of 25 dB, which appears to provide a near optimal tradeoff in terms of a precise representation of the channel and its implementation complexity.
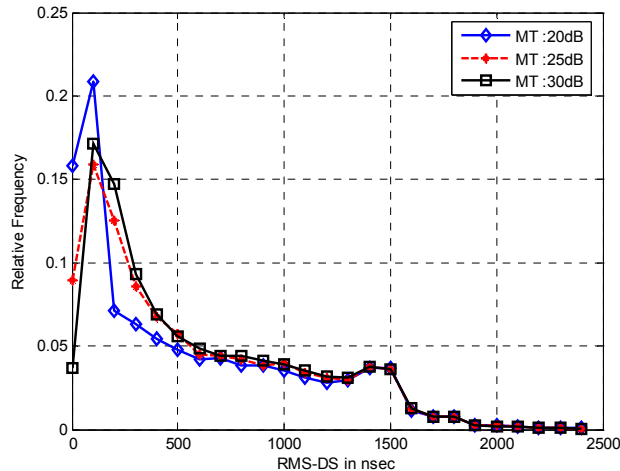
Figure 5.6. Example RMS-DS values for CLE data applying different values of *MT*.

As noted, there is some difference in results for *MT*s of 25 dB and 30 dB at lower values of the RMS-DS statistic. To further support our use of 25 dB as an appropriate *MT*, we compare

the FCE (Table 4.5) for CLE-LOSO for a BW of 50 MHz, using three different *MT*s. The results are provided in Figure 5.7. The figure further justifies our use of an *MT* of 25 dB, due to the negligible differences in the FCEs for *MT*s of 25 dB and 30 dB.
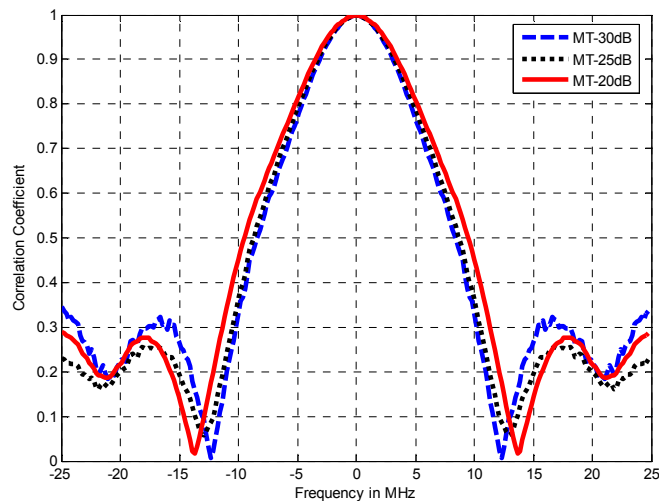
Figure 5.7. Example FCEs for CLE data applying different values of *MT*.

Finally here, we list the steps used to apply the multipath threshold on the PDPs:
1. For the jth PDP, find the maximum strength chip sample *(max$_j$)*;
2. In the jth PDP, set all chip samples that are 25 dB or more below *max$_j$* to the minimum value, -130 dBm;
3. Repeat steps 1 and 2 for all PDPs.

Figure 5.8 summarizes all the steps in our pre-processing discussed thus far.

```
┌─────────────────────────────────────────────────────────────┐
│     Input: data recording from sounder in .rap format       │
└─────────────────────────────────────────────────────────────┘
                              │
                              ▼
┌─────────────────────────────────────────────────────────────┐
│    Convert data recording from .rap format to .out format.  │
│    Each data record is segregated into PowerRecord,         │
│    PhaseRecord, and GPS_RSSI (Table 5.2)                    │
└─────────────────────────────────────────────────────────────┘
                              │
                              ▼
┌─────────────────────────────────────────────────────────────┐
│    Apply noise thresholding algorithm to remove potential   │
│    noise samples from PowerRecord.                          │
└─────────────────────────────────────────────────────────────┘
                              │
                              ▼
┌─────────────────────────────────────────────────────────────┐
│    Use eq. (5.5) to obtain PDPs for different BWs using the  │
│    PowerRecords.                                            │
└─────────────────────────────────────────────────────────────┘
                              │
                              ▼
┌─────────────────────────────────────────────────────────────┐
│    Apply the multipath threshold to separate the useful     │
│    multipath from very-low-energy multipath.               │
└─────────────────────────────────────────────────────────────┘
                              │
                              ▼
┌─────────────────────────────────────────────────────────────┐
│        Output: Preprocessed PDPs ready for analysis         │
└─────────────────────────────────────────────────────────────┘
```

Figure 5.8. Summary flow diagram of pre-processing steps of Section 5.2.

5.3 Key Parameters and Definitions

In this section, we review descriptions of several parameters that are essential in understanding and representing our channel models. Some of these parameters have already been briefly discussed via Table 3.1.

5.3.1 Parameters Obtained Directly from the IREs

Here we describe the parameters that are determined from the PDPs (5.5) or IREs (3.7) directly; that is, those channel statistics computed from the pre-processed PDP and IRE data files.

1.   Mean energy delay (μ_τ): The mean energy delay is simply the mean value of the energy (or power) delay. The value of μ_τ for a PDP can be obtained as,

$$\mu_\tau = \frac{\displaystyle\sum_{k=0}^{L-1} \tau_k \alpha_k^2}{\displaystyle\sum_{k=0}^{L-1} \alpha_k^2} \tag{5.6}$$

The mean delay provides a measure of the average delay associated with all multipath components in a PDP. Sometimes this information can be misleading in terms of providing a perspective regarding the dispersive nature of the channel. For example, consider Figure 5.9: part (a) and part (b) are identical in terms of the number of multipath components and their relative power, but part (b) is displaced in time by 3 seconds. So, even though both PDPs might have been obtained by passing through similar channels, μ_τ for part (a) is 2.1 seconds, and that for part (b) is 5.1 seconds. As noted in Chapter 3, absolute signal delay is not as important as the spread of delays; for completeness we have gathered statistics on this common parameter.
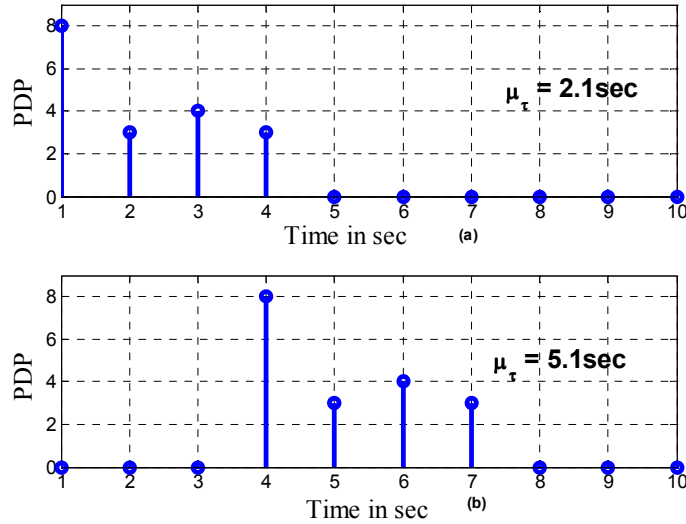
Figure 5.9. Example PDPs with same multipath behavior and different μ_τ.

2.   Root Mean Square (RMS) Delay Spread (σ_τ): The root mean square delay spread provides the *rms* value of the multipath delay spread (T_M). This is of course relative to the mean energy delay. In this report, we use the abbreviation RMS-DS for σ_τ. The value of σ_τ for any PDP can be obtained as

$$\sigma_\tau = \sqrt{\frac{\displaystyle\sum_{k=0}^{L-1} \tau_k^2 \alpha_k^2}{\displaystyle\sum_{k=0}^{L-1} \alpha_k^2} - \mu_\tau^2} \tag{5.7}$$

The RMS-DS provides a measure of the spread of the signal in time. As noted, in computing the RMS-DS, we remove the mean delay. Due to this, the information regarding the dispersive nature of the channel—in terms of the spread or extent in delay—is correctly represented irrespective of any absolute (bulk, or group) delays associated with the multipath components. For example, consider again Figure 5.9, whose parts (a) and (b) have an identical number of multipath components and the same relative power: they have the exact same value of σ_τ=1.15 seconds. Due to this unambiguous indication regarding the physical environment, many communication system designers use σ_τ to provide an indication of the frequency selectivity of the channel. It is well known that σ_τ can be used to quantify a channel's dispersiveness, and can help with design of mitigation techniques (e.g., equalizer lengths).

In Figure 5.10, we have provided the RMS-DSs for a certain segment of a measurement run at MIA. Part (a) of this figure is the photograph of Figure 4.9, showing the measurement locations. Part (b) shows the corresponding RMS-DS values recorded in these locations, versus IRE number (time). We see multiple "transitions" within the recorded RMS-DS time series. This is because the mobile Rx was getting a strong specular signal when the LOS signal from the ATCT was not blocked by the parked aircraft, yielding low values of RMS-DS. For the PDP recordings taken when the mobile van was in the shadow of an aircraft, the value of σ_τ was considerably larger.

Figure 5.10 (a). Example measurement location at MIA.
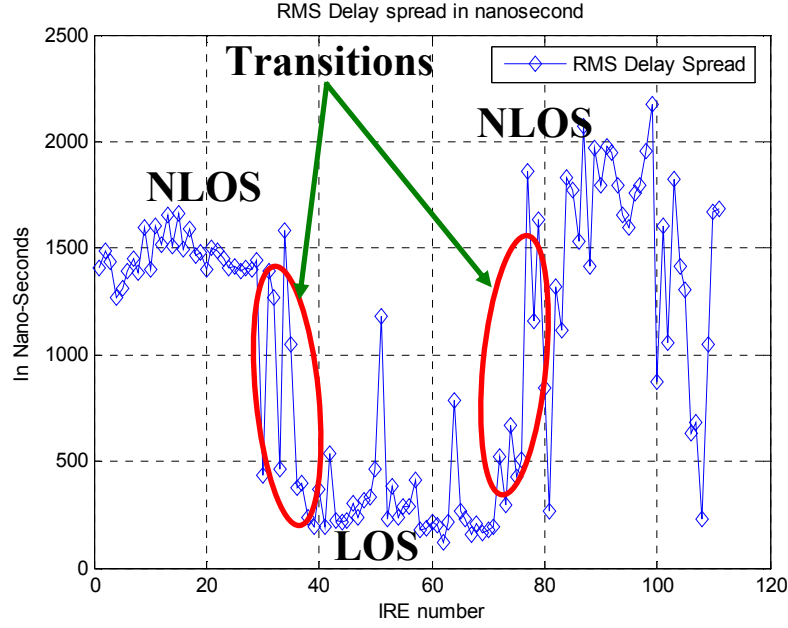
Figure 5.10 (b). RMS-DS vs. IRE number (time) for locations in MIA of Fig. 5.9(a).

3.   Delay Window $(W_{\tau,x})$: The delay widow is defined as the length of the middle portion of the IRE containing $x\%$ of the total energy of the IRE. Parameter $W_{\tau,x}$ provides another measure of the spread of the signal in time. For most of the cases, $W_{\tau,x}$ can be interpreted in the same manner as σ_τ; the larger the value of $W_{\tau,x}$, the more dispersive the channel. In Figure 5.11, we compare values σ_τ and $W_{\tau,x}$ for another segment of a measurement run at MIA. Although the absolute values of the two parameters often differ, the important thing to note is the highly correlated behavior of σ_τ and $W_{\tau,x}$; this agrees with our intuition, since as noted, both provide a measure of the "temporal smearing" caused by the channel.
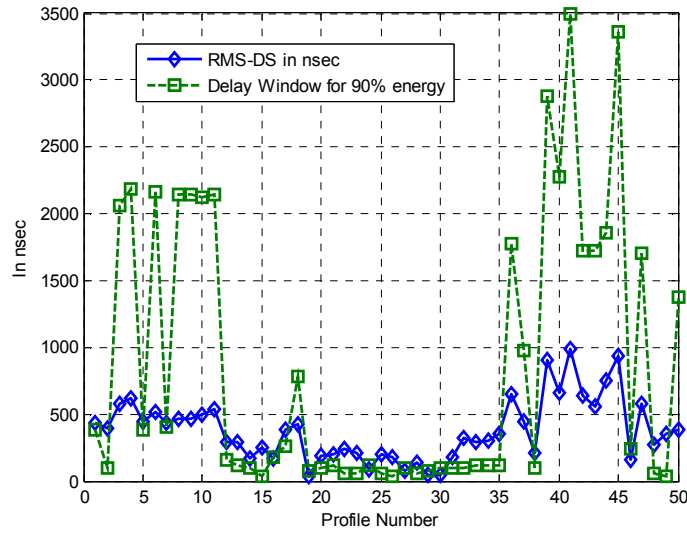
Figure 5.11. RMS-DS and Delay Window vs. IRE number (time) for a measurement segment at MIA.

4.   Persistence Process Parameters: As is extensively reported in the literature on channel modeling, all multipath components can realistically be associated with a "birth and death" (i.e., on/off) process. Chapter 9 in reference [18] describes this nicely. The reason for the on/off behavior is simply the dynamic nature of the propagation physics: the orientation and position of reflectors and scatterers changes with platform mobility, often in such a way that these reflections (giving rise to received multipath components) "come and go." Recall from eq. (3.7) that we account for this on/off behavior in our channel model using the persistence process $z_k(t)$, in that formulation applied to the kth multipath amplitude. A widely employed way of modeling such an on/off process (for numerous applications) is by using a Markov chain model. A Markov chain produces a sequence of random variables in which the future variable at time $n+1$ depends on the present variable at time n, but is independent of how the present variable arose from its predecessors. In signal processing terms, a Markov chain has memory of one time unit, and this pertains strictly to a 1st-order Markov chain. A Markov chain model is typically specified using two matrices, the transition *(TS)* matrix and the emission *(ES)* matrix. An example *TS* matrix for a 3-state Markov chain is given in (5.8). Each element P_{ij} in the matrix *TS* is defined as the probability of going from state i to state j. In our CIR application, the states for the persistence process are two: either on ($z_k(n)=1$) or off ($z_k(n)=0$). Thus the persistence process *TS* matrix for any channel tap is a two by two matrix.

$$TS = \begin{bmatrix} P_{00} & P_{01} & P_{02} \\ P_{10} & P_{11} & P_{12} \\ P_{20} & P_{21} & P_{22} \end{bmatrix} \qquad (5.8)$$

An example three-state *ES* matrix is provided in (5.9), where each element P_j gives the "steady state probability" associated with the jth state. For CIR modeling, we obtain these (two) elements for the tap persistence as "fractions of time" the multipath components are present ($z_k(n)=1$) or not ($z_k(n)=0$), directly from the PDP data.

$$ES = \begin{bmatrix} P_0 \\ P_1 \\ P_2 \end{bmatrix} \qquad (5.9)$$

In Figure 5.12, parts (a) and (b) show example persistence processes associated with the 2nd and 5th taps, respectively (for the definition of tap, refer to Figure 3.1) for a segment of measurement data from JFK. We also show the *TS* and *ES* matrices for both the taps in the figure. As we can infer from the matrices, tap 2 has a higher probability of being on than tap 5, and this tendency is visible from the figure as well.
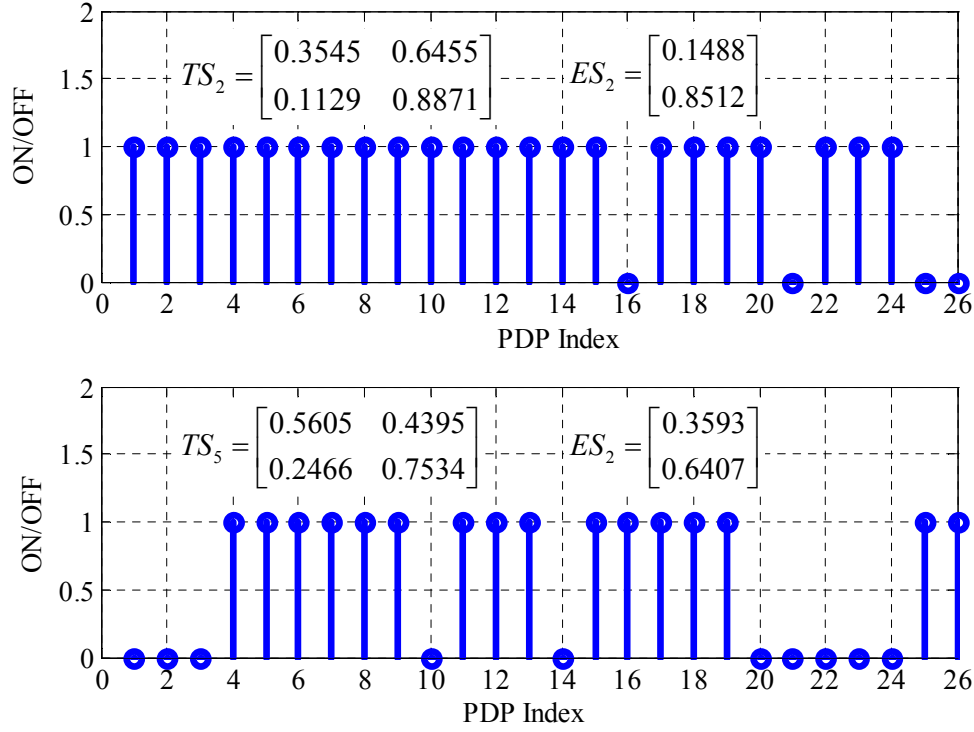
Figure 5.12. Example persistence processes for taps 2 and 5 for segment of travel at JFK.

5.   Tap Correlations: Depending on the nature of the physical channel, the multipath components associated with a channel can be correlated—their behavior in time has the same tendency.   We need to account for this correlation in our developed channel models.   The correlation matrix R_α can be defined as follows

$$R_\alpha = \begin{bmatrix} r_{11} & .. & r_{1n} \\ \vdots & \vdots & \vdots \\ r_{n1} & .. & r_{nn} \end{bmatrix} \tag{5.9a}$$

$$r_{i,j} = \frac{\text{cov}(\alpha_i \alpha_j)}{\sqrt{\text{var}(\alpha_i)\,\text{var}(\alpha_j)}} \tag{5.9b}$$

where in (5.9b), α_i stands for the amplitude of the ith tap, $r_{i,j}$ is the correlation coefficient between the ith and the jth tap, and *cov* and *var* stand for *covariance* and *variance*, respectively.

6.   Phase (ϕ_k): As seen in equations (3.7) and (3.8), each multipath component contains an associated phase.   Section 3.2 provides a description of the various factors contributing to this aggregate phase.   The value of the phase ϕ_k is obtained directly from the recorded data (Table 5.2).   Figure 5.13 shows an example of the variation of phase with time for the first tap for NLOS measurements at JFK.   The range of phase values is from $-\pi$ to π radians because as

distance changes, our (non-phase-locked) correlator receiver outputs phase corresponding to the change in distance.
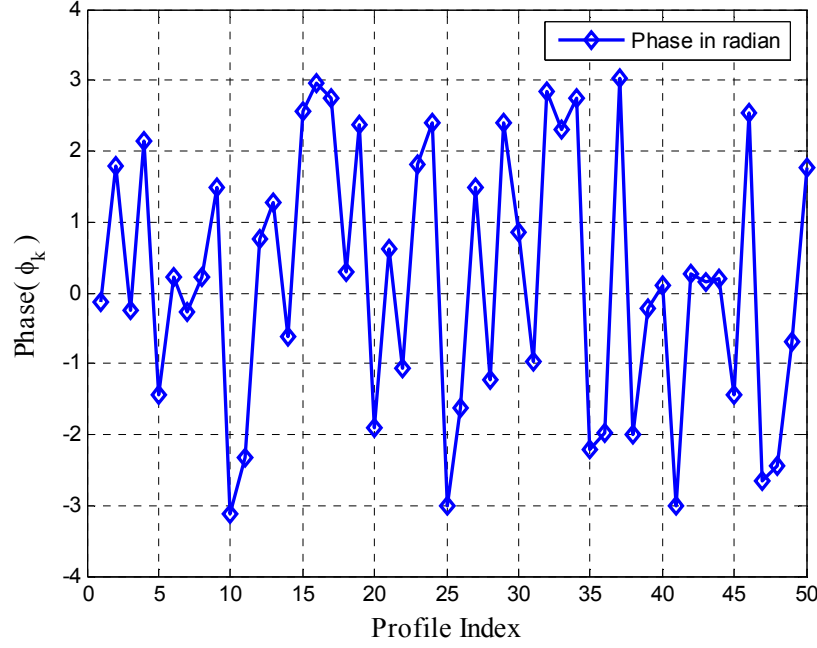
Figure 5.13. Example phase variation versus time for 1st tap for JFK-NLOS.

5.3.2 Parameters Obtained via Fourier Transform of IREs

1. Channel transfer function: from Chapter 3, the time-varying channel transfer function can be expressed as follows:

$$H(f;t) = F\{h(\tau;t)\} = \int_{-\infty}^{\infty} h(\tau;t)e^{-j2\pi f\tau}d\tau \qquad (5.10)$$

The function *H(f,t)* quantifies the time variation of the complex amplitudes of different "spectral lines," where by "spectral lines" we mean the values of *H(f,t)* at specific values of frequency *f* (the nomenclature arises from the finite dimensionality of the discrete Fourier transform, done numerically via the Fast Fourier Transform (FFT) algorithm).

2. Frequency correlation estimate (FCE): The FCE is analogous to the coherence bandwidth (Table 3.1). According to our analysis of the data, in the PDPs, neighboring multipath components often exhibit correlated behavior. Hence, for airport settings, we can not always assume the classical Wide Sense Stationary-Uncorrelated Scattering (WSSUS) environment widely used in other terrestrial channel models [34] (at least not over durations beyond the coherence time, typically on the order of milliseconds). We thus use a formula—for computing the FCE—that doesn't rely upon WSSUS to determine correlation in the frequency domain; the

formula in [47] satisfies this condition. In this method, the time variations of the complex amplitudes of different spectral lines are directly crosscorrelated with the time variations of a reference spectral line. The crosscorrelation is $\gamma_H(a_{ref}, a_i)$, where the term a_i is the amplitude of the spectral lines at frequency index i, and a_{ref} is the amplitude at the reference frequency, i.e., $a_{ref} = |H(f,t)||_{f=f_{ref}}$. The FCE is computed as follows, where index j orders the sequential time estimates:

$$FCE = \frac{\gamma_H(a_{ref}, a_i)}{\sqrt{\gamma_H(a_{ref}, a_{ref})\gamma_H(a_i, a_i)}};$$

$$\gamma_H(a_{ref}, a_i) = \frac{1}{N}\sum_{j=1}^{N} a_{ref,j} a^*_{i,j}$$

(5.11)

Figure 5.14 shows an example FCE plot for CLE NLOS-S (BW = 50 MHz). The abscissa is the frequency in MHz with respect to midband, and the ordinate is the estimate of the channel's correlation at the given frequency separation. From Figure 5.14, we see that the correlation falls to values of approximately 0.9, 0.5, and 0.1 at frequency separations of 4.86 MHz, 17.2 MHz, and 23 MHz, respectively. Note that we use the "two-sided" measure of frequency separation here, since this FCE applies to bandpass systems.
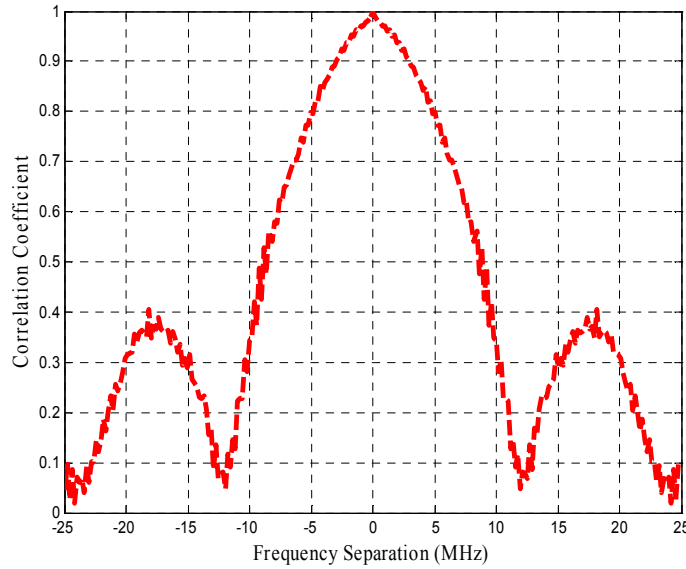
Figure 5.14. Example FCE for CLE.

2. Doppler Spread (f_D): The Doppler spread is defined as the maximum value of Doppler shift (f_d) incurred by the signal as it transits the channel. For a single plane wave, f_d is given as,

$$f_d = \frac{v}{\lambda}\cos(\theta)$$

(5.12)

In our case, since the measurements were conducted at a carrier frequency of 5.12 GHz, we have a wavelength (λ) of approximately 6 cm. The maximum speed *(v)* at which the measurement van traveled was approximately 30 miles/hour, which is 14 m/s. This yields a maximum Doppler shift f_D of 234 Hz. This is approximately the value of Doppler spread considered in [39] for "parking" and "taxi" scenarios. Note that in [39], the author has assumed these values without any actual measurements. The Doppler spread provides a measure of the rate of change of the fading samples across time for a given tap (multipath component). Depending on the relationship between the maximum communication system symbol rate and the coherence time, t_c (Table 3.1), the fading can be assumed to be fast or slow. Since f_D in our case is 234 Hz, its reciprocal t_c is approximately 4.3 millisec. Hence even for data rates as low as 10 kbps, our channel can be assumed to be *slowly fading*. In order to emulate this effect of the channel in our models, researchers often employ a low-pass filter (LPF) for each tap's fading process in the tapped-delay line model. The cut-off frequency of the LPF will depend on f_D, and the filter's shape depends upon the spatial distribution of scattering. Generally when the value of f_D is small relative to a symbol rate, the actual shape of the Doppler spectrum is immaterial.

The other method of determining f_D is using Fourier transform of $h(t,\tau)$ with respect to the *t* variable. The Doppler spread can then be determined from the width of $H(t,f)$. In our case, due to the slow measurement update rate of the channel sounder relative to f_D, we were unable to measure Doppler effects at all but the lowest values of velocity. Once again though, as long as the maximum Doppler frequency is low enough with respect to signaling rates, the use of a LPF to approximate the effects of Doppler spreading is a reliable approximation. Similar approximations can also be seen in [39].

5.3.3 Labeling Conventions

In this chapter and in subsequent ones, we present results for different airports, different airport propagation regions, and different bandwidths (BWs). To make this representation concise and interpretation easy, we define a convention for representing these cases. The ordered triple of the form [Airport Name, Region, BW] will define the name of the airport, the propagation region of the airport (LOSO, NLOS-S, NLOS) (see Chapter 4), and the BW in MHz, respectively. Values we use for the BW are {50, 10, 5, 1} MHz. In Table 5.5, we list some example cases.

Table 5.5. Examples of labeling convention used for results.

Case	Representation
NLOS-S category at JFK for 10 MHz BW	[JFK, NLOS-S, 10]
NLOS category at Burke Lakefront for 50 MHz BW	[BL, NLOS, 50]

5.4 Processing Considerations in Model Development

In this section, we focus on the several different considerations that need to be addressed when determining the number of taps in the channel model, and their properties (phase, energy, persistence, and correlation among them). We also provide a qualitative analysis using examples to illustrate some of the pros and cons associated with the different methods that can be used to determine these tap properties. Before proceeding, we first introduce another notation. This allows us to express (5.5) in a slightly different manner, which in some cases makes it easier to discuss the PDPs and CIRs: specifically, we let $p^{(e)}(j,k)$ represent the power in the kth tap of the jth PDP, where superscript e again denotes environment/region type.

5.4.1 Determination of the Number of Taps (L)

In this section, we discuss the different ways by which we can define the number of taps required to provide an accurate description of the underlying physical channel. This directly affects the model complexity.

5.4.1.1 Number of Taps within 25 dB of the Main Peak ($\widetilde{L}$)

As discussed in Section 5.2.5, only multipath components within 25 dB of the main (largest) component will be considered as valid components. Let $\widetilde{L}_j$ represent the number of taps that are within 25 dB of the main peak for the jth PDP. So for a given airport, region, and BW, we can determine the distribution of $\widetilde{L}_j$ for the collected PDPs. The algorithm to determine $\widetilde{L}_j$ is as follows:

1. For the jth PDP, find the maximum strength sample, $p^{(e)}(j,k_{max})=\max\limits_{k}[p^{(e)}(j,k)]$.
2. In the jth PDP, count all $p^{(e)}(j,k)$ values within 25 dB of $p^{(e)}(j,k_{max})$.
3. Denote the value obtained from step 2 by $\widetilde{L}_j$.
4. Repeat steps 1-3 for all PDPs.
5. $\widetilde{L}$ is determined as the mean value of set of $\widetilde{L}_j$. (We discuss the use of other statistics, such as maximum, in a subsequent section.)

Figure 5.15 shows the distribution of $\widetilde{L}_j$ for [JFK, NLOS, 50]. From the data for JFK, we obtain $\widetilde{L}$ as 75 taps!
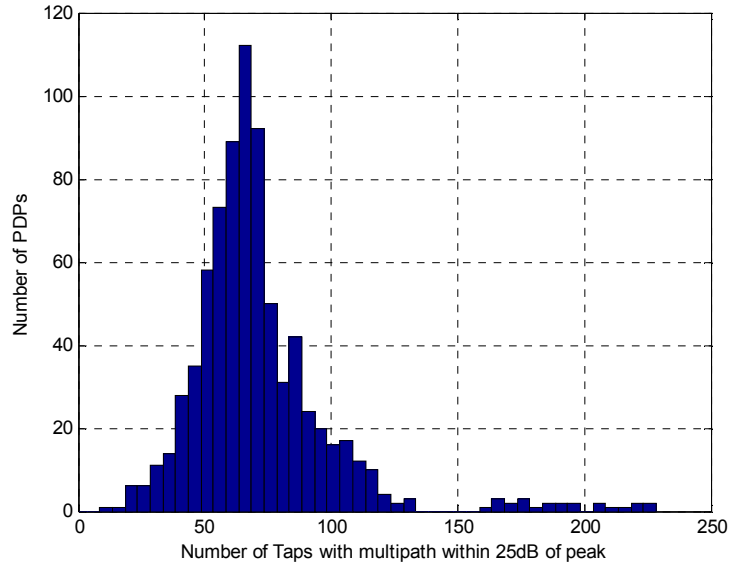
Figure 5.15. Histogram of $\widetilde{L}_j$ for [JFK, NLOS, 50].

5.4.1.2 Determining Number of Taps using RMS-DS (*L*)

As discussed in Sections 3.1 and 5.3, the RMS-DS is often used as a reliable indicator of the channel dispersion. The use of RMS-DS to determine the number of taps is also popular among researchers [5]. Figure 5.16 provides the distribution of RMS-DS for the same case as Figure 5.14, [JFK, NLOS, 50]. Table 4.3 provides summary statistics of the RMS-DS for all the airports.
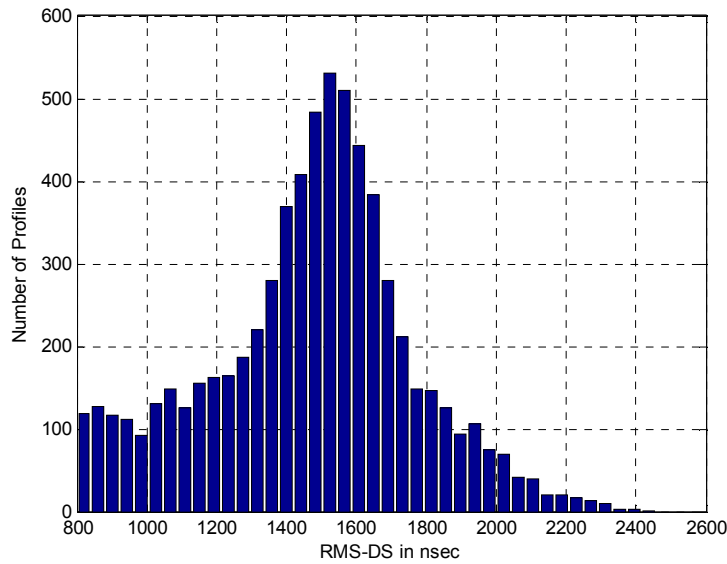
Figure 5.16. Histogram of RMS-DS for [JFK, NLOS, 50].

Broadly, any one of the statistics in Table 4.3 could be used to determine the number of taps (*L*) used in the tapped-delay model of the channel. That is, we could use the minimum, median, mean, or the maximum RMS-DS available from the data. (We could also use the mode, at least in these single-mode distributions.) To use the maximum RMS-DS would mean designing the entire model on the basis of a single (or very few) PDP(s). To design a model that better represents typical behavior, and one in which we have better statistical confidence, using the mean or the median value makes sense. The median is a reasonable statistic to use, but in some of our cases (e.g., when the number of samples is small), it may be biased toward the low end of the distribution. This is most noticeable in non uni-modal distributions, and in these cases, the rather long "tail" of some of the RMS-DS histograms is better captured by the mean value than by the median. Using the mean, the number of taps in the model is found by

$$L = \left\lceil \frac{mean(RMS-DS)}{T_c} \right\rceil + 1 \tag{5.13}$$

In (5.13), T_c is the chip time. For our example case of [JFK, NLOS, 50], *L* is then 75, which is *coincidentally* equal to $\widetilde{L}$ found in the previous section. Similarly, using Table 4.3 and (5.13), for [JFK, NLOS–S, 50], *L*=17.

5.4.1.3 Remarks Regarding $\widetilde{L}$ and *L*

The number of taps $\widetilde{L}$ quantifies the average number of taps (multipath components) that are within 25 dB of the main peak in a PDP. Yet when determining the number of components $\widetilde{L}_j$ in a given (j^{th}) PDP, no information regarding the relative delay and the energy distribution associated with those taps is taken into account (other than that they are above threshold). Determining *L* does account for this.

For an illustration of how these approaches differ, consider Figure 5.17, where we show three example PDPs (with values in dB), having different distributions of multipath components. The values for the multipath components in each PDP are scaled so that the total energy ($\sum_k \alpha_k^2$) in each PDP is unity. We can easily determine that the $\widetilde{L}_j$ values for the three PDPs are 6, 7, and 4, which yields $\widetilde{L}$ =6. The value of *L* determined from the mean RMS-DS for the three PDPs is 2—a significant difference.
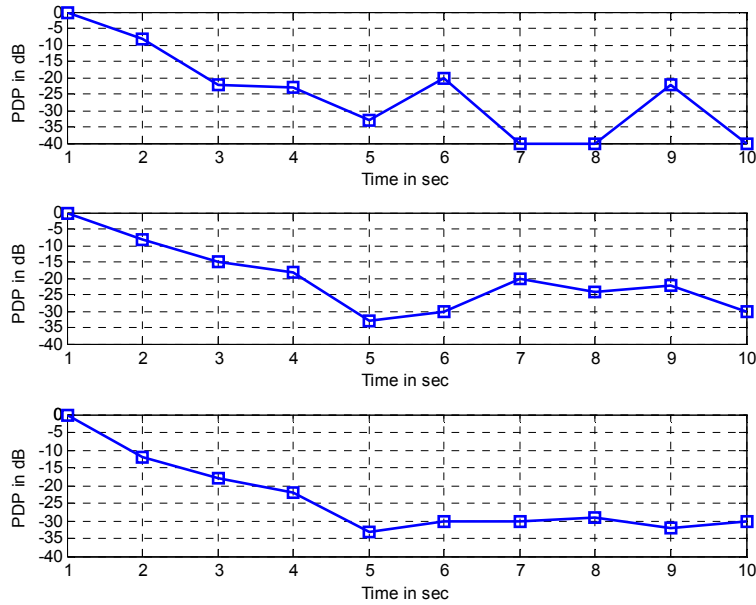
Figure 5.17. Example PDPs with varying number and energy multipath components.

One way of comparing these two approaches for selecting the number of taps in the channel model is to compare the amount of energy gathered via each method. Table 5.6 provides a relative comparison between the two approaches in terms of the cumulative energy gathered in the PDPs shown in Figure 5.17.

Table 5.6. Cumulative energy gathered using L and $\widetilde{L}$ for PDPs from Figure 5.17.

PDP Index	% Energy Gathered using $\widetilde{L}$ (6) Taps	% Energy Gathered using L (2) Taps
1	99.4	97.6
2	98.2	94.3
3	99.6	97.5

The difference between the approach for finding $\widetilde{L}$ and L is evident in the cumulative energy values provided in Table 5.6. The percent energy gathered using $\widetilde{L}$=6 taps is very near 100%, but is close to that attained using L=2 taps. So, it is at least reasonable to use L as the number of taps for a sufficient degree of fidelity between our empirical models and the real channel. Using $\widetilde{L}$ might be a good idea for applications that require very high fidelity; we address this issue in more detail in Section 5.8. For our "sufficient fidelity" models, and unless mentioned, we will use the mean RMS-DS to determine the number of model taps.

5.4.2 Markov Modeling: Transitions between Regions and Persistence Process

In this section, we discuss extraction of the parameters necessary for modeling the transitions between different regions on the airport. We also describe how we use a Markov chain to model the persistence process associated with the taps (our $z_k(t)$ processes of (3.7)). The former application is novel, and could be used in a high-fidelity model of the channel that would be applicable for vehicles traversing all three regions over a period of time.

5.4.2.1 Modeling Transitions between Regions

As discussed, while moving on the airport, the receiver passes through different regions—LOS-O, NLOS-S, and NLOS (Section 3.3). A realistic channel model should be able to emulate such conditions. The different regions can be modeled as different states of a Markov chain model. Notationally, the different regions can be assigned state numbers: the LOS-O, NLOS-S, and NLOS regions are denoted states 1, 2, and 3 respectively. The algorithm used to determine the *Region_TS* and *Region_ES* matrices for a given airport from the collected data is as follows:

1. Consider an airport (here for example, say CLE)
2. Associate a state index *(Reg_Status$_j$)* with the jth PDP of CLE depending on its RMS-DS. For example, for CLE, if the RMS-DS for the jth PDP is 234 nsec, then *Reg_Status$_j$=2*, denoting the NLOS-S region. (Refer to Table 4.3 for other demarcations for RMS-DS).
3. Repeat Step 2 for all the PDPs (for CLE).
4. Obtain *Region_TS* and *Region_ES* matrices for CLE using the *Reg_Status* vectors developed from steps 2 and 3. The *ES* matrices are the steady-state probabilities computed as fractions of time, and the *TS* matrices are transition probabilities computed by counting transitions and dividing by the total number of PDPs minus one.

Figure 5.18 provides an example measurement set obtained from CLE. The figure illustrates that the receiver inhabits different regions during the course of travel. Depending on the region, each profile has a region state associated with it. The top part of the figure provides the corresponding RMS-DS values of the profiles. It can be observed that as the RMS-DS changes, the profile moves from one region to another. The thresholds for each region in term of RMS-DS are provided in Table 4.3.
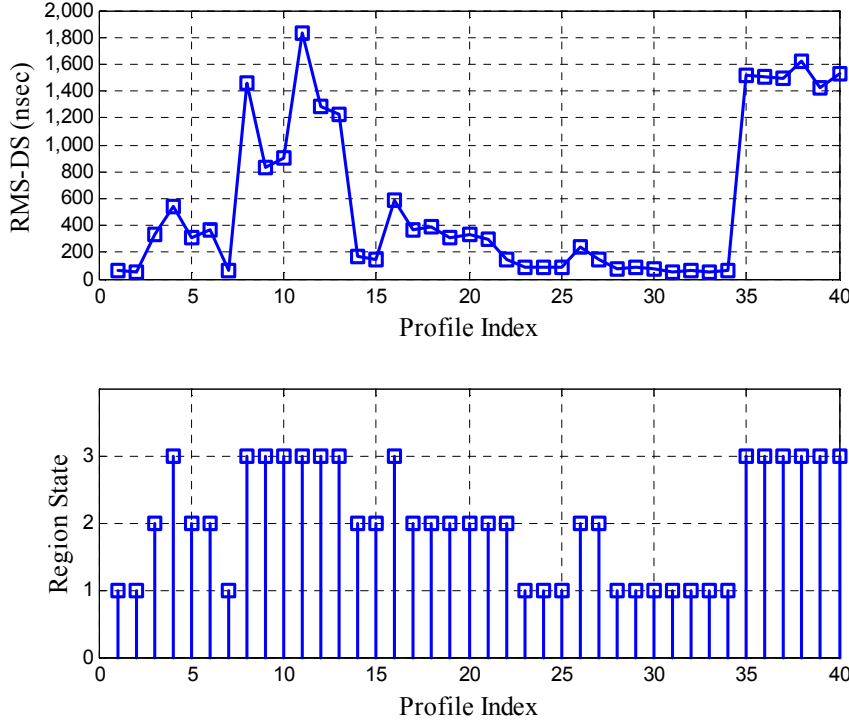
Figure 5.18. Region state and corresponding RMS-DS for an example measurement set at CLE.

The corresponding matrices *Region_TS* and *Region_ES* for CLE obtained using our measurements and the above algorithm are as follows:

$$Region\_TS = \begin{bmatrix} 0.4308 & 0.4099 & 0.1593 \\ 0.2193 & 0.5244 & 0.2563 \\ 0.0406 & 0.1586 & 0.8008 \end{bmatrix} \quad Region\_ES = \begin{bmatrix} 0.1582 \\ 0.3127 \\ 0.5291 \end{bmatrix} \tag{5.14}$$

Thus for CLE, from the state probability matrix *Region_ES*, we see that the receiver spent approximately 16% of the time in the LOS-O region, 31% of the time in the NLOS-S region, and 53% of the time in the NLOS region.

5.4.2.2 Modeling the Tap Persistence Processes

The airport surface channel is dynamic due to the changing fading conditions with time and locations across the airport. Specifically, due to platform and scatterer mobility, some of the multipath echoes may "persist" only for some duration, then "disappear" (or take amplitude values well below our threshold). As noted previously, we capture this effect by what we term a persistence random process, which takes values of only zero or one, with one corresponding to the presence of a tap value above threshold, and zero corresponding to its absence. The steady state probabilities are the probabilities of being in either the one or zero state, overall. The

transition probabilities are the probabilities of going from one state to itself, or to the other state. All these probabilities were determined empirically from our data. As discussed in Section 5.3.1, the persistence process will be modeled using a Markov chain.

During the course of model development, because of the prevalence of threshold crossings of the tap processes, we determined that the steady state probability associated with the taps is a key factor for providing realistic and accurate channel models. The steady state probability of a tap provides an idea regarding the percentage of time that this tap can be considered as a valid multipath component. So essentially, we need to extract *TS* and *ES* matrices from our collected data for each of the taps of each region for a particular airport. After the "quantization" of RMS-DS into state values as in Figure 5.18, these tap transition and emission matrices are empirically determined by relative frequency. The algorithm used in order to determine the TS_i^U and ES_i^U matrices for the ith tap of a *Region U* (*U* is NLOS-S, NLOS, or LOS-O) of the airport appears next:

1. Consider an airport and a specific region associated with it (here, say JFK and NLOS).
2. Consider the ith tap (for NLOS at JFK).
3. Associate a state index *(Multipath_Status$_j^i$)* with the jth PDP of the ith tap depending on whether the tap's power is within 25 dB of the maximum tap value for the jth PDP. For example, if the maximum power in the jth PDP is 0 dB, and the power associated with the ith tap of the jth PDP is -23 dB, then *Multipath_Status$_j^i$* is 1.
4. Repeat step 3 for all the PDPs (of JFK NLOS) for the ith tap and obtain a binary (0,1) vector *Multipath_Status^i* for the ith tap.
5. Obtain TS_i^{NLOS} and ES_i^{NLOS} matrices for the ith tap (of JFK NLOS) using the *Multipath_Status^i* vector. (The *TS* elements are determined by counting transitions among the various states.)
6. Repeat Steps 2-5 for all taps (*L* = 75 for JFK NLOS).

Figure 5.19 provides the steady state probability of having a multipath component (state *z*=1) for [JFK, NLOS, 50] and [JFK, NLOS-S, 50] versus tap index. We also provide example values of (TS_3^{NLOS}, ES_3^{NLOS}) and (TS_3^{NLOS-S}, ES_3^{NLOS-S}) for the 3rd tap. As expected, the steady state probability for State 1 (tap "on") decreases as the tap index increases. We also notice that the steady state probability for State 1 is higher in NLOS than in NLOS-S for higher index taps.

$$ES_3^{NLOS-S} = \begin{bmatrix} 0.1548 \\ 0.8452 \end{bmatrix} \quad TS_3^{NLOS-S} = \begin{bmatrix} 0.2939 & 0.7061 \\ 0.1292 & 0.8708 \end{bmatrix}$$

$$ES_3^{NLOS} = \begin{bmatrix} 0.3023 \\ 0.6977 \end{bmatrix} \quad TS_3^{NLOS} = \begin{bmatrix} 0.4921 & 0.5079 \\ 0.2201 & 0.7799 \end{bmatrix}$$
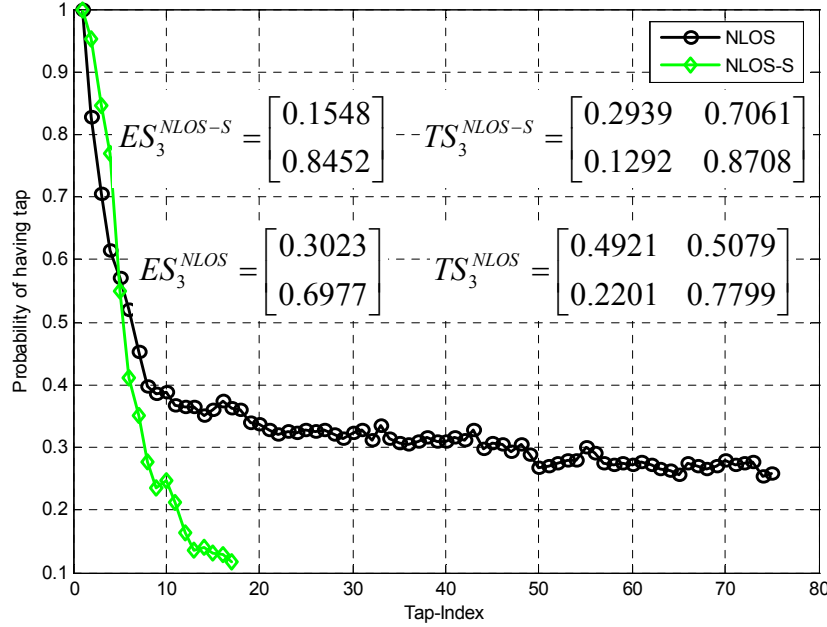
Figure 5.19. Steady state probabilities of State 1 for [JFK, NLOS, 50] and [JFK, NLOS-S, 50].

5.4.3 Tap Energies

In this section, we discuss the algorithm used to determine the energy associated with each tap. We follow with a discussion on cumulative energy gathered with each succeeding tap in the model.

5.4.3.1 Energy Determination for Each Tap

Each tap in the channel model is most likely an aggregate of multiple rays within the delay bin of the tap. For example, in the case of a 50 MHz BW, each tap is associated with a delay bin of 20 nanoseconds. Due to the different propagation effects associated with the rays, the relative energy in each tap is different. In all contemporary channel models, the energy associated with each tap is an essential element in defining the model. The relative energies in the tap yield insight into the underlying physical channel. The presence of high energy multipath components at higher-indexed taps points toward a highly dispersive channel. Conversely, in the case of a mildly dispersive channel, a large percentage of the aggregate energy is within the lower-indexed taps. We determine the energy associated with each tap from our measured data.

As discussed in Section 5.4.2, the multipath components (taps) each have a persistence process associated with them. This complicates somewhat the computation of average energy. Hence we need to be careful in defining the average energy for each tap. Clearly, for averaging we should consider only those PDPs in which the tap is recognized as a valid multipath component (i.e., the energy of the tap is within the *MT* of 25 dB of the maximum energy tap in

101

that PDP). We also account for the tap persistence. The algorithm used in order to determine $Energy_i^U$ for the ith tap of *Region U* of the airport is as follows:

1. Consider an airport and a specific region associated (here, say JFK and *U*=NLOS).
2. Consider the jth PDP (for NLOS at JFK)
3. Normalize the energy in the jth PDP so that the total energy in that PDP is unity.
4. Assign the energy of the ith tap in the jth PDP to $Temp\_Energy_j^i$.
5. Repeat step 4 for all taps (in JFK NLOS, $L = 66$)
6. Create $Valid\_Energy_j^i = Temp\_Energy_j^i \times Multipath\_Status_j^i$ for the jth PDP. Note: $Multipath\_Status_j^i$ =z is either 1 or 0 depending on whether or not the ith tap is a valid multipath component.
7. Repeat steps 3-6 for all PDPs collected (for JFK NLOS).
8. Find $Energy_i^U$ for the ith tap using the formula $\sum_j Valid\_Energy_j^i \Big/ \sum_j Multipath\_Status_j^i$.
9. Repeat step 8 for all taps.

Figure 5.20 provides the average energy associated with each tap for [JFK, NLOS, 50] and [JFK, NLOS-S, 50]. As expected, the average energy decreases as the tap index increases. We also notice that the rate at which the tap energy decreases with tap index is much faster for NLOS-S as compared to NLOS. We also provide an exponential curve fit for both the plots.
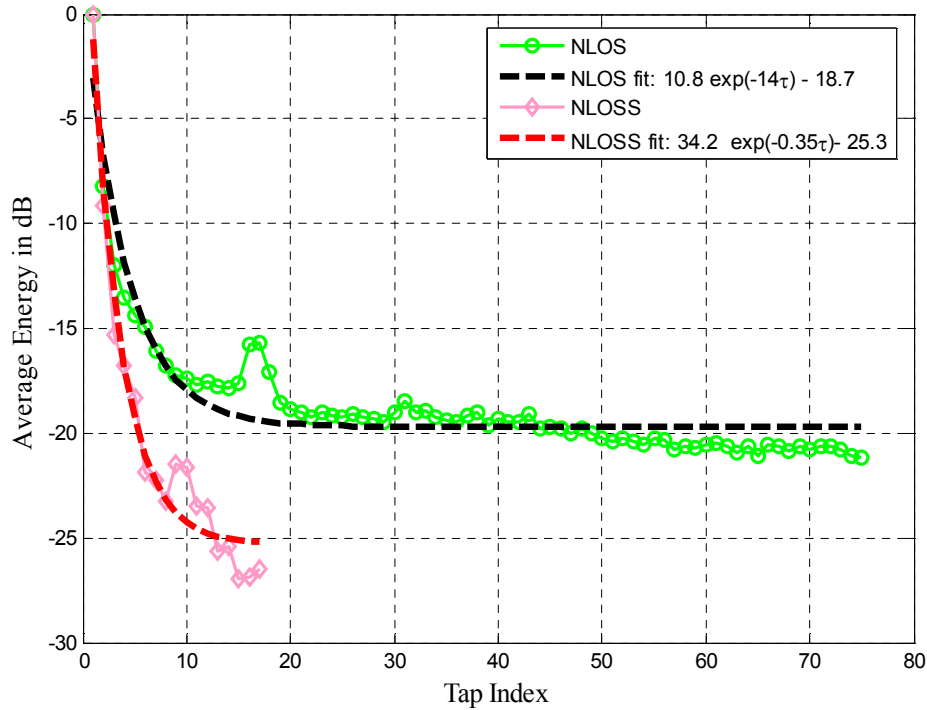
Figure 5.20. Average energy associated with tap for [JFK, NLOS, 50] and [JFK, NLOS-S, 50].

5.4.3.2 Cumulative Energy Gathered

Selection of an appropriate number of taps to fairly tradeoff implementation complexity and model fidelity is an important factor in creating channel models. In the open literature one can find different "metrics" that system designers have used to determine this tradeoff. The criterion most often used is the energy associated with the tap, or more precisely, its contribution towards the cumulative energy of the PDP. As noted, we maintain that the tap steady state probability, in addition to the energy contribution, should determine whether or not the tap should be considered in the model. In essence, we determine L or $\widetilde{L}$ from RMS-DS or the number of taps within 25 dB of the maximum, respectively, as an *upper bound* to the number of taps we plan to include in the model. In order to account for both tap energy and steady state probability, we define the cumulative energy of tap i as

$$Cumu\_Energy_i^U = Energy_i^U \times ES_i^U \tag{5.15}$$

We provide an example plot of this for [JFK, NLOS, 50] and [JFK, NLOS-S, 50] in Figure 5.21. This figure provides the cumulative energy for both these cases as a function of tap index, where we have used L taps for each region, as derived previously. As expected, the increase in cumulative energy is a much steeper function of tap index for NLOS-S than it is for NLOS.
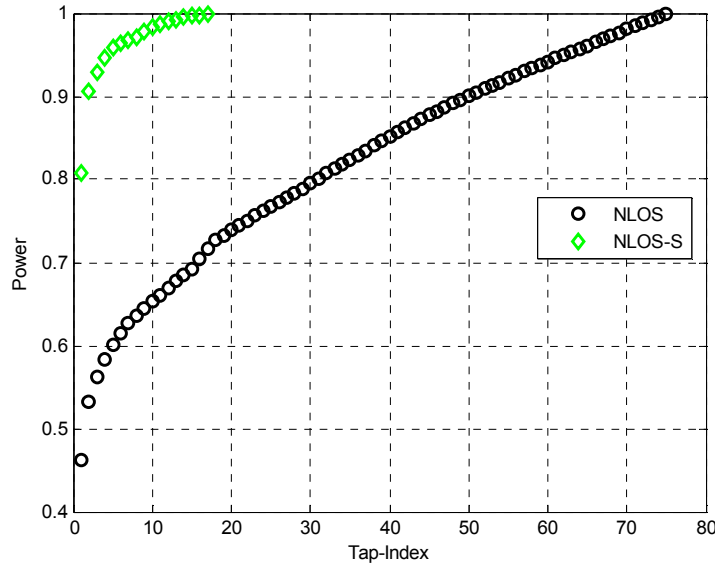
Figure 5.21. Cumulative energy gathered for [JFK, NLOS, 50] and [JFK, NLOS-S, 50].

5.4.4 Tap Correlation Matrix

Our measurements have shown that the airport surface channel can often be different from its terrestrial counterpart with regard to correlation among taps. Specifically, from our measurements at different airports, we have often found correlated scattering among taps. The

correlation matrix is calculated using (5.9). There are several things to note before determining these correlation matrices.

1. As described in Chapter 3, for a particular airport we have numbered the route of travel. During our measurement campaign, we move from one point to another. Due to the different behavior of the scatterers and the different physical structures at different locations on the airport, the correlation matrix needs to be evaluated for each segment of travel separately. For example, JFK airport was mapped into 26 points (25 segments of travel). The notation R_{mn}^{U} will mean that the correlation matrix was determined using the PDPs collected while traveling between points m and n in Region U.

2. For a particular R_{mn}^{U}, we compute its individual elements $r_{i,j}$ (5.9). Recall that each tap has a persistence process associated with it. So it is often not the case that both taps i and j exist for the same PDPs. Hence $r_{i,j}$ should be calculated using the PDPs only when *both* these taps are valid multipath components (z_i and z_j both equal 1). Because of this phenomenon, different numbers of PDPs may be used to compute the different $r_{i,j}$ entries for a particular R_{mn}^{U}. For example, in the case of R_{12}^{NLOS-S} for JFK, $r_{1,2}$ might have been computed using 45 PDPs, whereas $r_{3,8}$ was computed using only 10 PDPs. We illustrate this using Figure 5.22. This figure is plotted for R_{12}^{NLOS-S} for JFK, the third ("z") axis is the number of PDPs used, and the x and y axes are the tap indices. Note that it is possible that for higher-indexed taps, there might not be *any* PDPs in a given segment of travel where both the taps exist.
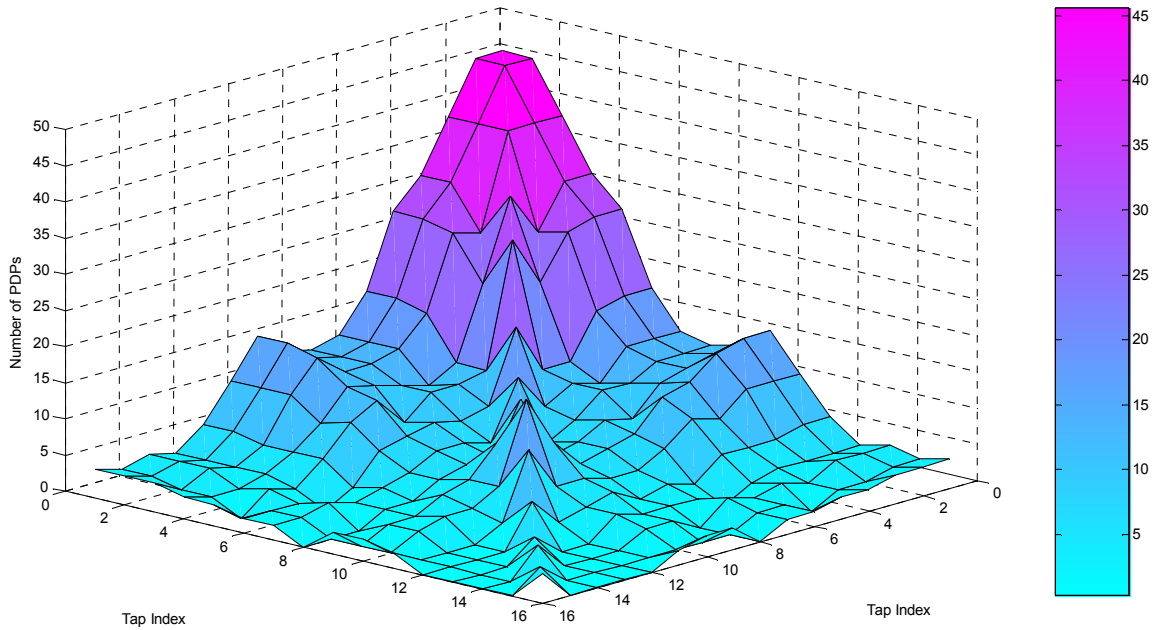
Figure 5.22. Number of PDPs used to determine R_{12}^{NLOS-S} for [JFK, NLOS-S, 50].

As is evident from the previous discussion, we have some amount of flexibility in determining matrices R^U_{mn} for each region and travel segment. One method could be averaging all the R^U_{mn}'s, but this would defeat the purpose of maintaining the integrity of the real fading behavior in each segment. There are though a number of ways of providing a representative correlation matrix. Here we address several ways: the first provides the worst-case correlations encountered on the airport surface, and the second presents the "most statistically confident" correlation matrix. Two other methods are also proposed.

5.4.4.1 Worse Case Correlation Matrix

The worst case correlation matrix R^U_{wc} has the individual worst case values for each matrix element $r_{i,j}$. We define the worst-case value as the $r_{i,j}$ value with the largest magnitude. For example, for an airport like JFK with 25 segments of travel, we have 25 possible values for each $r_{i,j}$. In actuality, since we made multiple measurement runs over some segments, we had a total of 42 measured correlation matrices. The entries of R^U_{wc} are the maximum $|r_{i,j}|$ from these 42 possible values, for each (i,j) pair. (Note that via symmetry, only the lower or upper triangular part of each matrix must be computed, so for an L-tap channel, there are $(L^2-L)/2$ unique elements.) The R^{NLOS}_{wc} for [JFK, NLOS, 5 MHz] is provided in (5.16). The number of taps $L=9$ was determined using (5.13).

$$
\begin{bmatrix}
1 & 0.4859 & 0.614 & 0.4503 & 0.7092 & 0.7456 & 0.4238 & 0.8633 & 0.7087 \\
0.4859 & 1 & 0.5448 & 0.8929 & 0.9453 & 0.5427 & 0.7310 & 0.7946 & 0.7046 \\
0.6410 & 0.5448 & 1 & 0.6603 & 0.5474 & 0.7943 & 0.5107 & 0.3491 & 0.6610 \\
0.4503 & 0.8929 & 0.6603 & 1 & 0.7849 & 0.8056 & 0.5386 & 0.4589 & 0.6839 \\
0.7092 & 0.9453 & 0.5474 & 0.7849 & 1 & 0.7006 & 0.4666 & 0.6691 & 0.6903 \\
0.7456 & 0.5427 & 0.7943 & 0.8056 & 0.7006 & 1 & 0.8208 & 0.5572 & 0.4562 \\
0.4238 & 0.7310 & 0.5107 & 0.5386 & 0.4666 & 0.8208 & 1 & 0.7626 & 0.6254 \\
0.8633 & 0.7946 & 0.3491 & 0.4589 & 0.6691 & 0.5572 & 0.7626 & 1 & 0.8456 \\
0.7087 & 0.7046 & 0.6610 & 0.6839 & 0.6903 & 0.4562 & 0.6254 & 0.8456 & 1
\end{bmatrix}
\quad (5.16)
$$

In the next equation (5.17), we present the matrix containing the number of PDPs that were used in determining the elements in R^{NLOS}_{wc} of (5.16):

$$
\begin{bmatrix}
1 & 196 & 8 & 8 & 8 & 5 & 13 & 11 & 7 \\
196 & 1 & 78 & 5 & 5 & 8 & 8 & 10 & 12 \\
8 & 78 & 1 & 17 & 37 & 7 & 25 & 28 & 27 \\
8 & 5 & 17 & 1 & 6 & 11 & 21 & 9 & 5 \\
8 & 5 & 37 & 6 & 1 & 34 & 6 & 8 & 9 \\
5 & 8 & 7 & 11 & 34 & 1 & 6 & 8 & 13 \\
13 & 8 & 25 & 21 & 6 & 6 & 1 & 8 & 21 \\
11 & 10 & 28 & 9 & 8 & 5 & 8 & 1 & 9 \\
7 & 12 & 27 & 5 & 9 & 13 & 21 & 9 & 1
\end{bmatrix}
\qquad (5.17)
$$

In (5.17), for the diagonal elements, the number of PDPs is 1. This is because we don't actually estimate the correlation value of the tap with itself from our data. From (5.17), we can observe that some of the correlations were determined using very few PDPs. Hence, we can't be statistically confident of those values. Yet we can not deny the occurrence of the small number of PDPs that yielded these worst case correlations on the airport surface. To be confident that we are accounting for the worst case, we thus need to include such "low-confidence" correlations. Note that since there can't be any PDP on the airport where we have worst case correlations for all taps simultaneously, R_{wc}^{U} is a (pessimistic) upper bound for the correlation values.

5.4.4.2 "Maximum Confidence" Correlation Matrix

We consider the same example of JFK with 25 segments of travel, and 42 possible values for each $r_{i,j}$, with each value $r_{i,j}$ computed using some number of PDPs. Out of these 42 values, we select the $r_{i,j}$ that is computed using the maximum number of PDPs. We denote the resulting correlation matrix the "maximum confidence" correlation matrix, R_{mc}^{U}. The R_{mc}^{NLOS-S} matrix for [JFK, NLOS, 5 MHz] is provided in (5.18).

$$
\begin{bmatrix}
1 & 0.4043 & 0.3085 & 0.2245 & 0.1435 & 0.1329 & 0.1112 & 0.1146 & 0.0663 \\
0.4043 & 1 & 0.1923 & 0.0677 & 0.0707 & 0.0256 & -0.0038 & 0.1052 & -0.0239 \\
0.3085 & 0.1923 & 1 & 0.1399 & 0.1374 & 0.0990 & 0.0836 & 0.0698 & 0.0039 \\
0.2245 & 0.0677 & 0.1399 & 1 & 0.1165 & 0.1023 & 0.0862 & 0.0633 & 0.0761 \\
0.1435 & 0.0707 & 0.1374 & 0.1165 & 1 & 0.1348 & 0.0702 & 0.0335 & 0.0712 \\
0.1329 & 0.0256 & 0.0990 & 0.1023 & 0.1348 & 1 & 0.1249 & 0.0302 & 0.0287 \\
0.1112 & -0.0038 & 0.0836 & 0.0862 & 0.0702 & 0.1249 & 1 & 0.0737 & 0.1076 \\
0.1146 & 0.1052 & 0.0698 & 0.0633 & 0.0335 & 0.0302 & 0.0737 & 1 & 0.0369 \\
0.0663 & -0.0239 & 0.0039 & 0.0761 & 0.0712 & 0.0287 & 0.1076 & 0.0369 & 1
\end{bmatrix}
\qquad (5.18)
$$

Equation (5.19) displays the number of PDPs used to compute the elements in R_{mc}^{NLOS}.

$$\begin{bmatrix} 1 & 722 & 693 & 661 & 635 & 615 & 573 & 582 & 558 \\ 722 & 1 & 657 & 623 & 601 & 581 & 542 & 547 & 525 \\ 693 & 657 & 1 & 616 & 586 & 565 & 528 & 534 & 516 \\ 661 & 623 & 616 & 1 & 575 & 547 & 514 & 517 & 497 \\ 635 & 601 & 586 & 575 & 1 & 538 & 504 & 503 & 490 \\ 615 & 581 & 565 & 547 & 538 & 1 & 506 & 505 & 490 \\ 573 & 542 & 528 & 514 & 504 & 506 & 1 & 489 & 475 \\ 582 & 547 & 534 & 517 & 503 & 505 & 489 & 1 & 483 \\ 558 & 525 & 516 & 497 & 490 & 490 & 475 & 483 & 1 \end{bmatrix} \quad (5.19)$$

From (5.19), we can observe that number of PDPs used to determine the correlation matrix is large compared to the entries in (5.17).

5.4.4.3 Realistic "Worse Case" Correlation Matrix

As discussed previously, R_{wc}^{NLOS-S} is not a practical correlation matrix that we actually measured. So to provide a more realistic correlated channel, we introduce R_{rwc}^{U}. We consider the same example of JFK with 25 segments of travel and 42 measured correlation matrices. Out of the 42 matrices, we select the single correlation matrix that is the worst. We determine this "worst" rating by assigning a "severity value" to each matrix. The "severity value" of the matrix is the sum of the absolute values of the $r_{i,j}$ for that matrix in the lower triangular portion. The R_{rwc}^{NLOS-S} matrix for [JFK, NLOS, 5 MHz] is provided in (5.20).

$$\begin{bmatrix} 1 & -0.0879 & 0.5921 & 0.1238 & -1 & -0.2259 & 0.2411 & 0.8121 & 1 \\ -0.0879 & 1 & -0.0714 & -0.7769 & -1 & -0.1029 & -0.8518 & 0.3173 & 1 \\ 0.5921 & -0.0714 & 1 & -0.0201 & -1 & -1 & -0.1952 & 0.8708 & 0 \\ 0.1238 & -0.7769 & -0.0201 & 1 & -1 & -1 & 0.9403 & -0.3097 & 1 \\ -1 & -1 & -1 & -1 & 1 & 1 & 1 & -1 & 0 \\ -0.2259 & -0.1029 & -1 & -1 & 1 & 1 & -1 & 1 & 1 \\ 0.2411 & -0.8518 & -0.1952 & 0.9403 & 1 & -1 & 1 & -0.3782 & 1 \\ 0.8121 & 0.3173 & 0.8708 & -0.3097 & -1 & 1 & -0.3782 & 1 & 1 \\ 1 & 1 & 0 & 1 & 0 & 1 & 1 & 1 & 1 \end{bmatrix} \quad (5.20)$$

As can be noticed from (5.20), some of the elements are 1, -1 or 0, and these actually result from the small number of PDPs (fewer than 5) used to determine the corresponding $r_{i,j}$ values. Thus, these correlation values are "low confidence" ones. The zeros denote the complete absence of PDPs in common (e.g. $r_{9,3}=0$ means tap 9 was never present above threshold when tap 3 was above threshold). The values +1 and -1 mean that for the very few PDPs in common, the correlation coefficient was near +1 or -1.

5.4.4.4 Realistic "Maximum Confidence" Correlation Matrix

Similarly to R_{rmc}^U, to obtain a realistic "high confidence" correlated channel, we introduce R_{rmc}^U. We consider the same example of JFK with 25 segments of travel (in total 42 sets), yielding 42 possible values for the correlation matrix. Out of these 42 matrices, we select the correlation matrix that is calculated using the maximum number of PDPs. We determine this by assigning a "confidence value" to each matrix. The "confidence value" of element $r_{i,j}$ is the number of PDPs used to determine $r_{i,j}$ divided by the maximum number of PDPs ever used to determine any $r_{i,j}$, over the entire airport in this region. Then the "confidence value" of a segment is the sum of all "confidence values" of the elements in its matrix. The R_{rwc}^{NLOS-S} matrix for [JFK, NLOS, 5 MHz] turns out to be the same as (5.18). This might not be the case for other airports, of course, which may have distinct matrices R_{rmc}^U and R_{mc}^U.

Figure 5.23 summarizes all the steps involved in extraction of channel related parameters from the pre-processed PDPs. This figure can be viewed as a continuation of Figure 5.7.
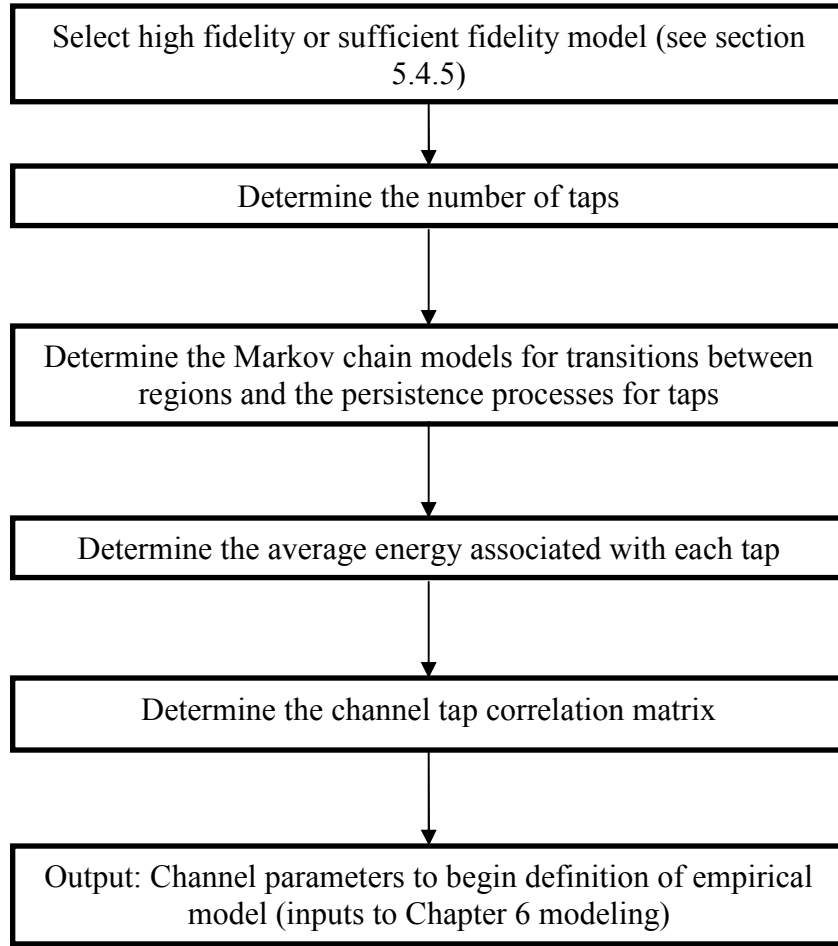
Figure 5.23. Summary of model extraction steps of Section 5.4.

5.4.5 Model Fidelity: Definitions for High-Fidelity and Sufficient Fidelity

From the discussions in the prior sections, it is clear that there are a number of options possible in determining the channel parameters. We describe here the two approaches to this model fidelity issue we have used.

1. Sufficient-fidelity model: This model provides a practical emulation of the channel with realistic (moderate) implementation complexity. In this model, at each step of channel parameter extraction, we make calculated judgments on the parameter values, based upon prior research and as much quantitative comparison as we can apply. The sufficient fidelity model could be used by researchers interested in studying either the higher-layer or lower layer performance of a communication system deployed on the airport surface. For the higher layers, such researchers might be primarily interested in implementing the model for the sake of completion, while still capturing the major channel effects, and allowing them to concentrate their computer resources towards their own research goals. *This model uses empirical fits to our data to obtain estimates of random process parameters; it then uses random number generators to provide simulated random processes with the desired statistics, for any simulation duration.*

2. High-fidelity model: This model is more applicable to a high-precision simulation of the channel. This model involves fewer approximations than the sufficient fidelity model, and may be necessary for a comprehensive and highly accurate depiction of the underlying physical channel at airports. This model is directed more toward academic investigations (at least at present). *This model also uses empirical fits to data, but employs a larger number of taps, and uses stored correlation matrices to specify channel tap random processes for a specific segment of time. The random number generators then simulate the tap random processes with desired statistics over this time segment, and the process is repeated.*

In the subsequent discussion, we provide appropriate selection of parameters to determine the high-fidelity or sufficient-fidelity model for any airport, region, or channel bandwidth. For brevity in illustrating this, we restrict attention to only one example case: [JFK, NLOS, 50].

5.4.5.1 Number of Taps for Each Fidelity Class

The number of taps can be determined using different criteria, as discussed. We first describe these criteria and provide a method (based on cumulative energy gathered with the taps) to further *refine* the actual number of taps to be used in the implementation of the model.

1. For the sufficient fidelity class, we provide four potential methods to determine the number of taps (here for [JFK, NLOS, 50]):
   a. The number of taps is determined using the *mean RMS-DS* (using 5.13). This method is discussed in detail in Section 5.4.1.2. The number of taps is then $L=75$.
   b. Use the *maximum RMS-DS* to determine the number of taps. The number of taps (L) is then 124. We need to keep in mind that the maximum *RMS-DS* is applicable only for one (or a few) PDP(s). Hence, the model obtained from this method relies on a single

realization of the channel, from which we use other realizations to develop statistics for the stochastic channel model.

c. Figure 5.24 provides a cumulative distribution function (*cdf*) for the distribution of RMS-DS for [JFK, NLOS, 50]. We can determine the *threshold RMS-DS* which has *x%* of PDPs with RMS-DS below this value and term this the *threshold RMS-DS*. Table 5.7 provides example numbers of taps using the *threshold RMS-DS*.
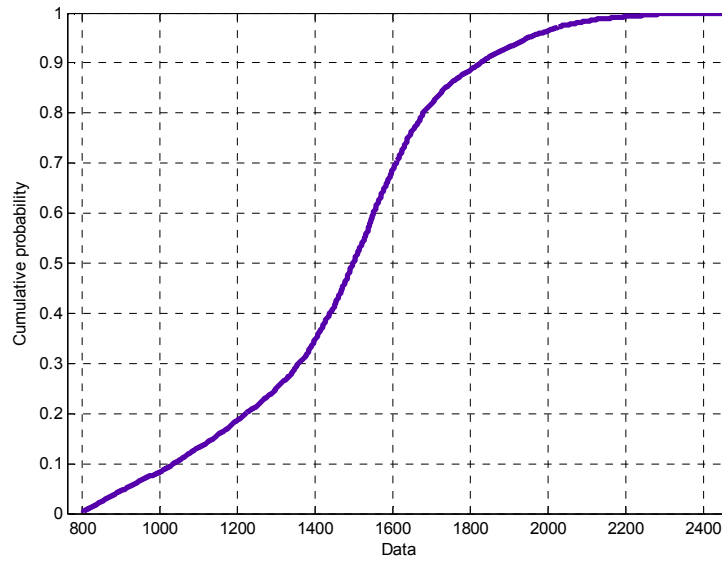
Figure 5.24. CDF of RMS-DS for [JFK, NLOS, 50].

Table 5.7. Number of taps for x% PDPs.

Percentage of Profiles	RMS-DS Threshold	Number of Taps
90%	1827 nsec	93
95%	1947 nsec	99

d. Figure 5.25 provides a *cdf* for the distribution of $\tilde{L}_j$ for [JFK, NLOS, 50]. We can determine the number of taps $(\tilde{L})$ which can account for *x%* of PDPs with $\tilde{L}_j$ below *L*.
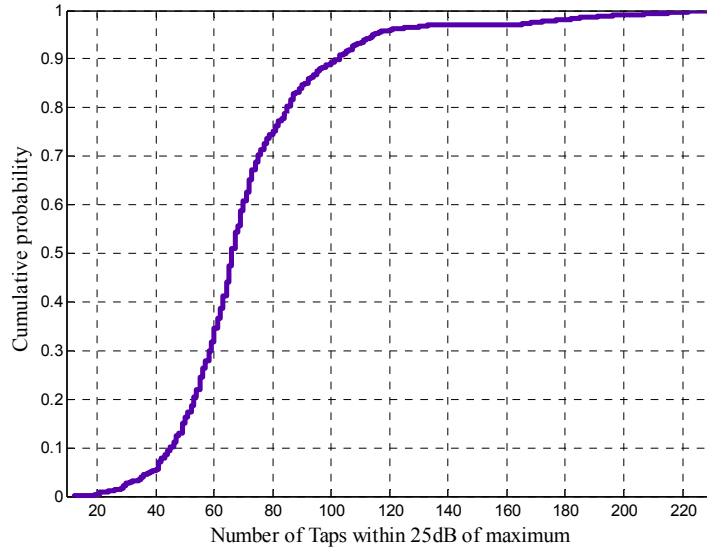
Figure 5.25. CDF of $\widetilde{L}_j$ for [JFK, NLOS, 50].

From Figure 5.25, we observe that we require $L = 100$ taps to account for 90% of the collected PDPs or 120 taps for 95% of the PDPs.

2. For the high fidelity model, we consider only one method for determining the number of taps L: we use the maximum number of taps that are within 25 dB of the maximum in a PDP, i.e., the maximum value of $\widetilde{L}$. For our example airport, region, and bandwidth, from Figure 5.24, we observe that for [JFK, NLOS, 50] the maximum number of taps is 220.

3. Using tap cumulative energy for refinement: The cumulative energy collected with each tap can be used to further refine (reduce) the number of taps obtained using any of the methods described in the previous methods (1 or 2).

a. Figure 5.21 shows the cumulative energy gathered with each tap for [JFK NLOS 50] and [JFK NLOS-S 50]. The number of taps used in Figure 5.21 is derived using 1a, although as noted, we could create similar plots for different values of L obtained from the other methods in either 1 or 2 above. The plot can be used directly, or we can create a table for the number of taps required to gather x% of the energy. Table 5.8 illustrates this for our example case.

Table 5.8. Number of taps for x% energy for [JFK, NLOS, 50].

Tap Index	Cumulative Energy (%)
10	62
20	71
30	77
40	83
50	88
55	91

b. We can also use *all* the taps necessary to gather *all* the energy. So for the case of Figure 5.21, we would require 75 taps for [JFK, NLOS, 50]. This can apply to either the high-fidelity or sufficient fidelity model.

5.4.5.3 Correlation Matrices for Different Fidelity Classes

For the correlation matrices, we propose the following criteria for the two different fidelity classes:

1. For the sufficient fidelity case, use either the worst case or the maximum confidence correlation matrices (realistic or overall). As a further reduction in model complexity, for any correlation values $r_{i,j}$ with magnitude less than some threshold value, e.g., 0.1, set those values to zero. For example, using R_{mc}^{NLOS-S} of (5.18) for the 5 MHz model and setting all elements with $|r_{i,j}|<0.1$ to zero, we reduce the number of unique non-zero elements from $(L^2-L)/2=36$ down to only 15. As we discuss in Chapter 6 though, this may not always appreciably reduce the complexity of the channel simulation.

2. For the high fidelity channel model, in the actual channel model simulation, change the correlation matrix after every *n* realizations of the channel. This would realistically simulate moving from one point in the airport to another. Naturally this would increase the simulation complexity of the model considerably. The value of *n* would generally be random, and the changing of correlation matrices could for example be based upon actual measured matrices and travel times and regions being simulated.

5.4.5.4 Amplitude Distribution for Different Fidelity Classes

For the amplitude statistics of the taps, we propose the following criteria:

1. For the sufficient fidelity case, if the empirical amplitude statistic is ($0.9 < m < 1.1$), then we approximate the distribution as Rayleigh, where *m* is the Nakagami fading factor. Approximating the distribution as Rayleigh for a wider range of values of *m* about unity would further reduce model complexity.

2. For the high fidelity channel model, we use the actual empirical amplitude statistics obtained from the data, without any further approximation.

Table 5.9 provides an overall summary for the concepts described in Section 5.4.5. In order to generate a channel model, the user can employ any permutation of the provided options (one from each row), depending on requirements. In Chapter 6, after providing several channel models, we illustrate the entire procedure by specifying a complete channel model for an example airport size, fidelity, and channel bandwidth.

Table 5.9. Model fidelity criteria applied to a given airport size, region U, and channel bandwidth.

Parameter	Criteria	Fidelity: HF or SF
1. Initial number of taps	1a. Mean RMS-DS 1b. Maximum RMS-DS 1c. Percentage of profiles below an RMS-DS threshold 1d. $\widetilde{L}$ (within 25 dB of maximum tap) for a percentage of profiles 1e. Maximum $\widetilde{L}$	1a. SF 1b. SF 1c. SF 1d. SF 1e. HF
2. Refine 1 using cumulative energy to obtain L	2a. Number of taps required for $x\%$ of the total energy 2b. *All* taps from 1 (i.e., 100% cumulative energy)	2a. SF 2b. HF
3. Correlation matrix	3a. R_{wc}^{U} 3b. R_{mc}^{U} 3c. R_{rwc}^{U} 3d. R_{rmc}^{U} 3e. Distinct correlation matrix for each segment of travel	3a. SF 3b. SF 3c. SF 3d. SF 3e. HF
4. Amplitude statistics	4a. Approximate taps with *0.9<m<1.1* as Rayleigh 4b. Use empirical models without any approximation	4a. SF 4b. HF

Chapter 6: Channel Models

6.1 Introduction

In this chapter, we present the actual channel models we have developed for the airport surface area in the MLS extension band. We first provide a description of our path loss models. Discussions regarding the trade-off between implementation complexity and a sufficiently accurate description of the channel are provided, augmenting similar discussions in the previous chapter. Example channel models in the form of tapped-delay line models for different settings (mobile or fixed point-to-point), different regions (NLOS-S, NLOS, and LOS-O), different airport sizes (small, medium, and large), and bandwidths are presented.

6.2 Path Loss Modeling

As explained in Chapter 3, we use the widely known "$10nlog_{10}(distance)$" formulation for path-loss modeling. This is explicitly given by eq. (3.5). Before discussing further, we point out some restrictions encountered during measurements.

- During the initial measurement campaigns, due to a software error, our sounder was unable to record GPS data. This prevented us from doing any path loss modeling for CLE, OU, and BL airports.
- After the above-mentioned software problem was corrected, we were still unable to record GPS altitude data while logging our channel measurement data. Due to cost constraints, we were not able to fix this problem. This meant that we could record GPS data (latitude, longitude, and altitude) only when we were stationary (non mobile). Hence, for path loss, our data was gathered for several seconds near each numbered stopping point on the routes of travel (see Chapter 4).
- Our sounder is not capable of recording its Received Signal Strength Indication (RSSI) below a power level of -111 dBm. This limited our modeling only to the NLOS-S region for the MIA airport. For the remaining regions of JFK, MIA, and Tamiami, we were always below the threshold of -111 dBm.

Despite these limitations, we do have some data of value, and from this we have developed an initial path loss model for the NLOS-S regions. For MIA, we have used a reference distance d_0 of 462.2 meters. Using this reference distance, our curve fit parameter A (eq. (3.5)) is 103 dB (this is close to the free-space loss at d_0, approximately 100 dB). We used a linear least squares regression fit to obtain the path loss exponent $n \cong 2.23$. Keeping the airport conditions in mind, one would expect a path loss exponent close to free space, especially in the open areas. (In fact, the free-space model was found to hold quite well for open areas at distances up to our limit of approximately 4 km.) The large difference in the relative heights of the transmitting and receiving antennas, and the imperfect reflection property of the ground contribute to our path loss exponent result. The standard deviation of the Gaussian random variable X of eq. (3.5) was determined to be 5.3 dB. Figure 6.1 shows the path loss model for

MIA-NLOS-S along with the actual data. The path loss plotted here in dB is that with the intercept *A* subtracted, so for any given distance, path loss is computed as that given by the figure, plus the 103 dB intercept value.
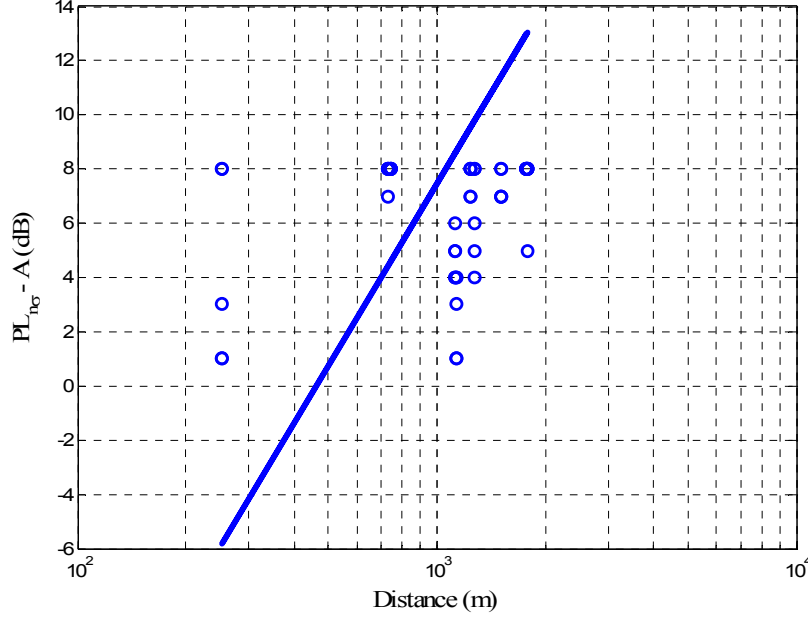
Figure 6.1. Path loss modeling for MIA-NLOS-S; *A*=103 dB, *n*=2.23, σ=5.3 dB.

6.3 Large Airport Channel Model

In this section, we begin by providing justification for a single model for any given region of the large airport, i.e., a single large airport model for region *U*, with $U \in$ {LOS-O, NLOS-S, NLOS}. We then provide detailed channel models for NLOS-S and NLOS regions for a 50 MHz BW. The models are provided for both transmission settings: transmitting from the ATCT or from an airport field site (AFS). We also present comparisons among channel models of different bandwidths for the above cases.

6.3.1 Justification for a Single Large Airport Model

We performed measurement campaigns at two large airports, JFK and MIA. The airports are similar with respect to airport layout and size, traffic (planes and ground vehicles), heights of ATCTs, and these airports also exhibited similar channel characteristics, including RMS-DS and energy distribution among taps, etc. Tables 4.4-4.6 further illustrate the similarity in the two airports in terms of RMS-DS, FCE, and the ranges of channel tap fading parameters (*m* and *K* factors for Nakagami and Ricean models, respectively). Recall from Figure 4.31 that JFK has two distinct regions on the basis of the bi-modal nature of the RMS-DS distribution. Figure 6.2 shows the RMS-DS distribution for MIA. The similarity in the plots (Figures 4.31 and 6.2) is evident.
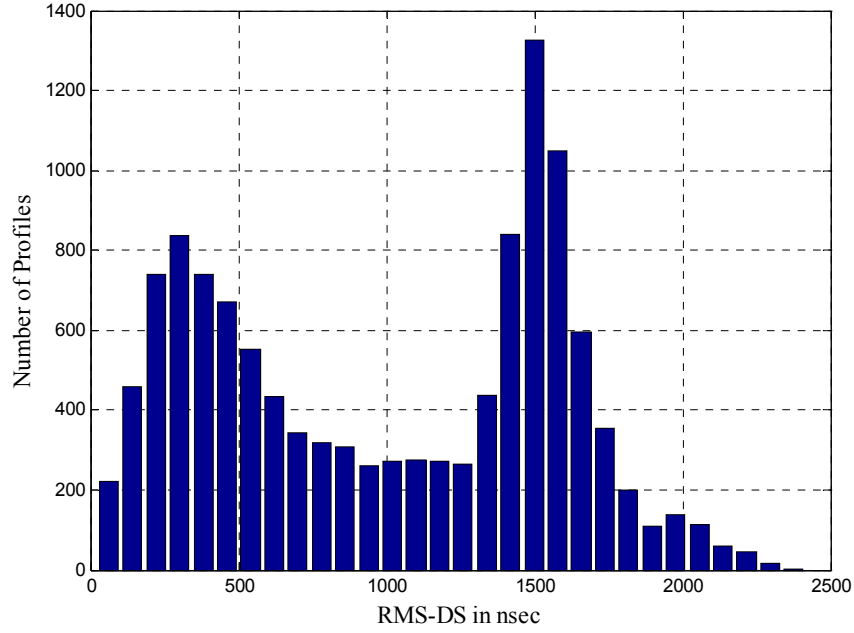
Figure 6.2. RMS-DS distribution for MIA.

A similar comparison using the delay window (DW) parameter $W_{\tau,90}$ for MIA and JFK is provided in Figure 6.3. As with RMS-DS, the bi-modal nature of the distribution of $W_{\tau,90}$ provides further justification for the demarcation of large airports into two regions.
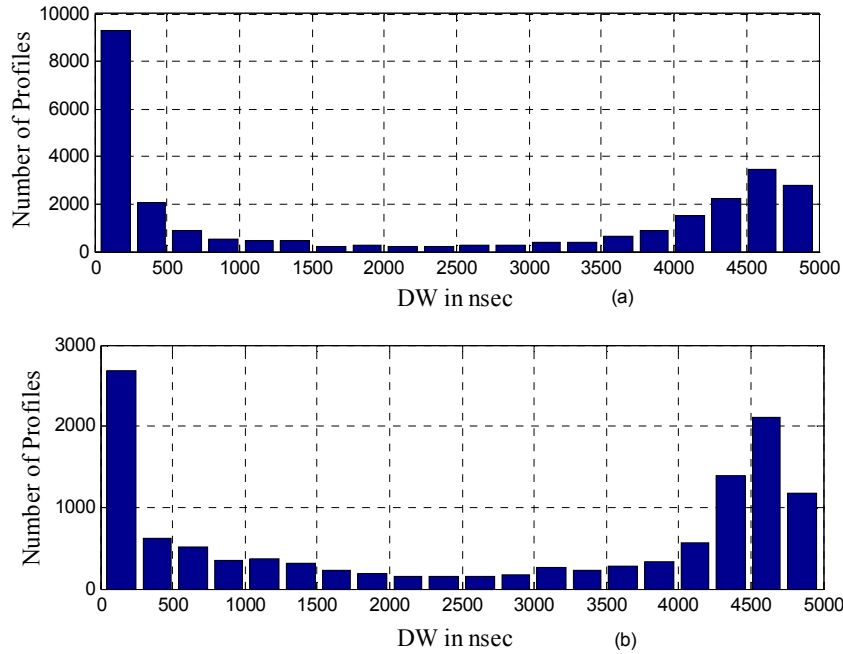
Figure 6.3. Distribution of $W_{\tau,90}$ for (a) [MIA, 50] and (b) [JFK, 50].

Figure 6.4 compares the steady state probability of state 1 for MIA and JFK, versus tap index (recall the steady state probability is approximately the fraction of time a given tap exists above threshold). Very similar trends for the two airports in the reduction of tap existence probability with increasing tap index can be observed from the figure.
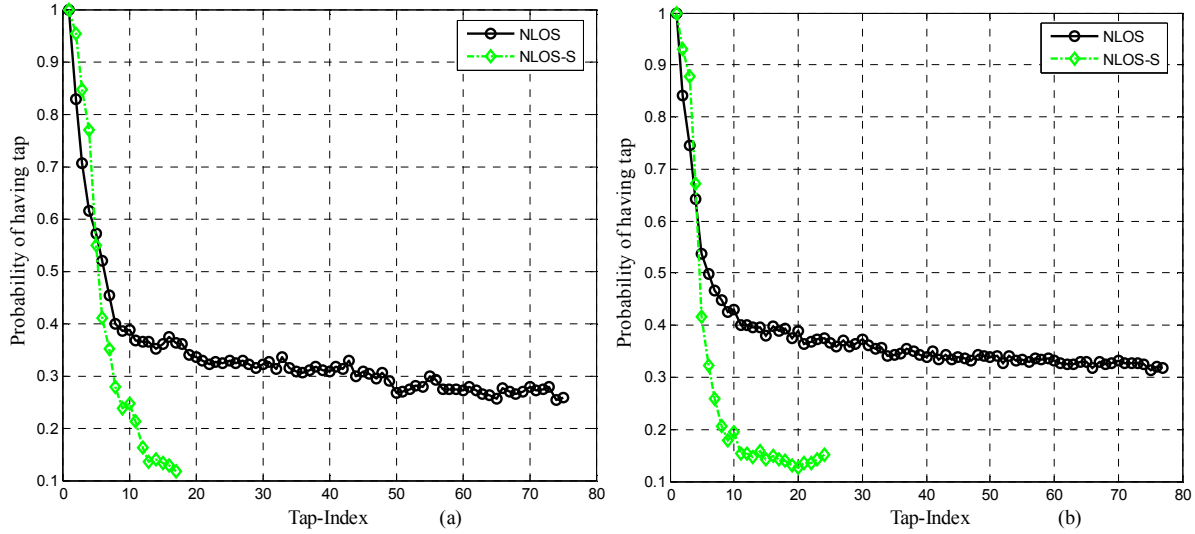
Figure 6.4. Steady state probability for State 1 (tap "on") for (a) [MIA, 50], and (b) [JFK, 50].

Figure 6.5 compares the cumulative energy as function of the number of taps for MIA and JFK. The rate of increase in cumulative energy is similar for the two airports in both regions.
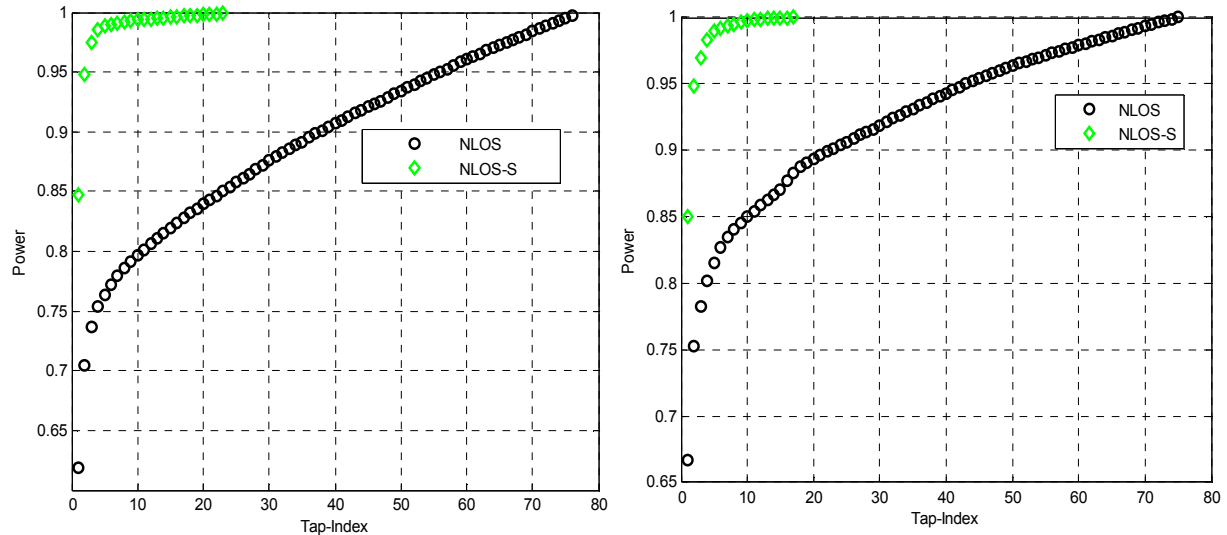
Figure 6.5. Cumulative energy for (a) [MIA 50], and (b) [JFK 50].

Figure 6.6 compares the FCEs for both the airports. Again we find a strong resemblance in the FCEs of the two airports. The slightly wider FCE for JFK as compared to MIA can be attributed to the slightly different values of RMS-DS (refer to Table 4.4 for an RMS-DS description).
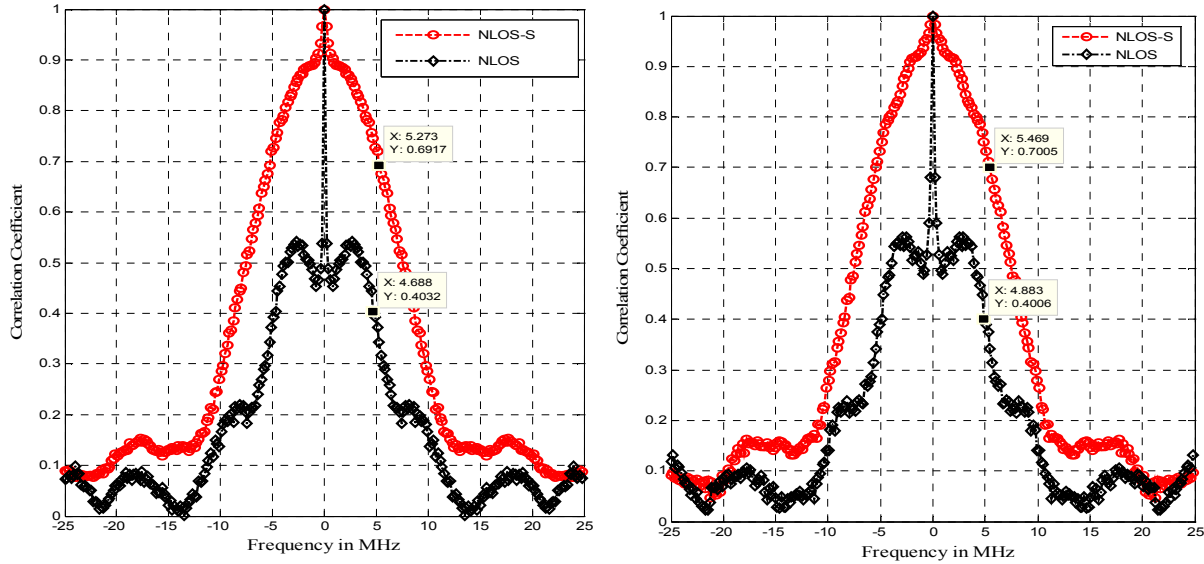
Figure 6.6. FCE for (a) [MIA, 50], and (b) [JFK, 50].

On the basis of the above discussion and the multiple parameter comparisons, we substantiate our claim of using a single model for a given region to apply to any large airport. Since we have two regions (NLOS and NLOS-S), we have two models, one for each region. Since MIA and JFK are among the biggest and busiest airports in the USA, the models presented here can be used for any other large airport as long as its physical characteristics are similar.

6.3.2 Sufficient Fidelity Model, Large Airport NLOS-S Region, 50 MHz

Recall from Table 5.9 that the first step in developing the channel model is to determine the number of taps. We use the mean RMS-DS to determine the number of taps *(L)*. Thus using Table 4.3, we determine that the number of taps for the NLOS-S model is 24. As discussed in Chapter 5, to alleviate the complexity of realizing this channel model, we can further reduce the number of taps without much loss in fidelity. Table 6.1 shows the cumulative energy versus tap index for the NLOS-S case. Clearly, the "law of diminishing returns" is in effect as the number of taps increases. As a suitable threshold, we consider the number of taps *L* to be 8, which accounts for ~99.3% of the energy. By doing this, we have selected option (2b) from Table 5.9, and have substantially reduced the model complexity by using only *L*=8 out of the 24 taps.

Table 6.1. Cumulative energy for [Large Airport, NLOS-S, 50].

Tap Index	Cumulative Energy (%)
1	85
2	95
3	97.5
4	98.5
6	99
8	99.3
12	99.5

For the channel tap correlation matrix, we use R_{wc}^{NLOS-S} to account for the worst case scenario. This correlation matrix is given in (6.1).

$$
\begin{bmatrix}
1 & 0.7881 & 0.2940 & 0.3485 & 0.4782 & 0.4581 & 0.8969 & 0.5644 \\
0.7881 & 1 & 0.3134 & 0.6588 & 0.4255 & 0.8239 & 0.7768 & 0.6160 \\
0.2940 & 0.3134 & 1 & 0.5758 & 0.8606 & 0.6958 & 0.4222 & 0.9695 \\
0.3485 & 0.6588 & 0.5758 & 1 & 0.6939 & 0.6605 & 0.9513 & 0.7965 \\
0.4782 & 0.4255 & 0.8606 & 0.6939 & 1 & 0.9181 & 0.4653 & 0.8869 \\
0.4581 & 0.8239 & 0.6958 & 0.6605 & 0.9181 & 1 & 0.6528 & 0.6052 \\
0.8969 & 0.7768 & 0.4222 & 0.9513 & 0.4653 & 0.6528 & 1 & 0.7502 \\
0.5644 & 0.6160 & 0.9695 & 0.7965 & 0.8869 & 0.6052 & 0.7502 & 1
\end{bmatrix}
\tag{6.1}
$$

Table 6.2 provides some of the channel model parameters for the NLOS-S region of a large airport. The symbols used in the table were introduced in Table 3.2. This table contains the fading amplitude parameter (b) and tap energy, which together can be used to specify the Weibull density to model amplitude fading. Alternate distribution parameters (K for Ricean, m for Nakagami) are also provided, as is the steady state probability of each tap. Results for other channel models use this same format.

Table 6.2. Amplitude statistics for [Large Airport, NLOS-S, 50].

Tap Index	Weibull Shape Factor (b)	Tap Energy	Alternate Distribution Parameter	Steady State Probability for State 1
1	4.83	0.7878	$K = 9.3$ dB	1.0000
2	1.7	0.1011	$m = 0.8$	0.9304
3	1.86	0.0281	$m = 0.98$	0.8768
4	1.91	0.0148	$m = 1.09$	0.6723
5	1.97	0.0068	$m = 1.16$	0.4166
6	1.86	0.0054	$m = 1.04$	0.3230
7	1.88	0.0039	$m = 1.1$	0.2588
8	1.89	0.0039	$m = 1.01$	0.2069

Figure 6.7 provides curve fits to the measured data for the amplitudes of the 1st and 2nd taps for [Large Airport, NLOS-S, 50]. Fits for other taps are similarly good; we have plotted only the first two tap fits—which contain about 88% of the channel energy—for brevity.
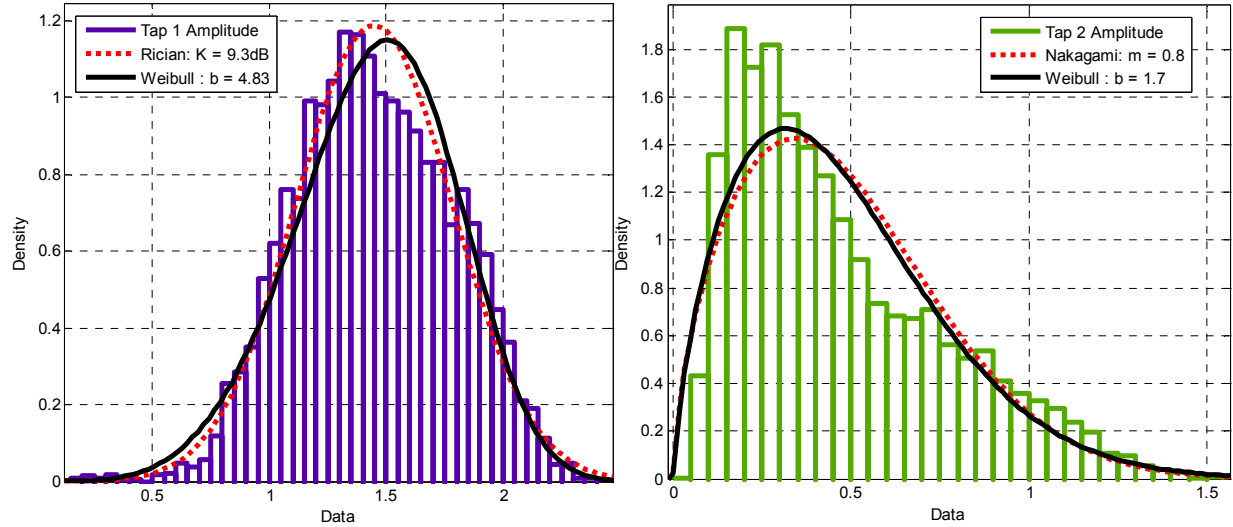
Figure 6.7. Amplitude statistics of taps 1 and 2 for [Large Airport, NLOS-S, 50].

Recall that each tap also has a 2-state Markov chain model associated with it. This Markov random process implements the persistence process (Chapter 3). Table 6.3 provides the steady state and the transition probabilities for all the taps of our large airport NLOS-S model.

Table 6.3. Persistence process parameters for [Large Airport, NLOS-S, 50].

Tap Index	Steady State Probability for State 1	Steady State Probability for State 0	Transition Probability (P_{00})	Transition Probability (P_{01})	Transition Probability (P_{10})	Transition Probability (P_{11})
1	1.0000	0	*n/a*	*n/a*	0	1.0000
2	0.9304	0.0696	0.2319	0.7681	0.0575	0.9425
3	0.8768	0.1232	0.2224	0.7776	0.1093	0.8907
4	0.6723	0.3277	0.4600	0.5400	0.2633	0.7367
5	0.4166	0.5834	0.6674	0.3326	0.4659	0.5341
6	0.3230	0.6770	0.7403	0.2597	0.5447	0.4553
7	0.2588	0.7412	0.7895	0.2105	0.6032	0.3968
8	0.2069	0.7931	0.8536	0.1464	0.5618	0.4382

6.3.3 Sufficient Fidelity Model, Large Airport NLOS Region, 50 MHz

Using Table 4.3, we determine that the number of taps for the NLOS model is 77! As with the NLOS-S case, we simplify this by further reducing the number of taps based upon

cumulative energy. Table 6.4 shows the cumulative energy with increasing tap index for the NLOS case. Behavior similar to that shown in Figure 6.4 obtains. Here we select the number of taps L as 57, which accounts for ~95% of the energy. By doing this, we have used option (2b) again from Table 5.9. Note that we would require 72 taps to collect 99% of the energy.

Table 6.4. Cumulative energy for [Large Airport, NLOS, 50].

Tap Index	Cumulative Energy (%)
5	76.4
10	80
20	84
30	87.6
35	89
40	90.7
45	92.1
50	93.5
57	95.2
72	99

For the correlation matrix, we again use R_{wc}^{NLOS} to account for the worst case conditions. Since we have 57 taps for our channel model, R_{wc}^{NLOS} would be a (57×57) matrix. It is cumbersome to represent the entire matrix here, so we provide only $r_{i,1}$ and $r_{i,2}$ in Table 6.5. The full correlation matrix appears in the files of Appendix D. This table also provides the amplitude statistics for the taps in the channel model.

Table 6.5. Amplitude statistics and example tap correlations for [Large Airport, NLOS, 50].

Tap Index	Weibull Shape Factor (b)	Tap Energy	Alternative Distribution Parameter (Lognormal or Nakagami)	Steady State Probability for State 1	$r_{i,1}$	$r_{i,2}$
1	1.9	0.4243	$(\mu,\sigma^2) = (0.55, 0.1)$	1.0000	1	0.6511
2	1.50	0.0698	$m = 0.67$	0.8408	0.6511	1
3	1.7	0.0301	$m = 0.83$	0.7449	0.6245	0.8163
4	1.8	0.0181	$m = 0.92$	0.6422	0.4904	0.4923
5	1.81	0.0126	$m = 0.95$	0.5383	0.4437	0.5727
6	1.74	0.0118	$m = 0.9$	0.4980	0.6144	0.5653
7	1.78	0.0099	$m = 0.91$	0.4664	0.4078	0.4322
8	1.8	0.0095	$m = 0.94$	0.4490	0.6010	0.4296
9	1.73	0.0089	$m = 0.88$	0.4255	0.5825	0.5070
10	1.75	0.0091	$m = 0.9$	0.4301	0.7644	0.4591
11	1.69	0.0083	$m = 0.85$	0.4002	0.7109	0.5465
12	1.77	0.0080	$m = 0.89$	0.4010	0.7383	0.5492

13	1.91	0.0072	$m = 1.03$	0.3951	0.6841	0.4969
14	1.92	0.0072	$m = 1.04$	0.3953	0.7579	0.8334
15	1.62	0.0085	$m = 0.77$	0.3799	0.5049	0.5696
16	1.76	0.0081	$m = 0.89$	0.3972	0.7692	0.8101
17	1.85	0.0069	$m = 0.99$	0.3897	0.6615	0.7339
18	1.91	0.0069	$m = 1.03$	0.3932	0.8052	0.4233
19	1.85	0.0067	$m = 0.97$	0.3763	0.8001	0.7362
20	1.85	0.0071	$m = 0.97$	0.3894	0.4892	0.7651
21	1.86	0.0065	$m = 0.97$	0.3642	0.9180	0.6594
22	1.79	0.0068	$m = 0.99$	0.3675	0.4837	0.7339
23	1.9	0.0066	$m = 0.95$	0.3734	0.6803	0.3282
24	1.86	0.0067	$m = 1.03$	0.3748	0.4971	0.6047
25	1.81	0.0068	$m = 0.98$	0.3653	0.5119	0.5274
26	1.82	0.0063	$m = 0.95$	0.3586	0.8506	0.4323
27	1.78	0.0070	$m = 0.96$	0.3699	0.5638	0.7056
28	1.72	0.0069	$m = 0.94$	0.3604	0.9437	0.7280
29	1.82	0.0066	$m = 0.88$	0.3648	0.8545	0.4808
30	1.69	0.0070	$m = 0.85$	0.3739	0.4447	0.8495
31	1.87	0.0063	$m = 0.99$	0.3612	0.6354	0.5281
32	1.83	0.0063	$m = 0.97$	0.3539	0.9358	0.9717
33	1.81	0.0064	$m = 0.97$	0.3566	0.4883	0.8996
34	1.74	0.0062	$m = 0.91$	0.3420	0.6701	0.5504
35	1.8	0.0061	$m = 0.94$	0.3437	0.8836	0.5613
36	1.57	0.0068	$m = 0.76$	0.3455	0.5147	0.5011
37	1.8	0.0064	$m = 0.94$	0.3556	0.6563	0.6439
38	1.93	0.0056	$m = 1.06$	0.3494	0.6712	0.8136
39	2.07	0.0056	$m = 1.15$	0.3435	0.7179	0.6138
40	1.97	0.0054	$m = 1.08$	0.3386	0.9348	0.4479
41	1.86	0.0060	$m = 0.99$	0.3512	0.6076	0.5359
42	1.97	0.0054	$m = 1.09$	0.3331	0.5730	0.5371
43	1.85	0.0057	$m = 1$	0.3443	0.7096	0.3591
44	2	0.0054	$m = 1.12$	0.3348	0.8212	0.6271
45	1.85	0.0055	$m = 1$	0.3383	0.8930	0.5153
46	1.98	0.0056	$m = 1.1$	0.3366	0.8330	0.9147
47	1.96	0.0053	$m = 1.07$	0.3308	0.6704	0.6520
48	1.81	0.0060	$m = 0.98$	0.3443	0.5831	0.6442
49	1.84	0.0055	$m = 1$	0.3412	0.7045	0.9352
50	1.87	0.0057	$m = 1.03$	0.3385	0.6509	0.8808
51	1.92	0.0056	$m = 1.06$	0.3407	0.8367	0.8988
52	1.91	0.0054	$m = 1.05$	0.3275	0.7955	0.6597
53	2.02	0.0053	$m = 1.11$	0.3404	0.6477	0.8731
54	1.92	0.0053	$m = 1.05$	0.3312	0.6737	0.4121
55	2.05	0.0052	$m = 1.14$	0.3332	0.6642	0.6110
56	1.97	0.0050	$m = 1.11$	0.3291	0.4833	0.7194
57	1.96	0.4243	$m = 1.07$	0.3364	0.8154	0.3843

Figure 6.8 provides curve fits for the amplitudes of the 1st and 3rd taps for the [Large Airport, NLOS, 50] channel, similar to Figure 6.6 for the NLOS-S case.
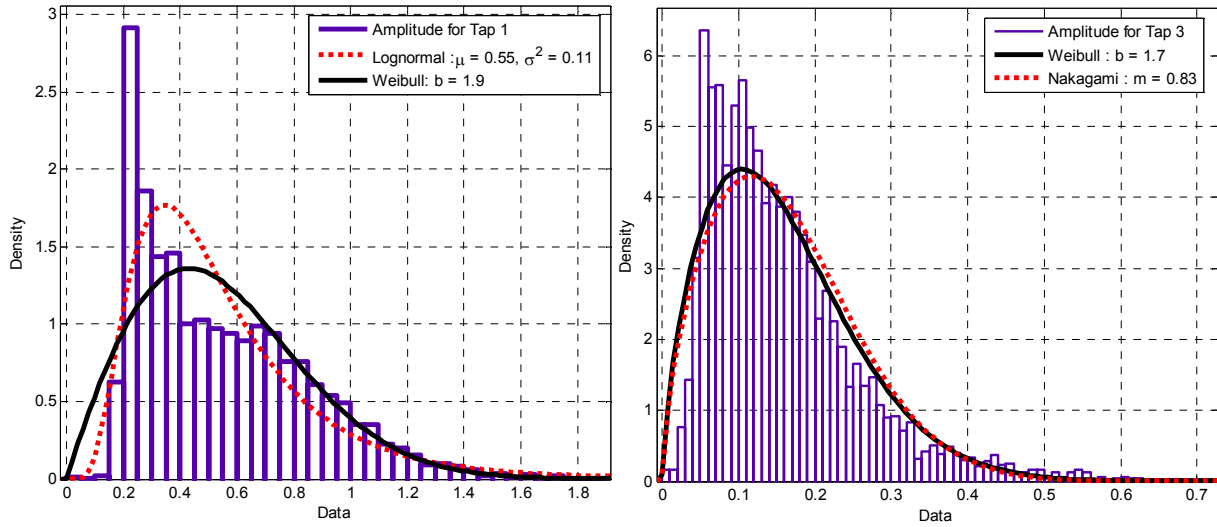
Figure 6.8. Amplitude statistics of taps 1 and 3 for [Large Airport, NLOS, 50].

Table 6.6 provides the Markov chain steady state and transition probabilities for all the taps in the NLOS case.

Table 6.6. Persistence process parameters for [Large Airport, NLOS, 50].

Tap Index	Steady State Probability for State 1	Steady State Probability for State 0	Transition Probability (P_{00})	Transition Probability (P_{01})	Transition Probability (P_{10})	Transition Probability (P_{11})
1	1.0000	0	n/a	n/a	0	1.0000
2	0.8408	0.1592	0.3569	0.6431	0.1218	0.8782
3	0.7449	0.2551	0.4259	0.5741	0.1965	0.8035
4	0.6422	0.3578	0.4942	0.5058	0.2819	0.7181
5	0.5383	0.4617	0.5710	0.4290	0.3677	0.6323
6	0.4980	0.5020	0.5951	0.4049	0.4084	0.5916
7	0.4664	0.5336	0.6217	0.3783	0.4329	0.5671
8	0.4490	0.5510	0.6435	0.3565	0.4378	0.5622
9	0.4255	0.5745	0.6642	0.3358	0.4534	0.5466
10	0.4301	0.5699	0.6646	0.3354	0.4446	0.5554
11	0.4002	0.5998	0.6889	0.3111	0.4665	0.5335
12	0.4010	0.5990	0.6827	0.3173	0.4737	0.5263
13	0.3951	0.6049	0.6963	0.3037	0.4646	0.5354
14	0.3953	0.6047	0.7001	0.2999	0.4590	0.5410

15	0.3799	0.6201	0.7268	0.2732	0.4459	0.5541
16	0.3972	0.6028	0.6942	0.3058	0.4640	0.5360
17	0.3897	0.6103	0.7063	0.2937	0.4601	0.5399
18	0.3932	0.6068	0.7011	0.2989	0.4614	0.5386
19	0.3763	0.6237	0.7078	0.2922	0.4846	0.5154
20	0.3894	0.6106	0.7163	0.2837	0.4445	0.5555
21	0.3642	0.6358	0.7184	0.2816	0.4915	0.5085
22	0.3675	0.6325	0.7128	0.2872	0.4942	0.5058
23	0.3734	0.6266	0.7063	0.2937	0.4928	0.5072
24	0.3748	0.6252	0.7209	0.2791	0.4653	0.5347
25	0.3653	0.6347	0.7195	0.2805	0.4872	0.5128
26	0.3586	0.6414	0.7193	0.2807	0.5018	0.4982
27	0.3699	0.6301	0.7170	0.2830	0.4820	0.5180
28	0.3604	0.6396	0.7295	0.2705	0.4799	0.5201
29	0.3648	0.6352	0.7321	0.2679	0.4667	0.5333
30	0.3739	0.6261	0.7220	0.2780	0.4654	0.5346
31	0.3612	0.6388	0.7320	0.2680	0.4738	0.5262
32	0.3539	0.6461	0.7365	0.2635	0.4809	0.5191
33	0.3566	0.6434	0.7300	0.2700	0.4871	0.5129
34	0.3420	0.6580	0.7522	0.2478	0.4765	0.5235
35	0.3437	0.6563	0.7540	0.2460	0.4695	0.5305
36	0.3455	0.6545	0.7453	0.2547	0.4823	0.5177
37	0.3556	0.6444	0.7410	0.2590	0.4692	0.5308
38	0.3494	0.6506	0.7454	0.2546	0.4739	0.5261
39	0.3435	0.6565	0.7460	0.2540	0.4852	0.5148
40	0.3386	0.6614	0.7549	0.2451	0.4787	0.5213
41	0.3512	0.6488	0.7484	0.2516	0.4647	0.5353
42	0.3331	0.6669	0.7576	0.2424	0.4852	0.5148
43	0.3443	0.6557	0.7418	0.2582	0.4915	0.5085
44	0.3348	0.6652	0.7501	0.2499	0.4964	0.5036
45	0.3383	0.6617	0.7488	0.2512	0.4911	0.5089
46	0.3366	0.6634	0.7516	0.2484	0.4896	0.5104
47	0.3308	0.6692	0.7591	0.2409	0.4870	0.5130
48	0.3443	0.6557	0.7462	0.2538	0.4832	0.5168
49	0.3412	0.6588	0.7479	0.2521	0.4867	0.5133
50	0.3385	0.6615	0.7518	0.2482	0.4850	0.5150
51	0.3407	0.6593	0.7534	0.2466	0.4772	0.5228
52	0.3275	0.6725	0.7615	0.2385	0.4896	0.5104
53	0.3404	0.6596	0.7520	0.2480	0.4804	0.5196
54	0.3312	0.6688	0.7550	0.2450	0.4947	0.5053
55	0.3332	0.6668	0.7471	0.2529	0.5060	0.4940
56	0.3291	0.6709	0.7621	0.2379	0.4848	0.5152
57	0.3364	0.6636	0.7492	0.2508	0.4946	0.5054

6.3.4 Summary of Sufficient Fidelity Models for Other Channel Bandwidths

Similar to the approach for modeling for the full 50 MHz BW, we have also provided models for other values of channel bandwidth (1, 5, 10 MHz). The details are given in Appendix D. Table 6.7 provides the number of taps in the channel models for different regions, BWs and airports. Note: for a specific value of BW, the number of taps used is the *maximum* value of the two (JFK and MIA) for the given airport region, e.g., for 50 MHz NLOS-S we use 8 taps, and for 10 MHz NLOS we use 14 taps.

Table 6.7. Number of taps for large airport channel model with different bandwidths (BW).

BW = 50 MHz		
Airport	**NLOS-S (99% energy)**	**NLOS (95% energy)**
MIA	8	57
JFK	5	43
BW = 10 MHz		
MIA	4	14
JFK	2	9
BW = 5 MHz		
MIA	3	8
JFK	2	6
BW = 1 MHz		
MIA	2	2
JFK	2	2

6.3.5 Justification for Airport Field Site (AFS) Transmission

On the airport surface, there are many areas where it is difficult to receive a strong signal from the ATCT due to local obstacles, that is, obstruction of the LOS and of many Fresnel zones. In this section, we illustrate the importance of using field site transmitters in an airport surface network, and then provide a channel model for the airport field site. Clearly, these field sites can be used as relays or access points by the mobile units, and by virtue of shorter distances, these sites can enable mobiles (planes, ground vehicles, pedestrians) to obtain a stronger signal than is possible from the ATCT. In addition to signal strength, channel dispersion, quantified by RMS-DS, is also of great interest in signal design and system performance. We note that the AFS transmitter covered only a certain section of the airport. For comparison we will use the data obtained from those same travel segments (same receiver locations) with data taken when the transmitter was the ATCT. Figure 6.9 compares the RMS-DS for these locations in MIA when transmitting from either the AFS or the ATCT.

In these sections where we compare the AFS channel and the ATCT channel over the same (subset of) airport areas, we refer to the ATCT channel for these areas as the "partial ATCT" channel, to distinguish these from the channel models developed for the total airport surface area. The partial ATCT channel is primarily of use for this comparison, and is not for actual models.
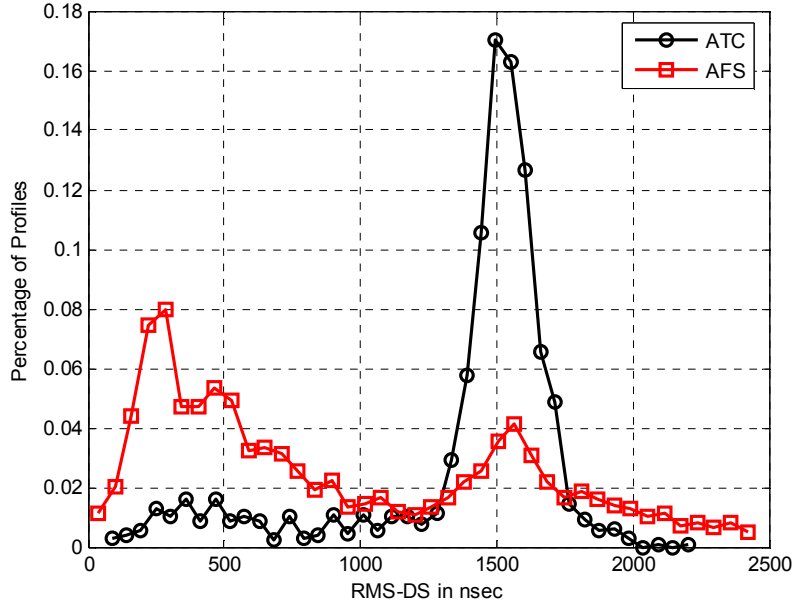
Figure 6.9. Distribution of RMS-DS over common receive areas, AFS and ATCT transmitters, MIA.

From Figure 6.9, we observe that most of the data collected using the AFS belongs to the NLOS-S category, whereas that for the ATCT in these same portions of the airport surface area belongs to the NLOS category (recall from Table 4.3 that the RMS-DS threshold for MIA is 1000 nsec). It is obvious that we are able to reduce the channel dispersion in the "difficult-to-reach" locations on the airport surface by transmitting from an AFS. Table 6.8 compares the RMS-DS statistics for both settings. As a single metric for comparison of these two settings—but *not* for use in actual channel modeling—we compute an "average number of taps," L_{avg}, calculated using the following formula:

L_{avg}=(% time in NLOS-S) × (L for NLOS-S) + (% time in NLOS) × (L for NLOS).

The number of taps L for each region was determined using the mean RMS-DS.

Table 6.8. RMS-DS statistics for common receiving areas, with AFS and ATCT transmission at MIA.

Region	% Profiles in NLOS-S	RMS-DS (nsec), NLOS-S [Min, Mean, Max]	% Profiles in NLOS-S	RMS-DS (nsec), NLOS [Min, Mean, Max]	Average Number of Taps L_{avg}
AFS	61	[8, 443, 997]	39	[1000, 1625, 2451]	47
ATCT	14	[60, 512, 996]	86	[1002, 1524, 2228]	71

From Table 6.8, we see that by virtue of the lower dispersion, use of an AFS can significantly reduce the complexity of the channel model. The reader may notice that the AFS results have a higher mean (and max) value of RMS-DS for the NLOS case; this is due to the low height of the

AFS antenna as compared to that of the ATCT. The fact that the AFS reduces the dispersion of the channel can also be demonstrated by comparing the FCEs of the AFS and partial ATCT channels. This is shown in Figure 6.10.
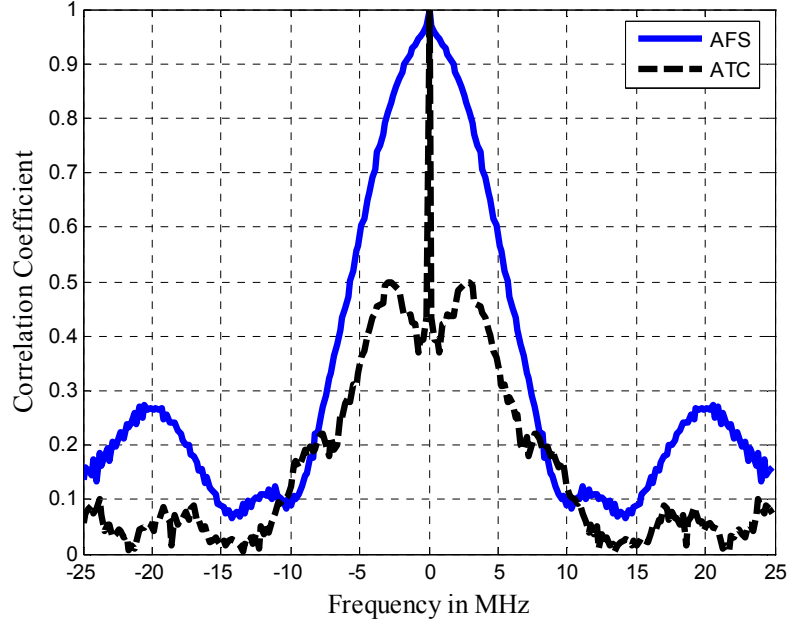
Figure 6.10. Comparing FCEs obtained with common receive areas, AFS and ATCT transmitters, MIA.

As before, to simplify the channel models, we reduce the number of taps from the value based upon mean RMS-DS by accounting for cumulative energy. Table 6.9 shows the cumulative energy with increasing numbers of taps for the NLOS and NLOS-S cases for AFS and ATCT transmissions. The average number of taps metric L_{avg} is again determined using the above mentioned formula and the largest percentage energy values for each region, e.g., for NLOS-S using the AFS we use 9 taps and 61%, and for NLOS using the AFS we use 56 taps and 39%.

Table 6.9. Cumulative energy for AFS and partial ATCT for NLOS-S, NLOS, 50 MHz BW.

Transmitting Site	Taps Required for Given % Energy, NLOS-S			Taps required for Given % Energy, NLOS					Average Number of Taps for Site,
	85	*96*	*99*	*60*	*70*	*80*	*85*	*95*	L_{avg}
AFS	3	6	9	1	3	9	20	56	27
ATCT	1	2	5	3	19	39	48	67	58

We can obtain similar comparisons for the AFS and partial ATCT channels at JFK. The reader can see these details in Appendix D.

6.3.6 Comparison of Sufficient Fidelity Model for AFS and ATCT for [MIA, NLOS-S, 50]

From Table 6.9, we obtain the number of taps for the AFS channel model for [MIA, NLOS-S, 50] as $L=9$. For the tap correlation matrix, we again use R_{wc}^{NLOS-S} to account for the worst case.

$$
\begin{bmatrix}
1 & 0.1006 & 0.3386 & 0.5372 & 0.3214 & 0.5746 & 0.3520 & 0.3802 & 0.4561 \\
0.1006 & 1 & 0.0988 & 0.5860 & 0.0916 & 0.7418 & 0.5554 & 0.0880 & 0.0849 \\
0.3386 & 0.0988 & 1 & 0.7839 & 0.5875 & 0.0981 & 0.5803 & 0.2346 & 0.4681 \\
0.5371 & 0.5860 & 0.7839 & 1 & 0.5971 & 0.6651 & 0.2568 & -0.0032 & 0.4402 \\
0.3214 & 0.0916 & 0.5875 & 0.5971 & 1 & 0.3441 & 0.3695 & 0.5799 & 0.5065 \\
0.5746 & 0.7418 & 0.0981 & 0.6651 & 0.3441 & 1 & 0.6098 & 0.2222 & 0.6555 \\
0.3520 & 0.5554 & 0.5803 & 0.2568 & 0.3695 & 0.6098 & 1 & 0.4238 & 0.5224 \\
0.3802 & 0.0880 & 0.2346 & -0.0032 & 0.5799 & 0.2222 & 0.4238 & 1 & 0.7985 \\
0.4561 & 0.0849 & 0.4681 & 0.4402 & 0.5065 & 0.6555 & 0.5224 & 0.7985 & 1
\end{bmatrix}
\quad (6.2)
$$

For the ATCT, in these common areas, the number of taps in the model is $L=5^{4}$. The R_{wc}^{NLOS} for ATCT is shown in (6.3). The amplitude statistics for the AFS channel model are in Table 6.10.

$$
\begin{bmatrix}
1 & 0.1498 & -0.115 & 0.0460 & -0.0367 \\
0.1498 & 1 & 0.2686 & 0.1391 & -0.2005 \\
-0.1105 & 0.2686 & 1 & 0.4321 & 0.0712 \\
0.0460 & 0.1391 & 0.4321 & 1 & 0.2281 \\
-0.0367 & -0.2005 & 0.0712 & 0.2281 & 1
\end{bmatrix}
\quad (6.3)
$$

Table 6.10 Amplitude statistics for AFS [MIA, NLOS-S, 50].

Tap Index	Weibull Shape Factor (b)	Tap Energy	Alternative Distribution Parameter
1	4.47	0.6662	$K = 9$dB
2	1.63	0.0801	$m = 0.76$
3	1.7	0.0221	$m = 0.85$
4	1.63	0.0393	$m = 0.79$
5	1.66	0.0620	$m = 0.75$
6	1.41	0.0567	$m = 0.6$
7	1.84	0.0115	$m = 1.01$
8	1.67	0.0062	$m = 0.87$
9	1.81	0.0050	$m = 1.03$

---

[4] Recall $L=8$ for the complete ATCT channel for [Large Airport, NLOS-S, 50] over the entire airport.

Figure 6.11 provides curve fits for tap amplitude distributions for the 1st, 2nd, 3rd, and 7th taps for the AFS channel for [MIA, NLOS-S, 50].
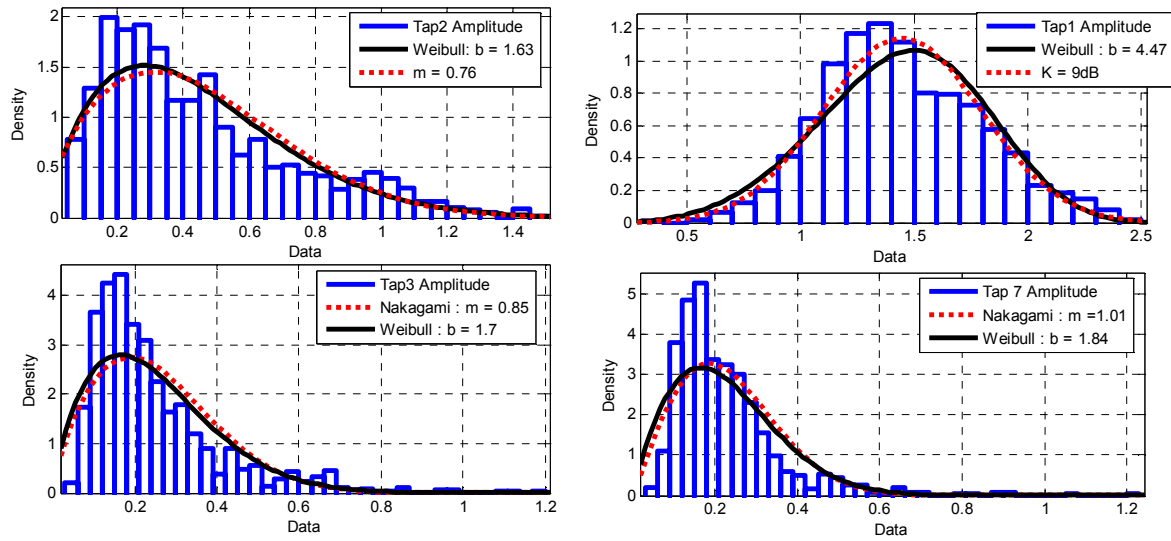
Figure 6.11. Amplitude statistics of taps 1, 2, 3, and 7 for AFS channel [MIA, NLOS-S, 50].

Amplitude statistics for the partial ATCT channel model for this subset of areas on the airport surface are listed in Table 6.11.

Table 6.11 Amplitude statistics for partial ATCT channel [MIA, NLOS-S, 50].

Tap Index	Weibull Shape Factor (b)	Tap Energy	Alternative Distribution Parameter
1	5.56	0.8076	$K = 10.4$ dB
2	1.92	0.1031	$m = 0.96$
3	2.04	0.0247	$m = 1.18$
4	2.2	0.0124	$m = 1.5$
5	2.5	0.0055	$m = 1.7$

Figure 6.12 provides example curve fits for the tap amplitude distributions of the 1st, 2nd, and 3rd taps for this partial ATCT channel for [MIA, NLOS-S, 50].
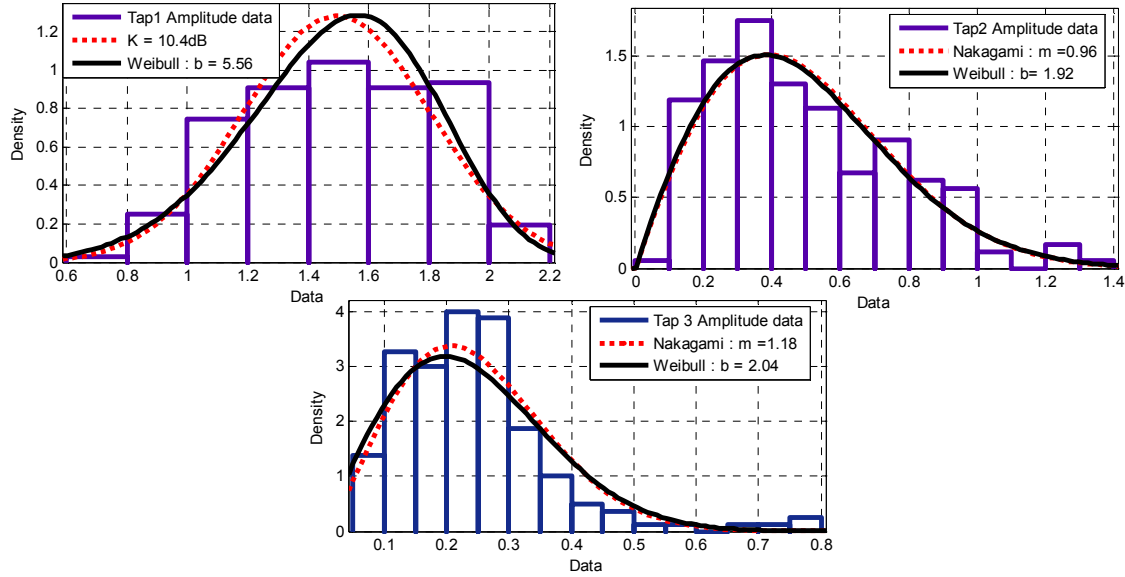
Figure 6.12. Amplitude statistics of taps 1, 2, and 3 for partial ATCT channel [MIA, NLOS-S, 50].

The Markov process associated with the persistence process for each tap in the AFS channel model is provided in Table 6.12

Table 6.12. Persistence process parameters for AFS [MIA, NLOS-S, 50].

Tap Index	Steady State Probability for State 1	Steady State Probability for State 0	Transition probability (P_{00})	Transition probability (P_{01})	Transition probability (P_{10})	Transition probability (P_{11})
1	1.0000	0	n/a	n/a	0	1.0000
2	0.9396	0.0604	0.1765	0.8235	0.0530	0.9470
3	0.8260	0.1740	0.3714	0.6286	0.1325	0.8675
4	0.8651	0.1349	0.2421	0.7579	0.1183	0.8817
5	0.7706	0.2294	0.5542	0.4458	0.1328	0.8672
6	0.6982	0.3018	0.5976	0.4024	0.1741	0.8259
7	0.5739	0.4261	0.6450	0.3550	0.2627	0.7373
8	0.4169	0.5831	0.7012	0.2988	0.4174	0.5826
9	0.3203	0.6797	0.7952	0.2048	0.4356	0.5644

A similar table for the Markov process parameters for the partial ATCT channel model is Table 6.13.

Table 6.13. Persistence process parameters for partial ATCT channel [MIA, NLOS-S, 50].

Tap Index	Steady State Probability for State 1	Steady State Probability for State 0	Transition probability (P_{00})	Transition probability (P_{01})	Transition probability (P_{10})	Transition probability (P_{11})
1	1.0000	0	n/a	n/a	0	1.0000
2	0.9725	0.0275	0	1.0000	0.0284	0.9716
3	0.8791	0.1209	0.2727	0.7273	0.0943	0.9057
4	0.6978	0.3022	0.3889	0.6111	0.2598	0.7402
5	0.3956	0.6044	0.6182	0.3818	0.5775	0.4225

6.3.7 Comparison of Sufficient Fidelity Model for AFS and ATCT [MIA, NLOS, 50]

As in the previous section for the NLOS-S region, in this section we describe the models for the two settings in the common NLOS regions. From Table 6.9, we obtain the number of taps for the AFS model for [MIA, NLOS, 50] as L=56. For the correlation matrix; we again use R_{wc}^{NLOS}. As before, since it is difficult to represent the entire matrix here, we provide only elements $r_{i,1}$ and $r_{i,2}$ in Table 6.14. Table 6.14 also provides the amplitude statistics for the taps in the channel model for AFS [MIA, NLOS, 50].

Table 6.14 Amplitude statistics for AFS channel [MIA, NLOS, 50].

Tap Index	Weibull Shape Factor (b)	Tap Energy	Alternative Distribution Parameter	$r_{i,1}$	$r_{i,2}$
1	2.12	0.4327	$m = 1.19$	1.0000	0.5653
2	1.49	0.0494	$m = 0.67$	0.5653	1.0000
3	1.87	0.0177	$m = 0.98$	0.5244	0.2365
4	1.76	0.0236	$m = 0.89$	0.5604	0.2835
5	1.47	0.0402	$m = 0.65$	0.5481	0.2257
6	1.5	0.0191	$m = 0.69$	0.6583	0.5275
7	1.85	0.0113	$m = 0.95$	0.5113	0.3071
8	1.8	0.0083	$m = 0.94$	0.3347	0.2830
9	1.75	0.0094	$m = 0.88$	0.4499	0.6156
10	1.69	0.0087	$m = 0.86$	0.2345	0.3421
11	1.75	0.0077	$m = 0.9$	0.4410	0.3169
12	1.88	0.0076	$m = 1.01$	0.4368	0.2759
13	1.85	0.0064	$m = 1.04$	0.3756	0.4274
14	2	0.0061	$m = 1.11$	0.3007	0.6227
15	1.8	0.0067	$m = 0.96$	0.5523	0.2629
16	1.77	0.0069	$m = 0.88$	0.4306	0.4300
17	1.42	0.0099	$m = 0.63$	0.4570	0.3189
18	1.67	0.0077	$m = 0.83$	0.2764	0.3025
19	1.51	0.0087	$m = 0.69$	0.3897	0.4496

20	1.85	0.0070	$m = 0.95$	0.3940	0.2092
21	1.98	0.0066	$m = 0.9$	0.3184	0.2945
22	1.78	0.0065	$m = 0.91$	0.3302	0.3802
23	1.59	0.0085	$m = 0.75$	0.3376	0.5315
24	1.74	0.0078	$m = 0.88$	0.3643	0.2130
25	1.67	0.0070	$m = 0.83$	0.4332	0.3025
26	1.82	0.0064	$m = 0.99$	0.2082	0.3200
27	1.9	0.0071	$m = 1.02$	0.2079	0.2048
28	1.88	0.0076	$m = 1.01$	0.1966	0.3833
29	1.89	0.0066	$m = 1$	0.4191	0.2866
30	1.93	0.0061	$m = 1.04$	0.2301	0.1438
31	1.92	0.0061	$m = 1.06$	0.2297	0.2094
32	1.94	0.0077	$m = 1.03$	0.3775	0.3259
33	1.98	0.0054	$m = 0.91$	0.4043	0.3568
34	1.74	0.0052	$m = 0.9$	0.1997	0.2253
35	1.86	0.0048	$m = 0.83$	0.5256	0.4784
36	2.35	0.0037	$m = 1.33$	0.3853	0.2546
37	1.86	0.0044	$m = 0.98$	0.4274	0.2010
38	2.01	0.0041	$m = 1.06$	0.4326	0.2275
39	2.04	0.0044	$m = 2.04$	0.5377	0.2442
40	1.95	0.0040	$m = 1.02$	0.4023	0.3008
41	2.15	0.0040	$m = 1.19$	0.4182	0.3539
42	2.11	0.0041	$m = 1.15$	0.3643	0.4102
43	2.02	0.0038	$m = 1.15$	0.5564	0.1002
44	2.13	0.0036	$m = 1.23$	0.2626	0.3012
45	1.74	0.0044	$m = 0.85$	0.3440	0.4132
46	1.74	0.0062	$m = 0.88$	0.3493	0.3708
47	1.77	0.0049	$m = 0.89$	0.5514	0.5975
48	1.7	0.0036	$m = 0.91$	0.3995	0.2183
49	1.97	0.0035	$m = 1.05$	0.3748	0.2180
50	1.92	0.0046	$m = 1.06$	0.2860	0.1852
51	1.38	0.0062	$m = 0.6$	0.7453	0.4194
52	1.54	0.0049	$m = 0.72$	0.4969	0.5661
53	1.62	0.0038	$m = 0.81$	0.5491	0.3261
54	1.75	0.0039	$m = 0.95$	0.2678	0.3190
55	1.7	0.0067	$m = 0.85$	0.4718	0.2918
56	1.48	0.0053	$m = 0.68$	0.4015	0.4866

Figure 6.13 provides curve fits for the amplitudes of the 1st, 2nd, 5th, and 23rd taps for the AFS channel model for [MIA, NLOS, 50].
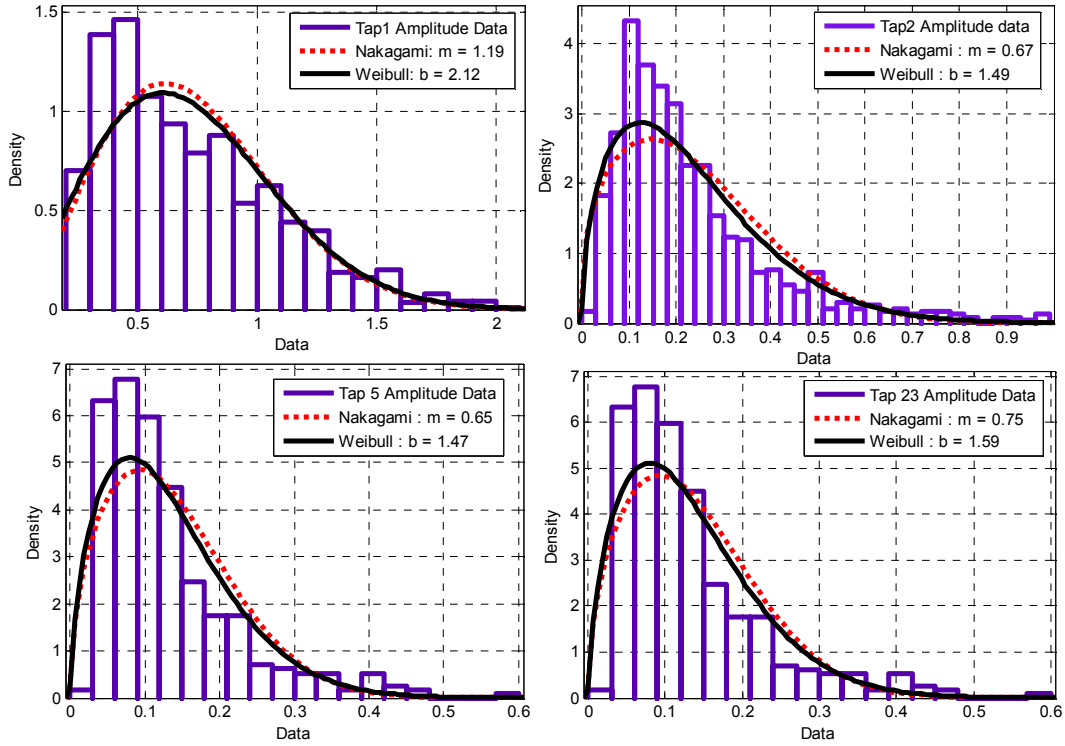
Figure 6.13. Amplitude fits for taps 1, 2, 5, and 23 for AFS channel [MIA, NLOS, 50].

From Table 6.9, in this case we obtain the number of taps for the partial ATCT model for the [MIA, NLOS, 50] setting as L=67 taps[5]. Again we use R_{wc}^{NLOS} for the correlation matrix, and provide only elements $r_{i,1}$ and $r_{i,2}$ in Table 6.15. This table also provides the amplitude statistics for the taps in the channel model for partial ATCT [MIA, NLOS, 50].

Table 6.15. Amplitude statistics for partial ATCT channel [MIA, NLOS, 50].

Tap Index	Weibull Shape Factor (b)	Tap Energy	Alternative Distribution Parameters (Lognormal or Nakagami)	$r_{i,1}$	$r_{i,2}$
1	1.95	0.3493	$(\mu,\sigma^2) = (0.47, 0.06)$	1.0000	0.5049
2	1.54	0.0521	$m = 0.7$	0.5049	1.0000
3	1.94	0.0193	$m = 1.04$	0.4404	0.2753
4	2.15	0.0131	$m = 1.18$	0.3669	0.4923
5	1.95	0.0097	$m = 1.04$	0.2010	0.2238

---

[5] Note here that in the NLOS case, for this partial ATCT channel, L is larger than the value of 57 found for the entire airport in the [Large Airport, NLOS, 50] case.

6	2.23	0.0089	$m = 1.29$	0.1701	0.1453
7	1.99	0.0081	$m = 1.09$	0.2063	0.1160
8	2.13	0.0095	$m = 1.18$	0.1831	0.0627
9	2.1	0.0084	$m = 1.15$	0.1368	0.1147
10	2.18	0.0088	$m = 1.23$	0.3417	0.2094
11	2.17	0.0078	$m = 1.21$	0.1559	0.2522
12	1.91	0.0088	$m = 1.04$	0.3351	0.0814
13	2	0.0081	$m = 1.12$	0.2928	0.1862
14	2	0.0076	$m = 1.12$	0.3955	0.3338
15	1.93	0.0080	$m = 1.04$	0.2649	0.1972
16	1.86	0.0085	$m = 1.02$	0.3416	0.3458
17	1.97	0.0086	$m = 1.06$	0.4025	0.1932
18	1.92	0.0092	$m = 1.06$	0.5537	0.3560
19	1.75	0.0092	$m = 0.89$	0.2634	0.2088
20	1.86	0.0084	$m = 0.99$	0.3590	0.2708
21	2.12	0.0072	$m = 1.17$	0.1995	0.2073
22	1.95	0.0079	$m = 1.09$	0.2031	0.3156
23	2.18	0.0070	$m = 1.21$	0.3308	0.1694
24	2.15	0.0069	$m = 1.19$	0.2051	0.1635
25	2.27	0.0072	$m = 1.33$	0.1721	0.1829
26	2.2	0.0067	$m = 1.24$	0.6066	0.2008
27	2.32	0.0062	$m = 1.33$	0.3862	0.2114
28	2.21	0.0070	$m = 1.25$	0.3876	0.4496
29	2.23	0.0070	$m = 1.25$	0.2491	0.3517
30	2.03	0.0075	$m = 1.1$	0.2236	0.2755
31	1.94	0.0079	$m = 1.06$	0.4354	0.1871
32	2.25	0.0072	$m = 1.27$	0.0941	0.0845
33	1.95	0.0074	$m = 1.07$	0.2306	0.0724
34	2.09	0.0070	$m = 1.17$	0.3079	0.2001
35	2.05	0.0069	$m = 1.13$	0.2669	0.0147
36	2.18	0.0070	$m = 1.21$	0.1224	0.2329
37	2.16	0.0069	$m = 1.18$	0.2835	0.1701
38	1.84	0.0084	$m = 1$	0.5437	0.1523
39	2.36	0.0076	$m = 1.36$	0.2384	0.2327
40	2.16	0.0079	$m = 1.19$	0.3301	0.2593
41	1.77	0.0093	$m = 0.93$	0.2614	0.1954
42	2.0	0.0079	$m = 1.1$	0.1953	0.1468
43	1.93	0.0086	$m = 1.05$	0.1315	0.1214
44	2.16	0.0071	$m = 1.24$	0.1396	0.0621
45	2.14	0.0079	$m = 1.18$	0.2715	0.2595
46	2.06	0.0079	$m = 1.15$	0.4425	0.4832
47	2.12	0.0067	$m = 1.22$	0.3190	0.1132
48	1.58	0.0099	$m = 0.77$	0.3506	0.0768
49	1.58	0.0094	$m = 0.72$	0.5167	0.1612
50	1.66	0.0096	$m = 0.84$	0.6509	0.1093

51	1.74	0.0072	$m = 0.94$	0.2855	0.0647
52	1.75	0.0092	$m = 0.95$	0.3338	0.3543
53	2.01	0.0081	$m = 1.11$	0.2392	0.0983
54	1.89	0.0081	$m = 1.03$	0.1923	0.1744
55	1.99	0.0074	$m = 1.12$	0.5653	0.6110
56	1.94	0.0073	$m = 1.11$	0.4833	0.4147
57	1.99	0.0072	$m = 1.14$	0.2668	0.2861
58	1.93	0.0070	$m = 1.12$	0.2255	0.1011
59	2.2	0.0068	$m = 1.23$	0.2684	0.2502
60	2.19	0.0075	$m = 1.2$	0.0902	0.0815
61	2.06	0.0073	$m = 1.17$	0.2268	0.2255
62	1.95	0.0073	$m = 1.07$	0.1335	0.2553
63	2.1	0.0075	$m = 1.17$	0.2827	0.1949
64	2.07	0.0070	$m = 1.21$	0.2169	0.2309
65	1.94	0.0072	$m = 1.06$	0.0069	0.2512
66	1.98	0.0069	$m = 1.10$	0.2279	-0.0638
67	1.93	0.0065	$m = 1.12$	0.1757	-0.0376

Figure 6.14 provides curve fits for the amplitudes of the 1st, 2nd, 19th, and 48th taps for the partial ATCT channel for the [MIA, NLOS, 50] setting.
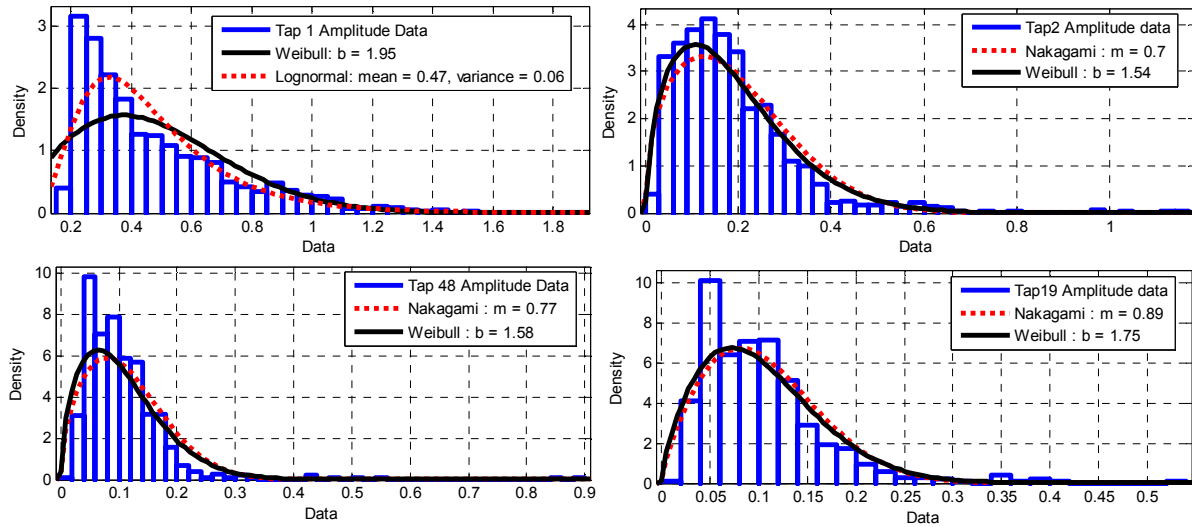
Figure 6.14. Amplitude statistics of taps 1, 2, 19 and 48 for partial ATCT channel [MIA, NLOS, 50].

The Markov process parameters associated with the persistence process for each tap in the AFS model are provided in Table 6.16.

Table 6.16. Persistence process parameters for AFS channel [MIA, NLOS, 50].

Tap Index	Steady State Probability for State 1	Steady State Probability for State 0	Transition probability (P_{00})	Transition probability (P_{01})	Transition probability (P_{10})	Transition probability (P_{11})
1	1.0000	0	n/a	n/a	0	1.0000
2	0.8636	0.1364	0.2581	0.7419	0.1173	0.8827
3	0.7613	0.2387	0.2995	0.7005	0.2200	0.7800
4	0.7327	0.2673	0.3416	0.6584	0.2406	0.7594
5	0.6810	0.3190	0.4690	0.5310	0.2492	0.7508
6	0.6161	0.3839	0.4900	0.5100	0.3184	0.6816
7	0.5237	0.4763	0.5612	0.4388	0.4000	0.6000
8	0.4972	0.5028	0.6039	0.3961	0.4013	0.5987
9	0.4631	0.5369	0.6078	0.3922	0.4537	0.5463
10	0.4521	0.5479	0.6767	0.3233	0.3927	0.6073
11	0.4268	0.5732	0.6846	0.3154	0.4253	0.5747
12	0.4466	0.5534	0.6793	0.3207	0.3990	0.6010
13	0.4048	0.5952	0.6852	0.3148	0.4647	0.5353
14	0.4136	0.5864	0.6811	0.3189	0.4533	0.5467
15	0.4026	0.5974	0.7109	0.2891	0.4301	0.5699
16	0.4433	0.5567	0.6818	0.3182	0.4005	0.5995
17	0.4345	0.5655	0.7043	0.2957	0.3858	0.6142
18	0.4213	0.5787	0.6882	0.3118	0.4293	0.5707
19	0.3916	0.6084	0.6975	0.3025	0.4719	0.5281
20	0.4268	0.5732	0.6865	0.3135	0.4227	0.5773
21	0.4136	0.5864	0.6842	0.3158	0.4495	0.5505
22	0.4114	0.5886	0.7191	0.2809	0.4037	0.5963
23	0.4169	0.5831	0.6673	0.3327	0.4670	0.5330
24	0.4070	0.5930	0.6877	0.3123	0.4568	0.5432
25	0.3872	0.6128	0.6984	0.3016	0.4786	0.5214
26	0.3927	0.6073	0.6987	0.3013	0.4678	0.5322
27	0.3949	0.6051	0.7195	0.2805	0.4318	0.5682
28	0.4180	0.5820	0.7216	0.2784	0.3895	0.6105
29	0.4037	0.5963	0.7190	0.2810	0.4169	0.5831
30	0.4004	0.5996	0.7132	0.2868	0.4313	0.5687
31	0.4081	0.5919	0.7300	0.2700	0.3935	0.6065
32	0.4026	0.5974	0.7072	0.2928	0.4356	0.5644
33	0.3762	0.6238	0.7266	0.2734	0.4516	0.5484
34	0.3784	0.6216	0.7465	0.2535	0.4157	0.5843
35	0.3509	0.6491	0.7419	0.2581	0.4796	0.5204
36	0.3333	0.6667	0.7388	0.2612	0.5248	0.4752
37	0.3421	0.6579	0.7605	0.2395	0.4630	0.5370

38	0.3355	0.6645	0.7297	0.2703	0.5377	0.4623
39	0.3234	0.6766	0.7427	0.2573	0.5408	0.4592
40	0.3201	0.6799	0.7553	0.2447	0.5223	0.4777
41	0.3223	0.6777	0.7740	0.2260	0.4778	0.5222
42	0.3069	0.6931	0.8076	0.1924	0.4373	0.5627
43	0.3234	0.6766	0.7752	0.2248	0.4728	0.5272
44	0.3377	0.6623	0.7671	0.2329	0.4593	0.5407
45	0.3322	0.6678	0.7607	0.2393	0.4801	0.5199
46	0.3674	0.6326	0.7509	0.2491	0.4281	0.5719
47	0.3245	0.6755	0.7765	0.2235	0.4678	0.5322
48	0.3102	0.6898	0.7875	0.2125	0.4752	0.5248
49	0.3113	0.6887	0.7904	0.2096	0.4629	0.5371
50	0.3421	0.6579	0.7521	0.2479	0.4791	0.5209
51	0.3465	0.6535	0.7656	0.2344	0.4444	0.5556
52	0.3190	0.6810	0.7654	0.2346	0.5034	0.4966
53	0.2915	0.7085	0.7900	0.2100	0.5132	0.4868
54	0.3014	0.6986	0.7918	0.2082	0.4854	0.5146
55	0.3102	0.6898	0.7843	0.2157	0.4823	0.5177
56	0.3157	0.6843	0.7874	0.2126	0.4599	0.5401

The Markov chain model parameters associated with the persistence processes for each tap in the partial ATCT model are provided in Table 6.17.

Table 6.17. Persistence process for partial ATCT channel [MIA, NLOS, 50].

Tap Index	Steady State Probability for State 1	Steady State Probability for State 0	Transition probability (P_{00})	Transition probability (P_{01})	Transition probability (P_{10})	Transition probability (P_{11})
1	1.0000	0	n/a	n/a	0	1.0000
2	0.8386	0.1614	0.3222	0.6778	0.1306	0.8694
3	0.7139	0.2861	0.4357	0.5643	0.2252	0.7748
4	0.6395	0.3605	0.5149	0.4851	0.2739	0.7261
5	0.5525	0.4475	0.5562	0.4438	0.3588	0.6412
6	0.5193	0.4807	0.5439	0.4561	0.4231	0.5769
7	0.5103	0.4897	0.5982	0.4018	0.3866	0.6134
8	0.4987	0.5013	0.5832	0.4168	0.4198	0.5802
9	0.5013	0.4987	0.5730	0.4270	0.4258	0.5742
10	0.4888	0.5112	0.6116	0.3884	0.4055	0.5945
11	0.4753	0.5247	0.5959	0.4041	0.4472	0.5528
12	0.4753	0.5247	0.6045	0.3955	0.4377	0.5623
13	0.4906	0.5094	0.5785	0.4215	0.4369	0.5631
14	0.4709	0.5291	0.6017	0.3983	0.4466	0.5534
15	0.4664	0.5336	0.6178	0.3822	0.4365	0.5635

16	0.4861	0.5139	0.6066	0.3934	0.4170	0.5830
17	0.4915	0.5085	0.6343	0.3657	0.3777	0.6223
18	0.5094	0.4906	0.5923	0.4077	0.3915	0.6085
19	0.4682	0.5318	0.5963	0.4037	0.4579	0.5421
20	0.4789	0.5211	0.6103	0.3897	0.4232	0.5768
21	0.4691	0.5309	0.6091	0.3909	0.4417	0.5583
22	0.4834	0.5166	0.6094	0.3906	0.4164	0.5836
23	0.4556	0.5444	0.6106	0.3894	0.4646	0.5354
24	0.4350	0.5650	0.6407	0.3593	0.4660	0.5340
25	0.4547	0.5453	0.6293	0.3707	0.4438	0.5562
26	0.4332	0.5668	0.6260	0.3740	0.4907	0.5093
27	0.4484	0.5516	0.6319	0.3681	0.4520	0.5480
28	0.4493	0.5507	0.6281	0.3719	0.4551	0.5449
29	0.4753	0.5247	0.6045	0.3955	0.4358	0.5642
30	0.4565	0.5435	0.6518	0.3482	0.4134	0.5866
31	0.4422	0.5578	0.6634	0.3366	0.4239	0.5761
32	0.4547	0.5453	0.6161	0.3839	0.4596	0.5404
33	0.4439	0.5561	0.6220	0.3780	0.4727	0.5273
34	0.4368	0.5632	0.6576	0.3424	0.4403	0.5597
35	0.4278	0.5722	0.6771	0.3229	0.4307	0.5693
36	0.4430	0.5570	0.6280	0.3720	0.4665	0.5335
37	0.4691	0.5309	0.6351	0.3649	0.4138	0.5862
38	0.4646	0.5354	0.6633	0.3367	0.3868	0.6132
39	0.4628	0.5372	0.6137	0.3863	0.4477	0.5523
40	0.4789	0.5211	0.6282	0.3718	0.4034	0.5966
41	0.4753	0.5247	0.6513	0.3487	0.3837	0.6163
42	0.4439	0.5561	0.6365	0.3635	0.4566	0.5434
43	0.4960	0.5040	0.6275	0.3725	0.3779	0.6221
44	0.4601	0.5399	0.6329	0.3671	0.4297	0.5703
45	0.4753	0.5247	0.5908	0.4092	0.4509	0.5491
46	0.4816	0.5184	0.6031	0.3969	0.4264	0.5736
47	0.4493	0.5507	0.6401	0.3599	0.4400	0.5600
48	0.4646	0.5354	0.6449	0.3551	0.4081	0.5919
49	0.4691	0.5309	0.6132	0.3868	0.4368	0.5632
50	0.4601	0.5399	0.6312	0.3688	0.4316	0.5684
51	0.4610	0.5390	0.6356	0.3644	0.4269	0.5731
52	0.4798	0.5202	0.6190	0.3810	0.4139	0.5861
53	0.4646	0.5354	0.6007	0.3993	0.4595	0.5405
54	0.4726	0.5274	0.6116	0.3884	0.4326	0.5674
55	0.4493	0.5507	0.6450	0.3550	0.4340	0.5660
56	0.4511	0.5489	0.6209	0.3791	0.4602	0.5398
57	0.4395	0.5605	0.6256	0.3744	0.4765	0.5235
58	0.4413	0.5587	0.6356	0.3644	0.4603	0.5397
59	0.4422	0.5578	0.6479	0.3521	0.4431	0.5569
60	0.4664	0.5336	0.6118	0.3882	0.4432	0.5568

61	0.4655	0.5345	0.6252	0.3748	0.4297	0.5703
62	0.4511	0.5489	0.6514	0.3486	0.4235	0.5765
63	0.4475	0.5525	0.6211	0.3789	0.4669	0.5331
64	0.4610	0.5390	0.6240	0.3760	0.4386	0.5614
65	0.4574	0.5426	0.6109	0.3891	0.4608	0.5392
66	0.4359	0.5641	0.6439	0.3561	0.4598	0.5402
67	0.4502	0.5498	0.6324	0.3676	0.4482	0.5518

Table 6.18 provides a summary comparison of the 10 MHz models developed for the AFS and partial ATCT channels for MIA.

Table 6.18. Number of taps for AFS and partial ATCT models for [MIA, 10].

Airport	NLOS-S (99% energy) [AFS, ATCT]	NLOS (95% energy) [AFS, ATCT]
MIA	[4, 2]	[15, 15]

Similar channel models were also developed from the AFS measurements made at JFK. These models are provided in Appendix D. For these measurements, the AFS regions at which we measured did not overlap with any of the ATCT measurements, so no direct comparison between the two settings can be made. The JFK AFS measurements do though provide additional data for modeling the AFS channel.

6.4 Medium Airport Channel Models

We performed the medium airport measurement campaign at CLE, which is among the 50 busiest airports in the USA. As discussed in Chapter 4, CLE is smaller than MIA and JFK in terms of the size of aircraft, the density of traffic (planes and ground vehicles) and the building structures on and near the airport property. In CLE, we also covered the LOS-O region. The characteristics of the LOS-O region are the presence of a dominant LOS component and the absence of large reflectors/scatterers in the local vicinity of the receiver. Hence the channel model for the LOS-O region should remain the same irrespective of the airport size: that is, the channel model presented here for LOS-O can be used for the large airports as well.

6.4.1 Representative Channel Parameters for Medium Airports

Figure 6.15 shows the RMS-DS distribution for CLE. Table 4.4 has the associated RMS-DS statistics for CLE. The multi-modal nature of the RMS-DS distribution illustrates the presence of multiple regions on the airport.
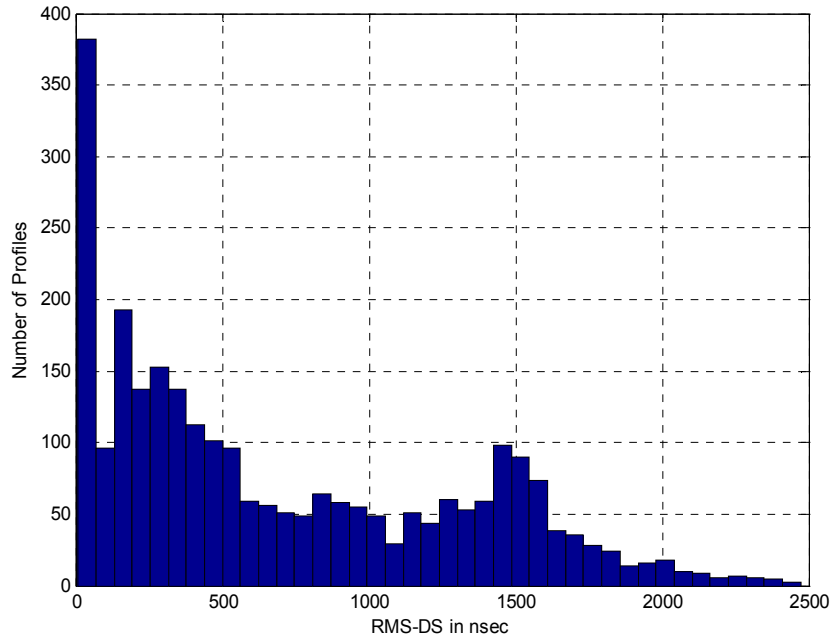
Figure 6.15. RMS-DS distribution for CLE.

Figure 6.16 shows the steady state probabilities of state 1 versus tap index for CLE. As expected, the reduction of probability with an increase in tap index is faster for the less dispersive regions (LOS-O and NLOS-S) than it is for the most dispersive region (NLOS).
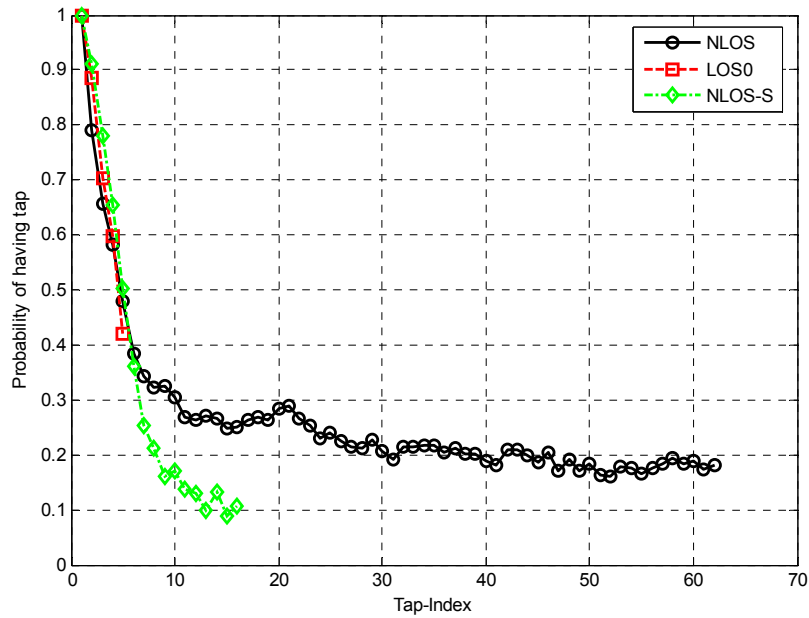
Figure 6.16. Steady state probability of state 1 versus tap index for [CLE, 50].

Figure 6.17 compares the cumulative energy as a function of the number of taps for the different airport regions at CLE. The rate of increase in the cumulative energy is highest for the least dispersive LOS-O region, as expected (approximately 97% of the energy is gathered with only two taps).
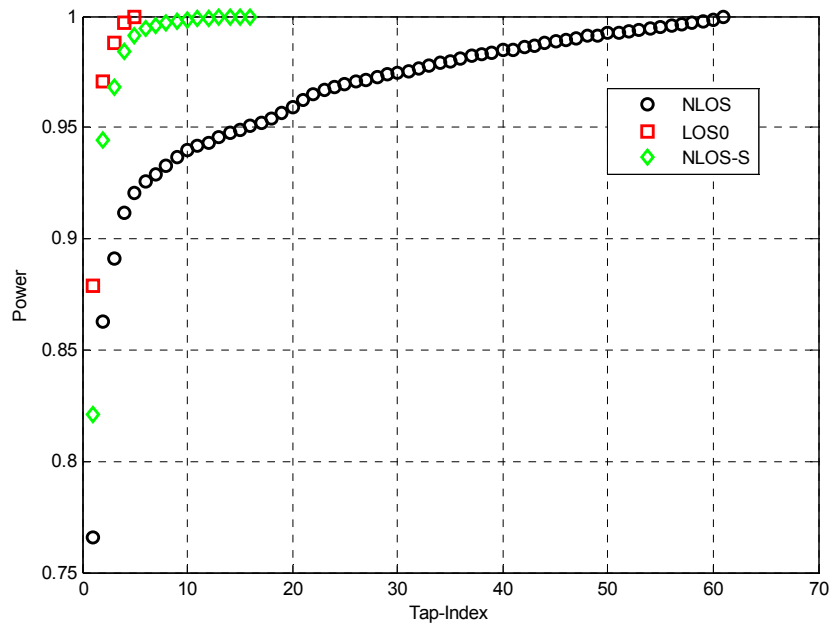
Figure 6.17. Cumulative energy versus tap index for [CLE, 50].

Figure 6.18 compares the FCEs for the different regions at CLE. The width of the main lobe is inversely proportional to the channel dispersion. The FCEs for LOS-O and NLOS-S are similar due to the similarity in their RMS-DSs. The width of the NLOS FCE is much narrower than the others.
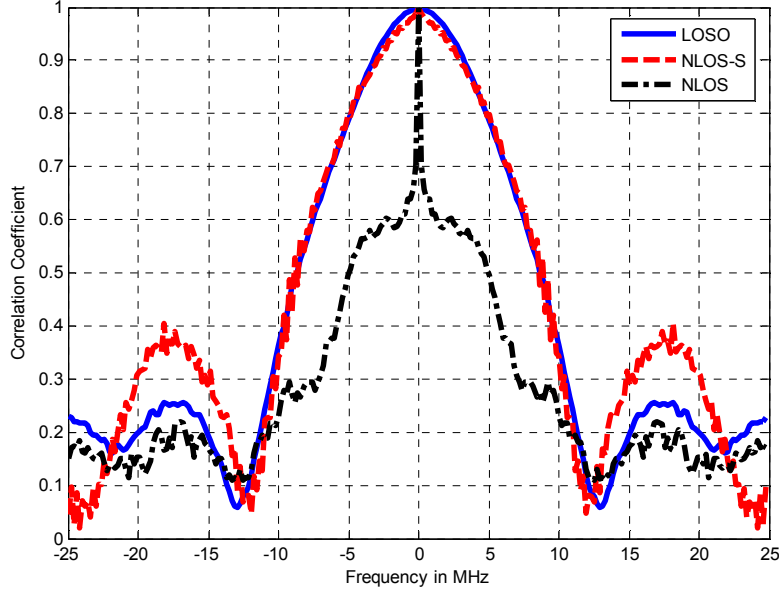
Figure 6.18. FCEs for [CLE, 50].

6.4.2 Sufficient Fidelity Model for [Medium Airports, LOS-O, 50]

Since we use the mean RMS-DS to determine the number of taps, using Table 4.3, we determine the number of taps for the LOS-O model as L=5. For the LOS-O region, we use the first 3 taps, which contain 98% of the energy. For the correlation matrix, we use R_{wc}^{LOS-O}.

$$\begin{bmatrix} 1 & 0.9734 & 0.9992 \\ 0.9734 & 1 & 0.9538 \\ 0.9992 & 0.9538 & 1 \end{bmatrix} \tag{6.4}$$

As can be observed from (6.4), the elements in R_{wc}^{LOS-O} are very close to 1. As described before, for LOS-O regions, there are not many mobile reflectors nor many large scatterers nearby, and hence all the taps emanate from stable reflections, and are hence highly correlated. The number of profiles used to determine the values of the correlation matrix in (6.4) are as follows:

$$\begin{bmatrix} 1 & 6 & 8 \\ 6 & 1 & 8 \\ 8 & 8 & 1 \end{bmatrix} \tag{6.5}$$

Table 6.19 provides the channel model parameters for the LOS-O region.

Table 6.19. Amplitude statistics for [Medium Airport, LOS-O, 50].

Tap Index	Weibull Shape Factor (*b*)	Tap Energy	Alternative Distribution Parameter
1	7.53	0.8539	$K = 13$ dB
2	1.65	0.1003	$m = 0.75$
3	1.91	0.0246	$m = 1.05$

Figure 6.19 provides curve fits for the amplitudes of the 1st and 2nd taps for the [Medium Airport, LOS-O, 50] model.

Figure 6.19. Amplitude statistics of taps 1 and 2 for [Medium Airport, LOS-O, 50].

Table 6.20 provides the steady state and the transition probabilities for all the taps required for the persistence processes of this model.

Table 6.20. Persistence process parameters for [Medium Airport, LOS-O, 50].

Tap Index	Steady State Probability for State 1	Steady State Probability for State 0	Transition probability (P_{00})	Transition probability (P_{01})	Transition probability (P_{10})	Transition probability (P_{11})
1	1.0000	0	n/a	n/a	0	1.0000
2	0.8851	0.1149	0.1778	0.8222	0.1065	0.8935
3	0.7023	0.2977	0.3739	0.6261	0.2649	0.7351

6.4.3 Sufficient Fidelity Model for [Medium Airports, NLOS-S, 50]

Using Table 4.3, the number of taps for the NLOS-S model is 16. Table 6.21 shows the cumulative energy versus tap index. As before we reduce this number, and consider the number of taps $L=5$, which accounts for ~99.1% of the energy. (This again pertains to option (2b) from Table 5.9.)

Table 6.21. Cumulative energy for [Medium Airport, NLOS-S, 50].

Tap Index	Cumulative Energy (%)
2	94.4
4	98.4
5	99.1
12	99.9

For the correlation matrix, R_{wc}^{NLOS-S} is as follows:

$$\begin{bmatrix} 1 & 0.8976 & 0.9924 & 0.9931 & 0.9725 \\ 0.8976 & 1 & 0.9379 & 0.9518 & 0.6381 \\ 0.9924 & 0.9379 & 1 & 0.9945 & 0.9763 \\ 0.9931 & 0.9518 & 0.9945 & 1 & 0.7920 \\ 0.9725 & 0.6381 & 0.9763 & 0.7920 & 1 \end{bmatrix} \tag{6.6}$$

The numbers of profiles used to determine the correlation matrix of (6.6) are given in (6.7).

$$\begin{bmatrix} 1 & 18 & 27 & 14 & 56 \\ 18 & 1 & 32 & 74 & 8 \\ 27 & 32 & 1 & 17 & 47 \\ 14 & 74 & 17 & 1 & 44 \\ 56 & 8 & 47 & 44 & 1 \end{bmatrix} \tag{6.7}$$

Table 6.22 provides the amplitude statistics for the taps in this channel model, and Figure 6.20 provides curve fits for th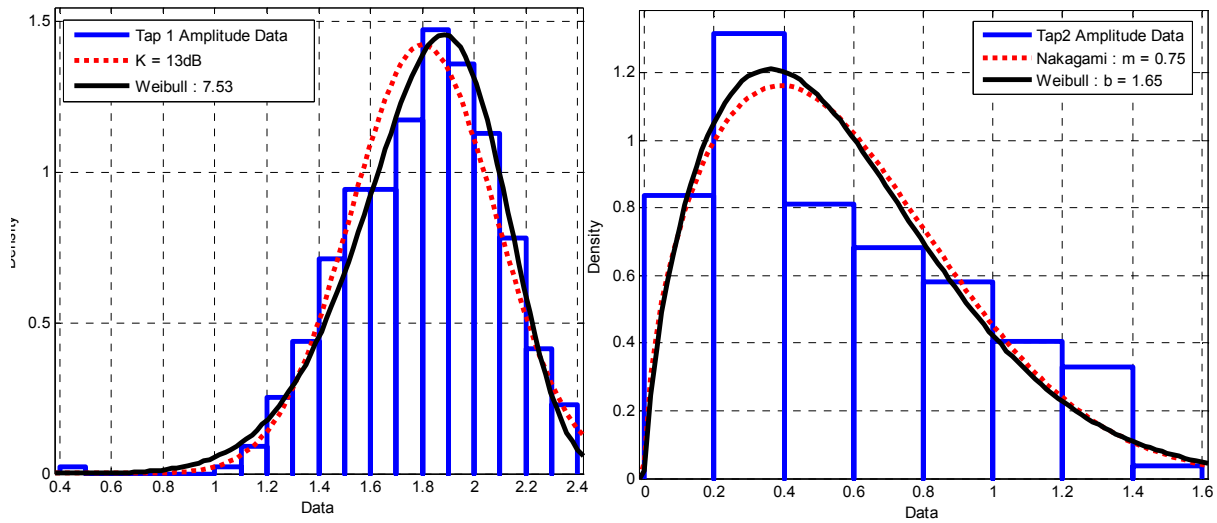e amplitudes of the 1st and 2nd taps for [Medium Airport, NLOS-S, 50]. Table 6.23 provides the steady state and the transition probabilities for all the taps.

Table 6.22. Amplitude statistics for [Medium Airport, NLOS-S, 50].

Tap Index	Weibull Shape Factor (b)	Tap Energy	Alternative Distribution Parameter
1	4.77	0.7692	$K = 9.5$ dB
2	0.82	0.1271	$m = 0.82$
3	0.94	0.0288	$m = 0.94$
4	0.96	0.0229	$m = 0.96$
5	0.91	0.0133	$m = 0.91$
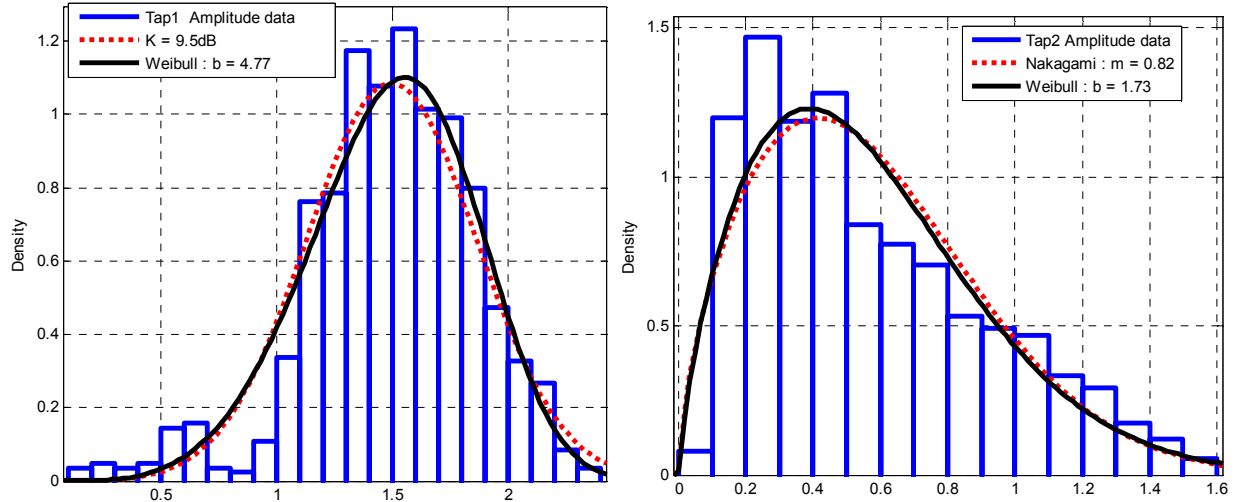
Figure 6.20. Amplitude statistics of taps 1 and 2 for [Medium Airport, NLOS-S, 50].

Table 6.23. Persistence process parameters for [Medium Airport, NLOS-S, 50].

Tap Index	Steady State Probability for State 1	Steady State Probability for State 0	Transition probability (P_{00})	Transition probability (P_{01})	Transition probability (P_{10})	Transition probability (P_{11})
1	1.0000	0	n/a	n/a	0	1.0000
2	0.9115	0.0885	0.1940	0.8060	0.0784	0.9216
3	0.7794	0.2206	0.2635	0.7365	0.2088	0.7912
4	0.6539	0.3461	0.4351	0.5649	0.2976	0.7024
5	0.5020	0.4980	0.6037	0.3963	0.3921	0.6079

6.4.4 Sufficient Fidelity Model for [Medium Airports, NLOS, 50]

Using Table 4.3, for the NLOS model we obtain 62 taps! Reducing this number via the cumulative energy criterion, Table 6.24 shows the cumulative energy for this NLOS case. Here

we select a threshold of 95% of the energy and obtain *L*=15 taps. (Again this pertains to option (2b) from Table 5.9.)

Table 6.24. Cumulative energy for [Medium Airport, NLOS, 50].

Tap Index	Cumulative Energy (%)
3	89.1
5	92.1
10	94
15	95
20	96
30	97.5
40	98.5
47	99

For the correlation matrix, R_{wc}^{NLOS} would be a (15×15) matrix for our 15 tap channel. Because of this size, we show only two elements in Table 6.24, along with the amplitude statistics for the taps in the channel model.

Table 6.25. Amplitude statistics for [Medium Airport, NLOS, 50].

Tap Index	Weibull Shape Factor (*b*)	Tap Energy	Alternative Distribution Parameter	$r_{i,1}$	$r_{i,2}$
1	1.64	0.5848	$m = 0.72$	1.0000	0.8976
2	1.45	0.0934	$m = 0.61$	0.8976	1.0000
3	1.44	0.0334	$m = 0.64$	0.9924	0.9379
4	1.48	0.0263	$m = 0.63$	0.9931	0.9518
5	1.49	0.0151	$m = 0.64$	0.9725	0.6381
6	1.52	0.0095	$m = 0.66$	0.9659	0.8455
7	1.51	0.0081	$m = 0.64$	0.8467	0.4487
8	1.52	0.0084	$m = 0.64$	0.5247	0.5560
9	1.43	0.0091	$m = 0.6$	0.5643	0.4301
10	1.45	0.0080	$m = 0.61$	0.7600	0.6832
11	1.49	0.0057	$m = 0.63$	0.7056	0.6116
12	1.52	0.0044	$m = 0.64$	0.8717	0.7162
13	1.57	0.0062	$m = 0.67$	0.8125	0.7534
14	1.53	0.0058	$m = 0.64$	0.8486	0.9272
15	1.46	0.0049	$m = 0.6$	0.8917	0.8098

Figure 6.21 provides curve fits for amplitudes of the 1st, 2nd, 10th, and 11th taps for the [Medium Airport, NLOS, 50] channel model. Note that all of these taps exhibit "worse than Rayleigh"

fading, with the Nakagami-*m* parameter *m*<1, or the Weibull "*b*" parameter less than two. Table 6.26 provides the steady state and the transition probabilities for all the taps in this model.
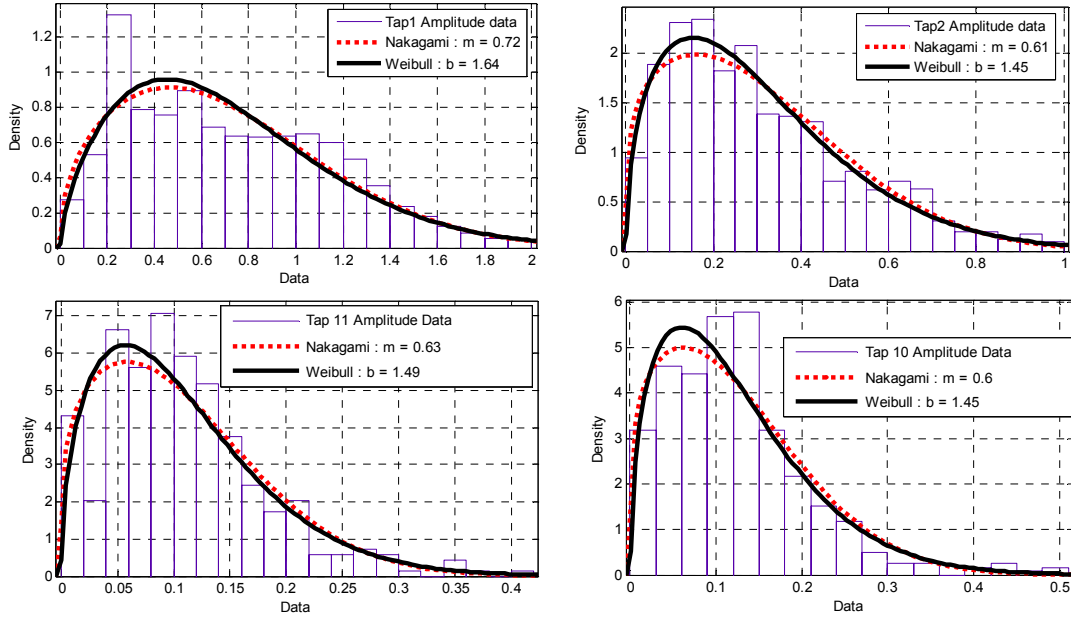
Figure 6.21. Amplitude statistics of taps 1, 2, 10, and 11 for [Medium Airport, NLOS, 50].

Table 6.26. Persistence process parameters for [Medium Airport, NLOS, 50].

Tap Index	Steady State Probability for State 1	Steady State Probability for State 0	Transition probability (P_{00})	Transition probability (P_{01})	Transition probability (P_{10})	Transition probability (P_{11})
1	1.0000	0	n/a	n/a	0	1.0000
2	0.7916	0.2084	0.4195	0.5805	0.1530	0.8470
3	0.6565	0.3435	0.5818	0.4182	0.2179	0.7821
4	0.5816	0.4184	0.5933	0.4067	0.2917	0.7083
5	0.4793	0.5207	0.6306	0.3694	0.4023	0.5977
6	0.3833	0.6167	0.6831	0.3169	0.5112	0.4888
7	0.3427	0.6573	0.7194	0.2806	0.5399	0.4601
8	0.3232	0.6768	0.7575	0.2425	0.5072	0.4928
9	0.3263	0.6737	0.7541	0.2459	0.5096	0.4904
10	0.3044	0.6956	0.7393	0.2607	0.5949	0.4051
11	0.2693	0.7307	0.7959	0.2041	0.5523	0.4477
12	0.2639	0.7361	0.7890	0.2110	0.5905	0.4095
13	0.2717	0.7283	0.7985	0.2015	0.5418	0.4582
14	0.2662	0.7338	0.7830	0.2170	0.5971	0.4029
15	0.2475	0.7525	0.8060	0.1940	0.5918	0.4082

6.4.5 Summary of Sufficient Fidelity Models for Other Bandwidths

Similar to the what we have provided above, we also provide models for other bandwidths (1, 5, 10 MHz) in Appendix D. Table 6.27 provides the number of taps in the channel models for the different airport regions and bandwidths. For the LOS-O region, the channel model has only 2 taps for these smaller bandwidths.

Table 6.27. Number of taps for Medium Airport channel model with different bandwidths.

BW = 10 MHz		
Airport	NLOS-S (99% energy)	NLOS (95% energy)
CLE	2	8
BW = 5 MHz		
CLE	2	5
BW = 1 MHz		
CLE	2	2

6.5 Small Airport Channel Models

We performed measurement campaigns at BL, TA, and OU GA airports to obtain data for developing models for small (GA) airports. Tamiami is actually one of the largest GAs in the USA. At Tamiami, due to staffing limitations and some other restrictions, we could not use the small ATCT as our transmission site. Instead we mounted our transmitter platform on the level roof of a small shed near an ILS site. The transmit antenna height was thus only about 5-6 meters. This limited transmitting antenna height prevented us from receiving a sufficiently strong signal at certain parts on the airport surface. The models that we developed for TA (Appendix D) can be considered as worst case channel models for GAs, where we might not have an antenna mounted at the ATCT or are for some reason unable to use it for transmission. The BL and OU airports are similar with respect to airport layout, traffic density (planes and ground vehicles), heights of ATCTs, and channel statistics. Our small airport channel models are based primarily on the data collected at BL. As noted in Chapter 4, in GA airports, we usually don't have a large percentage of NLOS regions, and most of the airport can be classified either as LOS-O or NLOS-S. Refer to Table 4.2 for statistics on the number of profiles collected in each region at the different GA airports.

6.5.1 Representative Channel Parameters for Small Airports

Figure 6.22 shows the RMS-DS distribution for BL; Table 4.4 has the corresponding RMS-DS statistics for BL. As in all the other cases, the RMS-DS distribution indicates multiple distinct airport regions.
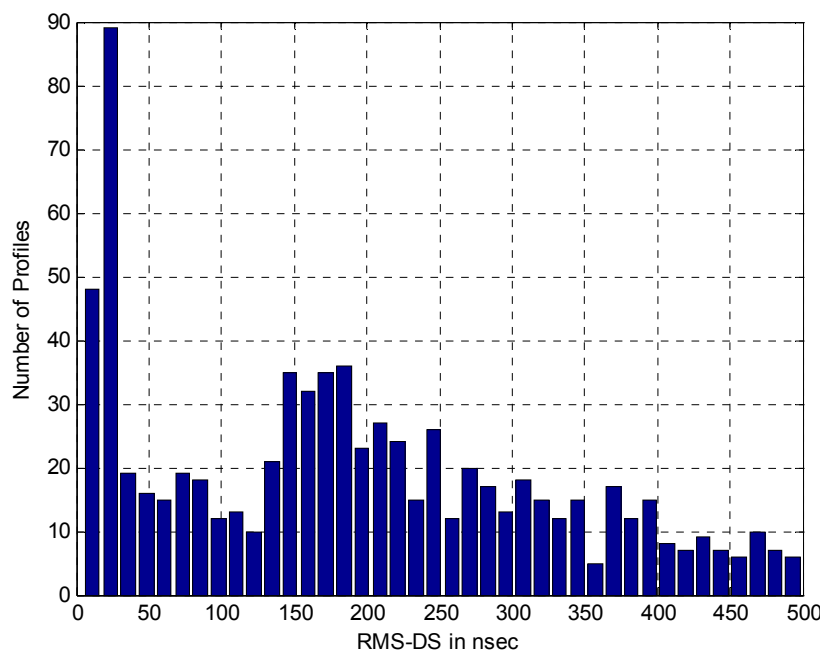
Figure 6.22. RMS-DS distribution for BL.

Figure 6.23 shows the steady state probability of state 1 for BL. In general, the behavior is similar to that seen for other airports. Figure 6.24 compares the cumulative energy vs. tap index for the different regions at BL. The trends again follow those shown for the larger airports, as expected. Figure 6.25 compares the FCEs for the two different BL channel regions.
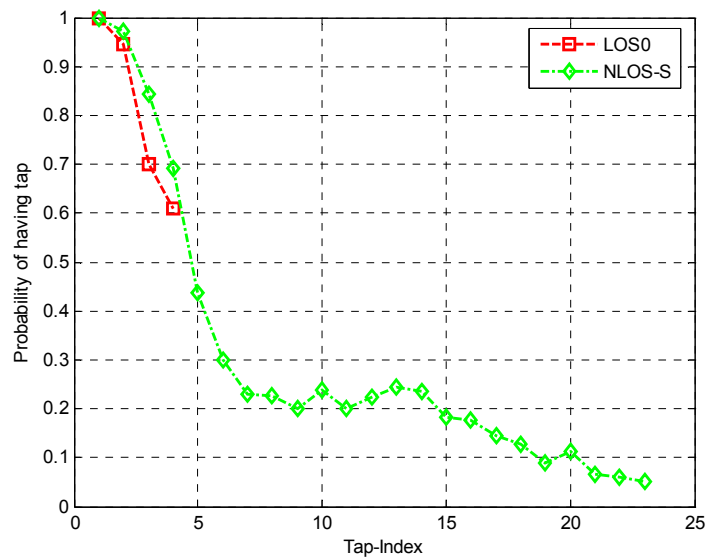
Figure 6.23. Steady state probability of state 1 for [BL, 50]
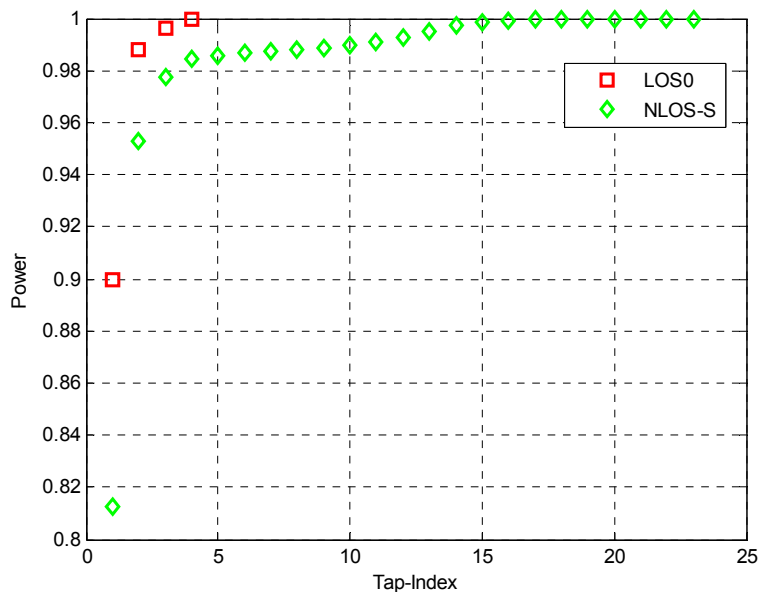
Figure 6.24. Cumulative energy vs. tap index for [BL, 50].
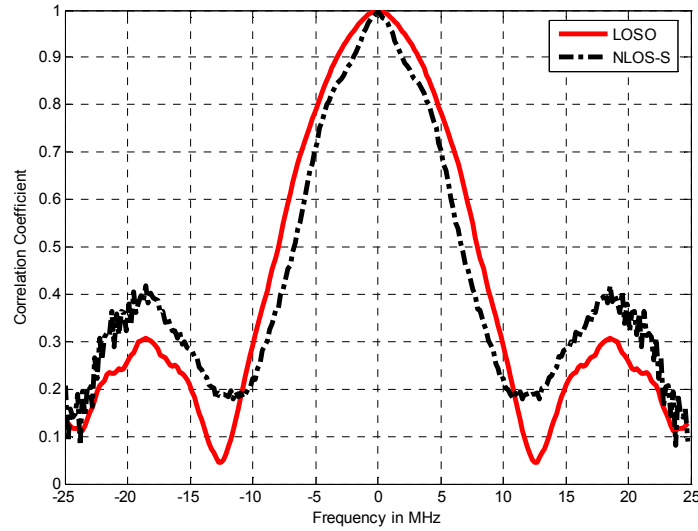
Figure 6.25. FCE for [BL, 50].

6.5.2 Sufficient Fidelity Model for [Small Airports, LOS-O, 50]

Using the mean RMS-DS to determine the number of taps, Table 4.3 enables us to specify L=4 for the LOS-O model. For our small airport LOS-O case, we consider only 2 taps for our channel model, which account for 98% of the cumulative energy. For the correlation matrix, R_{wc}^{LOS-O} is as follows:

$$\begin{bmatrix} 1 & 0.0312 \\ 0.0312 & 1 \end{bmatrix} \tag{6.8}$$

Table 6.28 provides the channel model data for the GA LOS-O region.

Table 6.28. Amplitude statistics for [Small Airport, LOS-O, 50].

Tap Index	Weibull Shape Factor (b)	Tap Energy	Alternative Distribution Parameter
1	10.1	0.8900	$K = 14.5$ dB
2	1.87	0.0921	$m = 0.93$

Figure 6.26 provides curve fits for the tap amplitudes of the 1st and 2nd taps for data obtained for the [Small Airport, LOS-O, 50] channel.

151

Figure 6.26. Amplitude statistics of taps 1 and 2 for [Small Airport, LOS-O, 50].

Table 6.29 provides the steady state and the transition probabilities for the two taps.

Table 6.29 Persistence process parameters for [Small Airport, LOS-O, 50].

Tap Index	Steady State Probability for State 1	Steady State Probability for State 0	Transition probability (P_{00})	Transition probability (P_{01})	Transition probability (P_{10})	Transition probability (P_{11})
1	1.0000	0	n/a	n/a	0	1.0000
2	0.9453	0.0547	0.1429	0.8571	0.0498	0.9502

6.5.3 Sufficient Fidelity Model for [Small Airport, NLOS-S, 50]

For this region at the small airports, via use of Table 4.3, we determine the number of taps for the NLOS-S model as 23. Table 6.30 shows the cumulative energy accretion with tap index for this case. We use here $L=10$ taps, and thus account for ~99% of the energy.

Table 6.30. Cumulative energy for [Small Airport, NLOS-S, 50].

Tap Index	Cumulative Energy (%)
2	95.3
4	98.4
10	99
15	99.8
23	1

The R_{wc}^U tap correlation matrix for this case is shown next, followed by Table 6.31, which provides the amplitude statistics for [Small Airport, NLOS-S, 50].

$$
\begin{bmatrix}
1 & -0.0419 & 0.0249 & -0.0710 & 0.3393 & 0.5048 & 0.8583 & 0.8270 & 0.0168 & 0.6043 \\
-0.0419 & 1 & 0.1904 & 0.4993 & 0.0989 & 0.0218 & 0.0665 & -0.0565 & -0.1870 & 0.1977 \\
0.0249 & 0.1904 & 1 & 0.4205 & 0.3469 & -0.0490 & -0.0341 & -0.0301 & -0.1726 & -0.0714 \\
-0.0710 & 0.4993 & 0.4025 & 1 & 0.0956 & 0.1393 & 0.0016 & -0.0554 & -0.0329 & 0.2003 \\
0.3393 & 0.0989 & 0.3469 & 0.0956 & 1 & 0.6944 & 0.1765 & 0.8924 & 0.1197 & 0.2007 \\
0.5048 & 0.0218 & -0.0490 & 0.1393 & 0.6944 & 1 & 0.8334 & 0.8873 & 0.6678 & 0.4322 \\
0.8583 & 0.0665 & -0.0341 & 0.0016 & 0.1765 & 0.8334 & 1 & 0.9282 & 0.8527 & 0.7094 \\
0.8270 & -0.0565 & -0.0301 & 0.0554 & 0.8924 & 0.8873 & 0.9282 & 1 & 0.8619 & 0.4099 \\
0.0168 & -0.1870 & -0.1726 & -0.0329 & 0.1197 & 0.6678 & 0.8527 & 0.8619 & 1 & 0.5558 \\
0.6043 & 0.1977 & -0.0714 & 0.2003 & 0.2007 & 0.4322 & 0.7094 & 0.4099 & 0.5558 & 1
\end{bmatrix}
\tag{6.9}
$$

Table 6.31. Amplitude statistics for [Small Airport, NLOS-S, 50].

Tap Index	Weibull Shape Factor (b)	Tap Energy	Alternative Distribution Parameters
1	7.12	0.7612	$K = 12.5$ dB
2	1.75	0.1353	$m = 0.83$
3	1.91	0.0272	$m = 1.05$
4	2.45	0.0095	$m = 1.68$
5	2.84	0.0031	$m = 2.36$
6	2.78	0.0027	$m = 2.12$
7	2.38	0.0032	$m = 1.54$
8	1.97	0.0031	$m = 1.1$
9	2.37	0.0031	$m = 1.46$
10	3.14	0.0027	$m = 2.56$

Figure 6.27 provides curve fits for the tap amplitudes of the 1st, 2nd, 5th, and 10th taps of this [Small Airport, NLOS-S, 50] channel.
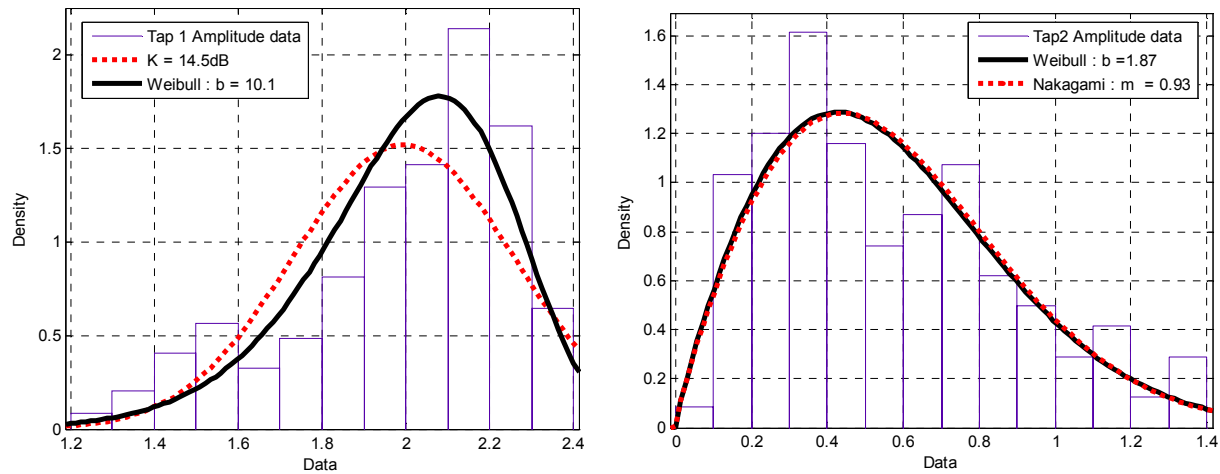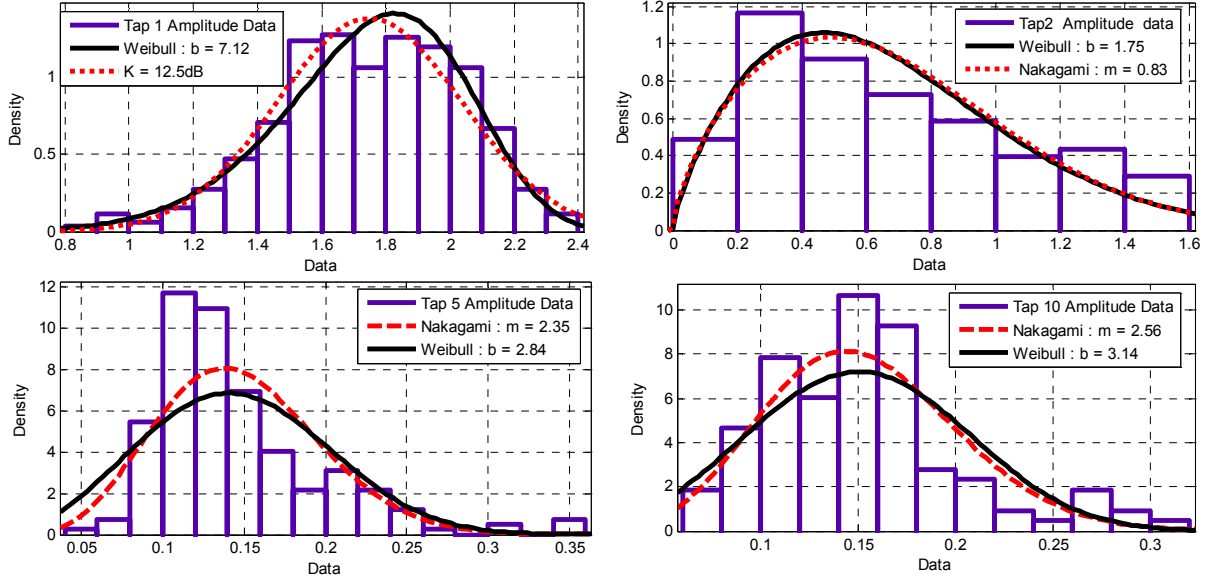
Figure 6.27. Amplitude statistics of taps 1, 2, 5, and 10 for [Small Airport, NLOS-S, 50].

Table 6.32 provides the steady state and the transition probabilities for the persistence model for all the model taps.

Table 6.32. Persistence process parameters for [Small Airport, NLOS-S, 50].

Tap Index	Steady State Probability for State 1	Steady State Probability for State 0	Transition probability (P_{00})	Transition probability (P_{01})	Transition probability (P_{10})	Transition probability (P_{11})
1	1.0000	0	n/a	n/a	0	1.0000
2	0.9709	0.0291	0	1.0000	0.0301	0.9699
3	0.8436	0.1564	0.2647	0.7353	0.1366	0.8634
4	0.6917	0.3083	0.3930	0.6070	0.2711	0.7289
5	0.4371	0.5629	0.6475	0.3525	0.4526	0.5474
6	0.2991	0.7009	0.7768	0.2232	0.5206	0.4794
7	0.2285	0.7715	0.8426	0.1574	0.5302	0.4698
8	0.2255	0.7745	0.8614	0.1386	0.4726	0.5274
9	0.1994	0.8006	0.8985	0.1015	0.4031	0.5969
10	0.2393	0.7607	0.8609	0.1391	0.4387	0.5613

6.5.5 Summary of Sufficient Fidelity Models for Other Bandwidths

As for the models for other airport sizes, we also provide GA channel models for other bandwidths (1, 5, 10 MHz) in Appendix D. Table 6.33 provides the numbers of taps in the channel models for the different regions and bandwidths. For LOS-O, all channel models have only a *single* tap for the smaller bandwidths (1, 5, 10 MHz). The largest numbers are used for the channel model for that particular bandwidth, e.g., 10 taps for NLOS-S and 50 MHz. Note

154

that Tamiami should not be considered for developing NLOS-S models due to its small transmitter height, unless GA deployment will actually use a similar, low value of antenna height. For completeness we have also provided the number of taps required for NLOS models, when available (TA only). As discussed previously, it is somewhat unlikely that one will encounter many NLOS regions at normal GA airports. An NLOS model (using Tamiami data) is provided in Appendix D for generating such a worst case scenario.

Table 6.33. Number of taps for small airport channel models with different bandwidths.

Airport	NLOS-S (99% energy)	NLOS (90% energy)	LOS-O (100% energy)
BW = 50 MHz			
BL	10	n/a	2
OU	8	n/a	n/a
TA	5	36	n/a
BW = 10 MHz			
BL	2	n/a	2
OU	2	n/a	n/a
TA	2	10	n/a
BW = 5 MHz			
BL	2	n/a	2
OU	2	n/a	n/a
TA	2	6	n/a
BW = 1 MHz			
BL	2	n/a	2
OU	2	n/a	n/a
TA	2	2	n/a

6.6 Channel Model for Fixed Point-to-Point Links

We collected data for fixed point-to-point links at CLE and at MIA. The purpose of these measurements was to collect RSSI and PDP data for several fixed locations, both "on boresight," and as a function of azimuth angle, for eventual use in evaluating communication schemes for such fixed links. Table 6.34 provides some information regarding the measurement locations.

Table 6.34. Fixed point-point measurement locations.

Airport	Location Name	Salient Features
CLE	Radar Site	• Good LOS condition, with two small buildings behind Rx van • 0 degrees: no observable multipath on Rx display • 90 degrees: strong multipath, possibly from a building reflection • 180 degrees: Rx main beam pointing directly *away* from, Tx so possible back lobe reception. Second multipath peak (larger delay) of greater strength than first peak • 270 degrees: Two nearly equal-strength peaks on Rx display. Likely reflection from the *IX Center*
CLE	Sensor Location (at point 16 of Figure 12)	• Good LOS location, one medium sized building NW of Rx van • 0 degrees: no observable multipath on Rx display • 90 degrees: 2 distinct peaks • 180 degrees: very low signal level, no significant reflections discernible • 270 degrees: small amount of observable multipath
CLE	RTR Site	• RTR site north of airport across Brookpark Road, adjacent to some NASA Glenn buildings • Clear LOS, with small buildings ~ 10 m behind Rx van • 0 degrees: no observable multipath on Rx display • 90 degrees: very small multipath • 180 degrees: several peaks observable, likely some from the small buildings in the main Rx lobe • 270 degrees: 2 strong multipath peaks, possibly due to Rx main lobe pointing toward large NASA hangar to SW
MIA	P1	• "GEM" site, very clear LOS, with no buildings within 100 m • Measurements at 24 azimuth angles, separated by 15° • See Figure 4.23
MIA	ILS (P2)	• ILS Site near American Airlines hangar (see Figure 4.23.) • Measurements at 24 azimuth angles, separated by 15° • "Blast fence" at approximately 150° azimuth from bore sight

For all the point-to-point channels, $L=1$, except for the first site at MIA (P1, or "GEM"), which had $L=2$, with the second tap in that case well modeled as Ricean with $K=19$ dB, with energy 5.6 dB down from that of the first tap. This pertains only to the 50 MHz case; for all locations and all smaller values of bandwidth, $L=1$.

To illustrate the orientation of the antennas for the fixed point-to-point locations at CLE, we provide Figure 6.28. This figure is similar to Figure 4.23, which shows the point-to-point measurement locations at MIA.
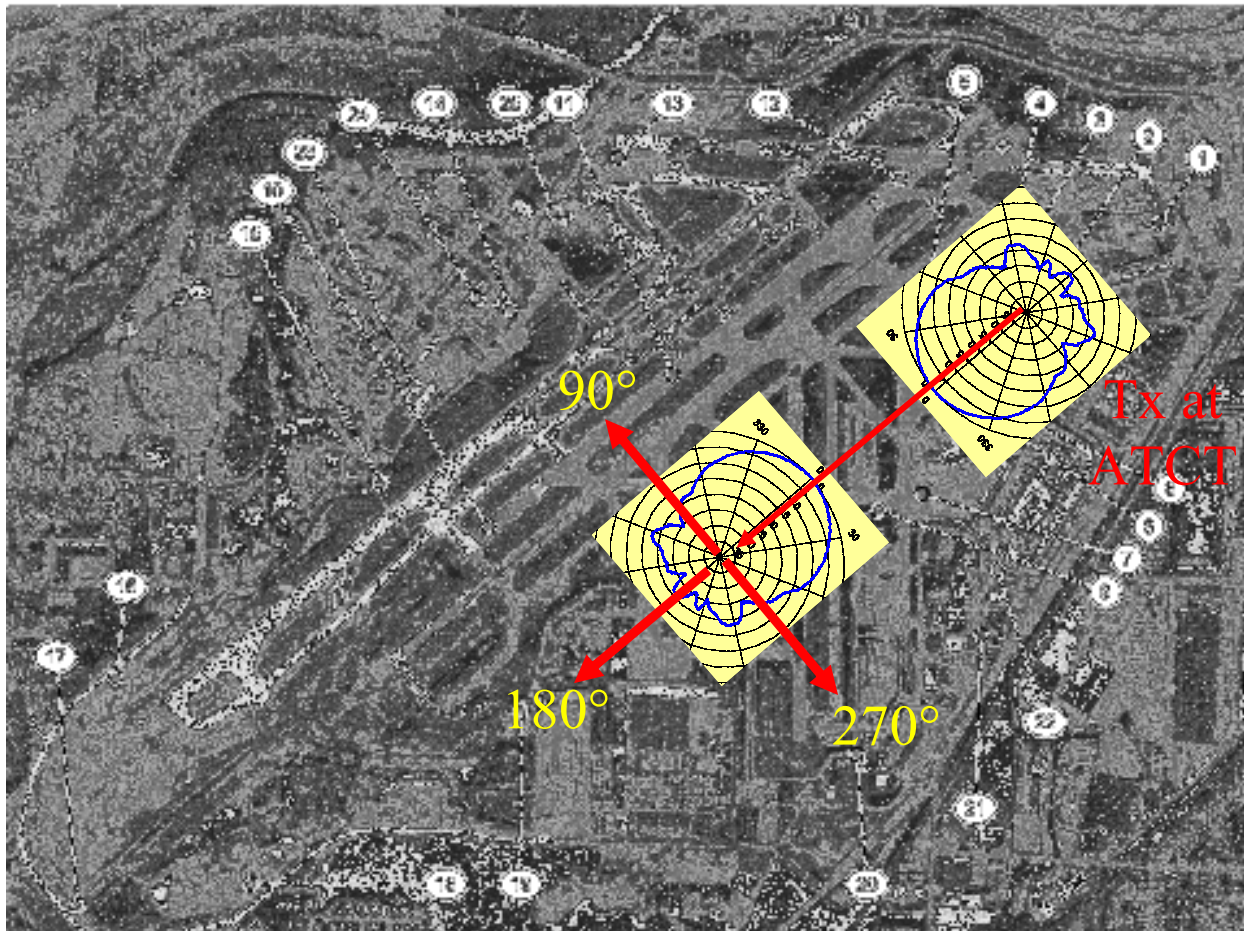
Figure 6.28. Antenna orientations at CLE fixed point-to-point locations.

6.6.1 CLE Point-to-Point Measurement Summary

Figure 6.29 is an example measurement picture from CLE. The figure shows the fixed point-to-point measurement location at the radar site.
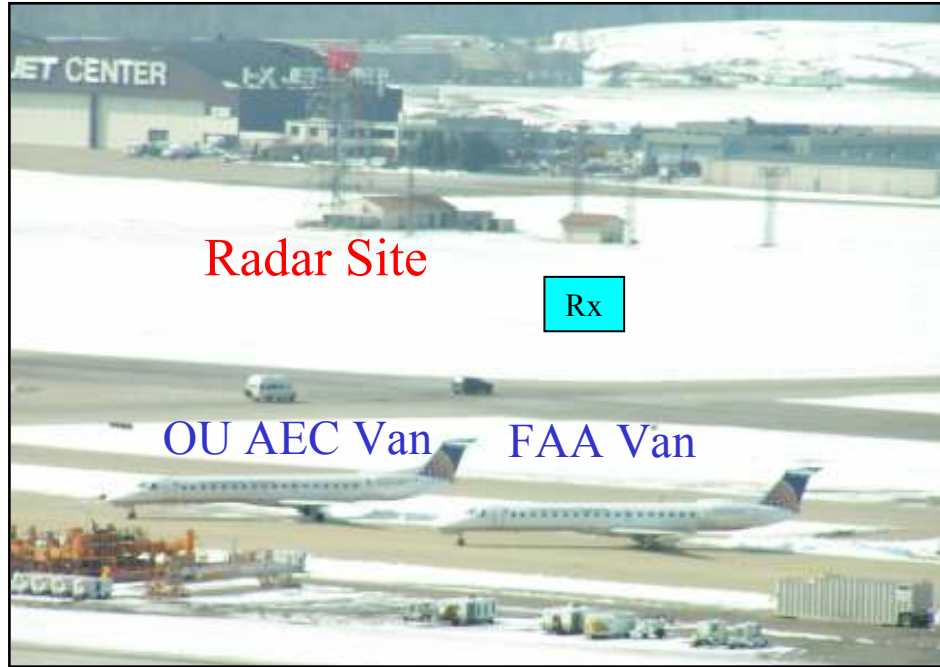
Figure 6.29. Radar measurement site at CLE.

Table 6.35 shows the RMS-DS for the fixed point-to-point locations at CLE, for four azimuth angles. With directional antennas, even the maximum RMS-DS is not very large (312 nanosec).

Table 6.35. RMS-DS for fixed point-to-point locations at CLE.

Location (link distance)	RMS Delay Spread (nanoseconds) for Four Azimuth Angle Orientations of Receive Antenna (0° is boresight)			
	0°	*90°*	*180°*	*270°*
1 (1.4 km)	31.8	101	70	273
2 (3.3 km)	48.2	101	170	312
3 (1.3 km)	40	294	239	146

Figure 6.30 provides the FCEs for all three locations, and also the aggregate (average) FCE. The broad main lobe of the FCE is an indication of small channel dispersion for the fixed point-to-point links.
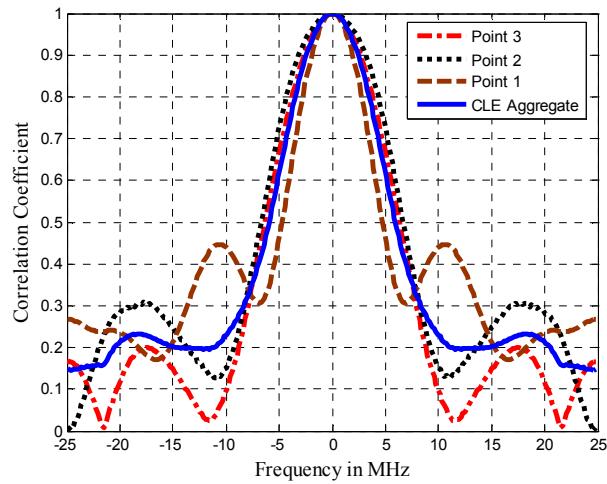
Figure 6.30. FCEs for CLE fixed point-to-point links.

The channel model for a fixed point-to-point link generally consists of a strong specular component which has a *very high* Ricean "K factor." The reasons for this are the lack of mobility and the use of high gain directional antennas for our measurements. Table 6.36 shows the Ricean K factors for the first taps of the channel models, for the boresight direction, at the CLE sites, for different channel bandwidths. All the CLE point-to-point channels have L=1.

Table 6.36 First tap channel Ricean K-factors at CLE for different locations and bandwidths.

Location	K factors (dB) for Different Channel Bandwidths (MHz)	
	50	**10**
P1	15	14
P2	14.1	12
P3	15	14

6.6.2 MIA Point-to-Point Measurement Summary

Figure 6.31 shows the power distribution versus azimuth angle for the two locations (P1 and P2) at MIA. Notice that for P2, the RSSI collected at angle 150° is greater than that at boresight, by approximately 2 dB. As mentioned in Table 6.34, there is a large blast fence at approximately that angle. Reflection of energy from that fence increases the amount of scattered energy collected at the receiver.
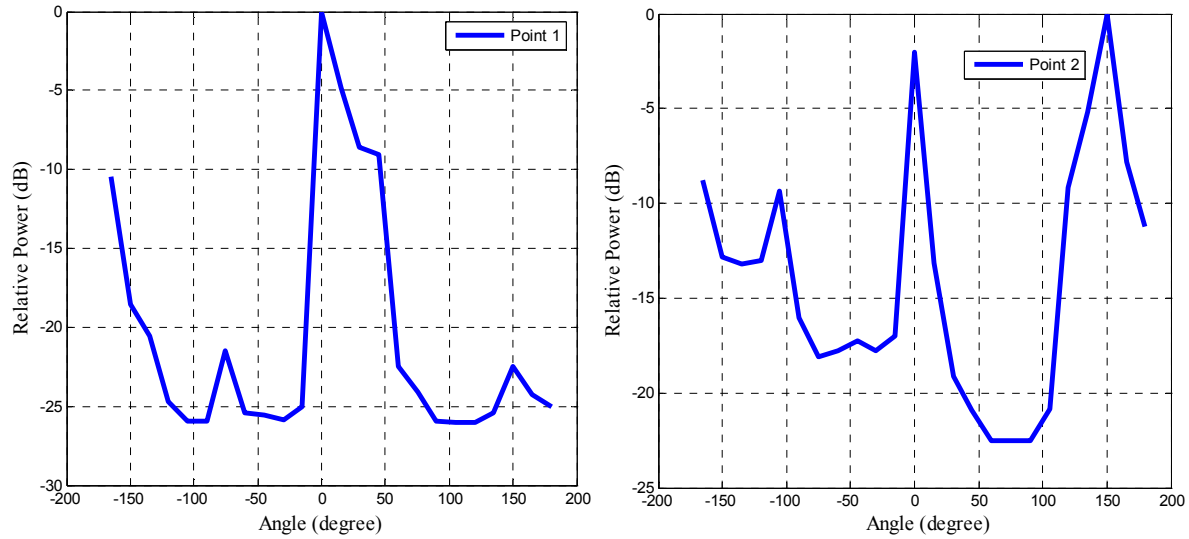
Figure 6.31. Power distribution versus azimuth angle for MIA fixed point-to-point links.

Figure 6.32 shows the RMS-DS distribution as a function of angle for the two MIA fixed point-to-point locations. Points 1 and 2 were referred to as "GEM" and "MFA," respectively, by the airport authorities.
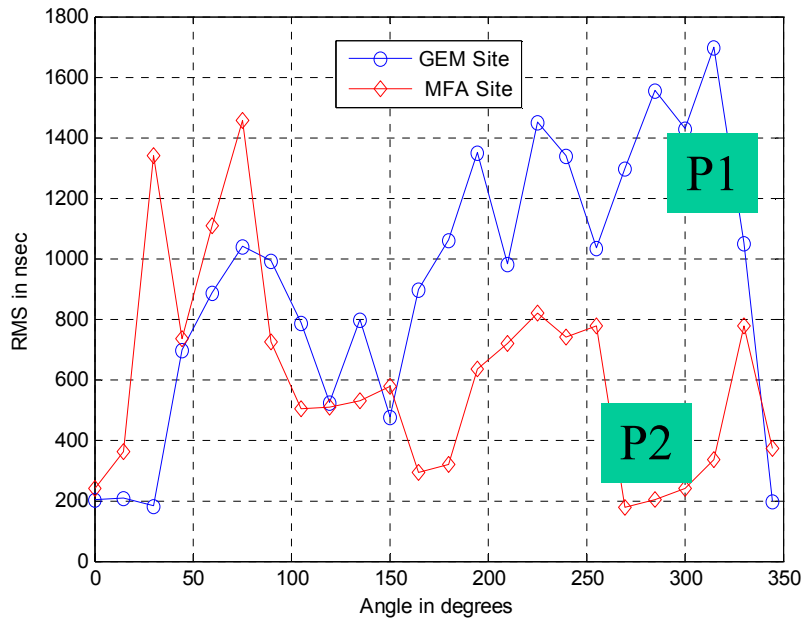
Figure 6.32. RMS-DS for MIA fixed point-to-point links versus azimuth angle.

Figure 6.33 shows the FCEs for the fixed point-to-point measurements at locations P1 and P2. We also provide the aggregate FCE in the figure. Since we used a higher gain antenna for the receiver at MIA than at CLE (see Table 4.1), the main lobe of these FCEs are wider than those of CLE.

160
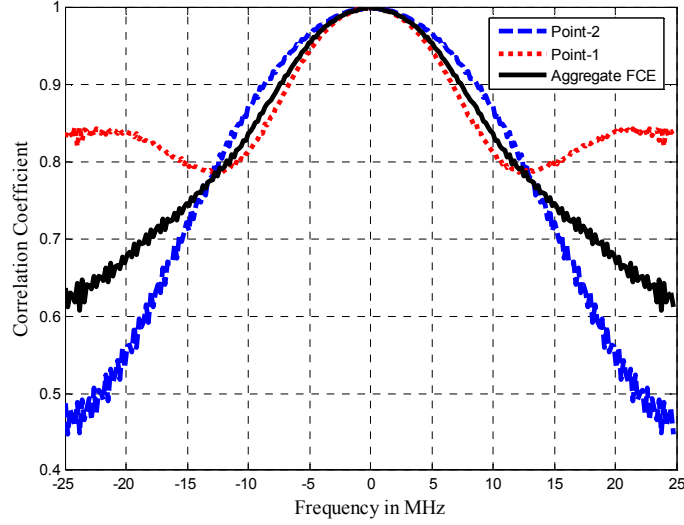
Figure 6.33. FCEs for MIA fixed point-to-point links.

Table 6.37 shows the Ricean *K* factors for the first taps of these channel models, for various azimuth angles, at the MIA sites, for different channel bandwidths. (Recall for P1 here, a second tap with *K*=19 dB exists, with energy 5.6 dB down from the first tap, but only for the 50 MHz bandwidth; *L*=1 for all smaller values of bandwidth.)

Table 6.37. First tap channel Rician *K*-factors at MIA (point 1, point 2) for different bandwidths.

Azimuth Angle (°)	Ricean K-factors (dB) for given Channel Bandwidth (MHz)		
	5	**10**	**50**
0	(24.4, 23)	(25.0, 23.1)	(24.3, 24.5)
90	(17.3, 13.1)	(17.2, 15.9)	(20.4, 18.6)
150	(18.5, 25.9)	(16.8, 21.3)	(19.8, 24.9)
180	(15, 20.2)	(17, 22)	(22, 23.6)
270	(11, 18.8)	(11.6, 21.3)	(15.6, 17.2)

6.7 High Fidelity Channel Model for [Large Airport, NLOS]

In this section, we introduce the high fidelity channel model for [Large Airport, NLOS, 50], and also provide the detailed high fidelity channel model for [Large Airport, NLOS, 20]. For comparison, we also provide the sufficient fidelity model for [Large Airport, NLOS, 20].

6.7.1 High Fidelity Channel Model for [Large Airport, NLOS, 50]

Table 6.38 provides the number of taps $\widetilde{L}$ (within 25 dB of the maximum tap) for a percentage of profiles for [Large Airport, NLOS, 50]. For comparison, recall that the sufficient fidelity model for this airport size and bandwidth was $L=57$.

Table 6.38. $\widetilde{L}$ for different % of profiles for [Large Airport, NLOS, 50]

Percentage of Profiles	Number of Taps $\widetilde{L}$
40	57
70	90
75	102
85	156
90	186
95	221

To account for 90% of the profiles, the high fidelity channel model needs 186 taps! Due to the very large number of taps, it is difficult to provide a full description of the high fidelity model for [Large Airport, NLOS, 50] in text form. Hence, here we provide the high fidelity model for [Large Airport, NLOS, 20], which will have a smaller number of taps by virtue of the smaller bandwidth. First, for comparison, we describe the sufficient fidelity model for this case.

6.7.2 Sufficient Fidelity Channel Model for [Large Airport, NLOS, 20]

Using the mean RMS-DS (Table 4.3), the number of taps is 32. Using the same approach as used in Section 6.3.2, we determine that the number of taps to account for 95% of the energy for [Large Airport, NLOS, 20] is $L=25$. For the correlation matrix, we use R_{wc}^{NLOS} to account for the worst case conditions. Instead of representing the entire matrix here, we provide only example values of correlations, for the first two taps, i.e., $r_{i,1}$ and $r_{i,2}$ in Table 6.39. The full correlation matrix appears in the files of Appendix D. This table also provides the amplitude statistics for the taps in the channel model.

Table 6.39. Amplitude statistics and example tap correlations for sufficient fidelity model for [Large Airport, NLOS, 20].

Tap Index	Weibull Shape Factor (b)	Tap Energy	Alternative Distribution Parameter	$r_{i,1}$	$r_{i,2}$
1	1.98	0.4953	$m = 1.08$	1.0000	0.6235
2	1.5	0.0587	$m = 0.7$	0.6235	1.0000
3	1.6	0.0261	$m = 0.74$	0.4584	0.4211
4	1.6	0.0223	$m = 0.75$	0.5606	0.6098
5	1.6	0.0191	$m = 0.75$	0.4416	0.6509
6	1.55	0.0193	$m = 0.71$	0.6619	0.8188
7	1.66	0.0174	$m = 0.79$	0.7928	0.6434
8	1.65	0.0164	$m = 0.79$	0.6281	0.3539
9	1.67	0.0155	$m = 0.8$	0.4879	0.6110
10	1.65	0.0159	$m = 0.78$	0.7358	0.7840
11	1.56	0.0168	$m = 0.72$	0.6849	0.6147
12	1.59	0.0164	$m = 0.74$	0.8020	0.7545
13	1.61	0.0154	$m = 0.75$	0.7964	0.4543
14	1.61	0.0151	$m = 0.75$	0.5024	0.3256
15	1.64	0.0142	$m = 0.77$	0.7701	0.5061
16	1.72	0.0140	$m = 0.83$	0.6866	0.5238
17	1.65	0.0139	$m = 0.77$	0.9256	0.7157
18	1.69	0.0132	$m = 0.8$	0.7119	0.9611
19	1.67	0.0129	$m = 0.81$	0.5126	0.7032
20	1.73	0.0129	$m = 0.83$	0.6610	0.5143
21	1.72	0.0135	$m = 0.83$	0.6768	0.8560
22	1.7	0.0132	$m = 0.82$	0.7285	0.4197
23	1.74	0.0134	$m = 0.84$	0.6560	0.6894
24	1.8	0.0125	$m = 0.88$	0.7717	0.8198
25	1.78	0.0124	$m = 0.87$	0.5558	0.5586

Table 6.40 provides the steady state and transition probabilities for all the taps in this NLOS case.

Table 6.40. Persistence process parameters for sufficient fidelity model for [Large Airport, NLOS, 20].

Tap Index	Steady State Probability for State 1	Steady State Probability for State 0	Transition Probability (P_{00})	Transition Probability (P_{01})	Transition Probability (P_{10})	Transition Probability (P_{11})
1	1.0000	0	n/a	n/a	0	1.0000
2	0.8540	0.1460	0.2409	0.7591	0.1298	0.8702
3	0.7168	0.2832	0.3772	0.6228	0.2462	0.7538
4	0.6563	0.3437	0.4535	0.5465	0.2863	0.7137

5	0.6321	0.3679	0.4875	0.5125	0.2981	0.7019
6	0.6065	0.3935	0.5119	0.4881	0.3168	0.6832
7	0.6000	0.4000	0.5075	0.4925	0.3285	0.6715
8	0.5973	0.4027	0.5086	0.4914	0.3314	0.6686
9	0.5837	0.4163	0.5254	0.4746	0.3386	0.6614
10	0.5774	0.4226	0.5328	0.4672	0.3420	0.6580
11	0.5742	0.4258	0.5428	0.4572	0.3389	0.6611
12	0.5773	0.4227	0.5444	0.4556	0.3337	0.6663
13	0.5637	0.4363	0.5394	0.4606	0.3563	0.6437
14	0.5516	0.4484	0.5647	0.4353	0.3536	0.6464
15	0.5471	0.4529	0.5637	0.4363	0.3610	0.6390
16	0.5419	0.4581	0.5801	0.4199	0.3551	0.6449
17	0.5455	0.4545	0.5662	0.4338	0.3613	0.6387
18	0.5465	0.4535	0.5713	0.4287	0.3557	0.6443
19	0.5398	0.4602	0.5860	0.4140	0.3527	0.6473
20	0.5413	0.4587	0.5837	0.4163	0.3526	0.6474
21	0.5447	0.4553	0.5741	0.4259	0.3559	0.6441
22	0.5339	0.4661	0.5886	0.4114	0.3593	0.6407
23	0.5350	0.4650	0.5815	0.4185	0.3636	0.6364
24	0.5350	0.4650	0.5756	0.4244	0.3687	0.6313
25	0.5247	0.4753	0.5952	0.4048	0.3669	0.6331

6.7.3 High Fidelity Channel Model for [Large Airport, NLOS, 20]

Table 6.41 provides the number of taps $\widetilde{L}$ (within 25 dB of the maximum tap) for various percentages of profiles for [Large Airport, NLOS, 20].

Table 6.41. $\widetilde{L}$ for different % of profiles for [Large Airport, NLOS, 20]

Percentage of Profiles	Number of Taps $\widetilde{L}$
40	46
70	64
75	69
85	86
90	94
95	97

To account for 90% of the profiles, the high fidelity channel model requires 94 taps. We can reduce the number of taps by accounting for only 95% of the cumulative energy. Table 6.42 shows the cumulative energy with increasing tap index. Using this approach, the number of taps we obtain is 83.

Table 6.42. Cumulative energy of high fidelity model for [Large Airport, NLOS, 20].

Tap Index	Cumulative Energy (%)
3	50
14	60
31	70
51	80
72	90
83	95
92	99

For the high fidelity channel model, in the actual channel model simulation, we *change* the correlation matrix after every *n* realizations of the channel. This would realistically simulate moving from one point in the airport to another. Naturally this would increase the simulation complexity of the model considerably. The value of *n* would generally be random, and the changing of correlation matrices could for example be based upon actual measured matrices and travel times and regions being simulated. Table 6.43. provides the amplitude statistics for the taps in the channel model.

Table 6.43. Amplitude statistics and example tap correlations for high fidelity model for [Large Airport, NLOS, 20].

Tap Index	Weibull Shape Factor (*b*)	Tap Energy	Alternative Distribution Parameter
1	1.98	0.2919	*m = 1.08*
2	1.5	0.0346	*m = 0.7*
3	1.6	0.0154	*m = 0.74*
4	1.6	0.0131	*m = 0.75*
5	1.6	0.0113	*m = 0.75*
6	1.55	0.0114	*m = 0.71*
7	1.66	0.0103	*m = 0.79*
8	1.65	0.0097	*m = 0.79*
9	1.67	0.0091	*m = 0.8*
10	1.65	0.0094	*m = 0.78*
11	1.56	0.0099	*m = 0.72*
12	1.59	0.0096	*m = 0.74*
13	1.61	0.0091	*m = 0.75*
14	1.61	0.0089	*m = 0.75*
15	1.64	0.0084	*m = 0.77*
16	1.72	0.0082	*m = 0.83*
17	1.65	0.0082	*m = 0.77*
18	1.69	0.0078	*m = 0.8*
19	1.67	0.0076	*m = 0.81*
20	1.73	0.0076	*m = 0.83*
21	1.72	0.0079	*m = 0.83*

22	1.7	0.0078	$m = 0.82$
23	1.74	0.0079	$m = 0.84$
24	1.8	0.0074	$m = 0.88$
25	1.78	0.0073	$m = 0.87$
26	1.82	0.0069	$m = 0.89$
27	1.77	0.0072	$m = 0.86$
28	1.87	0.0068	$m = 0.93$
29	1.76	0.0071	$m = 0.85$
30	1.79	0.0071	$m = 0.88$
31	1.79	0.0072	$m = 0.88$
32	1.71	0.0075	$m = 0.83$
33	1.79	0.0071	$m = 0.87$
34	1.78	0.0072	$m = 0.85$
35	1.74	0.0070	$m = 0.85$
36	1.77	0.0070	$m = 0.86$
37	1.79	0.0069	$m = 0.87$
38	1.76	0.0070	$m = 0.85$
39	1.86	0.0066	$m = 0.92$
40	1.8	0.0067	$m = 0.88$
41	1.75	0.0067	$m = 0.86$
42	1.77	0.0069	$m = 0.86$
43	1.82	0.0067	$m = 0.89$
44	1.81	0.0063	$m = 0.9$
45	1.81	0.0062	$m = 0.9$
46	1.84	0.0064	$m = 0.9$
47	1.82	0.0061	$m = 0.88$
48	1.89	0.0058	$m = 0.93$
49	1.89	0.0061	$m = 0.94$
50	1.87	0.0066	$m = 0.92$
51	1.83	0.0064	$m = 0.89$
52	1.82	0.0066	$m = 0.89$
53	1.84	0.0065	$m = 0.9$
54	1.9	0.0065	$m = 0.94$
55	1.9	0.0060	$m = 0.94$
56	1.8	0.0060	$m = 0.89$
57	1.87	0.0060	$m = 0.92$
58	1.78	0.0066	$m = 0.86$
59	1.75	0.0072	$m = 0.85$
60	1.78	0.0066	$m = 0.87$
61	1.77	0.0067	$m = 0.86$
62	1.8	0.0063	$m = 0.88$
63	1.85	0.0064	$m = 0.91$
64	1.72	0.0068	$m = 0.83$
65	1.61	0.0070	$m = 0.76$
66	1.77	0.0065	$m = 0.86$

67	1.77	0.0062	*m = 0.86*
68	1.78	0.0064	*m = 0.86*
69	1.72	0.0063	*m = 0.82*
70	1.7	0.0064	*m = 0.81*
71	1.7	0.0060	*m = 0.83*
72	1.69	0.0064	*m = 0.82*
73	1.75	0.0063	*m = 0.85*
74	1.72	0.0062	*m = 0.83*
75	1.73	0.0060	*m = 0.85*
76	1.73	0.0056	*m = 0.85*
77	1.65	0.0062	*m = 0.78*
78	1.59	0.0064	*m = 0.74*
79	1.71	0.0060	*m =0.83*
80	1.69	0.0062	*m = 0.82*
81	1.6	0.0064	*m = 0.75*
82	1.73	0.0059	*m = 0.84*
83	1.51	0.0066	*m = 0.69*

Table 6.44 provides the steady state and transition probabilities for all the taps in this NLOS case.

Table 6.44. Persistence process parameters for high fidelity model for [Large Airport, NLOS, 20].

Tap Index	Steady State Probability for State 1	Steady State Probability for State 0	Transition Probability (P_{00})	Transition Probability (P_{01})	Transition Probability (P_{10})	Transition Probability (P_{11})
1	1.0000	0	n/a	n/a	0	1.0000
2	0.8540	0.1460	0.2409	0.7591	0.1298	0.8702
3	0.7168	0.2832	0.3772	0.6228	0.2462	0.7538
4	0.6563	0.3437	0.4535	0.5465	0.2863	0.7137
5	0.6321	0.3679	0.4875	0.5125	0.2981	0.7019
6	0.6065	0.3935	0.5119	0.4881	0.3168	0.6832
7	0.6000	0.4000	0.5075	0.4925	0.3285	0.6715
8	0.5973	0.4027	0.5086	0.4914	0.3314	0.6686
9	0.5837	0.4163	0.5254	0.4746	0.3386	0.6614
10	0.5774	0.4226	0.5328	0.4672	0.3420	0.6580
11	0.5742	0.4258	0.5428	0.4572	0.3389	0.6611
12	0.5773	0.4227	0.5444	0.4556	0.3337	0.6663
13	0.5637	0.4363	0.5394	0.4606	0.3563	0.6437
14	0.5516	0.4484	0.5647	0.4353	0.3536	0.6464
15	0.5471	0.4529	0.5637	0.4363	0.3610	0.6390
16	0.5419	0.4581	0.5801	0.4199	0.3551	0.6449
17	0.5455	0.4545	0.5662	0.4338	0.3613	0.6387

18	0.5465	0.4535	0.5713	0.4287	0.3557	0.6443
19	0.5398	0.4602	0.5860	0.4140	0.3527	0.6473
20	0.5413	0.4587	0.5837	0.4163	0.3526	0.6474
21	0.5447	0.4553	0.5741	0.4259	0.3559	0.6441
22	0.5339	0.4661	0.5886	0.4114	0.3593	0.6407
23	0.5350	0.4650	0.5815	0.4185	0.3636	0.6364
24	0.5350	0.4650	0.5756	0.4244	0.3687	0.6313
25	0.5247	0.4753	0.5952	0.4048	0.3669	0.6331
26	0.5297	0.4703	0.5847	0.4153	0.3689	0.6311
27	0.5252	0.4748	0.6001	0.3999	0.3615	0.6385
28	0.5292	0.4708	0.5953	0.4047	0.3600	0.6400
29	0.5244	0.4756	0.5968	0.4032	0.3655	0.6345
30	0.5206	0.4794	0.5976	0.4024	0.3703	0.6297
31	0.5245	0.4755	0.5860	0.4140	0.3752	0.6248
32	0.5268	0.4732	0.5930	0.4070	0.3654	0.6346
33	0.5076	0.4924	0.6121	0.3879	0.3762	0.6238
34	0.5134	0.4866	0.6071	0.3929	0.3723	0.6277
35	0.5148	0.4852	0.5996	0.4004	0.3772	0.6228
36	0.5148	0.4852	0.5956	0.4044	0.3810	0.6190
37	0.5140	0.4860	0.6017	0.3983	0.3763	0.6237
38	0.5024	0.4976	0.6042	0.3958	0.3918	0.6082
39	0.5076	0.4924	0.6128	0.3872	0.3754	0.6246
40	0.5055	0.4945	0.5988	0.4012	0.3923	0.6077
41	0.5037	0.4963	0.6032	0.3968	0.3908	0.6092
42	0.5060	0.4940	0.6081	0.3919	0.3825	0.6175
43	0.5058	0.4942	0.6076	0.3924	0.3833	0.6167
44	0.4955	0.5045	0.6157	0.3843	0.3911	0.6089
45	0.4855	0.5145	0.6096	0.3904	0.4136	0.5864
46	0.4881	0.5119	0.6248	0.3752	0.3934	0.6066
47	0.4871	0.5129	0.6204	0.3796	0.3995	0.6005
48	0.4853	0.5147	0.6217	0.3783	0.4009	0.5991
49	0.5013	0.4987	0.6082	0.3918	0.3896	0.6104
50	0.5094	0.4906	0.6022	0.3978	0.3830	0.6170
51	0.4963	0.5037	0.6174	0.3826	0.3882	0.6118
52	0.5027	0.4973	0.5929	0.4071	0.4024	0.5976
53	0.4897	0.5103	0.6200	0.3800	0.3959	0.6041
54	0.5005	0.4995	0.6089	0.3911	0.3903	0.6097
55	0.4789	0.5211	0.6295	0.3705	0.4030	0.5970
56	0.4784	0.5216	0.6155	0.3845	0.4191	0.5809
57	0.4803	0.5197	0.6073	0.3927	0.4248	0.5752
58	0.4971	0.5029	0.6051	0.3949	0.3994	0.6006
59	0.5174	0.4826	0.5789	0.4211	0.3929	0.6071
60	0.5018	0.4982	0.5848	0.4152	0.4121	0.5879
61	0.5100	0.4900	0.5741	0.4259	0.4090	0.5910
62	0.4919	0.5081	0.5968	0.4032	0.4162	0.5838

63	0.4837	0.5163	0.6031	0.3969	0.4238	0.5762
64	0.4892	0.5108	0.5989	0.4011	0.4187	0.5813
65	0.4852	0.5148	0.6034	0.3966	0.4207	0.5793
66	0.4771	0.5229	0.6172	0.3828	0.4193	0.5807
67	0.4781	0.5219	0.6080	0.3920	0.4278	0.5722
68	0.4755	0.5245	0.6161	0.3839	0.4233	0.5767
69	0.4765	0.5235	0.5887	0.4113	0.4517	0.5483
70	0.4721	0.5279	0.6123	0.3877	0.4334	0.5666
71	0.4582	0.5418	0.6264	0.3736	0.4415	0.5585
72	0.4685	0.5315	0.6108	0.3892	0.4413	0.5587
73	0.4716	0.5284	0.6139	0.3861	0.4324	0.5676
74	0.4750	0.5250	0.6086	0.3914	0.4324	0.5676
75	0.4615	0.5385	0.6011	0.3989	0.4654	0.5346
76	0.4532	0.5468	0.6212	0.3788	0.4567	0.5433
77	0.4647	0.5353	0.6113	0.3887	0.4476	0.5524
78	0.4642	0.5358	0.6119	0.3881	0.4479	0.5521
79	0.4523	0.5477	0.6190	0.3810	0.4613	0.5387
80	0.4594	0.5406	0.6044	0.3956	0.4654	0.5346
81	0.4582	0.5418	0.5963	0.4037	0.4771	0.5229
82	0.4453	0.5547	0.6069	0.3931	0.4895	0.5105
83	0.4523	0.5477	0.6066	0.3934	0.4763	0.5237

6.8 Simulated High Fidelity and Sufficient Fidelity Models

In this section, we outline the steps for simulating the channel model using the parameters obtained from the previous sections. We then compare the data generated using the high and sufficient fidelity models with the actual collected data.

6.8.1 Channel Model Parameters

Considering an example case of [Large Airport, 50 MHz], we provide the steps to obtain the parameters required to simulate the tapped-delay model for the channel. (See Figure 3.1 for a diagrammatic depiction of the model structure.) For brevity, we consider the sufficient fidelity model for [Large Airport, 50 MHz], but do describe both NLOS-S and NLOS modeling. The sequence of steps is as follows:

1. Determine the number of taps needed, for each region, using Table 6.7. Note that via the sufficient fidelity criteria from Table 5.9, we use the mean RMS-DS to determine the number of taps. This results in the following numbers:
   - NLOS: number of taps L_{NLOS}=57
   - NLOS-S: number of taps L_{NLOS-S}=8

2. Determine the amplitude fading shape factors (parameters "*b*" in the *pdf* of the Weibull distribution, from Table 3.2) for each tap and for each region. The shape factors are listed in the following tables:
   - NLOS: Table 6.5
   - NLOS-S: Table 6.2

3. Determine the energy associated with each tap for both regions. The scale factor (parameter "*a*" in the Weibull *pdf* of Table 3.2) for a given tap can be obtained from the corresponding energy of the tap, and the shape factor *b* as follows: $a = \sqrt{Energy / \Gamma[(2/b)+1]}$. For the two regions, use the following tables:
   - NLOS: Table 6.5
   - NLOS-S: Table 6.2

4. Determine the persistence process (*z(t)*, eq. (3.7)) parameters for each tap, for both regions, via the following tables:
   - NLOS: Table 6.6
   - NLOS-S: Table 6.3

5. Determine the correlation matrix for each region. Note that the sufficient fidelity criteria of Table 5.9 employ the worst case correlation matrices (R_{wc}^{U}). For the two regions, these matrices are provided as follows:
   - NLOS: Appendix D
   - NLOS-S: Equation (6.1)

6. Assign *Region_TS* and *Region_ES* matrices to model the transitions between different regions on the airport via the "region-switching" Markov chain model. We have let these parameters be user-defined. An example case for a medium airport is provided in eq. (5.14).

6.8.2 Model Simulation

We provide the steps used to simulate the high and sufficient fidelity channel models. The steps outlined are for the following case: [Large Airport, NLOS, 20]. For the sufficient fidelity model, we are creating the CIRs via random simulation, hence in the context of [80], we can term these "synthetic" channel models. For the high-fidelity models, if we use actual measured data, this is termed a "stored" channel in the context of [80].

Sufficient Fidelity (SF) Model

Assumptions: We assume a maximum Doppler frequency ($f_{D,max}$) of 2500 Hz. This is obtained using a maximum velocity of 150 m/s for a plane during the landing/takeoff phase of flight. Generally, velocities of vehicles on the surface will be *much* smaller than this, resulting in much smaller Doppler frequencies. We generate the channel realizations in the form of channel impulse responses (CIRs, corresponding to PDPs) for 1 second of measurement time. The

sampling rate (f_s) for the generated CIRs will be 40 MHz (twice the bandwidth). This gives us a ratio $f_{D,max}/f_s=1.25\times10^{-4}$. It is difficult to generate a filter with such specifications due to stability issues. In our case, we use the approach followed by [80] and [81]. We assume that we are generating the CIRs at $f_{D,max}$ and then use interpolation to obtain the "in-between" samples. In this simulation, we will generate 2500 CIRs and interpolate them to obtain 20×10^6 CIRs.

Algorithm for SF Model

1. Determine the number of taps as 25 (refer to Section 6.7).
2. Obtain fading amplitude Weibull parameters "b" and "a" for the 25 taps. Also, provide the correlation matrix, R_{wc}^{NLOS}.
3. Using the correlated Weibull simulation program, generate 2500 CIRs, each having 25 taps. The algorithm used to generate the correlated Weibulls is provided in Appendix D.
4. Interpolate the 2500 CIRs to obtain 20×10^6 CIRs. We use cubic interpolation for this simulation. The matrix generated is of size 20×10^6 time samples per tap by 25 taps.
5. Generate the persistence process, $z(t)$, for each tap. Each persistence process has 2500 states. Increase the number of states to 20×10^6 by repeating each state 8000 times. Note that for the persistence process we can not use interpolation to obtain the "in-between" states since $z(t)$ is a two state Markov process that takes only values one and zero. The matrix generated is again of size 20×10^6 time samples per tap by 25 taps.
6. Multiply the matrices obtained in steps 4 and 5, per tap, in element by element fashion, to obtain the CIRs. In total, we have 20×10^6 CIRs.
7. If desired, the transfer functions (*TF*s) for the above CIRs can be obtained using a Fourier transform (FFT) on each CIR. Each *TF* is normalized such that maximum amplitude in the *TF* is unity.

High Fidelity (HF) Model

Assumptions: In Miami, we collected data using 41 segments of travel. For the HF model, we use an algorithm similar in principle to applying the SF model 41 consecutive times. Here note that the number of taps is 83 (refer to Section 6.7). For each iteration of the SF model, we have to use a different R_{wc}^{NLOS}. The Weibull *"a"* and *"b"* factors for the taps remain the same in all iterations. Since the number of CIRs collected in every segment (iteration) is different, we generate different numbers of CIRs for each segment (iteration). We assume that the maximum number of CIRs collected in any segment is 2500 (20×10^6 after interpolation). The numbers of CIRs for the remaining segments are scaled accordingly. Table 6.45 provides the number of CIRs generated for each iteration. The highlighted segment (35) is the one with maximum number of CIRs.

Table 6.45. Number of CIRs generated for [Large Airport, NLOS, 20] HF model.

Iteration Index (i)	Number of CIRs Generated ($f_{d,i}$)	Number of CIRs after Interpolation ($f_{s,i}$)
1	662	5,296,000
2	247	1,976,000
3	126	1,008,000
4	429	3,432,000
5	277	2,216,000
6	1108	8,864,000
7	982	7,856,000
8	191	1,528,000
9	602	4,816,000
10	273	2,184,000
11	199	1,592,000
12	174	1,392,000
13	143	1,144,000
14	736	5,888,000
15	407	3,256,000
16	727	5,816,000
17	472	3,776,000
18	926	7,408,000
19	225	1,800,000
20	135	1,080,000
21	256	2,048,000
22	52	416,000
23	91	728,000
24	135	1,080,000
25	161	1,288,000
26	238	1,904,001
27	1609	12,872,000
28	1744	13,952,000
29	1968	15,744,000
30	130	1,040,000
31	2172	17,376,000
32	1462	11,696,000
33	1588	12,704,000
34	1052	8,416,000
35	2500	20,000,000
36	468	3,744,000
37	433	3,464,000
38	411	3,288,000
39	74	592,000
40	169	1,352,000
41	1082	8,656,000

Algorithm for HF Model

1. Determine the number of taps as 83 (refer to Section 6.7).
2. Obtain Weibull parameters *"b"* and *"a"* for the 83 taps.
3. Consider the ith iteration. Load the corresponding correlation matrix, R_{wc}^{NLOS}, $f_{s,i}$ and $f_{d,i}$
4. Generate $f_{d,i}$ CIRs, each having 83 taps, using the correlated Weibull simulation program.
5. Interpolate the $f_{d,i}$ CIRs to obtain $f_{s,i}$ CIRs. We use cubic interpolation for this simulation. The matrix generated is of size ($f_{s,i} \times 83$).
6. Generate the persistence process, $z(t)$, for each tap. Each persistence process has $f_{d,i}$ states. Increase the number of states to $f_{s,i}$ by repeating each state 8000 times. The matrix generated is of size ($f_{s,i} \times 83$).
7. Multiply the matrices obtained in steps 5 and 6 for each tap, in element by element fashion, to obtain the CIRs. In total, we have $f_{s,i}$ CIRs.
8. If desired, the transfer functions (*TF*s) for the above CIRs can be obtained using a Fourier transform on each CIR. Each *TF* is normalized such that maximum amplitude in the *TF* is unity.
9. Repeat steps 3-8 for all iterations.
10. In total, this yields 41 data sets with varying number of PDPs in each set.

6.8.3 Comparison of High and Sufficient Fidelity Models with Actual Data

Section 6.9.2 has outlined steps to simulate the HF and SF models. In this section, we compare the fidelity of these models in depicting the actual channel. Recall from Table 5.9 that the HF and SF models are dependent on the RMS-DS of the collected PDPs. This means that in the delay domain, a direct comparison will not be very meaningful because the lengths of the CIRs are different, by construction. Hence, for comparison, we turn to the frequency domain to fairly compare the statistics obtained using the HF and SF models and the actual data.

The two statistics that we use are the *L₂-norm* and the mean square difference (MSD). These statistics have been used by previous researchers for validating simulated and collected data [81]. The *L₂-norm* of a function *f(x)*, with *x*=[$x_1, x_2, ... x_n$] is defined as follows:

$$L_2 - norm[\, f(x)\,] = \|f\|_2 \cong \left[\int ... \int \left| f(x_1,...x_n) \right|^2 dx_1...dx_n \right]^{1/2} \qquad (6.10)$$

In our case we use the discrete summation approximation to the integral, and our functions are the *differences* between SF, HF, and actual data functions.

6.8.3.1 Validation for Spectral Line Amplitude

We first compute the *L₂-norm* for the *difference* between each spectral line of the computed *TF* and a unit-amplitude distortionless channel. By "spectral line" we simply mean the response at a specific value of frequency. The reference channel has a flat amplitude spectrum, corresponding to a single impulse for its associated CIR. The *TF*s are computed for

the actual collected CIR data, and the SF and HF models. Figure 6.34 illustrates the process of the calculation of the difference, which is used in the discrete approximation to (6.10).
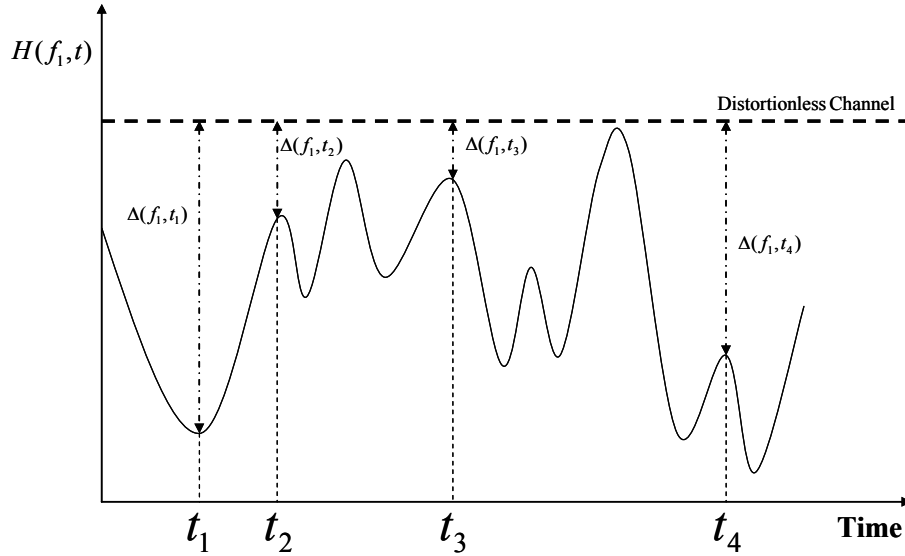

Figure 6.34. Illustration of computation of L_2-*norm* with respect to distortionless channel, for each spectral line.

Specifically for computing this, we define the function $\Delta_M(f,t)$ as follows:

$$\Delta_M(f,t) = 1 - H_M(f,t) \tag{6.11}$$

where the subscript M denotes the model, SF or HF, or the data. Using (6.10) then, for the jth spectral line (j^{th} frequency component), we compute

$$L_2 - norm_{(t)} = \left\| \Delta_M(f_j,t) \right\|_2 = \sqrt{\int_{\{t\}} \Delta_M^2(f_j,t)dt} \cong \sqrt{\sum_{i=1}^{N_M} \Delta_M^2(f_j,t_i)} \tag{6.12}$$

where the subscript *(t)* on the norm indicates integration over time, and *{t}* denotes the time interval of the model or data used. The number N_M is the number of time samples, which equals 200,000 for the SF and HF simulated transfer functions, and approximately 6,300 for the actual data. Then via (6.12) we obtain a set of 256 norms, one for each of the 256 frequencies.

Figure 6.35 compares the L_2-*norm* of these differences for the different channel models (normalized by the maximum value). We have shown the variation of the L_2-*norms* for the positive frequencies (with respect to center frequency) since the plot will be symmetric about the center frequency. The computed L_2-*norm* provides a measure of the channel dispersion, by quantifying the difference between the actual channel and a distortionless channel. Given the HF model uses "worst-case" parameter values, which represent only a small portion of the airport areas, its L_2-*norm* with respect to a distortionless channel will be larger than that of the actual data a majority of the time (recall the HF model uses 83 taps and that nearly 85% of the PDPs have fewer than 83 taps).
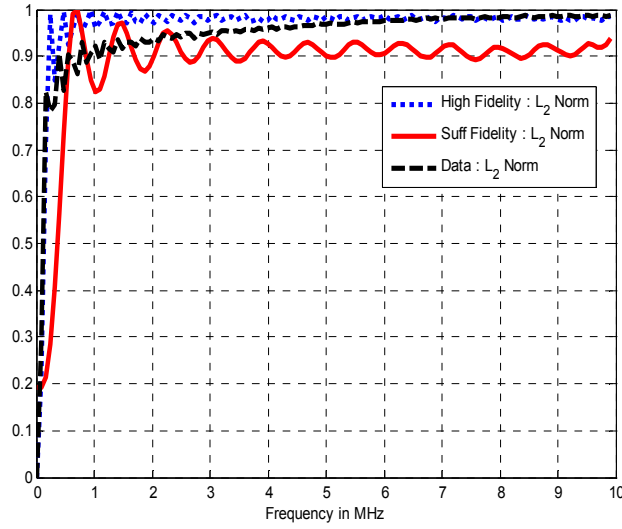
Figure 6.35. *L₂-norm* of [Large Airport, NLOS, 20] channel models with respect to distortionless channel, for each spectral line.

More significantly in terms of comparing the two models, Figure 6.36 compares the L_2-*norms* for the difference between the SF model and the actual data, and the HF model and the actual channel data, for each spectral line. These norms are obtained by replacing the value "1" in (6.11) by the actual data transfer function, $H_D(f,t)$. As expected, the L_2-*norm* for the HF model is smaller than that for the SF model, hence meaning the HF model is closer to the actual data. The previous figure (Figure 6.35) shows that the SF model is nonetheless a good approximation to the channel.
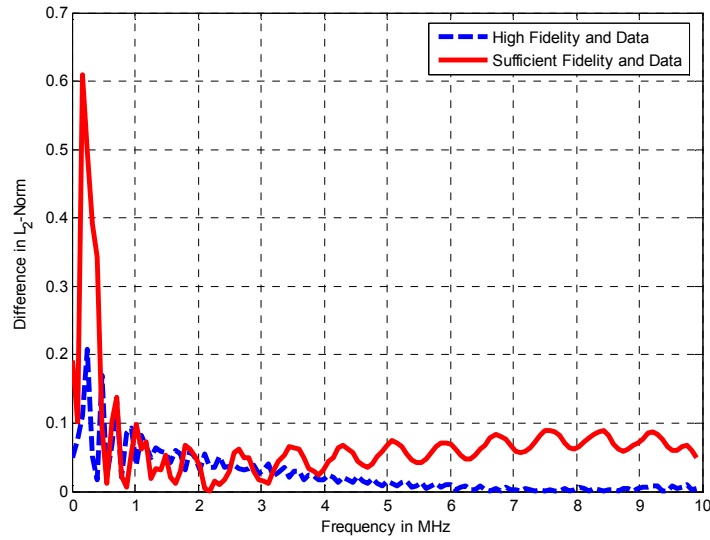

Figure 6.36. *L₂-norm* of differences between the SF and HF channel models and the actual data for [Large Airport, NLOS, 20] models, for each spectral line.

Similar to the *L₂-norm*, we compute the MSD between each spectral line of the computed *TF* and a distortionless channel. For computation, let

$$D_M(f,t) = \Delta_M^2(f,t). \tag{6.13}$$

Then, for the jth spectral line, we have

$$MSD_M(f_j) = \underset{\{t_i\}}{mean}\, D_M(f,t_i) \tag{6.14}$$

where "mean" denotes the mean over all time samples of D_M. Figure 6.37 compares the MSDs versus frequency for the two different channel models. As with the *L₂-norm*, the computed MSD also provides a measure of the channel's dispersiveness.
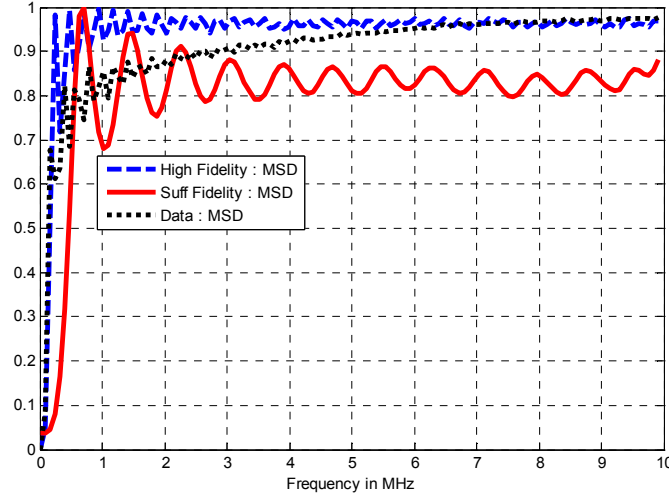

Figure 6.37. MSD of simulated SF and HF models and actual data for [Large Airport, NLOS, 20], for each spectral line.

Figure 6.38 compares the MSDs between the SF and HF *TF*s and that of the actual channel. Similar to the *L₂-norm* case, for this comparison, we replace the value "1" in (6.11) by the actual data transfer function, $H_D(f,t)$, before applying (6.13) and (6.14). Results similar to Figure 6.36 are observed.
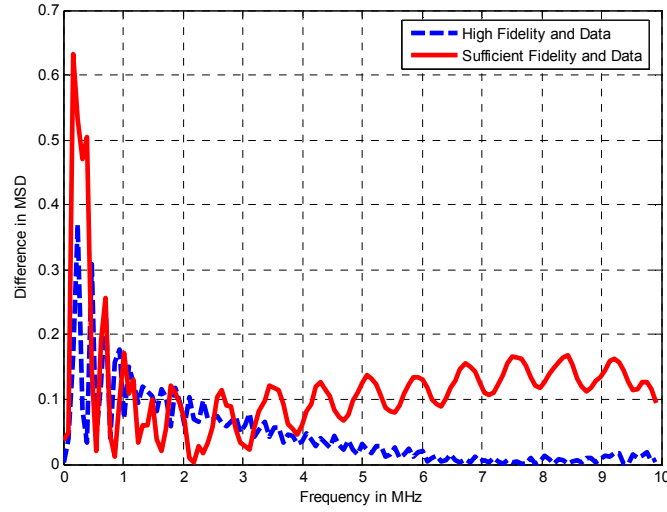
Figure 6.38. Mean-square difference between simulated SF and HF models, and actual data for [Large Airport, NLOS, 20], for each spectral line.

6.8.3.2 Validation for Transfer Function

In this section, we compute the *L₂-norm* for the difference between each *individual TF* and a distortionless channel. The *TF*s are computed for the actual collected CIRs, and the SF and HF models. Figure 6.39 illustrates the process of the calculation of this difference. Comparing to Figure 6.34, which has frequency fixed and time varying, in Figure 6.39, time is fixed and frequency is varying.
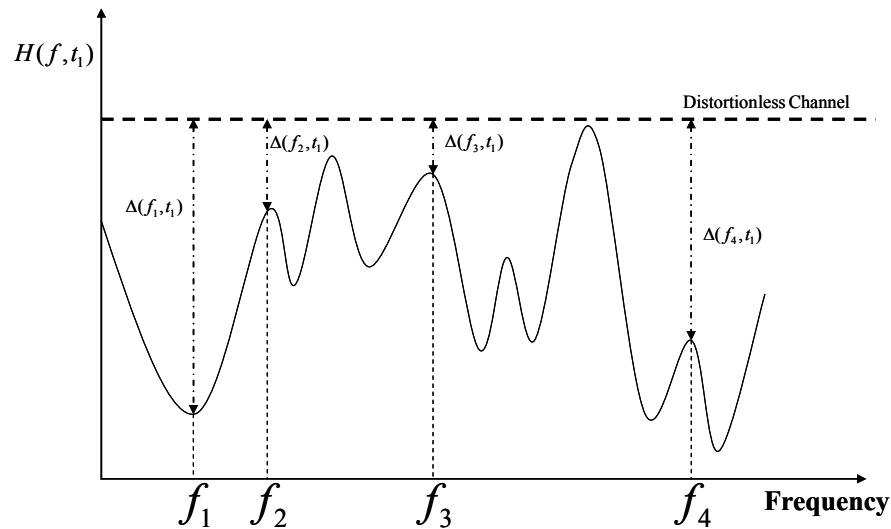

Figure 6.39. Illustration of computing *L₂-norm* with respect to distortionless channel, for each transfer function.

Computationally, we proceed in a manner similar to that for the plots versus frequency. Specifically, we define

$$L_2 - norm_{(f)} = \left\| \Delta_M(f,t_i) \right\|_2 = \sqrt{\int\limits_{\{f\}} \Delta_M^2(f,t_i)dt} \cong \sqrt{\sum_{j=1}^{256} \Delta_M^2(f_j,t_i)} \qquad (6.15)$$

where now the subscript *(f)* on the norm indicates integration over frequency, and *{f}* denotes the frequency span of the model or data used for *H*, for which we have values at 256 frequencies.

Figure 6.40 compares the *distributions* of the *L₂-norms* for the different channel models, where we have collected the *L₂-norms* over approximately 200,000 simulated transfer functions, and approximately 6,300 actual data *TF*s. As with the previous results, the distributions for the SF and HF models are similar to that of the real data, with the HF distribution being closer to the actual data than is the SF. A similar distribution for the MSD of the different models is plotted in Figure 6.41, where the MSD here is defined as

$$MSD_M(t_i) = \underset{\{f_j\}}{mean}\, D_M(f_j,t) . \qquad (6.16)$$

Figure 6.40. Distribution of *L₂-norm* of [Large Airport, NLOS, 20] SF and HF channel models with respect to distortionless channel, for transfer functions.

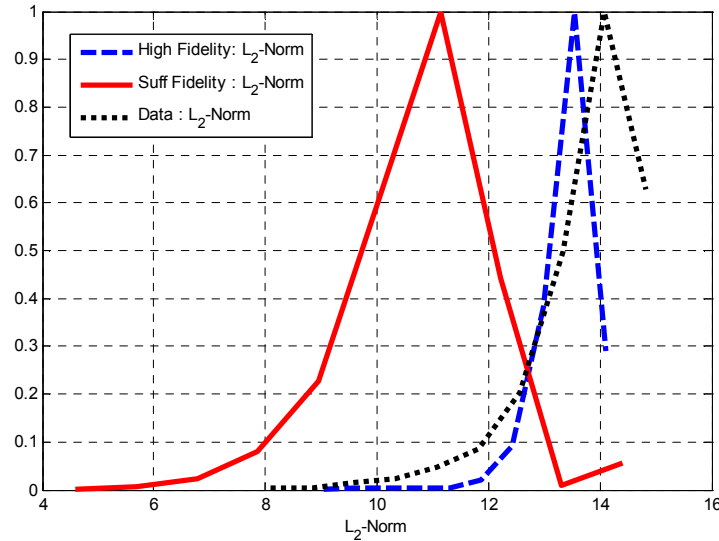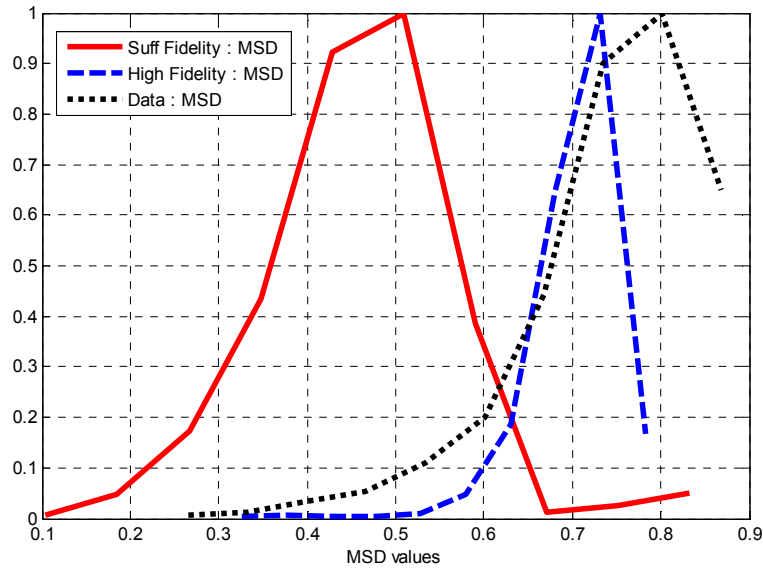**Figure 6.41.** Distribution of MSD of [Large Airport, NLOS, 20] SF and HF channel models with respect to distortionless channel, for transfer functions.

6.9 Chapter Summary

In this chapter, we have provided the parameters for developing channel models for all three airport sizes, all three airport propagation regions, and multiple values of channel bandwidth. We have also discussed example implementations of the tapped-delay line model for an example channel, and outlined steps for generating simulated CIRs. Figure 6.42 provides a block diagram representation for the generic channel model and the parameters involved.
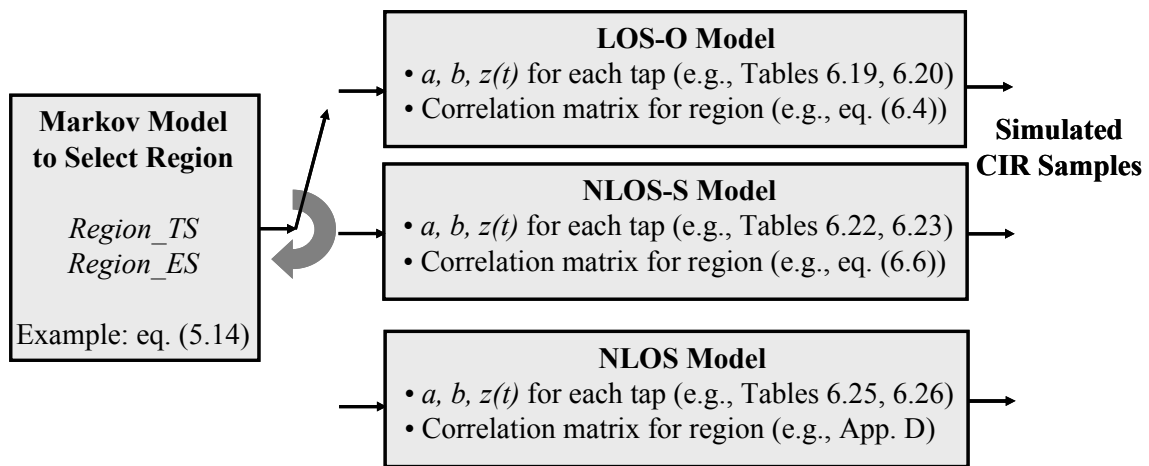

Figure 6.42. Generic channel model implementation diagram.

Chapter 7: Summary, Conclusions, and Recommendations

7.1 Introduction

In this final chapter, we summarize the project and this report. We also draw some conclusions, and provide a list of recommendations.

7.2 Summary

By all measures, the project was a resounding success. Through the cooperation of personnel from NASA, the FAA, and various airport authorities, a thorough set of channel impulse response measurement data was obtained for the 5 GHz band around airport surface areas. Coordination with airport authorities went smoothly at each airport, and their assistance was vital to the project success. In total, over 35,000 power delay profiles (PDPs) were taken for the mobile setting, just under 5,000 PDPs for the point-to-point setting, and over 11,800 PDPs for the airport field site measurements (totaling over 51,000 PDPs)[6]. This measurement data was used to develop detailed statistical channel models for this environment. These models will enable system designers to carefully and precisely analyze and simulate candidate communication system performance in this environment. This project, and any that make use of its results, will also be important in demonstrating the aviation community's commitment to preservation of the MLS extension band for exclusive aeronautical use.

The project objectives, detailed in Chapter 1, were all successfully achieved. One potential minor exception might be the restricted data and models obtained for modeling propagation path loss, for which we have models for only two of the three airport regions. As noted in the recommendations, the third (NLOS) region's path loss model could be based upon analysis and on measurements taken in other terrestrial environments; additional data could also be obtained during field trials of any system deployed in this environment. In the end, sufficient transmit power can be used to overcome the path loss for the short distances required on the airport surface. With sufficient received power, communication system performance is dominated by the small scale fading, which we have thoroughly characterized. The other objectives we achieved were compilation of a set of key references, development of a basic airport classification scheme, collection of representative channel measurement data, and development of the channel models.

This report described the importance and significance of this project, and began with the project goals and objectives. We also provided a detailed literature review and reference list, useful for archival purposes and for any continuation of this work. Worth citing here is the substantial number of publications generated from this project itself that were, or will be, published in the open literature, thus advancing the field.

An overview of channel modeling and key channel parameters was also provided in this report, to enable readers to properly interpret results. Along with this, examples of how and where the channel parameters themselves can be used in communication system design were

---

[6] As described in Chapter 4, each PDP consists of 255 chip samples, with each sample consisting of two-byte numbers for the *I*-channel, the *Q*-channel, the phase, etc.

given. Discussions regarding the uniqueness of the airport surface channel were provided, which included our division of the airport surface area into three distinct propagation regions.

The actual measurements at the six airports were also described, as was the test equipment used. As noted in Chapter Four, we also made measurements and developed models for two other channel settings, in addition to the primary setting of transmission between the air traffic control tower and a vehicle on the airport surface. These other models, which expanded the project outcomes beyond their original scope, were for the point-to-point channel from the air traffic control tower to an airport field site, and for the channel from an airport field site to a surface vehicle.

Due to the substantial amount of detail in our developed models, the report provides a thorough discussion of required data "pre-processing" needed to extract pertinent channel parameters and their statistics. This discussion also addresses other considerations encountered in developing the channel models, in which model fidelity must be balanced with model complexity. We thus have developed both "sufficient fidelity" and "high fidelity" models for all three airport sizes, all three propagation regions, for multiple values of channel bandwidth. Detailed appendices, the references, and data files support and complete the report.

7.3 Conclusions

The primary conclusions of this project are first, that the wireless channel in the MLS extension band in airport surface areas is a very dispersive fading channel, which is, over moderate durations (on the order of tens of milliseconds to a second, depending upon velocity), statistically *non*-stationary. For surface velocities up to 100 miles/hour, the channel will nonetheless be slowly fading for signaling rates larger than approximately 100 kbps. For smaller velocities, the fading is very slow for even lower signaling rates (e.g., for a velocity of 10 miles/hour, fading is very slow for any signaling rate above about 10 kbps). Thus, for all but the most narrowband transmissions, the Doppler spread induced upon signals by the multipath channel will be small, and hence the shape of the Doppler power spectrum will be immaterial to system performance.

In many cases, fading is severe, and exhibits statistical variation that is worse than the commonly used Rayleigh fading model. For this Rayleigh model, the probability that the signal power level fades to a level that is equal to F dB or more below its mean value is given by the formula $P_F = 1 - exp(10^{-(F/10)})$. Thus in our "worse than Rayleigh" case, the probability of an F dB fade is larger than this value, so for example the probability of a 10 dB fade is larger than about 0.1, the probability of a 20 dB fade is larger than about 0.01, etc. Exact values of the fading probabilities can be found by using the Weibull distribution we describe in Chapter 3.

Complicating the models is the conclusion drawn from the measured data that the multipath components are often highly correlated. The effect of this correlation on communication system performance will be to reduce the amount of "multipath diversity" attainable, resulting in error probabilities larger than those that would be obtained if all components were uncorrelated. We have developed a new method that enables us to generate the required correlated fading random processes, so that this important effect can be taken into account in any system evaluation.

To accurately model the channel dynamics over periods on the order of 0.5 second or longer requires that we account for the finite duration of multipath components. We have done

this by incorporating into the models a "persistence process," in addition to the small scale amplitude fading. Related to this in terms of simulation is our conclusion that the airport surface area channel can be divided into three different propagation regions, with different degrees of dispersion and fading in each. To realistically model the channel for any vehicle that travels throughout these regions requires another stochastic process model that switches between channel models for the various regions. As with the persistence process, we have also developed a model for this effect, based upon our measured data. For both these models, we have used the widely employed Markov chain random process model. The channel-region-occupancy model can be tailored by the model user to allow for arbitrary desired durations in each airport propagation region.

We also measured and modeled propagation path loss, and for two of the three regions, devised models. For line-of-sight (LOS) conditions in open areas, the free-space path loss model suffices, to first order; the plane-earth model could also be used for a generally conservative estimate (see Chapter 3). For the non-line-of-sight (NLOS) regions, we were unable to collect sufficient data to develop a model, but for the regions we denote non-line-of-sight-specular (NLOS-S), which contain a strong first-arriving component, we developed a log-distance path loss model with path loss exponent of n=2.23.

Generally speaking, the worst-case channels occur in large airports, in NLOS regions. These channel models contain a large number of multipath components, whose amplitudes fade randomly and often deeply, and as mentioned, in a correlated fashion. The channels measured in the GA airports were less dispersive than those in the large and medium airports.

For transmission from an airport field site (AFS) to a surface vehicle, for the shorter distances, the AFS channel will be less dispersive than if transmission were from the air traffic control tower. This is often true even with fairly low field site antenna heights. In the case of point-to-point transmission from an AFS to the control tower using directive antennas, multipath can be strongly attenuated by the antennas, but stable strong reflections can occur from large buildings. These reflections could be used to advantage in spatial (angle) diversity configurations; at minimum their presence should be kept in mind for selection of site locations and antenna directivities.

The scattering encountered by any vehicle on the airport surface will be non-isotropic in azimuth for all but the rarest of cases (e.g., when a vehicle is completely surrounded by other large vehicles in all azimuth directions). Thus for assessing the rate of fading and Doppler spreading, asymmetric Doppler spectra will pertain. As noted previously, due to the very small velocities expected, this will not generally pose any difficulty for most communication signaling schemes. To generate the very slowly fading random amplitude processes, one generally employs a low pass filter; for the extremely slow fading that will be encountered in the airport surface environment, this approach poses difficulties in implementation due to the very small filter bandwidth required. To circumvent this problem, we use an interpolation method of filtering, which has also been used in other channel modeling approaches such as cellular radio.

7.4 Recommendations

Given our conclusions, the first major recommendation is that any designers who evaluate communication system performance on the airport surface channel in the MLS extension band employ the models we have developed, and do not use models developed for

other environments. Although much can be drawn from work done for other settings (e.g., cellular), the physical environment of the airport surface channel is distinct from other commonly encountered terrestrial environments. For this evaluation, we recommend use of our "sufficient fidelity" models, for the airport size, channel region, and bandwidth of interest. The "high fidelity" models, although "closer to" the actual measured channel (by construction), are complex and computationally intensive; they are thus more of interest from an academic perspective.

Another recommendation would be to extend our path loss models to the NLOS regions, via a small measurement and modeling effort. Since the MLS extension band has no inherent transmit power limitations (as do the unlicensed bands), actual system deployment experiments might suffice to characterize the path loss for these regions without any formal measurement and modeling campaign.

To allow the widest possible use of an airport surface network in this band, some means of extending the network extent to include "terminal airspace" should be devised. For the 5 GHz band, extending the range will necessitate either directional antennas, or fairly high-power amplifiers, or both, depending upon the range desired. For the "takeoff/landing" phase of flight, the channel will be comparatively benign due to the clear line of sight available from the ground site to an aircraft. Depending upon the communication requirements, some mechanism to enable "handoff" from the surface network to the network that carries communications for the takeoff/landing phase of flight, and beyond, might need to be developed.

Finally, the airport surface network is likely to use a mix of mobile and non-mobile (point-to-point) links. These mobile links will most likely be between vehicles on the airport surface and a fixed transceiver, either at the air traffic control tower or an airport field site, although direct mobile-to-mobile links are possible, depending upon the network design. In any case, a carefully designed partition of the band should be done, for allocating portions of the spectrum to the various links. This "channelization" will of course be guided by data throughput and integrity requirements, but should also make use of our channel characterization results, in particular the frequency correlation estimates for the various types of links.

References

[1] D. W. Matolak, "Wireless Channel Characterization: Overview and Application to 5 GHz Band Airport Surface/Terminal Environments," Ohio University Report for NASA Glenn Research Center, May 2004.

[2] D. W. Matolak, "5 GHz Wireless Channel Characterization for Airport Surface Areas: Project Workplan and Approximate Schedule," Ohio University Report for NASA Glenn Research Center, September 2004.

[3] J. G. Proakis, *Digital Communications*, 2nd ed., McGraw-Hill, New York, NY, 1989.

[4] W. Stallings, *Data and Computer Communications*, 7th ed., Prentice Hall, Upper Saddle River, NJ, 2004.

[5] G. Stuber, *Principles of Mobile Communications*, Kluwer Academic Publishers, Norwell, MA, 1996.

[6] S. G. Wilson, *Digital Modulation and Coding*, Prentice Hall, Upper Saddle River, NJ, 1996.

[7] H. V. Poor, G. W. Wornell, (editors), *Wireless Communications: Signal Processing Perspectives*, Prentice Hall, Upper Saddle River, NJ, 1998.

[8] A. F. Molisch (editor), *Wideband Wireless Digital Communications*, Prentice-Hall, Upper Saddle River, NJ, 2001.

[9] L-L Yang, L. Hanzo, "Multicarrier DS-CDMA: A Multiple Access Scheme for Ubiquitous Broadband Wireless Communications," *IEEE Comm. Mag.*, vol. 41, no. 10, pp. 116-124, October 2003.

[10] J. D. Parsons, *The Mobile Radio Propagation Channel*, 2nd ed., John Wiley & Sons, New York, NY, 2000.

[11] D. J. Torrieri, *Principles of Secure Communication Systems*, 2nd ed., Artech-House, Boston, MA, 1992.

[12] M. C. Jeruchim, P. Balaban, K. S. Shanmugan, *Simulation of Communication Systems; Modeling, Methodology, and Techniques*, 2nd ed., Kluwer Academic Press, Boston, MA, 2000.

[13] W. H. Tranter, K. S. Shanmugan, T. S. Rappaport, K. L. Kosbar, *Principles of Communication System Simulation with Wireless Applications*, Prentice-Hall, Upper Saddle River, NJ, 2004.

[14] M. Patzold, *Mobile Fading Channels*, John Wiley & Sons, New York, NY, 2002.

[15] IEEE 802 standards web site, www.ieee.org, 30 September 2005.

[16] H. L. Bertoni, *Radio Propagation for Modern Wireless Systems*, Prentice Hall, Upper Saddle River, NJ, 2000.

[17] W. C. Jakes (editor), *Microwave Mobile Communications*, New York: Wiley, 1974.

[18] M. Schwartz, W. R. Bennett, S. Stein, *Communication Systems and Techniques*, New York: McGraw-Hill, 1966.

[19] P. Bello, "Characterization of Random Time-Variant Linear Channels," *IEEE Trans. Comm.*, vol. 11, pp. 360-393, December 1963.

[20] S. Stein, "Fading Channel Issues in System Engineering," *IEEE Journal on Selected Areas in Comm.*, vol. SAC-5, no. 2, February 1987.

[21] ITU document ITU-R P.1407-1, "Multipath Propagation and Parameterization of its Characteristics," 1999-2003.

[22] H. Suzuki, "A Statistical Model for Urban Radio Propagation," *IEEE Trans. Comm.*, vol. COM-25, no. 7, July 1977.

[23] Y. Okumura, E. Ohmori, T. Kawano, K. Fukuda, "Field strength and its variability in the VHF and UHF land mobile radio services," *Rev. Elec. Commun. Lab.*, vol. 16, Sept.-Oct. 1968.

[24] M. Hata, "Empirical Formula for Propagation Loss in Land Mobile Radio Services," *IEEE Trans. Vech. Tech.*, vol. VT-29, no. 3, 1980.

[25] J. B. Anderson, T. S. Rappaport, S. Yoshida, "Propagation Measurements and Models for Wireless Communications Channel," *IEEE Comm. Mag.*, vol. 33, no. 1, pp. 42-49, January 1995.

[26] ITU document ITU-R 528-2, "Propagation Curves for Aeronautical Mobile and Radionavigation Services Using the VHF, UHF, and SHF Bands," 1978-1982-1986.

[27] ITU document ITU-R P.1411-2, "Propagation Data and Prediction Methods for the Planning of Short-Range Outdoor Radiocommunication Systems and Radio Local Area Networks in the Frequency Range 300 MHz to 100 GHz," 1999-2001-2003.

[28] V. Erceg, L. J. Greenstein, S. Y. Tjandra. S. R. Parkoff, A. Gupta, B. Kulik, A. A. Julius, R. Bianchi, "An Empirically Based Path Loss Model for Wireless Channels in Suburban Environments," *IEEE Journal Selected Areas Comm.*, vol. 17, no. 7, pp. 1205-1211, July 1999.

[29] ITU document ITU-R P.838-2, "Specific Attenuation Model for Rain for use in Prediction Methods," 1992-1999-2003.

[30] W. M. Merrill, H. L. N. Liu, J. Leond, K. Sohrabi, G. J. Pottie, "Quantifying Short Range Surface to Surface Communication Links," *IEEE Antennas & Propagation Magazine,* vol. 46, no. 3, pp. 36-46, June 2004.

[31] W. C. Y. Lee and Y. S. Yeh, "On the Estimation of the Second-Order Statistics of Log-normal Fading in Mobile Radio Environment," *IEEE Trans. Comm.*, vol. 22, pp. 869-873, June 1974.

[32] M. Gudmundson, "Correlation Model for Shadow Fading in Mobile Radio Systems," *Electronics Letters*, vol. 27, pp. 2145-2146, November 1991.

[33] X. Cai, G. B. Giannakis, "A Two-Dimensional Channel Simulation Model for Shadowing Processes," *IEEE Trans. Veh. Tech.*, vol. 52, no.6, pp. 1558-1567, November 2003.

[34] P. A. Bello, "Aeronautical Channel Characterization," *IEEE Trans. Comm.*, vol. COM-21, no. 5, pp. 548-563, May 1973.

[35] E. Lutz, D. Cygan, M. Dippold, F. Dolainsky, and W. Papke, "The Land Mobile Satellite Communication Channel-Recording, Statistics, and Channel Model," *IEEE Trans. Veh. Tech.*, vol. 40, no. 2, pp. 375-385, May 1991.

[36] ITU document ITU-R P.682-1, "Propagation Data Required for the Design of Earth-Space Aeronautical Mobile Telecommunication Systems," 1990-1992.

[37] J. Painter, S. Gupta, L. Wilson, "Multipath Modeling for Aeronautical Communications," *IEEE Trans. Comm.*, vol. 21, issue 5, pp. 658-662, May 1973.

[38] S. M. Elnoubi, "A Simplified Stochastic Model for the Aeronautical Mobile Radio Channel," *Proc. IEEE Vehicular Tech. Conf.*, pp. 960-963, 1992.

[39] E. Haas, "Aeronautical Channel Modeling," *IEEE Trans. Veh. Tech.*, vol. 51, no. 2, pp. 254-264, March 2002.

[40] M. Rice, A. Davis, C. Bettweiser, "Wideband Channel Model for Aeronautical Telemetry," *IEEE Trans. Aerospace and Electronic Systems*, vol. 40, issue 1, pp. 57-69, Jan. 2004.

[41] D. C. Cox, "Delay Doppler Characteristics of Multipath Propagation at 910 MHz in a Suburban Mobile Radio Environment," *IEEE Trans. Ant. Prop.*, vol. AP-20, no. 5, pp. 625-635, September 1972.

[42] T. S. Rappaport, S. Y. Seidel, K. Takamizawa, "Statistical Channel Impulse Response Models for Factory and Open Plan Building Radio Communication System Design," *IEEE Trans. Comm.*, vol. 39, no. 5, pp. 794-807, May 1991.

[43] L. J. Greenstein, D. G. Michelson, V. Erceg, "Moment Method Estimation of the Ricean *K*-Factor," *IEEE Comm. Letters*, vol. 3, no. 6, pp. 175-176, June 1999.

[44] A. Domazetovic, L. J. Greenstein, N. B. Mandayam, I. Seskar, "Estimating the Doppler Spectrum of a Short-Range Fixed Wireless Channel," *IEEE Comm. Letters*, vol. 7, no pp. 5,. 227-229, May 2003.

[45] M. Patzold, U. Killat, F. Laue, Y. Li, "On the Statistical Properties of Deterministic Simulation Models for Mobile Fading Channels," *IEEE Trans. Veh. Tech.*, vol. 47, no. 1, pp. 254-269, Feb. 1998.

[46] E. S. Sousa, V. M. Jovanovic, C. Daigneault, "Delay Spread Measurements for the Digital Cellular Channel in Toronto," *IEEE Trans. Veh. Tech.*, vol. 43, no. 4, pp. 837-847, Nov. 1994.

[47] R. J. C. Bultitude, "Estimating Frequency Correlation Functions from Propagation Measurements on Fading Channels: A Critical Review," *IEEE Journal Selected Areas Comm*, vol. 20, no. 6, pp. 1133-1143, August 2002.

[48] J. Kivinen, X. Zhao, P. Vainikainen, "Empirical Characterization of Wideband Indoor Radio Channel at 5.3 GHz," *IEEE Trans. Antennas & Propagation*, vol. 49, no. 8, pp. 1192-1203, August 2001.

[49] X. Zhao, J. Kivinen, P. Vainikainen, K. Skog, "Propagation Characteristics for Wideband Outdoor Mobile Communications at 5.3 GHz," *IEEE Journal Selected Areas Comm.*, vol. 20, no. 3, pp. 507-514, April 2002.

[50] J. Capon, "Multipath Parameter Computations for the MLS Simulation Computer Program," MIT Lincoln Laboratories Technical Report ATC-68, 8 April 1976.

[51] M. Steinbauer, A. F. Molisch, E. Bonek, "The Double Directional Radio Channel," *IEEE Antennas and Propagation Magazine*, vol. 43, no. 4, pp. 51-63, August 2001.

[52] W. Rummler, "A New Selective Fading Model: Application to Propagation Data," *Bell System Technical Journal*, vol. 58, pp. 1037-1071, May-June 1979.

[53] L. J. Greenstein, M. Shafi (editors), *Microwave Digital Radio*, IEEE Press Selected Reprint Series, IEEE Press, 1988.

[54] C. Oestges, D. Vanhoenacker-Janvier, B. Clerkx, "Wide-Band SIMO 1×2 Measurements and Characterization of Outdoor Wireless Channels at 1.9 GHz," *IEEE Trans. Veh. Tech.*, vol. 53, no. 4, pp. 1190-1202, July 2004.

[55] A. F. Molisch, J. R. Foerster, M. Pendergrass, "Channel Models for Ultrawideband Personal Area Networks," *IEEE Wireless Communications Magazine*, vol. 10, no. 6, pp. 14-21, December 2003.

[56] A. M. Saleh, R. Valenzuela, "A Statistical Model for Indoor Multipath Propagation," *IEEE Journal Selected Areas Comm*, vol. 11, no. 7, pp. 967-978, Sept. 1993.

[57] D. W. Matolak, L. Foore, R. Apaza, "Channel Characterization in the 5 GHz Microwave Landing System Extension Band for Future Airport Surface Communications," *Proc. 5th NASA Integrated Communications, Navigation and Surveillance (ICNS) Conf. & Workshop*, Fairfax, VA, 2-5 May 2005.

[58] I. Sen, D. W. Matolak, W. Xiong, N. T. Yaskoff, "5 GHz Wireless Channel Characterization for Airport Surface Areas," *Proc. 15th Virginia Tech Symp. on Wireless Pers. Comm.*, Blacksburg, VA, June 8-10, 2005.

[59] R. D. Apaza, D. W. Matolak, "Wireless Communications for Airport Surface: 5 GHz Measurement Procedures and Results," *Proc. 11th Ka and Broadband Communications Conf.*, Rome, IT, September 25-28, 2005.

[60] D. W. Matolak, I. Sen, W. Xiong, N. T. Yaskoff, "5 GHz Wireless Channel Characterization for Vehicle to Vehicle Communications," *Proc. MILCOM 2005,* Atlantic City, NJ, Oct. 17-20, 2005.

[61] D. W. Matolak, I. Sen, W. Xiong, N. T. Yaskoff, "Characterization of the 5 GHz Wireless Channel for Small Airport Surface Areas," *Proc. of 24th Digital Avionics Systems Conference*, Arlington, VA, Oct. 30-Nov. 3, 2005.

[62] D. W. Matolak, I. Sen, W. Xiong, N. T. Yaskoff, "Measurement and Modeling Results for the 5 GHz Airport Surface Area Channel: Part I, Large Airports," (in preparation), to be submitted to *IEEE Trans. Veh. Tech.*, 2005/2006.

[63] D. W. Matolak, I. Sen, W. Xiong, N. T. Yaskoff, "Measurement and Modeling Results for the 5 GHz Airport Surface Area Channel: Part II, Small Airports," (in preparation), to be submitted to *IEEE Trans. Veh. Tech.*, 2005/2006.

[64] D. W. Matolak, I. Sen, W. Xiong, N. T. Yaskoff, "New Vehicle-to-Vehicle Channel Models for the 5 GHz ISM Band," (in preparation), to be submitted to *IEEE Trans. Veh. Tech.*, 2005/2006.

[65] S. Weinberg, *The First Three Minutes: A Modern View of the Origin of the Universe*, Basic Books, New York, NY, June 1993.

[66] T. Pratt, C. Bostian, J. Allnut, *Satellite Communications*, 2nd ed., John Wiley and Sons, Somerset, NJ, 2003.

[67] S. Ramo, J. R. Whinnery, T. Van Duzer, *Fields and Waves in Communication Electronics*, John Wiley & Sons, New York, NY, 1965.

[68] Remcom, Inc., world wide web site, http://www.remcom.com, November 2005.

[69] R. C. Qiu, I. T. Lu, "Multipath Resolving with Frequency Dependence for Wide-Band Wireless Channel Modeling," *IEEE Trans. Veh. Tech.*, vol. 48, no. 1, pp. 273-285, January 1999.

[70] R. F. Harrington, *Time-Harmonic Electromagnetic Fields*, McGraw-Hill, New York, NY, 1961.

[71] W. C. Y. Lee, Y. S. Yeh, "On the Estimation of the Second-Order Statistics of Log-normal Fading in Mobile Radio Environment," *IEEE Trans. Comm.*, vol. 22, pp. 869-873, June 1974.

[72] W. R. Bennett, "Distribution of the Sum of Randomly Phased Components," *Quarterly of Applied Mathematics*, vol. 5, pp. 385-393, January 1948.

[73] M-S. Alouini, A. J. Goldsmith, "A Unified Approach for Calculating Error Rates of Linearly Modulated Signals over Generalized Fading Channels," *IEEE Trans. on Comm.*, vol. 47, no. 9, pp. 1324-1334, September 1999.

[74] A. Papoulis, U. Pillai, *Probability, Random Variables, and Stochastic Processes*, 4th ed., McGraw-Hill, NY, NY, 2001.

[75] J. T. Neville, Lewis Educational and Research Collaborative Internship Program (L.E.R.C.I.P.) Summer Internship, NASA Glenn Research Center, Final Report, September 2004.

[76] R. E. Ziemer, R. L. Peterson, D. E. Borth, *Introduction to Spread Spectrum Communications*, Prentice Hall, Upper Saddle River, NJ, 1995.

[77] D. C. Cox, "910 MHz Urban Mobile Radio Propagation: Multipath Characteristics in New York City," *IEEE Trans. Comm.*, vol. COM-21, no. 11, pp. 1188-1194, November 1973.

[78] Berkeley Varitronics, Inc., website, http://www.bvsystems.com/, January 2006.

[79] ITU document Rec.ITU-R M.1225, "Guidelines for Evaluation of Radio Transmission Technologies for IMT- 2000 Systems," 1998.

[80] COST 231 Final Report, world wide website, http://www.lx.it.pt/cost231/final_report.htm, March 2006.

[81] G. Matz, A. F. Molisch, F. Hlawatsch, M. Steinbauer, I. Gaspard, "On the Systematic Measurement Errors of Correlative Mobile Radio Channel Sounders," *IEEE Trans. Comm.,* vol. 50, no. 5, pp. 808-821, May 2002.

List of Abbreviations and Symbols

Abbreviations

2D	Two dimensional
ACAST	Advanced Communications, Navigation, and Surveillance (CNS), Architectures and System Technologies program
AEC	Avionics Engineering Center
AFS	Airport Field Site
A/G	Air to Ground
AM(R)S	Aeronautical Mobile Route Service
ASCII	American Standard Code for Information Interchange
ATCT	Air Traffic Control Tower
BER	Bit Error Ratio
BL	Burke Lakefront Airport (Cleveland, OH)
BPSK	Binary Phase Shift Keying
BVS	Berkeley Varitronics Systems, Inc.
BW	Bandwidth
cdf	cumulative distribution function
CDMA	Code Division Multiple Access
CFAP	Constant False Alarm Probability
CFAR	Constant False Alarm Rate
CIR	Channel Impulse Response
CLE	Cleveland Hopkins International Airport
cm	centimeter
CNS	Communications, Navigation, and Surveillance
dB	decibel
dBm	decibels above 1 milliwatt
DLL	Data Link Layer (of the communications protocol stack)
DS	Direct Sequence
DOD	Direction of Departure
DoD	Department of Defense
FAA	Federal Aviation Administration
FCE	Frequency Correlation Estimate
FEC	Forward Error Correction
FFT	Fast Fourier Transform
FH	Frequency Hopped
GA	General Aviation

G/A	Ground to Air
GHz	giga Hertz
Gi	Goal number i (i=1, 2, …)
GPS	Global Positioning System
GRC	Glenn Research Center
HF	High Fidelity
Hz	Hertz
ICAO	International Civil Aviation Organization
ICNS	Integrated Communications, Navigation, and Surveillance Conference
IEEE	Institute of Electrical and Electronics Engineers
ILS	Instrument Landing System
IRE	Impulse Response Estimate
ISM	Industrial, Scientific, and Medical
ITU	International Telecommunications Union
JFK	John F. Kennedy International Airport
km	kilometer
LAAS	Local Area Augmentation System
LAN	Local Area Network
LOS-O	Line-of-sight-Open
LPF	Low Pass Filter
m	meter
mm	millimeter
mph	miles per hour
ms	milli second
μs	micro second
MAC	Medium Access Control (layer of the communications protocol stack)
MC	Multi-carrier
Mcps	mega Chips per Second
MHz	mega Hertz
MIA	Miami International Airport
MLS	Microwave Landing System
MSD	Mean-Square Difference
NASA	National Aeronautics and Space Administration
NLOS-S	Non-line-of-sight-Specular
ns	nano second
OEM	Original Equipment Manufacturer
OFDM	Orthogonal Frequency Division Multiplexing
Oi	Objective number i (i=1, 2, …)

OU	Ohio University, or Ohio University Airport
PAN	Personal Area Network
pc	personal computer
PDP	Power Delay Profile
pdf	Probability Density Function
PHY	Physical Layer (layer 1 of the communications protocol stack)
PL	path loss
RF	Radio Frequency
RFI	Radio Frequency Interference
RMS-DS	Root-mean-square value of (multipath) Delay Spread
RSSI	Received Signal Strength Information
Rx	receiver
sec	seconds
SF	Sufficient Fidelity
SHF	Super High Frequency
SIMO	Single-Input Multiple-Output
SNR	Signal to Noise Ratio
SS	Spread Spectrum
TA	Tamiami Airport (Kendall, FL)
TDL	Tapped Delay Line
TF	Transfer Function
Tx	transmitter
UHF	Ultra High Frequency
US	Uncorrelated Scattering
USDR	User Selected Dynamic Range
UPS	Uninterruptible Power Supply
UWB	Ultra Wideband
VHF	Very High Frequency
VTV	Vehicle to Vehicle
WAAS	Wide Area Augmentation System
WLAN	Wireless Local Area Network
WRC	World Radio Conference
WSS	Wide Sense Stationary

Symbols

α	attenuation (dimensionless, or in dB)
a	Weibull pdf scale factor
b	Weibull pdf shape factor
β	Weibull pdf shape factor
B_c	Coherence (or, correlation) bandwidth (Hz)
c	speed of light (m/sec)
δ	delta function (ideal impulse)
d_0	reference distance (m)
ES	Markov chain emission matrix
f_c	carrier frequency (Hz)
f_d	Doppler shift (Hz)
f_D	Doppler spread (Hz)
ϕ	phase (radians)
h	CIR function
H	channel transfer function
K	in Ricean distribution, parameter K indicates fading severity
λ	wavelength (m)
L	impulse response length
m	in Nakagami-m distribution, parameter m indicates fading severity
μ	mean value
μ_τ	mean value of energy delay (sec)
MT	Multipath Threshold (dB)
NT_j	noise threshold of jth power record
P_t	Transmit power (watts, or dBm)
P_{ij}	Transition probability, from state i to state j
ρ_s	spatial correlation (dimensionless)
ρ_t	temporal correlation (dimensionless)
$r_{i,j}$	correlation coefficient between amplitude of channel taps i and j (dimensionless)
R_α	Correlation coefficent matrix of vector α
R_c	Chip rate (chips/sec)

R_s	Symbol rate (symbols/sec)
Region_TS	Markov chain transition matrix for a given propagation region
Region_ES	Markov chain emission matrix for a given propagation region
σ	standard deviation
σ_τ	standard deviation of delay spread
t	time (sec)
τ	delay variable (sec)
t_c	Coherence (or, correlation) time (sec)
T_c	Chip duration (sec)
T_M	Multipath Delay Spread (sec)
TS	Markov chain transition matrix
Ω	average energy or power (mean-square value of random process)
W_{90}	90% energy delay window
z	persistence random process

Appendix A. Motivation for Heightened Interest in MLS Band

As noted in Chapter 1, the MLS extension band is great current interest to the aeronautical community. It is not widely used at present, and because of this, it is subject to scrutiny by national and international organizations in charge of allocating and regulating spectrum usage. Specifically, the International Civil Aviation Organization (ICAO) is working to ensure that this spectral band remains allocated for aeronautical services.

The use of the MLS band, and in particular the extension band, has been scrutinized for several reasons. First, GPS navigation and WAAS/LAAS enhancements were circumventing the need for MLS deployments, thus leaving much of the MLS band either quiet or underutilized. Second, the spectrum in the area of 5 GHz presents an enormous potential for revenue to short range, wideband wireless networking OEMs (i.e., 802.11 systems). Third, spectrum auctions in or near this band present potential revenue streams for the federal government. The combination of these factors has emphasized the need to justify the continued use of this spectrum for aviation purposes.

For this effort, various groups in ICAO are preparing documents for submission at the International Telecommunication Union's (ITU) World Radio Conference (WRC), whose next major meeting is in 2007. At these conferences, member nations discuss and decide upon the global use of radio spectrum for multiple applications. Supporting ICAO in the effort to protect the MLS extension band are the United States Federal Aviation Administration, and the European Union's aviation administration, EuroControl. Through the ACAST project, NASA's intent was to demonstrate the applicability of this band for wideband airport surface area signaling. Enabling wideband signaling could potentially alleviate some of the congested VHF voice bands used by pilots and air traffic controllers. The first step in this effort was a thorough characterization of the MLS band radio channel. This characterization will support a sound engineering argument for the use of this band for wideband signaling on the airport surface, and hence provide real evidence that the aeronautical community is serious about utilizing the band, hence justifying that this band should be included in regards to Agenda Item 1.6 in preliminary views.

At the WRC-2007, the allocation of various aeronautical bands from 108 MHz to 6 GHz will be under discussion. One of ICAO's intents is to reserve these bands to allow development of *new* aeronautical mobile route services (AM(R)S). It is intended that the MLS band channel characterization effort support the inclusion of the MLS band as an integral piece of the modernization of the civil aviation communication systems.

Appendix B: Original Work Plan Objectives Document

This appendix contains the original project plan and objectives. It was an unofficial "final draft" version. The proposed schedule and some of the objectives were superseded as the project progressed. The section headings were re-labeled to fit this appendix. The reference list repeats some citations from the main report, but was left as it was, so that this appendix is self-contained.

---

5 GHz Wireless Channel Characterization for Airport Surface Areas: Project Workplan and Approximate Schedule

David W. Matolak
23 September 2004

The purpose of this document is to specify the work plan for the wireless channel characterization project. We aim to specify the required tasks as explicitly as possible for all phases of the work. This plan, which will be modified accordingly throughout the project, will also depend upon available equipment, personnel, schedule constraints, and any unforeseen problems or program changes. [Although such a plan is not specifically required for the grant, for maximal quality and quantity of work outputs, we will work closely with both NASA and the FAA in planning and conducting this work.]

In Section I we provide the initial task plan [B1], and provide a status update. Section II lists planned objectives and Section III describes the project deliverables. In Section IV, we provide a list of required and desired support from NASA/FAA for conducting the work. Finally, in Section V, the work plan for the year is described in some detail.

B.1 Initial Task Plan

1. *Literature Review and Initial Parameter Bounding*: the initial parameter bounding has been done, and may be revised slightly, in the upcoming month. The initial literature review is complete. We are currently developing a project literature list, as literature review will be ongoing throughout the project.

2. *Channel Classification*: this task was to use detailed data on airport size, building characteristics, dimensions, and local area information to classify airports into various categories, where each category would be associated with a particular set of channel characteristics. Difficulty in obtaining the required data has postponed this task; ultimately it may be done only after all measurements are taken, and then at a fairly high level. At present, we plan to use the classifications of small and large airports only.

195

3. *Software Modeling of Attenuations, Delay Spreads, and Validation*: standard channel path loss (attenuation) models have been developed, in MATLAB®. The framework for incorporating a new model based upon conventional $(distance)^{-n}$ models is in place, and either this model or a new one will be easily developed once measured data is obtained. The framework for the (statistical) dispersive channel models is currently being developed, and will also be refined once measurements are obtained. We also plan to purchase some commercial propagation modeling software, by RemCom. This package will enable modeling of channel impulse responses given some input data regarding the environment, and can be used to aid in the development of both of our new models (path loss and impulse response).

4. *Channel Sounding & Interference Characterization*: We plan to do interference characterization when we take the sounding measurements, using a spectrum analyzer. Both short term and some longer term (~hour) measurements will be taken at different times of day. The channel sounder will likely be able to measure propagation path loss with some level of accuracy, but it would be desirable to also measure narrowband path loss, which will require a 5 GHz tone source. Ideally, path loss vs. distance would be measured over an area, radially away from the Tx, in moderate distance increments, whereas the channel impulse response (CIR) measurements would ideally follow aircraft landing and taxi routes. The channel sounder will be used to collect many CIR measurements at each airport, at a number of locations, and for both stationary and mobile receiver conditions.

5. *Channel Simulations and Analysis*: as noted above in task 3, a path loss routine has been developed, and the dispersive (tapped-delay line) channel model is under development. The dispersive channel model will allow an arbitrary number of channel taps, each with its own independent statistics, and Doppler spectrum. All these will be done in MATLAB. The basic model statistics (#taps, amplitude, phase, pdf, Doppler, Rice/Nakagami factor, etc.) will be updated as measurements are taken. Analysis of the model consists first of deriving statistics from measured data, then validating the developed models against the measurements.

6. *Refinement*: This will be ongoing throughout the project, as we learn more regarding both the path loss and CIR models.

B.2 Project Objectives

These objectives, from [B2], are comprehensive, and constitute the ultimate goals of the project. They are closely aligned with the initial tasks described above, and provide more detail. It is likely that after one year of this effort, we may still have some uncovered work that can be conducted in the future. A set of "minimal," or "critical" goals, based upon a subset of the objectives, will be created as part of the first phase of the work.

1. *Channel classification*: ideally we will devise a channel classification method, which will define the various classes of airport channels. The definition will be as precise as is feasible, and will include factors such as building density and composition on/around the airport, amount and type of local foliage, and the surrounding terrain features. We will also provide example airport listings for each of the channel classes. We anticipate at most 3 or 4 channel classes, but this

depends highly upon the type and quantity of data we obtain on airport environments. At minimum, we can classify into large and small airports.

2. *Path loss models*: the ideal goal for this objective is to specify which path loss model is most appropriate for each class of channel. Standard models such as free-space, plane-earth, and empirical models such as Okumura-Hata, and the COST models [B3] will be explored and compared with measured results. Parameter definition will be based upon measurements. For narrowband measurements we will require a signal generator that can output a sinusoidal tone in the 5 GHz band (we already have the receiver—a spectrum analyzer). If this is possible, for cases where a line-of-sight (LOS) exists between transmitter and receiver, we can estimate a Ricean *K*-factor with received power vs. time data via the method given in [B4]. In addition, commercial propagation modeling software (RemCom) will be employed to assist in path loss modeling.

3. *Power delay profiles*: the goal for this objective is to both model and measure power delay profiles for as many airport channels and conditions as possible. The profiles obtained should
- account for variation with link range
- provide data on time variation, to allow development of channel "tap" statistics. This will allow computation of typical fading statistics such as approximate probability density functions, and other statistics such as the level crossing rate, and average fade duration [B5], useful in waveform design
- enable computation of rms and maximum values of delay spread, mean excess delay, and the "shape" of the profile (typical shapes have included exponentially decaying, linearly decaying, and uniform). The time and spatial variation of the profile shape is also of interest.
- take into account the use of directive antennas
- enable plotting of the channel scattering function [B5], which depicts received signal power versus both delay and Doppler shift (related to objective 4)

The modeling will initially employ the commercial propagation software, as feasible—model accuracy will be a strong function of the number and quality of input parameters. Depending upon the measured statistics obtained, new software models will be developed (in MATLAB®). Also, channel coherence bandwidths for the time-series data of received signal samples at a given delay will be computed (via FFT).

4. *Doppler power spectra*: the goal of this objective is to obtain both software estimates and measured values for Doppler spectra of received signals. The Doppler spectra for most cases are not likely to conform to the conventional "Clarke" spectrum shape, as assumed in sections of [B6], since scattering about the receiver is not likely to be uniform in much of the airport environment. As noted in objective 3, we will ideally combine these spectra with the power delay profiles to obtain scattering function plots. The two primary parameters for which estimates are to be obtained for each channel class are the Doppler spectrum shape, and the maximum Doppler spread. The time variation of the Doppler spectra is also of interest.

5. *Database development*: all measurement data and pertinent statistical parameters and their extrema derived from these measurements will be compiled into a repository for future use.

Developed software models will also reside here, along with a description of their appropriate use and application.

B.3 Deliverables

Some deliverables for this work were also described in [B2], and are listed next. As with the objectives themselves, the deliverables will be adapted according to limitations and customer needs.

1. *Test plan description*: a thorough test plan is essential to the conduct of efficient measurements that yield desired results. Naturally, the test plan will evolve as measurements are taken, and data analysis is conducted. We envision the following
- An initial test plan, created before any measurements are taken
- A first revision, modified from the initial plan after "trial run" measurements are taken at the Ohio University airport
- A second revision, modified from the first, after measurements are made at one or more large airports
- A final version, to be provided after several sets of measurements are obtained. This final version will likely be produced no sooner than all measurement efforts of the first year are completed.

Also to be developed, prior to taking any measurements at airports, is a list of items and resources needed from airport operations organizations, including such things as approximate test duration and time of day preferences, number and specific buildings we need access to, radiating antenna locations, equipment powering (AC) requirements, and measurement receiver mobility requirements (e.g., access to taxiways, runways, etc.). A separate document specifically detailing these items is being developed; an earlier version of the required items and resources appears in the next section.

2. *Data and post-processing files from all measurement efforts*: these files will contain the actual measured data obtained from measurement efforts. This will include the "raw" data that the channel sounder provides, organized at minimum according to time, date, airport, transmit power, antenna type, and physical locations within the airport. Collecting and deriving statistics for the measured data will require development of some software (likely again in MATLAB®). These software routines will also be provided.

3. *Interim briefing*: after at least one measurement effort at a large airport, we will conduct a project briefing, whose goals will be to review progress, report problems and plan for solutions, and discuss modifications to the testing and characterization for future efforts. Example results will be presented. Naturally, throughout the project, discussions with appropriate NASA and FAA personnel will be ongoing.

4. *Software models*: this will include specification of the models and all parameters for modeling both attenuation and delay profiles in the commercial propagation software package (RemCom).

In addition, the software models developed to simulate the channel (MATLAB) will also be provided.

5. *Year-end report*: the contents of this report will include at least the following
- pertinent parts of the literature review and a comprehensive reference list
- initial channel parameter bounds
- both software modeled and measured channel parameters and their statistics
- discussion of measurement procedures and any problems
- example measurement data and interpretation
- interference characterization results
- proposed channel models and example model outputs and how they can be used
- plan for future measurement and modeling to close gaps and extend the database
- proposed budget for future efforts.

B.4 Required & Desired Support

This section lists expected support required (and "desired") from both NASA and the FAA for completion of the main objectives of the work planned for characterizing the wireless channel in the 5 GHz band around airports. Much of the planned analyses and computer simulations can be done with minimal support; review of these tasks' progress, findings, and general course will be sought continually throughout the project. One of the primary forms of support will be the assurance of efficient and timely access to airport facilities for conducting measurements.

1. *Airport access for measurements*: as noted, this will be one of the most critical items of support required for project success, particularly in terms of measurements. We will require the ability to gain access to several airports. This will mean the ability to set up the wireless channel sounder transmitter either inside or outside a (tall) building, and the ability to set up the sounder receiver on the airport surface. Ideally, the receiver will reside in a vehicle (for some cases, the Avionics Engineering Center (AEC) mobile van), so that actual platform mobility effects are incorporated into the measurements. In addition, obtaining actual permission (possibly a "license") to radiate energy in the 5 GHz band (from 5.091-5.15 GHz primarily) will be needed. As noted above under the test plan description (Deliverable #1), we will compose in a separate document a more explicit list of resources and access areas needed for completion of measurements at airports.

2. *Review of measurement procedures*: for all measurements, a test plan will be created, and we will require review of the test plan by both NASA and FAA personnel. As noted in [B2], the test plans will naturally evolve as we gain experience with both the actual measurement procedures, and the data post-processing required to obtain the desired channel statistics.

3. *General "ACAST guidance"*: given that the entire channel modeling effort is aimed at providing input for future wireless network designs, any characteristics of the envisioned network will be useful in guiding the channel modeling most fruitfully. Thus we desire recommendations/requirements on waveform characteristics, minimal capacity/data rates,

multiple access (MA) requirements, ranges, performance requirements, security requirements, siting requirements, etc.

4. *NASA/FAA data access*: access to any pertinent NASA and/or FAA publications, databases, software that pertains to the channel modeling will be, as with item #3, helpful in ensuring the thoroughness of the work.

5. *Equipment*: for completing this project, both hardware and software will need to be acquired. Several of these items have been discussed in other documents, but we list here the most critical ones. While this may not be explicitly classified as "support," the equipment is so crucial to the success of the project, that we list it for completeness.
- 5 GHz wireless channel sounder (Berkeley Varitronics)
- 5 GHz signal generator (tone) for path loss measurements (possibly via upgrade of our existing Agilent signal generator, which currently has an upper frequency limit of 3 GHz)
- one laptop computer dedicated to the channel sounder for data collection and initial processing
- Remcom wireless channel propagation software
- Two omnidirectional antennas
- One directional (standard gain horn) antenna
- Optional RF power amplifier for extending sounder measurement range
- Miscellaneous RF cables, connectors, attenuators, etc.
- Digital camera for recording measurement environment images

We will make use of as much of our existing equipment as possible. This includes a spectrum analyzer, various computers, the AEC mobile test van for some locations, and miscellaneous RF hardware.

B.5 Work Phase Definition

Phase 1: August 2004—December 2004

This phase will require the organization of the work, and the scheduling of the various tasks. Goals for this phase include the following:
1. Compilation of literature list, updated throughout the project
2. Compilation of initial list of bounds on parameter estimates: path loss, delay spread, Doppler spread
3. Compilation of reduced subset of "critical" or "minimal" objectives for project success.
4. Completion of SW path loss model framework development in MATLAB (validation with RemCom, if possible); parameters to include, as needed, are airport type, carrier frequency, antenna heights, LOS presence/absence, etc.
5. Design and development of framework for dispersive (tapped delay line) CIR model, that enables user selection of
   a. # channel taps L

b. amplitude & phase statistical distribution: for amplitude, from Rayleigh, Rician, Nakagami, lognormal, and for phase, uniform and Gaussian; for LOS case, both Rice factor and $f_{D,LOS}$ specified; allow for future inclusion of any NEW derived distributions

c. power delay profile: relative power in each tap, either individually, or via PDP shape (exponential, uniform, linear, etc.)

d. tap Doppler spectrum: classical (Clarke), Gaussian, conventional lowpass, including any LOS Doppler, etc.

e. number of total samples generated, and any normalizations (e.g., mean power=1)

f. (future work): multi-state modeling, which requires development of a switching process. For this application, likely only 2 states (e.g., LOS and NLOS), and only one (or a few) switch(es) per run, to emulate different phases of flight such as landing→taxi. This will require change in average power, and change in tap stats such as Rician→Rayleigh, and high→low Doppler

6. Development of initial test plan: first for measurements in Stocker, then at the OU airport, then the general plan for a larger airport (possibly Detroit)

7. Collection of information on MLS signal and spectra (consult Dr. M. DiBenedetto, OU AEC). Obtain information on what is required to operate MLS at OU airport, and if needed and feasible, plan for MLS signal spectrum measurements.

8. Development of equipment list and potential vendors, for basic conduct of measurements. This includes antennas, cables, connectors. If possible, purchase minimal RF equipment set to enable sounder use.

9. Receipt of funding increment; placement of sounder order

10. Receipt of additional funding increment; purchase of RemCom Wireless InSite Software, followed by initial developments of RemCom path loss models, and CIR models, first for indoors at 2.4 GHz, then for the OU airport. Path loss models at 2.4 GHz can be experimentally validated for calibration and experience.

11. Order remaining equipment for measurements (laptop, horn antenna, cables, etc.)

12. Receipt of channel sounder, followed by initial calibration and simple testing (indoor, at Stocker Center)

Personnel Required: PI Matolak; Graduate Students: Sen, Xiong, Yaskoff, occasionally Neville

Resources Required: literature, MATLAB & pcs, spectrum analyzer, signal generator (for 2.4 GHz path loss measurements), and the RemCom Wireless InSite SW, Berkeley Varitronics Channel Sounder and laptop pc, miscellaneous RF hardware

Phase 2: December 2004—April 2005

This phase will correspond to the first sets of measurements. Ongoing model development will take place concurrently, as will any literature list updating. Goals for this phase are as follows:

1. Finish indoor channel sounding in Stocker Center. Perform data analysis for PDP statistics, and Doppler. Incorporate observations/issues into test plan, and refine test plan for first outdoor measurements.
2. Conduct outdoor measurements at OU airport: if possible, perform path loss measurements at 5 GHz first. Then use Sounder to take PDP measurements at various distances, and for various GG (& GA?) settings, including LOS and NLOS, non-mobile and mobile. Also, if available, employ directional antennas and repeat some measurements.
3. Perform data analysis on OU airport channel data. Derive PDP statistics including mean, max delay spreads; PDP shapes; amplitude histograms and fitting to pdfs; mean and max Doppler spreads, and Doppler power spectrum shapes; Rice factors; composite scattering functions; estimation of coherence bandwidths and coherence times; and identification of anomalies for future study. Communicate findings to NASA/FAA.
4. RemCom SW analysis of OU airport channel (path loss & CIR). Compare with measured data, and refine model parameters. Develop initial models for large airport.
5. Begin design of channel characterization database, including measured data, models, etc.
6. Revise test plan for measurements at a large airport. Coordinate travel, equipment shipping, airport access, and FAA/NASA support required for sounding at large airport.
7. Conduct sounding at large airport #1. Revise test plan as needed. Communicate findings and process to NASA/FAA, including anomalies, impediments, and successes.
8. Perform data analysis on airport #1 measurements, as per step 3 here. Identify gaps and anomalies, and incorporate into test plan.
9. Incorporate measured channel statistics into MATLAB software models.
10. Interim project briefing to NASA/FAA.
11. Conduct sounding at large airport #2 as per step 6 here.
12. Data analysis and test plan refinement as per step 7 here.
13. Incorporate sponsor input and all experience gained to refine test plan again, for subsequent large airport measurements.

Personnel Required: PI Matolak; Graduate Students: Sen, Xiong, Yaskoff, occasionally Neville, one AEC engineer, possibly also an undergraduate student

Resources Required: literature, MATLAB & pcs, spectrum analyzer, signal generator (if we can obtain one for 5 GHz path loss measurements), RemCom Wireless InSite SW, Berkeley Varitronics Channel Sounder and laptop, miscellaneous RF hardware, AEC van, access to airports

Phase 3: April 2005—August 31, 2005

This phase is the final phase of the project first year. Goals for this phase are as follows:

1. Conduct sounding at large airport #3. Again, revise test plan as needed. Communicate findings and process to NASA/FAA.
2. Data analysis and test plan refinement as per step 7 of Phase 2.
3. Schedule channel characterization year-1 final project briefing and outline year-1 final report, coordinating contents with NASA/FAA.
4. Complete incorporation of measured channel statistics (both path loss and CIR) into MATLAB SW models. Validate these models against measured data sets.
5. Identify key gaps in project to date, and develop plan for a few additional measurement efforts to fill these gaps.
6. Complete project briefing and year-1 final report. Final report to include summary of key channel characterization findings, including those most pertinent to waveform and multiple access network design.
7. Submit channel characterization database to NASA/FAA.

Personnel & Resources Required: same as for Phase 2.

References

[B1] D. W. Matolak, "Wireless Channel Characterization: Overview and Application to 5 GHz Band Airport Surface/Terminal Environments," Ohio University Report for NASA Glenn Research Center, May 2004.

[B2] D. W. Matolak, "5 GHz Airport Wireless Channel Characterization Objectives and Associated Deliverables," DRAFT document for NASA GRC, 26 July 2004.

[B3] G. Stuber, *Principles of Mobile Communications*, Kluwer Academic Publishers, Norwell, MA, 1996.

[B4] L. J. Greenstein, D. G. Michelson, V. Erceg, "Moment-Method Estimation of the Ricean K-Factor," *IEEE Comm. Letters*, vol. 3, no. 6, pp. 175-176, June 1999.

[B5] J. D. Parsons, *The Mobile Radio Propagation Channel*, 2nd ed., John Wiley & Sons, New York, NY, 2000.

[B6] M. Haas, "Aeronautical Channel Modeling," *IEEE Trans. Vehicular Tech.*, vol. 51, no. 2, pp. 254-264, March 2002.

Appendix C: Detailed Test Plan and Procedures Document

This appendix provides descriptions of the test plan and procedures used for conducting the channel sounding measurements. It is the final version of a test plan and procedures document written and updated throughout the project. As such, some material is specific to JFK International Airport, the last large airport at which sounding measurements were made. Section headings were re-labeled to fit this appendix. The reference list repeats some citations from the main report, but was left as it was, so that this appendix is self-contained.

ACAST 5 GHZ Wireless Channel Characterization: Test Plan

David W. Matolak
School of Electrical Engineering and Computer Science
Avionics Engineering Center
322E Stocker Center
Ohio University
Athens, OH 45701
phone: 740.593.1241
fax: 740.593.0007
email: matolak@ohiou.edu

Version 4
July 2005

C.1 Introduction

This document serves as a working plan, or "framework," for the measurements done for characterizing the wireless channel in the 5 GHz microwave landing system (MLS) "extension band," from 5.091-5.15 GHz, around airport surface areas. This project is supported by the NASA Advanced CNS (Communications, Navigation, Surveillance) and Systems Technologies (ACAST) program [C1], and the Federal Aviation Administration (FAA) research office. The objectives for this work were outlined in [C2]. Briefly, the objectives are to take measurement data in the form of power delay profiles (PDPs), and to use this data to develop models for both propagation path loss (PL) and channel impulse response (CIR) characteristics. The measurements will be automated as much as is possible, and to this end, a wideband measurement set—the channel sounder—is employed. This channel sounder is a modified version of the "Raptor" spread spectrum stepped correlator by Berkeley Varitronics Systems, Inc. [C3]. Additional details regarding the sounder, and the other major equipment components, are given in a subsequent section.

As with any test plan, this document will need to be updated on occasion to take into account unforeseen circumstances and conditions, and alterations in the testing procedure based upon experience with initial tests. Thus far, the document has had only minor revisions after each of the measurement campaigns at the two large airports, Cleveland in March 2005, and Miami in June 2005. In addition, local environment characteristics unique to a given area may necessitate revisions to procedures, or omissions of some test activities. Thus far, the procedural

steps employed have not changed significantly; if any significant test planning or procedural changes are needed, they will be recorded for future reference.

The test plan is divided into several sections: Section C.2 discusses logistics, and the actual activities undertaken by the project personnel. Actual specifics in this version of the test plan pertain primarily to testing at the John F. Kennedy (JFK) International airport in New York City, NY. The previous versions, upon which this version is largely based, pertained to testing at both Cleveland Hopkins International and Miami International airports. As noted, only minor changes have been made between test plan versions, and each version of the plan has improved its accuracy. Testing has also been performed at smaller airports. The test procedures are generally the same at the small airports as at the large.

Section C.3 provides a description of the test equipment employed. Additional detail on the sounder specifications, photographs, and example outputs, are provided in Section C6. In Section C.4, the specifics of the test plan for conducting PL measurements are provided, and Section C.5 provides a description of the test plan for the conduct of the CIR measurements. These two channel characteristics are closely related, and all of the measurements are actually taken simultaneously—the division of the description into separate sections is done for clarity. Section C7 provides a detailed description of the actual test procedures.

As described in [C2], the resulting measured data will form the basis for the channel models to be developed in this project. The actual models will require a substantial amount of data processing, in order to obtain statistics for the key channel parameters. These parameters are described in some detail in [C2]. The project final report will describe the processing, analysis, and results that constitute the channel models.

C.2. Logistics

Each airport environment in which measurements are taken is unique. Nevertheless, in this section we address aspects of the testing that should be applicable to most, if not all settings.

C.2.1 Physical Configuration and Considerations

To emulate future potential deployments, we wish to configure the tests so that the channel models developed closely represent what would be encountered in an actual working airport surface communication system. Thus, we mount the transmitter antenna at a fairly high elevation, with a clear view of the surrounding airport surface. This has been at or near the top of the air traffic control tower (ATCT) (e.g., on a "catwalk"). To discern the significance of the effect of transmitter antenna height upon the propagation characteristics, if time and space permit, we could also repeat measurements with the transmitter antenna at a lower elevation. Ideally this lower elevation location would be directly beneath the tower antenna position. This additional location for "low antenna elevation" tests will need to be identified prior to testing. Thus far, we have not had time to test with the transmit antenna at a lower height; we have though deployed the transmitter on the airport surface for some additional mobile testing.

The 5 GHz antennas we use are of two general types: omnidirectional, and directional. In either case, the physical size of these antennas is not large. Mounting at the fixed transmitter site is via our custom built wooden platform, which has two shelves, the lower one to support the

transmitter electronics and any other miscellaneous devices (e.g., power cords), and the upper shelf to support the antennas. A photograph of this platform, along with the channel sounder transmitter and antennas, on the "catwalk" at the Cleveland Airport ATCT, is shown in Figure C.1. Depending upon weather conditions (primarily winds), we may need to secure the platform to a part of the building structure (e.g., hand rails). If precipitation is possible, we also cover the transmitter with a tarpaulin. Testing can proceed during rain if needed, but thus far we have not conducted measurements in rainy conditions. The primary concern is safety of the transmitter electronics and personnel. (The receiver electronics are secured inside a van, safe from the elements.)

We perform a "pre-test" "walkthrough," or "survey," prior to any testing, to help determine any physical constraints, and the actual physical stabilization method(s) we will employ. This "walkthrough" also enables us to determine other physical configuration issues such as connection to AC power, etc. The transmitter antenna main beam (even for the omnidirectional antenna) will need to be "downtilted" toward the ground slightly, as is done in terrestrial cellular applications, so that reception is possible directly beneath the tower. The amount of downtilt is estimated from the measured radiation pattern of our antennas, and can be adjusted during testing if needed.

For the sounder receiver, we move around the airport surface in a van. This van conveys the sounder receiver, laptop pc, cables, and the antenna, which ideally will be mounted atop the van roof. The receiver operates on battery power. For the point-to-point (non-mobile) measurements, we mount the directional antenna on a tripod, and keep the sounder receiver and laptop pc close by.
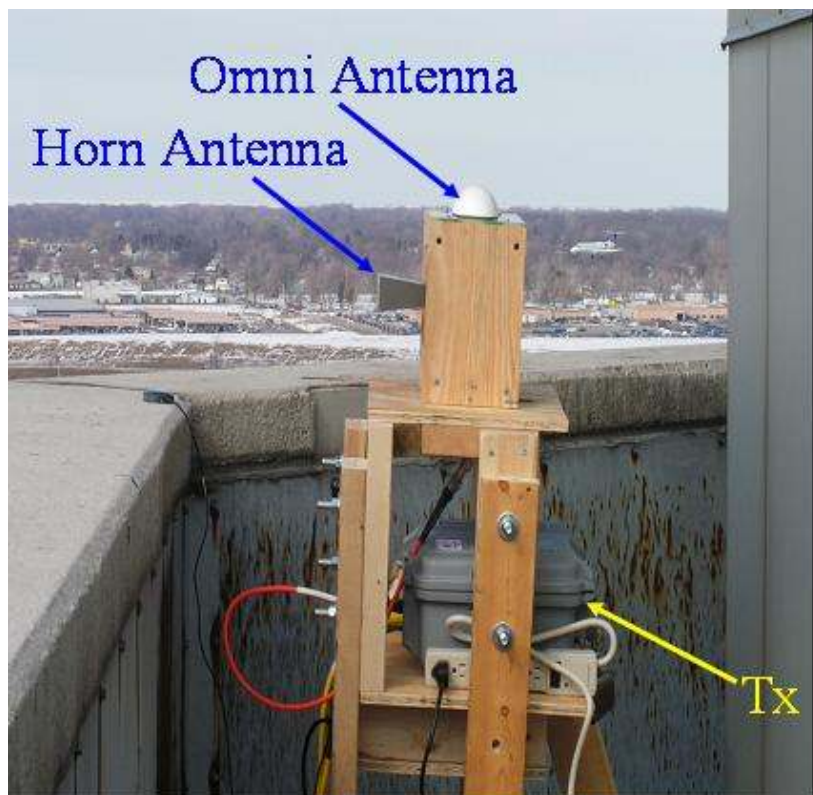

Figure C.1. Photograph of channel sounder transmitter (Tx) and antennas on the ATCT "catwalk" at Cleveland Hopkins International Airport.

C.2.2 Mobility

For both the PL and CIR measurements, we measure as a function of spatial dimensions and location. Specifically, for PL we would ideally measure as a function of the distance between transmitter (Tx) and receiver (Rx). Both line of sight (LOS) and non-LOS (NLOS) conditions are sampled. The accuracy of measuring the Tx-Rx distance is not critical, but the channel sounder transmitter and receiver both have internal GPS receivers that can be used to compute Tx-Rx distances reasonably accurately (an accuracy of approximately 1 meter is adequate for our purposes). If local GPS correction information is available (for example, for the tower), then fairly accurate distance measurement will be possible by post-processing the Tx and Rx GPS data.

The transmitter is fixed in position, and the receiver is mobile (except for the point-to-point measurements, where the Rx is also fixed). The receiver is portable, and can even be hand-carried, but since the data output from the receiver must be logged by a laptop computer, hand-carrying is cumbersome. Thus, as noted, we traverse distances on the airport surface primarily by vehicle. We provide a detailed description of the desired "sampling" areas and travel routes for FAA review and adjustment, based upon airport aerial photographs; an example of this is provided in a subsequent section of this document. In the tests in Cleveland, one of the Avionics Engineering Center's (AEC) mobile vans was used for mobile reception; for the Miami testing, we had use of an FAA/airport van. Any vehicle used for this task should have room for mounting the receiver antennas, and room for at least two persons in addition to the driver; the availability of independent power for the equipment is also desirable, but not essential.

For PL measurements, ideal testing would be done by traveling radially away from the transmitter location, at multiple radials that span a large angular range, e.g., 180° or more. At each radial position (distance), the PL measurement would be taken at several points separated by at least a quarter-wavelength (wavelength λ is approximately 5.8 centimeters), and the results averaged. Due to the extremely small value of wavelength, precision is difficult, but fortunately not necessary. Even with a moderate vehicle velocity (several meters/second) and a measurement update rate of several times per second, a large amount of useful data can be obtained quickly. Alternatively, traveling at a constant distance (circumferential route about the Tx) would enable good path loss data collection for that specific distance, and repeating at multiple values of distance would allow accurate subsequent model development. Either of these approaches would enable a very large number of sample points for developing a path loss vs. distance model.

For practical reasons, and so as not to interfere with airport operations, the number of radials and circumferential routes for which this can be done will likely be small (typically zero, in the strict senses of these terms), hence the PL is "sampled" at far fewer distance points. This does not pose a problem as long as a sufficient number of points at a given distance (e.g., 10 or more) are used. Our travel routes cover points along typical airport vehicle routes, where by airport vehicle we mean both ground vehicles and taxiing aircraft.

For the CIR measurements, the ideal travel routes are exactly those traversed by the airport ground vehicles. As with the PL measurements, there are limitations to this, so we sample spatially at points along as many "real" routes as is feasible. Because of channel dynamics, there may be cases where the measured power delay profile (PDP) is observed to change rapidly due to either mobile receiver motion or movement of local scatterers. In the former case, we may wish to repeat some measurements with the channel sounder configured to

search over a smaller range of delays with a faster PDP output rate. The latter type of effect (motion of local scatterers) can only be captured when the sounder is already in this mode.

The testing personnel consists of teams at both the transmitter and receiver, and having one person at each end observing the local environment, and relaying observations to those operating the test equipment, may allow "flagging" of the associated PDPs that correspond to measurements taken during significant scattering environment changes (e.g., an aircraft moving quickly nearby). In previous testing (at Cleveland), we also found it useful to identify explicitly the LOS and NLOS regions so that data files could be tagged appropriately. Having a second test team member at the receiver specifically dedicated to taking notes regarding the physical environment (e.g., passing near building, moving aircraft between Tx and Rx, etc.) is also extremely valuable. By making marks on the airport surface with paint, we can return to the same spot on the surface multiple times, for repeated measurements.

Finally, for the potential deployment of fixed (non-mobile) links, we take measurements of both PL and CIR at designated fixed stations on the airport surface, some of which may be current data collecting points for airport communications (for example, at Cleveland, we measured from near the radar site, and an RTR site). These measurements use directional antennas to ascertain the spatial (azimuth) variations of channel parameters at these points.

C.2.3 Calibrations

For both PL and CIR measurements, the equipment must be calibrated before data collection begins. The sounder manufacturer recommends a warm-up time for the sounder Tx and Rx of at least thirty (30) minutes. This is to ensure the stability of the precise Rubidium oscillators used to frequency-lock the Tx-Rx pair. For a measurement period of approximately T_t minutes, the Tx and Rx are connected back to back (via cable) during a training period, and "trained" for approximately $2T_t$ minutes. Typically we desire T_t to be at least 60 minutes, to enable sample measurements at all the desired airport locations. We can also train the units over night, to minimize time dedicated to training during the day, and maximize reliable testing time. For overnight training, we must keep the units (both Tx and Rx and their power supplies, and the laptop pc) at the Tx location overnight, in preparation for the morning test runs. For the afternoon test runs, we train the unit during midday. In both cases, we train via AC power, then switch the Rx to battery power for mobile testing.

In Cleveland, we "surveyed" the local frequency spectrum in our band of interest. This amounted to measuring the local power spectrum in the frequency band with a spectrum analyzer (SA). The SA was set to sweep the frequency range at various rates and frequency resolutions. No spurious transmissions were identified. Since it is believed that the frequency band should be "quiet," and this was confirmed in Cleveland, we do not plan to survey the spectrum in future testing unless we have reason to believe there may be interference present. If needed, the spectrum survey can be done just before the channel sounder is in its "warm up" period.

Path loss modeling is typically done using a "*10nlog$_{10}$(distance)*" formulation, where the parameter *n* is denoted the path loss exponent. Most often this path loss equation is given in the following form [C4]:

$$PL(d) = A + 10n\log(d / d_0) + X \qquad\qquad (C.1)$$

where the path loss at Tx-Rx distance d, *PL(d)*, and quantities A and X are in decibels (dB), and distances d and d_0 are typically in meters. The parameter A can be thought of as a "fitting parameter," that in effect adjusts the intercept point of this equation: the path loss is a linear function of the logarithm of the distance ratio d/d_0. The parameter A is found by using the known transmit power, antenna gains, and RF line losses, along with the measured received power at reference distance d_0. The parameter X is a Gaussian (normal) random variable, with zero mean. Its variance is found from measured data, conventionally obtained using least-squares curve fits. Typical values for the standard deviation of X are from 6-12 dB in urban areas [C4]. The reference distance d_0 is generally chosen to be a small distance, within the far field of the antennas, and based upon the intended link range. For example, in indoor areas where maximum link distances are on the order of tens of meters, d_0=1 m, and for large outdoor terrestrial cells where maximum link distances are on the order of a few tens of kilometers, d_0=1 km [C5]. For the airport surface communication system, the link ranges are likely to be on the order of a few kilometers, hence a reference distance value of 10-50 m or so would be convenient. For the Tx antenna mounted on the ATCT, it is generally not possible to obtain measurements at 10m, so a larger value—roughly the minimum attainable with the Tx antenna atop the tower, say, 50 m—may be employed. The effect of this reference distance upon the resulting models is not critical.

We note that forms for path loss vs. distance other than (1) are occasionally used, e.g., the Okumura-Hata method [C7]. These alternative forms are typically based on *large* amounts of empirical data, with multiple correction factors for different antenna heights, terrain types, etc. We are not planning to develop such a detailed model under this project, and plan to employ the simple and effective form of (C1).

For the CIR measurements, the calibration is not done during the warm-up period, but takes place during data post processing. This amounts to determination (calculation) of the approximate noise median value, from which we can compute the noise standard deviation. This will enable the setting of a threshold, below which all measured "multipath impulses" will be considered as being attributable to noise. This also ensures that the probability of mistaking a noise "spike" for an actual multipath echo is small; we have selected this probability to be 1/1000 for each PDP. In regard to noise, two types of noise are of concern: (1) receiver thermal noise, which is well modeled as Gaussian, with zero mean; and (2) impulsive noise, often from other nearby electronics, e.g., automotive ignitions. The threshold referred to above pertains to thermal noise. The presence of impulsive noise will be ascertained during data processing, by comparing channel multipath values in consecutive PDPs—a true multipath echo will likely be present in multiple consecutive PDPs, whereas a burst of impulsive noise will not.

During actual CIR measurements, the total range of delays over which the sounder "searches" for multipath components can be adjusted. This also has the effect of changing the rate at which the sounder outputs PDPs. Typically for the first measurement run we employ the full delay range of the sounder (approximately 5.1 microseconds). After inspection of the actual delay spreads obtained in this initial measurement run, we can reduce the delay range for subsequent runs. Reduction of the delay range enables PDPs to be collected at a faster rate, which allows more PDPs to be collected in a given time. Yet, for large airports, with large reflectors (buildings and large planes), multipath echo delays of several microseconds have been observed, hence we generally employ the full delay span, unless confident that for a given travel segment in the local environment, reduction of this delay span is not going to cause an ambiguity in the measured value of delay.

Other calibrations that are of use include determination of antenna and cable parameters primarily gain/loss, and for the antennas, the radiation patterns. We have this information for all our cables and antennas.

C.2.4 Diurnal and Seasonal Considerations

Although we do not expect significant changes in channel characteristics from atmospheric effects on a diurnal basis, the local scattering environment, particularly that attributable to airport ground vehicles, may change substantially over the course of a day. Since airport traffic has both "peak" and "slow" times, it would be advantageous to conduct some measurements during both of these types of times. Thus, we try to take a set of measurements during a "busy" time of day, and repeat the measurements—with all configurations and routes as identical as possible to the "busy" time measurements—during a "quieter" time, for example early afternoon hours. Clearly this will require the appropriate coordination with airport personnel, and some restrictions may apply. In Cleveland, we took measurements during both mid-morning and late afternoon, with the latter being the busier time. Since the most severe channel effects are expected during the busiest times, measurements during the "quietest" times (e.g., very late at night or early morning) are of lesser interest.

Similarly, it is of interest to characterize the channel at different times of year. In contrast to the situation with diurnal changes, seasonal changes may yield effects primarily due to weather, and not to local scatterers (airport vehicles). For example, in northern US latitudes during the winter, plowed snow on the sides of runways may create significant scattering surfaces that are not present at all during the other seasons of the year. Gathering measured data during different seasons may not be possible.

C.2.5 Personnel

Conducting the tests will require several participants. For the mobile van, this will mean at minimum a driver and a person to operate and observe the receiver data collection. We have found that it is advantageous to have one additional person in the mobile van, to act as a coordinator and note taker. Likewise, operating the transmitter, and making sure all is configured properly and proceeding as expected, will require at least two people. Having at least one additional person to assist (at both Tx and Rx) would be highly desirable to help with communication and any unforeseen problems.

From Ohio University, the following personnel will be involved in the testing:

David W. Matolak	PI, OU Assoc. Prof.	US Citizen
Nicholas T. Yaskoff	Graduate (MS) student	US Citizen
Indranil Sen	Graduate (Ph.D.) student	non-US Citizen
Wenhui Xiong	Graduate (Ph.D.) student	non-US Citizen

We expect for some, if not all of the testing, to have additional ACAST project personnel available for assistance: from NASA Glenn Research Center (GRC), Lawrence Foore, and from the Federal Aviation Administration (FAA), Rafael Apaza. In addition, at all airports we have

taken measurements, local airport personnel have contributed to the testing, and this has been both helpful and appreciated.

C.3 Test Equipment

Table C1 lists the primary equipment required for the testing, and some descriptive comments. Not listed is the mobile van, or any items required for shipping or transport of the equipment.

Table C1. Description of major equipment items for channel sounding.

Equipment	Comments
1. BVS Wireless Channel Sounder (modified "Raptor") Either 25 Mchips/sec or 50 Mchips/sec, with multiple center frequencies in the MLS extension band, and adjustable transmitter output power. Typically operated in the 50 Mchips/sec mode, at full power.	• Two units: one Tx and one Rx, each approximately the size of a small suitcase • AC power supply for Tx • AC power supply for Rx • Battery belt for Rx, and battery charger • Power supply cables (one for Tx, one for Rx), and corresponding AC power cords • Serial port cable (for Rx) • Software CD (for Rx, already loaded onto laptop) • Manual • Specifications given in Appendix A
2. Agilent Spectrum Analyzer, model E4404B ESA-E series spectrum analyzer. Frequency range: 9 kHz -6.7 GHz	Output plots to floppy diskette, also GPIB (not currently configured) or RS-232 serial port. Usage not necessary unless some in-band interference suspected.
3. Antennas	• Mobile Mark omnidirectional monopoles, above ground plane, with radome; gain ~1.5 dBi • Monopoles (supplied by BVS); gain ~ 1.5 dBi • Three ATM microwave horn antennas, with coaxial adaptors, two with gain 10 dBi, beamwidth ~60°, and one with gain ~18 dBi, beamwidth ~15°
4. Konica Minolta Dimage Z2 digital camera	1GB memory card, AC power supply, and USB cable
5. Miscellaneous RF equipment	• Low loss RF cables with type N connectors • Attenuators and adaptors, type N
6. Laptop PCs	Gateway Model 450EB+, 1.6 GHz, 768 MB DRAM, extra batteries, recovery DVDs

Also not listed in Table C1 are other miscellaneous items that are essential to the conduct of the measurements. This includes two sets of Motorola "Talkabout" T5200 walkie-talkies, a toolbox with general purpose electrical tools (pliers, screwdrivers, etc.), spare batteries for the digital camera and walkie-talkies, additional spare RF cables, blank recordable CDs for permanent recording of logged data, a tripod, our transmitter mounting platform, several rolls of various types of tape, carrying bags, boxes, etc.

C.4 Path Loss Measurements

The general procedure we plan to follow is listed in this section. This procedure is described in greater detail in Section C7. For mobile measurements, both the Tx and Rx personnel need to know the measurement route and approximate travel time before beginning. This can be adjusted as needed. An aerial photograph of the JFK Airport, with numbered test points, is provided in Figure C2. We generally plan to proceed to the test points in numerical order, but this is not essential. Upon commencement of measurement, a data file is created, which contains the end points of the segment of the route, e.g., for travel from points 1 to 2, the file is tagged with a "1to2" label. Upon reaching a numbered point, we stop travel, and store the file, and open a new file for travel along the next segment. Typical stopping times are on the order of one minute. For the first run, marks can be painted on the airport surface at the measurement points.
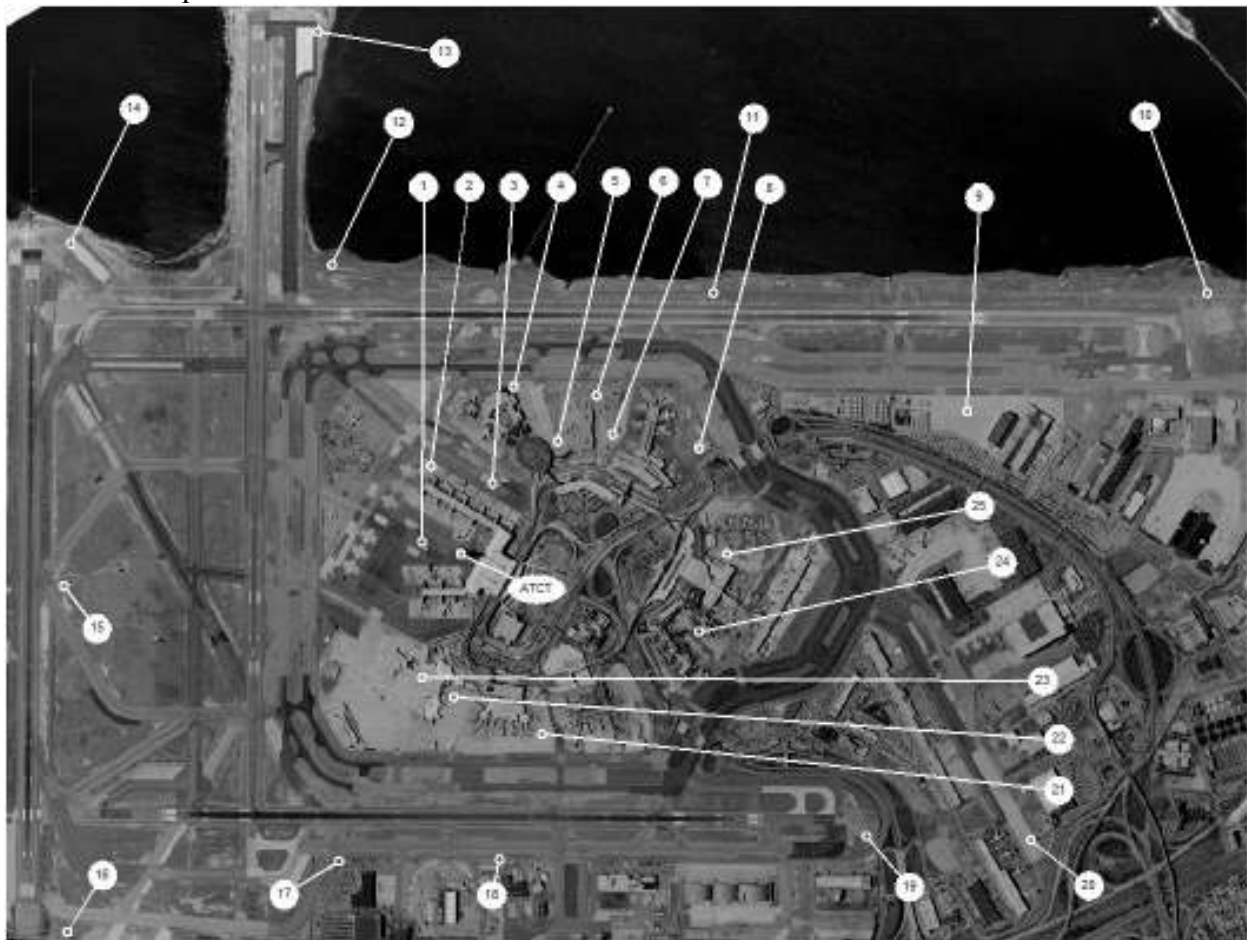

Figure C2. Aerial photograph of JFK International Airport and numbered measurement test points.

Here we describe the steps involved for measurement for mobile testing. The testing for data aimed at fixed-site (point-to-point) communications will be a subset of the steps for the mobile testing. Throughout testing, identification of line-of-sight (LOS) and non-LOS conditions are logged in time to enable parsing of the collected data into these two categories.

1. Meet with airport personnel, discuss plans for testing, set up Tx site. Begin Tx-Rx training.
2. Revise testing, route, etc., according to local airport requirements
3. Mount receiver antenna in mobile van.
[Optional: 4. Turn on spectrum analyzer and conduct spectrum survey (adjacent to Tx or Rx). Record spectrum data.]
5. If done, when spectrum survey complete, and Tx-Rx training completed, separate Rx and convey to mobile van (keeping powered via battery)
6. Find PL at reference distance, for several points near the Tx location.
7. Data collection
       a. Obtain GPS lock at both Tx and Rx
       b. Begin mobile van travel along route, and log PL data
       c. Adjust route or velocity to repeat at additional routes or distances
       d. Periodically take photographs of the local environment, and note observations such as obstruction of LOS, nearby vehicles moving, etc.
8. Review and discuss observations and results; repeat parts of data collection if needed

C.5 CIR Measurements

As with the PL measurements, calibrations must be completed before CIR measurements can be taken. During the sounder "warm-up" period, initial estimates of absolute delay (corroborated by analysis based upon the measurement geometry and physical principles) may be obtained, although absolute delay is not of primary interest in channel modeling. We approximate the noise threshold precisely during data post-processing. One of the first calibrations is a type of "sanity" check regarding the observed PDPs: this amounts to ensuring that, given the observed physical environment, the PDPs do not exhibit any unrealistic values of delay. (For example, for an LOS environment, we should see one strong multipath component at a small value of delay, and if the link is a short range one, the maximum delay should also be small—this delay can also be estimated analytically.) This sanity check is completed quickly.

The actual data collection for CIRs will be done concurrent with the PL data collection. The general steps involved are essentially the same as those described for PL data collection in the previous section. Step 7.b would replace "…log PL data" with "…log CIR data." As with the PL measurements, collecting CIR data with directional antennas, to obtain CIR information as a function of spatial (azimuthal) angle, is useful, and this is done, as feasible, at several selected fixed locations on the airport surface in a non-mobile setting.

To obtain information on the channel time rate of change (quantified by the coherence time t_c, or its reciprocal, the Doppler spread f_D), requires analysis of the PDPs over time [C8]. The maximum Doppler spread discernable is one for which f_D is less than twice the sampling rate, where the sampling rate is the output, or update rate, of the PDPs from the sounder. The enhanced sounder software enables us to adjust this sampling rate, from its smallest value of once per 0.5 seconds (2 Hz), to its largest value of once per 16 milliseconds (62.5 Hz). These values apply to the 50 Mcps signaling rate. During conduct of the CIR measurements, we observe the delay profiles on the laptop computer screen. The maximum delay range of the sounder is 5.1 microseconds (5.1 μs). At this delay range, the sounder outputs one PDP every 0.5 second. This range of delay corresponds to path length differences of approximately 1.53 km

(between the first observed, e.g., LOS component, and a reflected, scattered, or diffracted component). This distance difference is unlikely to be present for many of the short range settings, but can be encountered when very large buildings are present. Thus as noted previously, if appropriate, we can reduce the range of delay values over which the PDPs are taken, and consequently increase the update rate.

What this means in terms of the testing is that once we begin measurements, we will have some understanding of the maximum delay incurred for a given local area (by local area we would mean for example an area over which we have purely LOS conditions, or purely NLOS conditions, etc.). With this knowledge, we can reduce the delay range and consequently increase the data update rate. We adapt this (delay range, update rate) setting accordingly.

C.6 Test Equipment Specifications and Configurations

C.6.1 BVS "Raptor" Channel Sounder Specifications

The wireless channel sounder was purchased from Berkeley Varitronics Systems, Inc. The information below was received by email on 7 October 2004, from Gary Shober, CTO of Berkeley Varitronics.

TO:
  David W. Matolak, Ph.D.
  Assistant Professor
  School of Electrical Engineering & Computer Science
  322E Stocker Center
  Ohio University
  Athens, OH 45701
  phone: 740-593-1241
  fax: 740-593-0007
  email: matolak@ohiou.edu

October 7, 2004   Custom Raptor quote #242175r

The cost for a Raptor 25MC/s with 4X oversampling we discussed with transmitter and receiver tuning the 5.090 to 5.250 GHz ISM band at $67,000 complete**, including the two Rubidium oscillators and a GPS 12- channel receiver on the Raptor receiver. Delivery would be 5-6 weeks, ARO.

RF Specifications (transmitter):

Transmit Frequency	5.090 to 5.250 GHz
Frequency Synthesizer Step size	± 25 MHZ
Transmit Power (Maximum)	+33 dBm (2.0 watts)
Transmit Power (Minimum)	+6 dBm (4.0 mw)
Power Control	± 1.0 dB steps
Transmit Power accuracy	± 1.0 dB
Modulation Bandwidth	50 MHz
Modulation Type	BPSK (same I&Q on PN)
Code Length:	255 chips @ 25 Megachips/sec
Code Length:	510 chips @ 50 Megachips/sec
Transmitter Power Requirements:	+12 volts DC from vehicle or 117 volts AC for switching power supply (incl)
RF Connection:	"N" type female bulkhead mount

RF Specifications (receiver):

RF Band-width:	5.090 to 5.250 GHz
Synthesizer step:	25 MHz
Receiver Dynamic Range:	- 20 dBm maximum - 85 dBm minimum
Receiver RSSI (Receiver Signal Strength Indication):	- 85dBm minimum
Baseband Bandwidth:	50 MHz
Multipath Delay Resolution (1):	40 ns at 25 Megachips/sec
Multipath Delay Resolution (2):	20 ns at 50 Megachips/sec
Code Rate:	25 Megachips/sec with 4X oversampling
Code Rate:	50 Megachips/sec with 2X oversampling
System Synchronization:	Rubidium Standard in both Rx and Tx
Clocking Accuracy*:	10^{-9} without clock training
Clocking Accuracy*:	$5*10-12$ after slaving the Rubidium Transmit clock to the Receiver Rubidium clock
Multipath Power Dynamic Range:	-16 dB minimum
GPS Receivers:	Both Transmitter and Receiver will include GPS 12 channel receivers for navigation
Unambiguous Delay:	10.2 μs, or a distance of 10,000 feet
Time of arrival measurement:	10ns. (w/o post processing to calculate sub-sample position)
Maximum Jitter:	10ns (with standard deviation < 5ns)
Receiver Power Requirements:	Portable battery powered, 12 volts DC at 20 watts running power, 75 watts at start for Rubidium warmup
PC Interface:	DB-9 RS-232C interface at 115 kbaud
RF Connection:	"N" type female bulkhead mount

*both the transmitter and receiver will clock from a Rubidium oscillator which can be phase-trained (master/slave fashion) to align precisely one to the other.

C.6.2 Channel Sounder Photographs and Example Outputs

Figure C3 displays the Raptor receive and transmit units side-by-side. This photograph was taken in the Multiuser Mobile Communications Laboratory (MMCL), in the School of Electrical Engineering and Computer Science (EECS) at Ohio University.

Figure C3. Raptor Channel Sounding System (Left – Receiver, Right – Transmitter).

Figure C4 displays the Raptor transmit configuration as seen in the MMCL. Note that the transmitter is connected to an omni antenna. These antennas have an approximate 1.6 dBi gain.

Figure C4. Raptor transmitter and omni antenna.

In Figure C5, we show the Raptor receiver configuration as seen in the MMCL.

Figure C5. Raptor receiver, omni antenna, and data logging laptop.

As noted in [C2], the desired output from the receiver comes in the form of power-delay profiles (PDPs). The power-delay data will be post processed to determine important channel parameters such as the correlation bandwidth and RMS delay spread. The following two plots are examples of power-delay profiles obtained with the Raptor system. These data sets were obtained from indoor testing inside Stocker Center at Ohio University, on the 3rd floor (where the School of EECS resides), so the measured values of delay spread are small, as expected.
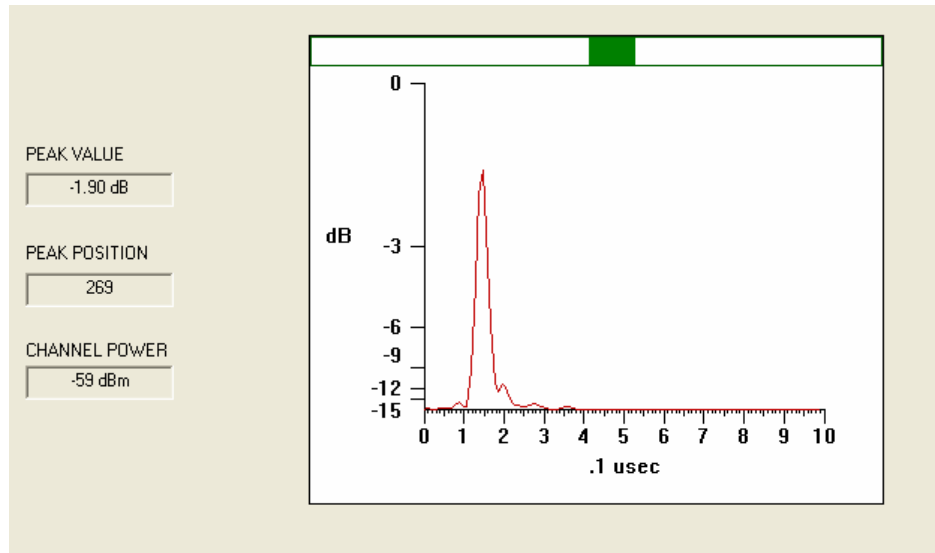

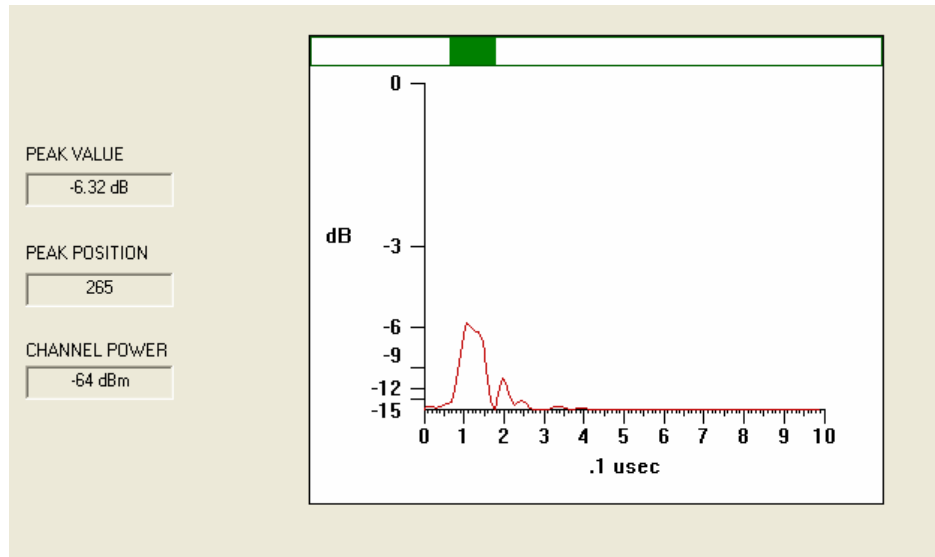**Figure C6**. Power-delay profile, indoor, minimal multipath.

Figure C7. Power-delay profile, indoor, observable multipath.

The first plot (Fig. C6) displays a strong Line-of-Sight (LOS) component, with some correlated power received afterwards. There was no significant multipath component from this collection. The second plot (Fig. C7) shows not only a primary component, but a secondary echo that is 5-6 dB down from the primary. This demonstrates the Raptor's capability to discern multipath components.

These PDPs are those which actually appear on the display of the PC, when employing the Raptor SW. This display has a limited dynamic range of 16 dB, significantly smaller than the usable dynamic range of the collected data. As an example illustration of this, Fig. C8 shows a PDP obtained in an LOS environment at the Cleveland airport (after data processing). The plot is received power in dBm versus delay in microsec. The dynamic range is greater than 30 dB.
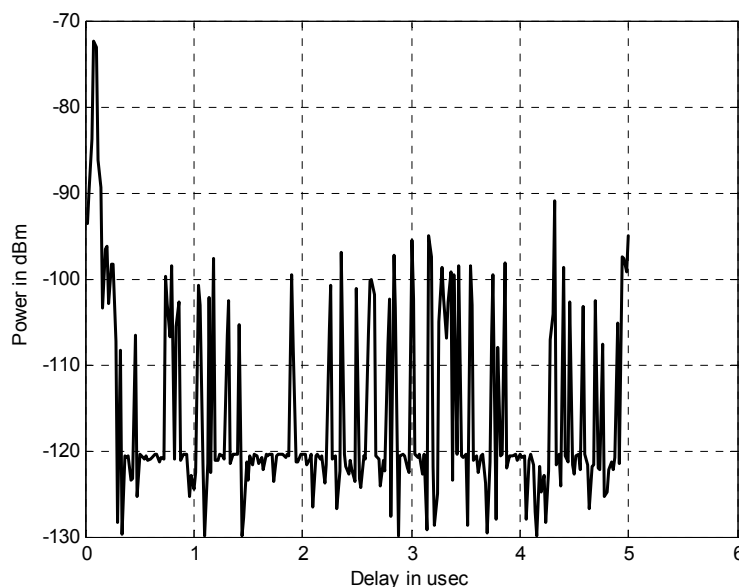

Figure C8. Power-delay profile, in LOS setting at Cleveland airport.

Shown in Figure C9 is a plot of the transmitted power spectrum. The signal is set to transmit at 50 Mcps, and from the display (averaged over ten sweeps across the 100 MHz bandwidth), the 99% power bandwidth of the signal is approximately 52.76 MHz.
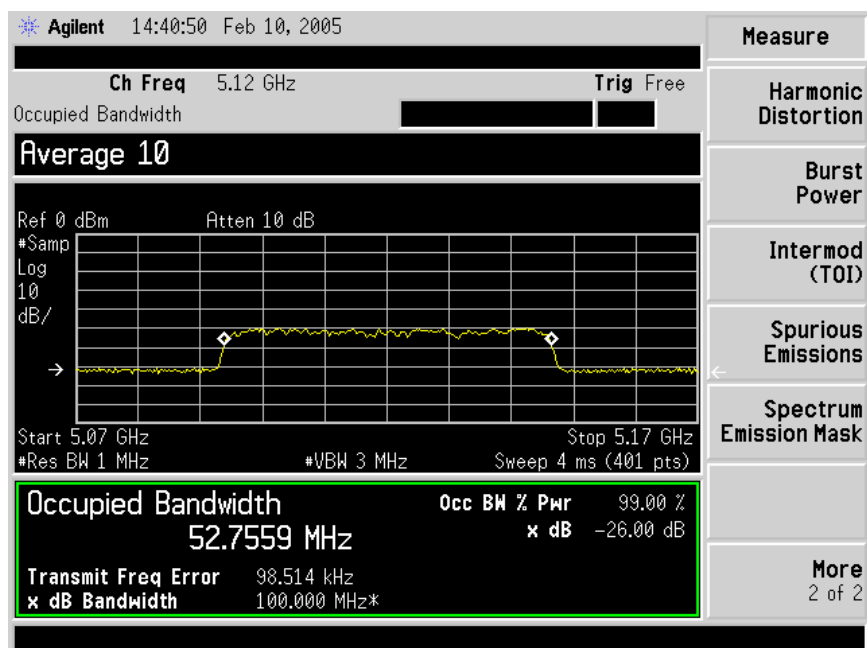

Figure C9. Transmitted power spectrum, 50 Mcps setting, f_c=5.12 GHz.

C.7 Detailed Test Procedures

In this section, we provide description of detailed test procedures and estimates of time durations required for these procedures. The procedures are divided into four categories: physical setup; initialization and training; sounding (mobile); and sounding (point to point, non-mobile). Table C2 describes the test procedures required for physical setup, and for measuring the local interference spectrum. The entire set up procedure should be completed <u>before</u> the initialization (Tx/Rx training) period. This is because even when the Tx and Rx are connected back to back through a cable, the Tx emits some small amount of "leakage" power, with PSD essentially that of the actual transmitted signal. Worth noting is that the interference characterization—if conducted at all—need only be conducted once, or possibly twice (once at the tower, and once on the ground).

Table C2. Test procedure for physical setup and interference characterization phase.

#	Procedure Description	Estimated Duration (minutes)	Notes
	Physical Setup	~15	*Completed during Tx/Rx training period*
1	For mobile receiver, attach omni antenna to van roof, and connect to RF cable, run to van interior. Repeat for horn antenna if needed.	5-7	Horn antenna should have main lobe pointing to either *side* of van. Generally, horns not used in mobile testing.
2	For stationary transmitter, attach omni antenna to mounting location. Horn antenna may also be mounted (single platform). Downtilt omni by ~45°	5-8	Mount on platform (weighted or anchored in some fashion for stability, if needed).
	Interference Spectrum Measurement	19-22	*Completed BEFORE Tx/Rx training period*
1	Connect spectrum analyzer (SA) to omni at Tx site, and power up SA.	2	For additional interference measurement, SA should be used *at Rx site*, to obtain spectra on the ground.
2	Set SA f_c=5120 MHz, span 60 MHz, resolution BW=100 kHz, attenuation 0 dB, 10 dB/division	2-5	Resolution BW may be varied, to capture several spectral plots.
3	Observe MLS extension band power spectrum, and record for various settings of resolution and video bandwidths.	10	Employ averaging; if some signals are evident, max hold mode of display may be useful.
4	Widen frequency span, and observe spectrum; record if any appreciable signals observed.	5	

For the initialization, which requires the transmitter and receiver be connected in a back to back mode, via cable, through an attenuator, for stabilizing and locking the precision oscillators, the test procedure is provided in Table C3. Note that some procedures can be completed simultaneously, because of the different durations. A diagram of the configuration used for training is given in Figure C10.
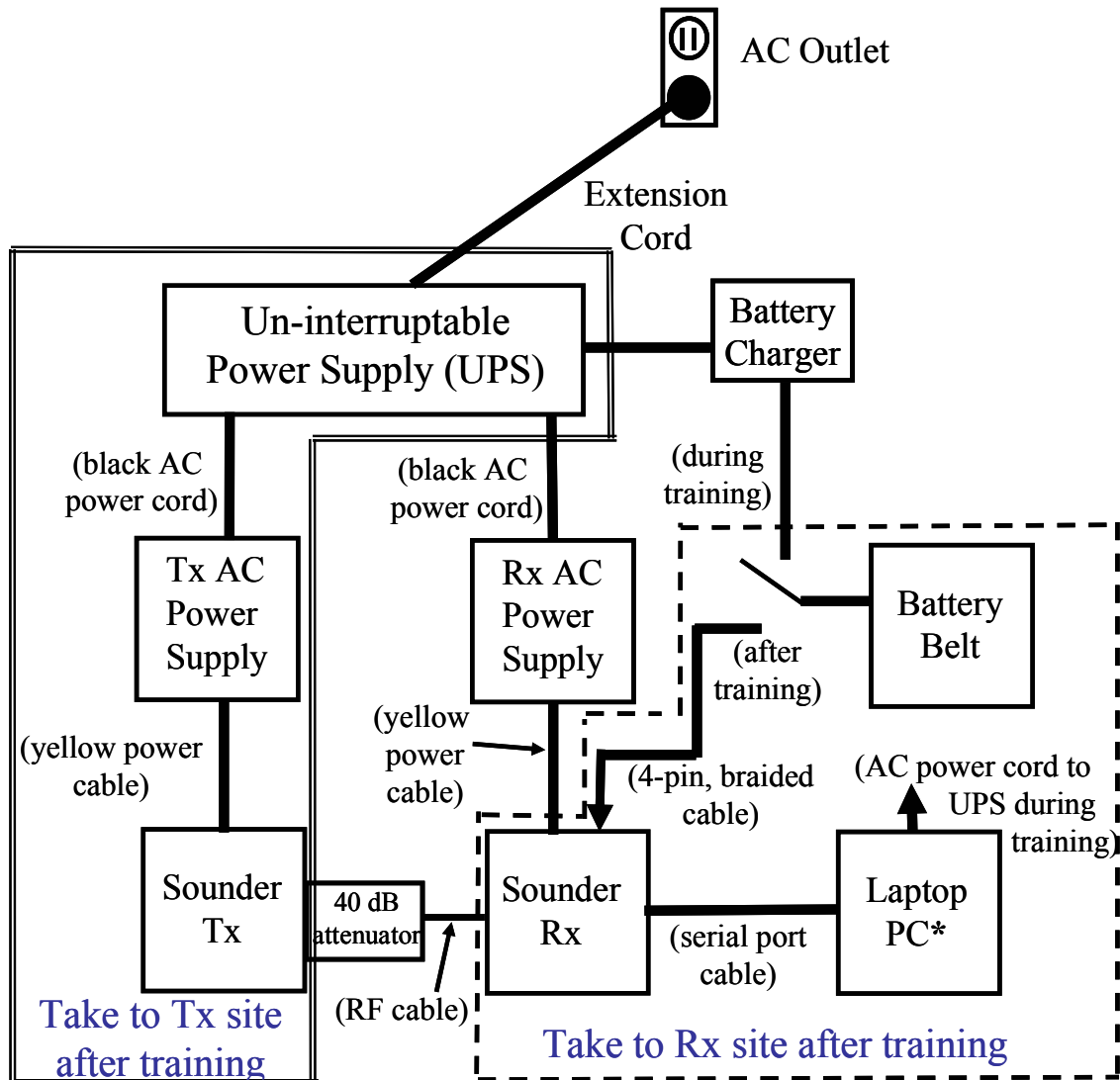

Figure C10. Connection diagram for sounder training.

Notes:

1. Items within box bounded by double line to be taken from training site to Tx site upon completion of training. Items within box bounded by dashed line to be taken to Rx site (fixed or mobile) upon completion of training.

2. The 4-pin, braided cable must be connected to the sounder Rx and battery belt BEFORE the yellow power supply cable is removed from the sounder Rx ("make before break"). Battery charger must be disconnected before the 4-pin cable connects to battery belt.

2. The 40 dB attenuator is used only for training, and should be disconnected from the sounder Tx before moving to the Tx site.

3. * indicates that Laptop PC should be connected to UPS (or AC outlet) for its AC power during training, and Laptop will operate on its battery during sounding measurements.

Table C3. Test procedure for initialization and training phases.

#	Procedure Description	Estimated Duration (minutes)	Notes
	Initialization and Training	45-105	Training (step 13) can be conducted overnight, in which case total duration is of course increased.
1	Position Tx platform, Tx and its power supply, and connect	5	If training to be conducted overnight, Tx need not be on the transmitting platform.
2	Turn on Tx power (not RF), and warm up	3	
3	Connect laptop to Rx, and power up laptop	0	During Tx warmup
4	Connect power (both AC and battery) to Rx	0	During Tx warmup; AC power provided through UPS if training in location not actual transmission location
5	Turn on Rx power	0.5	
6	Connect RF cable from Tx to Rx, through attenuator	1	Use 40 dB attenuation, minimum, and ensure received power $\leq$ -10dBm
7	Set Tx RF f_c	0.25	f_c=5120 MHz
8	Set Tx output power P_{Tx}	0.25	Use P_{Tx}=+5 dBm for training; the maximum value 33 dBm is used for sounding
9	Set Tx chip rate R_c	0.25	R_c=50 Mcps
10	Turn on Tx RF power output	0.25	Again: $P_{Tx}\sim$ +5 dBm, with $\geq$40 dB attenuator between Tx and Rx for training
11	Invoke Raptor SW on Rx, and make sure display indicates "Raptor Stable," "Raptor Locked," and received power $P_{Rx}>$ "-3 dB"	2	

12	Configure Raptor Rx SW
	    a. set f_c and R_c to match those of Tx
	    b. initiate training
		1	During training, do NOT change any settings or display on laptop

13	Train for desired duration, depending upon desired measurement duration	30-90+	Measurement duration displayed via max(Current Count, Last Count)

In Table C4, the test procedures for the actual (mobile) channel sounding are provided. This includes the procedures for the transition between training mode and measurement mode. All mobile measurement runs employ omnidirectional antennas at both the Tx and Rx.

Since the Rx GPS must be turned off when the number of points in the PDP is reduced below the full number, if the reduced delay span is employed, GPS location information will not be logged except at the designated measurement location points. For modeling path loss vs. distance, this will reduce the number of data points (to the total number of measurement location points). Because of this, as noted in the main body of this test plan, it is desirable to conduct a complete sounding (at all location points and during travel between them) with the sounder set to log the maximum number of points (full delay span). This yields an update rate of 2 PDPs/second, but allows each RSSI measurement to contain an associated GPS tag, hence enabling a much richer set of data for modeling path loss. The procedure for the "full span RSSI only" soundings is essentially the same as that in Table C4, but without turning off the GPS at the Rx at any time.

Table C4. Test procedure for transition from training to measurement, & mobile channel sounding phase.

#	Procedure Description	Estimated Duration (minutes)	Notes
	Transition and Sounding	95-110	*Begin this procedure <u>after</u> desired training duration, when ready to begin mobile tests.*
1	Ensure that the Rx is connected to the charged battery pack	0.5	Secure the battery pack cable connection to the 4-pin cable leading to Rx via tape.
2	At the Rx laptop pc, click on the box to "accept" the Raptor training value.	0.5	Note training value and convert to minutes of measurement time. Note time that training stopped (beginning of measurement time).
3	At the Tx, turn off the RF transmission power, and disconnect RF cable from sounder Rx.	0.5	Keep Tx powered up!
4	Rx Team: Gather battery pack and Rx cables together for imminent transport; also gather laptop pc, in its case.	1	
5	Rx Team: Connect <u>charged</u> battery pack to Rx through 4-pin cable, then disconnect the AC power supply from the Rx. Begin transport or Rx, pc, and battery and cables, to mobile van	10	ENSURE battery does not become disconnected during transport, and use caution not to stress cables. Also ensure that both Tx Team and Rx team have walkie-talkies and spare batteries for them.
6	Tx Team: if locations for training and transmission are different, transport Tx to location, keeping powered via UPS	5	ENSURE Tx stays powered; if needed, re-connect UPS to AC power once Tx at location. (Done during Rx Team's step #5.)
7	Tx Team: Remove 40 dB attenuator from Tx RF input, and connect desired antenna to Tx.	1	Downtilt antenna if not already done. (Done during Rx Team's step #5.)
8	Tx Team: Once set in place, ensure f_c and R_c are correct, then await instructions to begin transmission from Rx team; set transmit power to maximum value (33 dBm), but still RF off	1	(Done during Rx Team's step #5.)
9	Rx Team: After step 5, transport to van is complete; set up Rx and laptop in stable position	1	Ensure physical stability of Rx and personnel during mobile travel.
10	Rx Team: connect antenna cable to Rx RF input	2	

11	Rx Team: connect GPS antenna to GPS antenna input port on Rx	1	Generally position Rx GPS antenna on dashboard of mobile Rx vehicle.
12	Rx Team: invoke the "Chameleon" SW and prepare to log data	1	
13	Rx Team: communicate readiness to log data to Tx Team via walkie-talkies, and proceed to first measurement point (PL reference location)	1	
14	Tx Team: upon receipt of message from Rx Team indicating readiness to transmit, turn on Tx RF power (P_{Tx}=33 dBm). Convey situation message to Rx team.	1	Take photos/videos of mobile van, and several views of airport surface environment
15	Rx Team: with Rx and laptop ready to log data, move van to measurement location point **1**.	1-5	If possible, during 1st measurement run, mark location points for repeatability
16	At Rx, turn GPS on and record GPS position information (GPS(1)). Then turn off GPS logging at Rx, unless full delay span sounding.	2	
17	At Rx, configure Raptor SW to measure delay span of N_p points. Record location **1** profile, and capture reference RSSI.	5	Begin with N_p on the order of 300 except for full-delay-span initial measurement run. As distance increases, and/or more large-delay multipath is observed, N_p can be increased.
18	At Rx, set up log file for initial course. Rx Team should communicate readiness to begin to Tx Team.	5	File names include date, area (e.g., JFK), antenna types, LOS or NLOS, and terminal points (e.g., from point **1** to point **2**, label 0102)
19	Begin moving from location point **1** to point **2**, and observe Rx display. Log power delay profiles (PDPs).	5	Tx team should communicate to Rx team impending change of location from LOS to NLOS. Rx team should communicate to Tx team the reverse condition. Rx team should also take notes on environment characteristics.
20	When location point **2** reached, stop van, end PDP logging.	2	Both teams should communicate status, and convey any descriptions of problems, anomalies, etc.
21	Turn GPS Rx on, and log GPS information (GPS(2)). Turn off GPS.	5	
22	Create new Rx log file, and move from	5	

	location point **2** to point **3**, and log PDPs.		
23	Repeat steps 20-22 for the remaining measurement location points.	~45	

Finally, Table C5 provides the test procedures for the non-mobile, point-to-point measurements. The goal with these measurements is to obtain information on the received power and delay statistics as a function of spatial angle, using horn antennas at both Tx and Rx.

Table C5. Test procedure for non-mobile (point to point) channel sounding tests.

#	Procedure Description	Estimated Duration (minutes)	Notes
	Point to Point (non-mobile) Measurements	40	*Description is for a single location.*
1	Ensure training was long enough to conduct these measurements, or re-train as per Table B.2. When training complete, proceed with steps for transition from training to measurements.	10	Note available measurement time and start time.
2	Configure stationary Tx to use horn antenna. Aim antenna directly toward Rx location point.	3	Tx team can do this while Rx team is traveling to location. Tx assumed secure in position.
3	Configure stationary Rx to use horn antenna. Secure Rx, laptop, and GPS antenna.	5	Horn antenna will be high-gain horn, mounted on tripod, with adjustable azimuth angle.
4	Set Tx to transmit at full power, 50 Mcps rate, f_c=5120 MHz, and turn RF on.	1	
5	With Rx horn aimed at Tx (azimuth angle θ=0), initiate measurement of RSSI and PDP, using full delay span (maximum N_p), and record GPS information. Optimize elevation angle of both Tx and Rx antennas.	3	Full delay span may NOT be needed, particularly if after mobile measurements, we have high confidence that maximum delay spread is less than 5 microsec
6	At Rx, if desired, reduce delay span to capture main multipath, and log approximately 30 seconds worth of PDP data.	3	Ensure log file name reflects Point-to-Point data, site location, and use of high-gain antenna.
7	Rotate Rx antenna by $\theta°$ and repeat step#6 for all attainable angles.	15	Angle θ will depend upon antenna platform limitations. Approximate value of $\theta_{min}=15°$ to be used.

C.8 References

[C1] NASA ACAST project website, http://acast.grc.nasa.gov/ , 11 January 2005.
[C2] D. W. Matolak, "Wireless Channel Characterization: Overview and Application to 5 GHz Band Airport Surface/Terminal Environments," Ohio University Report for NASA Glenn Research Center, May 2004.
[C3] Berkeley Varitronics, Inc., website, http://www.bvsystems.com/ , 11 January 2005.

[C4] G. Stuber, *Principles of Mobile Communications*, 2nd ed., Kluwer Academic Publishers, Norwell, MA, 2001.

[C5] J. B. Anderson, T. S. Rappaport, S. Yoshida, "Propagation Measurements and Models for Wireless Communications Channel," *IEEE Comm. Mag.*, vol. 33, no. 1, pp. 42-49, January 1995.

[C6] S. Stein, "Fading Channel Issues in System Engineering," *IEEE Journal on Selected Areas in Comm.*, vol. SAC-5, no. 2, February 1987.

[C7] J. D. Parsons, *The Mobile Radio Propagation Channel*, 2nd ed., John Wiley & Sons, New York, NY, 2000.

[C8] R. J. C. Bultitude, "Estimating Frequency Correlation Functions from Propagation Measurements on Fading Channels: A Critical Review," *IEEE JSAC*, vol. 20, no. 6, pp. 1133-1143, August 2002.

Appendix D: Detailed Channel Models (CD 1)

D.1 Matlab Routines and Documentation; Summary of CD Contents
D.2 Multi-variate Weibull random variable generation

Appendix E: Measurement Files (CD 2)

Appendix F: Measurement Photographs (CD 3)